Capturing the Energy Absorbing Mechanisms of Composite Structures under Crash Loading

Bonnie Wade

A dissertation submitted in partial
fulfillment of the requirements for
the degree of Doctor of Philosophy

University of Washington
2014

Reading Committee:
Paolo Feraboli, Chair
Kuen Lin
Larry Ilcewicz

Program Authorized to Offer Degree:
Aeronautics & Astronautics Engineering

University of Washington

Abstract

Capturing the Energy Absorbing Mechanisms of Composite Structures under Crash Loading

Bonnie Wade

Chair of Supervisory Committee:
Professor Paolo Feraboli
Department of Aeronautics and Astronautics Engineering

As fiber reinforced composite material systems become increasingly utilized in primary aircraft and automotive structures, the need to understand their contribution to the crashworthiness of the structure is of great interest to meet safety certification requirements. The energy absorbing behavior of a composite structure, however, is not easily predicted due to the great complexity of the failure mechanisms that occur within the material. Challenges arise both in the experimental characterization and in the numerical modeling of the material/structure combination. At present, there is no standardized test method to characterize the energy absorbing capability of composite materials to aide crashworthy structural design. In addition, although many commercial finite element analysis codes exist and offer a means to simulate composite failure initiation and propagation, these models are still under development and refinement. As more metallic structures are replaced by composite structures, the need for both experimental guidelines to characterize the energy absorbing capability of a composite structure, as well as guidelines for using numerical tools to simulate composite materials in crash conditions has become a critical matter.

This body of research addresses both the experimental characterization of the energy absorption mechanisms occurring in composite materials during crushing, as well as the numerical

simulation of composite materials undergoing crushing. In the experimental investigation, the specific energy absorption (SEA) of a composite material system is measured using a variety of test element geometries, such as corrugated plates and tubes. Results from several crush experiments reveal that SEA is not a constant material property for laminated composites, and varies significantly with the geometry of the test specimen used. The variation of SEA measured for a single material system requires that crush test data must be generated for a range of different test geometries in order to define the range of its energy absorption capability. Further investigation from the crush tests has led to the development of a direct link between geometric features of the crush specimen and its resulting SEA. Through micrographic analysis, distinct failure modes are shown to be guided by the geometry of the specimen, and subsequently are shown to directly influence energy absorption. A new relationship between geometry, failure mode, and SEA has been developed. This relationship has allowed for the reduction of the element-level crush testing requirement to characterize the composite material energy absorption capability.

In the numerical investigation, the LS-DYNA composite material model MAT54 is selected for its suitability to model composite materials beyond failure determination, as required by crush simulation, and its capability to remain within the scope of ultimately using this model for large-scale crash simulation. As a result of this research, this model has been thoroughly investigated in depth for its capacity to simulate composite materials in crush, and results from several simulations of the element-level crush experiments are presented. A modeling strategy has been developed to use MAT54 for crush simulation which involves using the experimental data collected from the coupon- and element-level crush tests to directly calibrate the crush damage parameter in MAT54 such that it may be used in higher-level simulations. In addition, the

source code of the material model is modified to improve upon its capability. The modifications include improving the elastic definition such that the elastic response to multi-axial load cases can be accurately portrayed simultaneously in each element, which is a capability not present in other composite material models. Modifications made to the failure determination and post-failure model have newly emphasized the post-failure stress degradation scheme rather than the failure criterion which is traditionally considered the most important composite material model definition for crush simulation. The modification efforts have also validated the use of the MAT54 failure criterion and post-failure model for crash modeling when its capabilities and limitations are well understood, and for this reason guidelines for using MAT54 for composite crush simulation are presented.

This research has effectively (a) developed and demonstrated a procedure that defines a set of experimental crush results that characterize the energy absorption capability of a composite material system, (b) used the experimental results in the development and refinement of a composite material model for crush simulation, (c) explored modifying the material model to improve its use in crush modeling, and (d) provided experimental and modeling guidelines for composite structures under crush at the element-level in the scope of the Building Block Approach.

Acknowledgements

I would like to express my sincere gratitude to the Federal Aviation Administration (FAA) and The Boeing Company, for providing technical guidance and for supporting me financially throughout the time of my doctorate. To Dr. Larry Ilcewicz (FAA), who granted my invaluable exposure to aircraft certification in collaboration with industry leaders, and who has always been deeply supportive of my scholarly efforts and personal wellbeing; to Dr. Mostafa Rassaian (Boeing Research & Technology), who generously shared his expertise in crash simulation, provided teaching and guidance, and who was an invaluable liaison with the analysis community without which I could not have completed my research, nor my dissertation; and to Allan Abramowitz (FAA) who provided guidance and important feedback in my experimental work.

My graduate studies and research was conducted in the *Automobili Lamborghini* Advanced Composite Structures Laboratory (ACSL) which provided the ultimately unique setting and opportunity to explore the very cutting edge of composite technologies. My research simply would not have been possible without the ACSL, and I am deeply thankful to have received the generous support of Maurizio Reggiani, Luciano DeOto and Attilio Masini (Automobili Lamborghini S.p.A). È stato davvero un piacere avere l'opportunità di lavorare e imparare dai miei colleghi italiani. Grazie mille.

Finally, I will forever be thankful and humbled to have received the guidance and support of my advisor, Dr. Paolo Feraboli. Under his guidance, I have grown intellectually, professionally, and personally in such a manner I could have never anticipated. I owe the completion of this body of research to his boundless support, leadership, and encouragement. His passion has inspired me deeply and I am truly honored and privileged to have been his student at the ACSL.

Table of Contents

List of Tables

List of Figures

Abbreviations

ACAP	Advanced Composite Airframe Program
ACC	Automotive Composites Consortium
AGATE	Advanced General Aviation Transport Experiment
BBA	Building Block Approach
CFC	Channel Frequency Class
CFRP	Carbon fiber reinforced plastic
CLT	Classical laminate theory
CMH-17	Composite Materials Handbook (Formerly MIL-HDBK-17)
DLR	German Aerospace Center
EA	Energy absorption
FAA	Federal Aviation Administration
FEA	Finite element analysis
LaRC	NASA Langley Research Center
NASA	National Aeronautics and Space Administration
NLR	National Aerospace Laboratory of the Netherlands
PW	Plain weave composite
RR	Round Robin (refers to the CMH-17 Crashworthiness Working Group Numeric Round Robin)
SAE	Society of Automotive Engineers
SEA	Specific energy absorption
TCA	Toray Composites America
UD	Unidirectional tape composite
WWFE	World-Wide Failure Exercise

Notations

A	Cross-sectional area
ε_1	Local material strain, 0º -direction
ε_2	Local material strain, 90º -direction
ε_{12}	Local material shear strain
ε_1^u	Ultimate local material strain, 0º -direction
ε_2^u	Ultimate local material strain, 90º -direction
ε_{12}^u	Ultimate local material shear strain
E_1^c	Compressive elastic modulus, 0º -direction
E_1^t	Tensile elastic modulus, 0º -direction
E_2^c	Compressive elastic modulus, 90º -direction
E_2^t	Tensile elastic modulus, 90º -direction
F_1^{cu}	Ultimate compressive strength, 0º -direction
F_1^{tu}	Ultimate tensile strength, 0º -direction
F_{12}^{su}	Ultimate shear strength
F_2^{cu}	Ultimate compressive strength, 90º -direction
F_2^{tu}	Ultimate tensile strength, 90º -direction
G_{12}	Shear modulus
P_{cr}	Crush load
$\overline{P}_{cr}$	Average crush load
ϕ	Degree of curvature
ρ	Material density
σ_1	Local material stress, 0º -direction
σ_2	Local material stress, 90º -direction
σ_{12}	Local material shear stress
S	Section length
Θ	Ply angle
t	Thickness
ν_{12}	Major Poisson's ratio
ν_{21}	Minor Poisson's ratio

Introduction

Carbon fiber reinforced plastic (CFRP) composite material systems are becoming increasingly common in primary aircraft and automotive structures due to the many structural and performance advantages they provide. The introduction of advanced composites in the primary structure of modern vehicles presents certain complications for the designer dealing with occupant safety and crashworthiness. The energy absorption provided by a composite structure is not easily predicted due to the complexity of the crush failure mechanisms that occur within the material. In order to be a feasible design choice, advanced composite vehicle structures must be able to provide the same level of crash safety or better as their metallic predecessors such that the crash certification requirements are satisfied.

Both the aircraft and automotive industries require extensive structural crash testing for safety certification. The basis of these tests is to verify that the four necessary conditions for survival during a vehicle collision are preserved. These conditions are (1) maintaining sufficient occupant space, (2) providing adequate occupant restraint, (3) employing energy-absorbing devices, and (4) allowing for a safe post-crash egress from the vehicle [1]. In general, the total vehicle deformation in a crash will determine the satisfaction of these conditions, however individual structural subcomponents that are specifically designed to absorb crash energy can provide a great increase in structural crashworthiness and survivability. For this reason, structural energy absorbers can be found in all modern vehicles: in the form of collapsible tubular rails in the front end of passenger cars [2] [3] [4] [5] and collapsible floor stanchions and beams in aircraft subfloor and cargo structures [6] [7] [8], Figure 1. These structural crash elements have traditionally been made from steel or aluminum which absorb energy through controlled collapse

by folding and hinging, involving extensive local plastic deformation. The fold geometry and energy absorption of these metallic elements depend on their geometry and can be predicted with accuracy. On the other hand, composite structures fail in crash through a complex combination of fracture mechanisms including fiber fracture, matrix cracking, fiber-matrix debonding, and interlaminar damage (delamination), all of which can occur alone or in combination [9]. The combination of several brittle and plastic failure modes make the design of composite energy-absorbing crash structures difficult, and the energy absorbing behavior of composites cannot be easily predicted. Thus, extensive substructure testing is usually required in the design of crashworthy composite structures in order to verify that a proposed configuration will perform as intended.

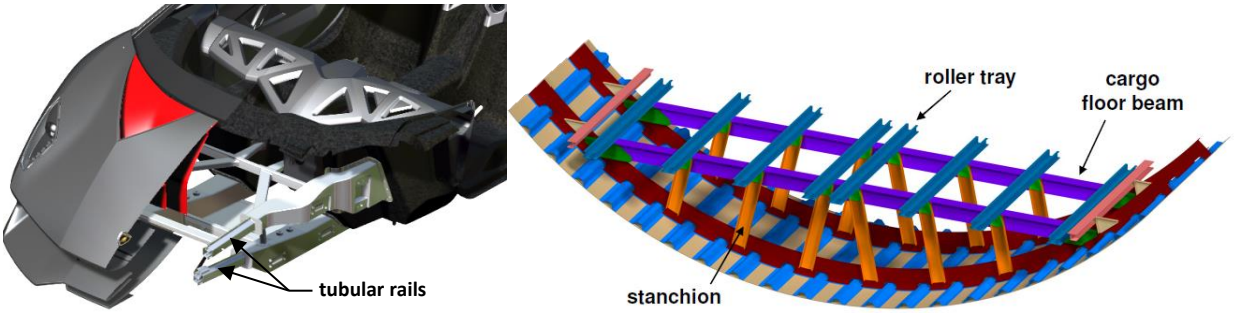

Figure 1. Crash structures in the front end of a passenger car (left) and in the subfloor of a typical Part 25 twin aisle aircraft (right).

While experimental crash testing remains an integral part of safety and certification, both the aerospace and automotive industries increasingly rely on the capability of Finite Element Analysis (FEA) codes to preemptively simulate structural tests in order to identify problems early in the design process, optimize the vehicle, and avoid excessive crash testing of costly prototype vehicles. Following a successful certification crash test, the validated FEA model is used to simulate a variety of other crash scenarios by varying parameters such as impact angle,

velocity, impactor etc. FEA models have been proven to simulate the elastic and plastic deformation of metallic structures very well and today, simulation is an indispensable part of the design and certification process, while limited experimental prototype testing is conducted to validate these simulated models [10] [11].

As metallic structures are replaced by composite structures, there is a need for a better understanding of the energy absorbing mechanisms occurring during composite crush failure. At present, there is not a standardized test method to characterize the energy absorbing capability of a composite material system because its energy absorbing mechanisms are not well understood. In addition, there is a need for the greater development of predictive tools to simulate the energy absorption capability of composite materials in FEA models. These issues pose a limitation on the wider introduction of composites in primary crashworthy structures, and impede the optimum design, safety, and performance of composite structures. The research presented here addresses both the experimental energy absorption characterization of composite materials, as well as the numerical simulation of the energy absorbing capability of composites undergoing crushing. It is the goal of this research to (a) develop and demonstrate a procedure that defines a set of experimental crush results that characterize the energy absorption capability of a composite material system, (b) use the experimental results in the development and refinement of a composite material model for crush simulation, (c) explore modifying the material model to improve its use in crush modeling, and (d) provide experimental and modeling guidelines for composite structures under crush at the element-level in the scope of the Building Block Approach.

Literature Review

Experimental characterization of composite energy absorption

Research began in the 1980's to understand the energy absorbing mechanisms of composite material systems undergoing crash failure. To this day, research in this field has focused exclusively on experimental investigation because the fundamental mechanisms that control the crushing behavior and energy absorption in composite materials are technically challenging and not well understood. In order to focus this discussion to be relevant to advanced structural composites, this review only considers CFRP systems which use a thermoset resin since these are traditionally the most common type of composite found in primary vehicle structures. These types of composite material systems experience a brittle crush failure response referred to as progressive crushing.

Before reviewing the literature on progressive crushing of composites, a brief discussion is necessary to identify the experimental parameters which define energy absorption. A simple cross-section schematic of a square tube undergoing progressive crushing due to the force F, along with a typical load-displacement curve representative of such failure, is shown in Figure 2. The cross-section in Figure 2 features the chamfered end, called a crush trigger, which prevents global buckling failure and allows for progressive crushing to initiate. The crush trigger is a necessary design feature for composites progressive crushing, and can take the form of a steeple, saw tooth, or chamfered edge machined into the coupon, or ply drop offs which also form a natural chamfer of the structure. Without the crush initiator, composite materials have a tendency to reach unacceptably high peak forces upon impact and oftentimes buckle in an unstable manner. Across experimental crush studies, it is widely accepted that a crush trigger is

crucial for composite materials, although the trigger geometry which produces the best result is not agreed upon [12] [13].

When evaluating the crash performance of a structure, the load-displacement curve from the crush experiment is analyzed, from which some key parameters can be determined:

- Peak load: the maximum point on the load-displacement diagram which initiates progressive crushing failure, noted as P_{max} in Figure 2.
- Average crush load (also referred to as the sustained crush force): the displacement-average value of the load history, noted as $\bar{P}$ in Figure 2.
- Energy absorbed (EA): total area under the load-displacement diagram.

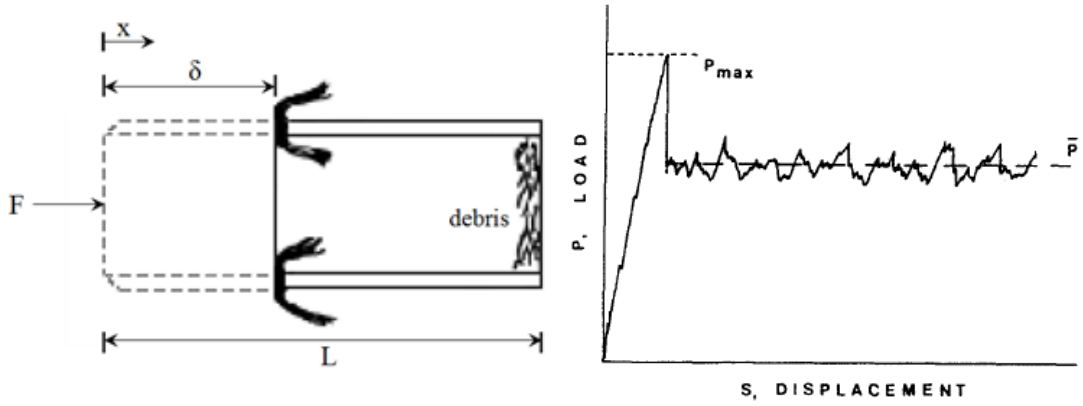

Figure 2. Schematic of composite tube with a chamfered crush initiator undergoing progressive crushing and the resulting load-displacement crush curve, from Hull [9].

Referring to the notation provided in Figure 2, the energy absorbed is given by,

$$EA = \int_0^{\delta} F \cdot dx \qquad \text{Eq. (1)}$$

The capability of a material to dissipate energy can be expressed in terms of specific energy absorption (SEA), which is the energy absorbed per unit mass of crushed structure and has units of J/g. Considering the mass of a structure that undergoes crushing as the product of the density,

ρ, displacement, δ, and cross-sectional area, A (which, in turn, is the product of the section length, S, and the thickness, t), the SEA is given by:

$$SEA = \frac{EA}{\rho \cdot \delta \cdot A} = \frac{\int F \cdot dx}{\rho \cdot \delta \cdot S \cdot t} \quad \text{Eq. (2)}$$

The SEA measured from crush testing is the primary value used to characterize the energy absorption capability of a material, and is reported by most authors reviewed here to quantify crush performance.

Most experimental research has focused on the axial crushing of thin-walled tubular specimens with chamfered crush initiators that are representative of elements found within crash structures, such as that shown in Figure 2. Such specimens are self-supporting and are therefore easy to subject to axial crush testing. Work performed to understand the physical energy absorbing failure mechanisms of progressive crushing using tubular specimens has been published by Farley and Jones [14] [15], Hull [9], Carruthers [16], and most recently reported by Bisagni [4].

To provide some perspective upon the technical challenge presented by this topic, Hull [9] states that a detailed understanding of the physical geometry of the crush zone (also called the crush front by other authors) is necessary to characterize progressive crushing. He identifies a list of several interacting variables which ultimately define the physical crush zone geometry and concludes in his paper that "a complete description of the interaction of all of these variables is impossible." This is a common conclusion amongst experimentalists in this area who uniformly recognize the technical challenge presented by composite crush failure.

In 1989, Farley and Jones [14] were two of the first researchers to attempt to develop a scientific understanding of the physical energy absorption mechanisms occurring during progressive crushing. Prior to this, the studies on composites energy absorption had consisted of reporting

the results from specific tests matrices comparing the energy absorption of one design against another. Farley and Jones identified three distinct crushing modes for which combinations of these three modes describe progressive crushing failure. These modes are transverse shearing, brittle fracturing, and lamina bending. In later publications, Farley and Jones [15] state that the brittle fracturing mode is in fact a combination of the transverse shearing and lamina bending modes, making these two the only distinct modes. As described by Farley and Jones, the transverse shearing mode, shown in in Figure 3a, is characterized by short interlaminar and longitudinal cracks which coalesce to form partial lamina bundles. The principal energy absorbing mechanism is the transverse shearing of the edges of the lamina bundles. The length of these cracks is typically less than the laminate thickness, but ultimately the number, location and length of the cracks are function of the specimen structure and constituent material properties. The lamina bending failure mode, shown in Figure 3b, is characterized by long interlaminar, intralaminar, and parallel-to-fiber cracks which do not coalesce, and the lamina bundles formed do not fracture. Instead, the lamina bundles exhibit significant bending deformation. The main energy absorbing mechanism of this failure mode is crack growth, which Farley and Jones describe as an inefficient crushing mode, alluding to its low energy absorption capability due to minimal of fiber fracture.

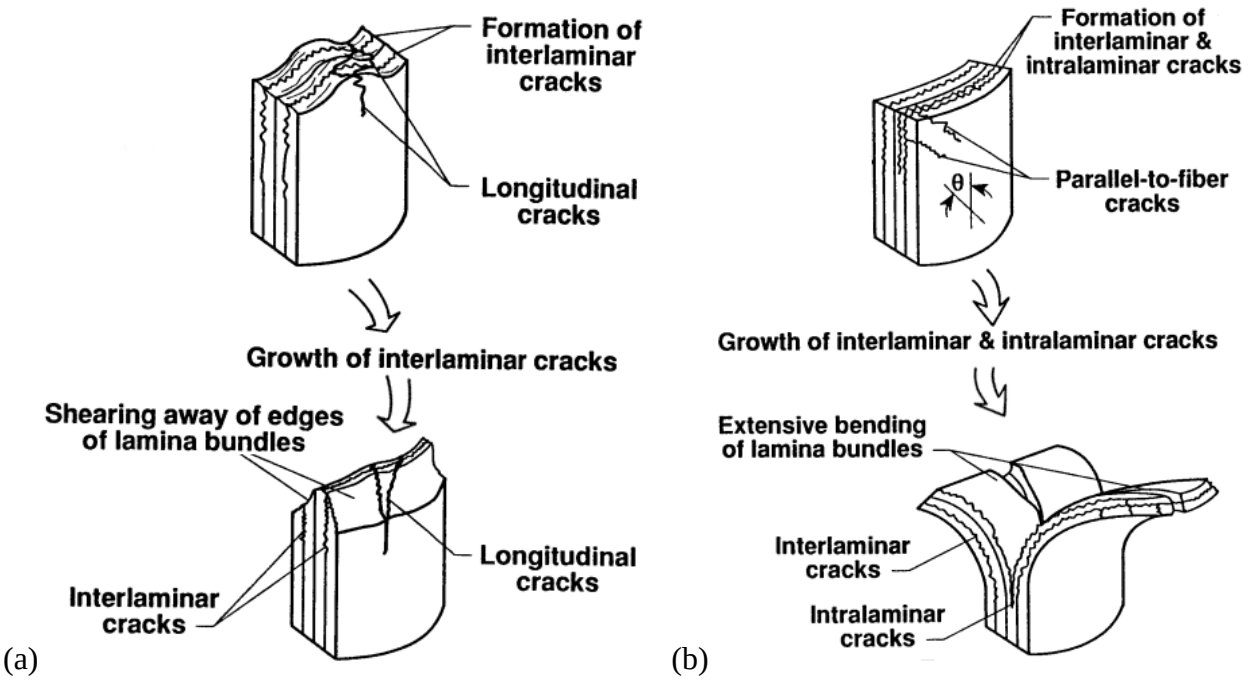

Figure 3. From Farley and Jones [14] (a) transverse shearing and (b) lamina bending failure modes of progressive crushing failure.

Hull [9] shortly followed the work of Farley and Jones, and provided his own scientific analysis of the energy absorbing mechanisms occurring during progressive crushing. Hull identifies eight theoretical failure modes relevant to crush failure, stating that fracture occurs in tension, compression and shear parallel and normal to the fiber direction, and that failure may also involve interlaminar fracture in tension and shear. In practice, Hull is able to identify two general modes of progressive crushing failure which he calls ‘splaying’ and ‘fragmentation’, for which crush failure is often a combination of differing degrees of both modes. The splaying mode is characterized by long cracks which propagate through the matrix and between plies while leaving most of the fiber bundles intact. Conversely, the fragmentation mode is characterized by abundant fiber fracture and matrix cracking, rendering most of the material as debris with little left intact. These two modes are shown in Figure 4. These two modes are essentially the same as those identified by Farley and Jones, as later noted by Carruthers [16].

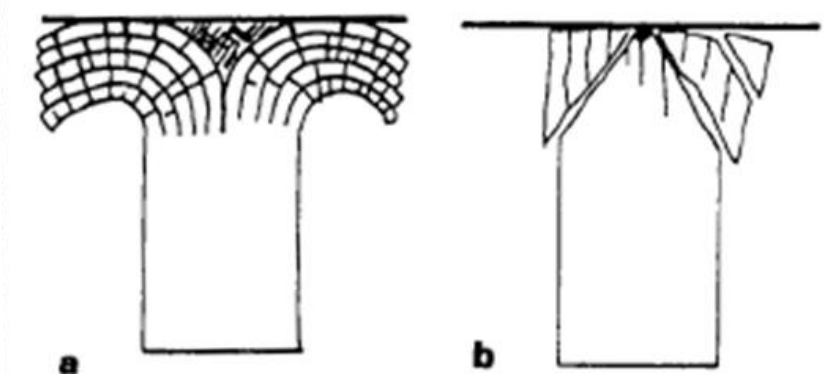

Figure 4. Schematics of the two extremes of composite crush failure modes: a) splaying mode and (b) fragmentation mode, from Hull [9].

By using micrographic analysis, Hull is able to identify several of the eight theoretical fracture modes as prevalent within both the splaying and fragmentation crushing failures. From this analysis, his statement of the impossibility of characterizing the crush zone comes to pass given its dependence on the microfracturing processes, forces acting at the crush zone, microstructural variables associated with the composite constituents, shape and dimensions of the crush specimen, and testing variables such as temperature and speed. Hull does not describe a difference in energy absorption potential between these two crushing modes. Hull shows that the arrangement of fibers (i.e. laminate lay-up) influences which failure mode is more dominant during progressive crushing. By increasing the ratio of hoop to axial fibers in composite tube the lay-up, Hull is able to change the failure mode from portraying primarily splaying failure to primarily fragmentation failure, proposing that hoop fibers contain the splaying of axial fibers during crushing. This conclusion is only applicable to closed section crush articles with hoop fibers such as the tubes Hull used in his investigation.

Carruthers [16] provides a review of several experimental studies of composite crush tubes conducted through its publication in 1998. This review summarizes that, of the many failure modes described, the most prominent include transverse shearing, brittle fracturing (both of the

fiber and of the matrix), lamina bending, delamination, and local buckling. Carruthers concludes that the many failure modes identified by several authors are bounded by the two extremes identified independently by Farley and Hull: splaying/lamina bending and fragmentation. Carruthers continues, "of the two brittle fracture failure modes, there is some evidence to suggest that the fragmentation mode of failure generally result in higher energy absorptions than the splaying mode" and refers the reader to the crush tube work of Hamada [17]. Determining which failure mode will be dominant during tube crushing, however, depends on several factors including the selection of fiber and matrix constituents, lamina angle, specimen geometry, lay-up, and testing speed. This result appears to be the consensus among experimental investigations to identify composite crush failure modes, however among these investigations there is conflicting data over what parameters influence the physical preference of one failure mode over the other, and how each parameter influences the result. The common conclusion among researchers to this day is that there are several different failure modes occurring simultaneously during composite material crushing, each of which provides a different capability for energy absorption, but a general disagreement of what parameters most influence these modes, and how their influence takes effect.

Beyond the extensive work of these authors, not much additional work has been done to scientifically characterize the physical energy absorbing mechanisms in progressive crushing. In more recent publications, authors often report observations of different failure modes as they appear within the context of a particular test matrix without delving into a scientific explanation of these modes. In this way, several crush failure modes are named, but are often not characterized within the greater context of the two established boundary modes of splaying and fragmentation. Most recently, for instance, Bisagni [4] presents a brief description of four failure

modes observed from crush testing circular carbon fiber tubes. These are the tearing, socking, splaying and microfragmentation modes, as shown from Bisagni in Figure 5. While Bisagni's microfragmentation mode appears to be the fragmentation mode identified by Hull, the other three modes appear to include combinations of fragmentation and bending crush modes.

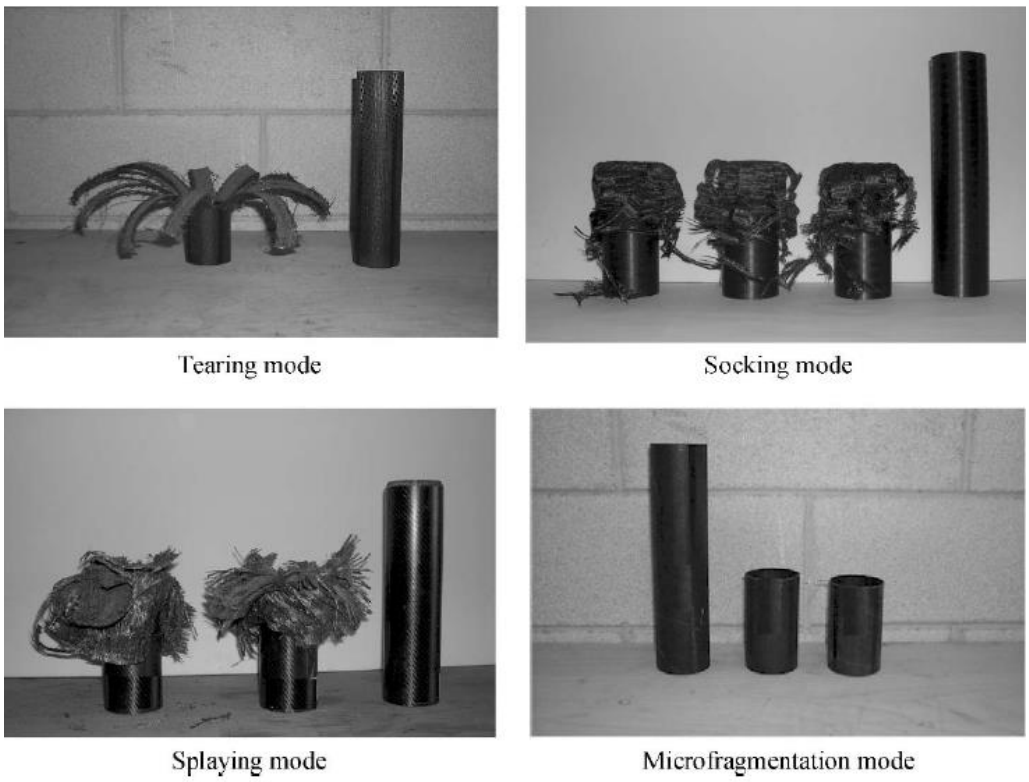

Figure 5. Four progressive crush failure modes as identified by Bisagni [4].

Underlying the scientific efforts to characterize the physical energy absorbing mechanisms present in composite progressive crushing has always been the fundamental desire to quantify and measure the energy absorbing capability of composites. As given in Equation 2, the SEA measured from crush testing is the primary value used to characterize the energy absorption capability of a material. Unfortunately, there is no standardized test method for SEA measurement, and therefore no way to systematically compare the energy absorption capability of different composite material systems. This means that the SEA values reported by different

research efforts cannot be directly compared as they likely used different test methods which can influence SEA results significantly.

The manner in which coupon-level testing is conducted for SEA characterization of composites varies greatly and has been the topic of recent research efforts. Only a selected number of attempts have been made at developing a coupon-sized test method to determine the SEA of composite materials. Such efforts are being made by the Crashworthiness Working Group of the CMH-17 [18] while operating in parallel with the ASTM International Committee D-30 on Composite Materials. Similarly, the Energy Management Working Group of the ACC [2], which comprises members of the three largest United States (US) automotive manufacturers and the US Department of Energy, has worked for over two decades on the topic of composite crash structures for automobiles. In addition, government organizations, such as the National Aeronautics and Space Administration (NASA) [19] in the US, the German Aerospace Center (DLR) [20], and the National Aerospace Laboratory of the Netherlands (NLR) [7], have also dedicated resources towards the experimental characterization of composite crash energy absorption.

One method for SEA measurement is to use a flat material coupon, similar to those used for standardized mechanical material property testing. Flat test coupons have the advantage of being easily manufactured with no requirement for special tooling. Because of the loading conditions required and failure modes desired, however, characterizing crush energy absorption using a flat coupon is a challenging and controversial task. A specialized fixture is required which must provide anti-buckling support for the flat coupon without inducing friction or suppressing crush failure. Several fixtures for flat coupon crush testing have been proposed over the years, and a good review of this work is provided by Feraboli [12]. Four such flat crush coupon fixtures are

shown in Figure 6, including one designed and manufactured at the University of Washington (UW), shown in Figure 7. Each of these fixtures features different mechanisms to provide lateral anti-buckling support, such as two vertical knife edge supports which pinch the flat test coupon vertically in place during crushing in the NASA fixture (Figure 6a), or the roller bearings which facilitate both vertical movement and lateral support of the test coupon in the University of Stuttgart fixture (Figure 6d). The UW fixture uses knife edge supports in a similar fashion to the NASA fixture, however these supports do not constrain the entire length of the specimen and an adjustable length of unsupported height of the coupon at the crush front is allowed, as highlighted in Figure 7.

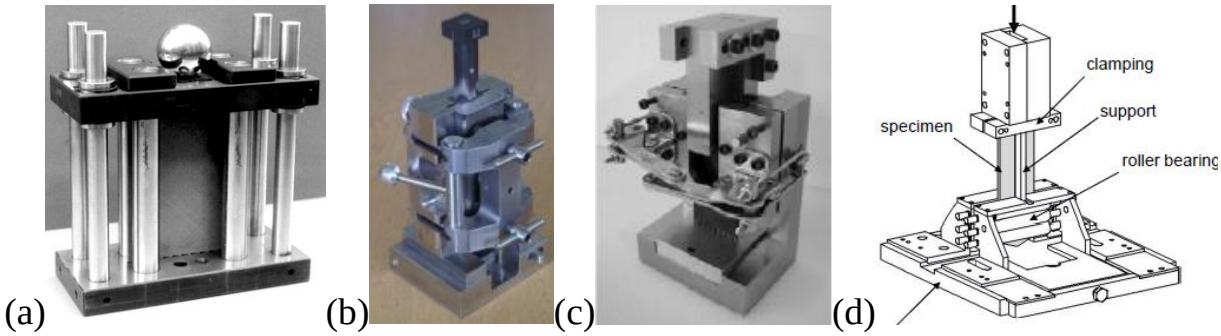

Figure 6. Flat coupon crush test fixtures from (a) NASA [19], (b) Engenuity [1], (c) Oakridge National Laboratory [21], and (d) University of Stuttgart [22].

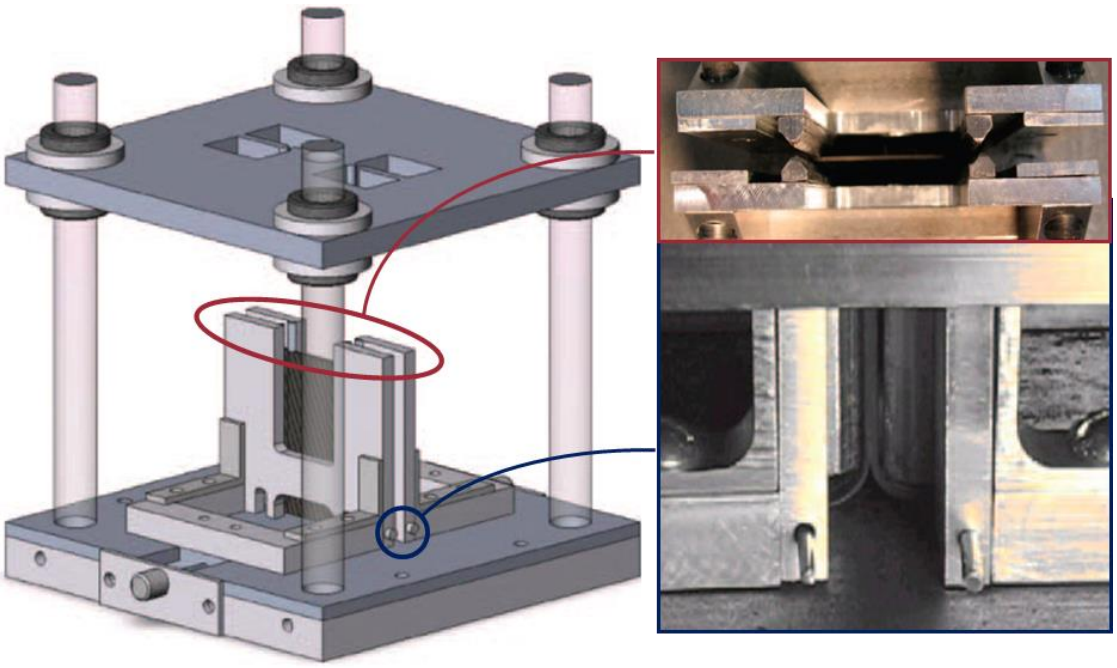

Figure 7. University of Washington flat crush coupon fixture, highlighting the details of the knife-edge supports (top right) and unsupported height of the crush coupon (bottom right) [12].

With the exception of the NASA flat coupon crush fixture, all fixtures feature a laterally unsupported distance at the crush front where the crushed material is free to naturally bend and form fronds, and the evacuation of debris is allowed in order to minimize interference with the remainder of the test coupon undergoing crushing. Crush tests conducted using the NASA fixture determined that without an unsupported region, a flat coupon is over-constrained at the crush-front and the collection of growing debris impedes the natural crushing of the coupon, causes great reaction forces, and consequently an artificially high SEA is measured due to these fixture effects [12]. Research conducted utilizing two of the fixtures, from the University of Stuttgart [22] and University of Washington [12], indicates the importance of the unsupported height distance on the measured SEA and crushing stress. While providing too little unsupported height causes an over-constrained situation such as experienced using the NASA fixture, providing too much unsupported height allows for buckling and crushing is not achieved, as

shown in Figure 8 and Figure 9. In comparing these two results, the unsupported height threshold at which the energy absorption trend changes is different, and may depend on either the material system tested or the test fixture itself. Several unsupported height distances must be tested to find the proper amount which allows for sustained crushing, and from which the flat coupon SEA can be measured. For all flat coupon anti-buckling tests fixtures, however, the influence of the test fixture cannot be definitively identified, and the adoption of a self-supporting element-level crush specimen is preferable to that of a flat specimen.

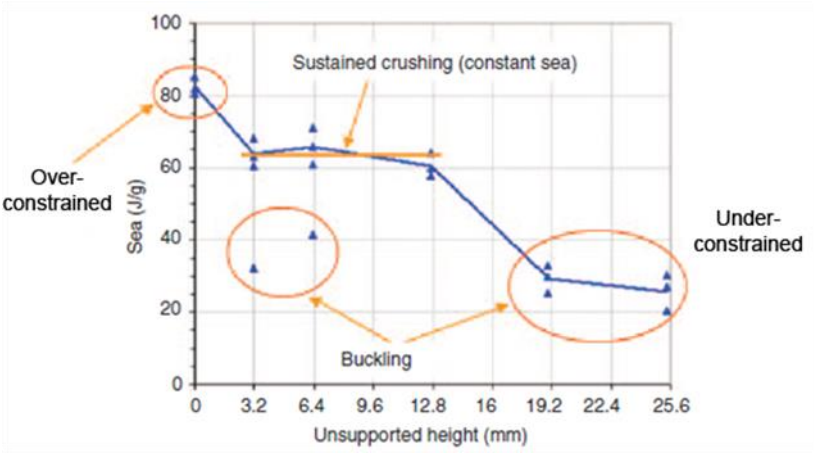

Figure 8. Influence of the unsupported height of the University of Washington flat crush test fixture on the SEA measurement, from Feraboli [12].

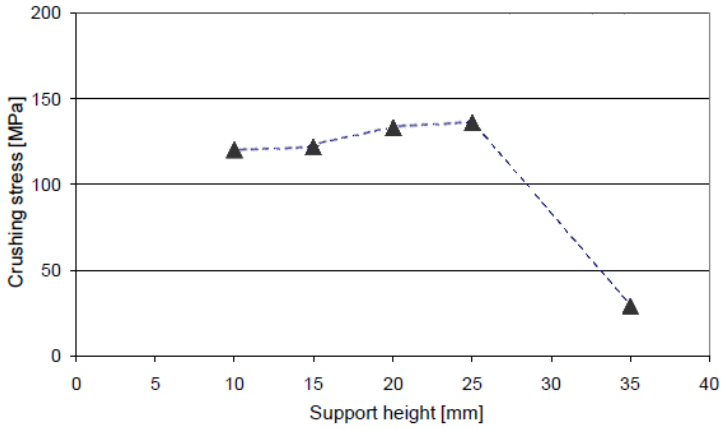

Figure 9. Influence of the unsupported height of the University of Stuttgart flat crush test fixture on the crushing stress measurement, from Feindler et al. [22].

The vast majority of the experimental research to determine the crush energy absorption of composite materials has used thin-walled tubular specimens rather than flat coupons or other shapes. Such research was underway prior to the development of flat coupon crush test fixtures, and tubes were selected because they are self-supporting and therefore do not require dedicated test fixtures, and they are representative of the tubular front rails traditionally found in automotive crash structures. Most work completed to date consists of reporting SEA results from varying test parameters, fiber and matrix constituent materials, the laminate lay-up, and geometric features of the tubes. Among this work, a wide range of experimental set-ups have been used, making comparisons across different test programs difficult. Furthermore, some of the observed trends reported by authors are contradictory those reported by others, leaving great question as to how exactly certain parameters influence results. For instance, some research has shown that the SEA can double between the dynamic and quasi-static crush tests of the same geometry [5], while other authors have reported a decrease over dynamic results [16], Thornton [23] reports no rate dependency across a velocity range of six orders of magnitude, and Mamalis [24] maintains that the strain-rate sensitivity of energy absorption depends on the dominant failure mode experienced by the composite crush coupon, where only particular crush failure modes are sensitive. The only consensus about the influence of test speed on energy absorption is that there is no consensus [16] [25]. The lack of an agreed upon test method makes the comparison of test results and research findings across the literature a challenging matter.

To further illustrate this point, key findings from a review of over 50 composite crush tube test programs published by Carruthers et al. [16], and by Jacob et al. [25] are reviewed. Among these test programs, the effect of various constituents, lay-ups, specimen geometries, loading rates, and other test parameters were investigated. The findings from Thornton [23], Farley [26],

and Schmueser and Wickcliffe [27], agree that carbon tubes consistently have the highest specific energy absorption than glass and aramid tubes. Regarding the matrix constituent, there is widespread disagreement of its direct influence on energy absorption and in particular which matrix properties constitute good energy absorption. For instance, Thornton [23] reports that higher tensile strength and modulus of the matrix contributes to higher energy absorption, while noting that there is no dependence of SEA upon the resin fracture toughness. Contrarily, Hamada et al [28] report that the high fracture toughness of a matrix directly resulted in the highest energy absorption of any CFRP. Finally, Tao et al [29] report that the increased compressive strength of a matrix is the most influential matrix property in providing better energy absorption. The influence of material lay-up upon energy absorption appears to be dependent on the constituent materials, as contrasting trends between ply angles and energy absorption capability of carbon composites versus glass and aramid composites have been reported by Carruthers et al. [16]. In this area there is also disagreement, where Schmueser and Wickcliffe [27] report the ply angle influence on energy absorption remains the same among all fiber types. Whenever there is disagreement of the general energy absorption data trends, each author has used a different test method which implements different loading rates and trigger mechanisms, for instance, making comparisons and drawing meaningful conclusions difficult.

Upon review of the relative available literature, studies of the effect of crush specimen geometry on SEA have focused on changes of small geometric features such as tube diameters and thicknesses. Among tubular specimens, several geometric features have been reported by several authors as influencing SEA, leading to the overall conclusion that geometry strongly influences energy absorption. In particular, Thornton [23], Mamalis et at. [24], and Kindervater [30] each reported that circular tubes had higher energy absorption than square tubes of the same

composite system. Farley [31] and Mamalis et al. [32] individually reported that increasing the diameter to thickness ratio of circular tubes nonlinearly decreased the energy absorption. Farley and Jones [15] reported upper and lower bounds for the thickness of the tube, where overly thick tubes tended to fail catastrophically when the hoop stress in the tube reached the strength of the material and overly thin tubes tended to buckle. In a separate publication, Farley and Jones [33] reported the influence of the eccentricity of 'near elliptical' tubes as determined by the included angle of the cross-section. As the tubes became more elliptical (i.e. the included angle decreased) the energy absorption of these tubes increased by up to 30%. Moving away from tubes for a moment, studies on the effect of crush specimen geometry were also carried out by Hanagud et al. [34] using corrugated plate specimens. Hanagud found that the web amplitude had a destabilizing effect when too low, while the number of repeated waves was not influential. In general, each study of the effect of crush specimen geometry on SEA has focused on small and specific geometric features, and there has been no work reported which compares the macro effects of different geometries upon energy absorption (i.e. comparing tubes to corrugated webs).

It has been suggested by Carruthers et al. [16] that the closed-section nature of tubes has unknown but evident effects on the crush performance. In particular, it is thought that stacking sequence affects the crush behavior since the hoop fibers constrain the axial fibers and prevent them from splaying, thereby suppressing the propagation of the crush front. Only a limited number of element-level crush experiments have used test specimens of geometries other than tubes. The aerospace community has focused mostly on test specimens that resemble subfloor structures, such as floor beams, longerons, stanchions, and stiffeners. Corrugated web geometries have a history of being employed as energy absorbers in the subfloors of aircraft to improve crashworthiness in both rotorcraft [20] [35] and large commercial transport aircraft [36].

Corrugation increases the stability of a vertical web, thereby increasing its crippling strength, and enables floor beams to carry higher design loads. By reducing the likelihood of macroscopic buckling, the corrugated geometry promotes stable crushing and significant energy absorption in a crash scenario [34]. Other possible test element geometries are open section and partially self-supporting, and are therefore more versatile from a manufacturing point of view, do not exhibit the same hoop fiber constraint as tubular shapes, and do not require a dedicated test fixture like flat coupons. Such geometries include semicircular segments [5], channel stiffeners [2], and the DLR omega specimen [37]. Like the crush tube studies, the goal within these individual test programs is often focused on understanding the influence of a specific effect from material, lay-up, loading rate, geometry effects, etc., and issue among these test programs remains the lack of an agreed upon test method. There has not been a systematic study of the influence of large geometric changes (i.e. using different shapes rather than different dimensions of the same shape) upon the SEA of a composite material system, and because of this there is not a clear way to compare the results of the corrugated web tests against the tubular tests. In the absence of a standardized experimental test method, there is a need to understand the influence on the crashworthiness of composite specimens with such large geometric differences.

Finally, the variability in SEA measurements for composite materials has been shown to be dependent on numerous testing variables, and this can make it difficult to understand exactly how composites perform with respect to crashworthiness. For this reason, it is useful to compare the performance of composite material systems against their predecessors (i.e.. metals) to develop a better understanding of composites. Indeed, most of the composite crush test programs reviewed often use an isotropic metal, such as steel or aluminum, as a baseline against which the composite SEA measurement is compared. Across these studies it is shown that the

SEA measurement of carbon fiber-epoxy composites in particular is consistently higher than that of isotropic metals, unless given very unfavorable conditions (i.e. poor lay-up, unstable geometry, etc.). Carruthers et al. [16] report that for axially compressed tubes, carbon fiber-epoxy tubes with a 0-degree biased lay-up have SEA measurements 1.6-2.2 times higher than metallic tubes, Table 1. Jacob et al. [25] compile a history of tube crush experiments, and report that the SEA of a carbon fiber-epoxy crush tube is 110 J/g compared against 78-89 J/g for aluminum tubes of different diameters.

Table 1. Comparison of SEA of carbon and glass composite tubes against steel and aluminum tubes, from Carruthers et al. [16].

Material	Lay-up	Thickness : Outside diameter ratio	SEA [J/g]
Carbon-epoxy	$[0/\pm 15]_3$	0.033	99
Carbon-epoxy	$[\pm 45]_3$	0.021	50
Glass-epoxy	$[0/\pm 15]_2$	0.060	30
1015 Steel		0.070	45
6061 Aluminum		0.070	60

The data from Carruthers et al. and Jacob et al. is in agreement with a chart published by the "Advanced General Aviation Transport Experiment" (AGATE) Small Airplane Crashworthiness Design Guide [38] which clearly shows the outperformance of graphite (carbon) tubes for SEA compared against various metals, reproduced in Figure 10. In general it is acknowledged that carbon fiber composites offer the increased capability for energy absorption over both isotropic materials and other composite types, although the variables which influence this capability are numerous and not all well understood.

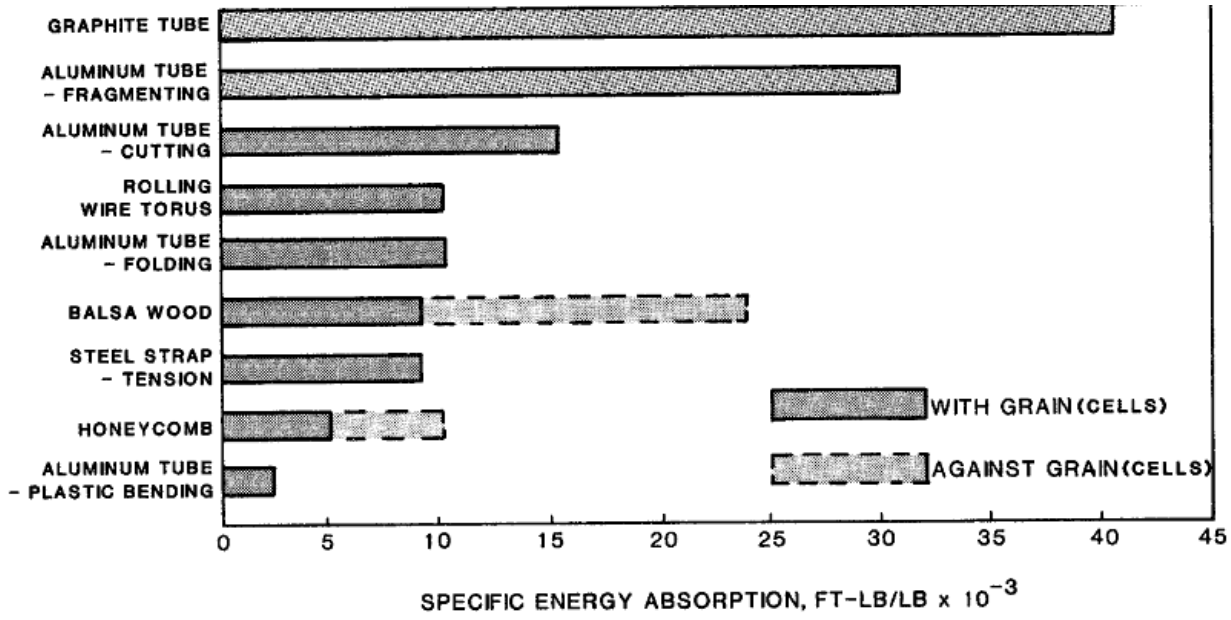

Figure 10. SEA values from tube crush testing of different materials, showing the outperformance of graphite (carbon) in the AGATE design guide [38].

Composite material models for crash simulation

The great challenge presented by the simulation of composite material systems beyond the elastic region is indeed the complex nature of the combination of individual failure mechanisms occurring in the damaged material. Each failure mechanism is demonstrably unique, and it has been shown that even in the experimental field of investigation there is disagreement concerning the prevalence of one failure mode over another given different material types, lay-ups, boundary conditions, etc. The development of composite materials capable of crash simulation has been pursued in two general areas: models which attempt to capture the detailed behavior of simple test specimens and model the individual crush failure mechanisms occurring within the material [39] [40] [41] [42] [43] [44] [45] [46], and crash modeling of large-scale composite components and structures using calibrated composite material models which capture the overall behavior of the crushing material rather than the details of the failure mechanisms [47] [48] [49] [50]. While the detailed damage mechanism models are important towards developing a better understanding of the fundamental material failure behaviors, computational limitations are such that capturing such detail in a large-scale composite crash model is not yet feasible and not currently attempted. Such small scale models are not within the scope of this research.

Composite material models which are suitable for full-scale crash simulations are often lamina-level models, meaning that the material properties are that of the lamina, the lay-up of the laminate is specified by the element formulation (not by the material model), and Classical Laminate Theory is used within the element formulation to calculate laminate stress and strains from the lamina stresses and strains determined by the material model. These models have three features: the elastic model, the failure criterion, and the post-failure damage model which includes progressive damage and ultimate material failure. The elastic model uses stress-strain

relations based on Hooke's Law and constitutive properties measured from standardized material property experiments. The failure criterion and damage model are the two features which distinguish most composite material models, and will be the focus of this review.

Predicting the initial failure of a composite lamina and developing failure criterion have been a topic of research since the 1960's. All failure criteria rely on extensive experimental data to define strength and strain parameters, and are therefore semi-empirical in nature. A review of early composite failure theory [51] [52] [53] [54] reveals numerous criteria have been developed with various degrees of success. Among these criteria there has been a lack of evidence to show whether any analysis method provides accurate and meaningful predictions for failure over anything other than a very limited range of conditions. To address this issue, Hinton et al. launched the first World Wide Failure Exercise (WWFE) in 1998 to assess and compare the prediction capabilities of a wide variety of composite failure theories. This large scale, multi-year collaborative effort demonstrated in its conclusion in 2004 that failure criteria for composites have several shortcomings, making it a challenge to predict even just the onset of damage, with particular deficiencies for predicting nonlinear responses [55]. Although crush failure was not addressed by the WWFE, crushing is a more complex failure mode than any of the nonlinear loading conditions investigated by the WWFE for which none of the failure criteria could adequately predict. This evaluation of composite failure criterion reveals the technical challenge presented by the development of a composite material model suitable for crash simulation, where even the prediction of the onset of damage is a great challenge, let alone the post-failure material deformation. For a more current and broad catalogue of existing failure criterion actively used in composite material models, a review published by Orifici et al. [56] is referenced.

Due to their anisotropic nature, failure criteria for composite materials treat different failure modes separately, at the very least defining unique criteria for fiber rupture and matrix failure. Typically, these modes separated further into different load cases of tension, compression, and shear, and can also include additional interactive criterion for complete ply failure. For both fiber and matrix failures, the most simple and most commonly used composite failure criteria are the maximum strain and maximum stress criteria [52] [56]. The maximum strain criterion states that a material fails under a stress state where any of the principal strains reaches an ultimate value. The expression for this in terms of 2D principle stresses is,

$$max\{|\sigma_1 - v\sigma_2|, |\sigma_2 - v\sigma_1|\} = \sigma_u \qquad \text{Eq. (3)}$$

where *v* is the Poisson's ratio of the material. Similarly, the maximum stress criterion states that a material fails when any of the principal stresses reaches the ultimate value as given by,

$$max\{|\sigma_1|, |\sigma_2|, |\sigma_{12}|\} = \sigma_u \qquad \text{Eq. (4)}$$

Either of these criteria can be used to define tensile and compressive failures in the fiber and matrix by using the appropriate tensile and compressive strengths measured from coupon testing of the lamina in the axial, transverse, and shear directions.

In 1980, Hashin [57] modified a general tensor polynomial criterion from which four distinct failure modes for a composite lamina were developed, each a quadratic interaction criterion involving an in-plane shear term. The Hashin failure criteria are given by,

Tensile Fiber Mode

$$\left(\frac{\sigma_{11}}{{F_1}^{tu}}\right)^2 + \left(\frac{\tau_{12}}{{F_{12}}^{u}}\right)^2 = 1 \qquad for\ \sigma_{11} > 0 \qquad \text{Eq. (5)}$$

Compressive Fiber Mode

$$\left(\frac{\sigma_{11}}{{F_1}^{cu}}\right)^2 = 1 \qquad for\ \sigma_{11} < 0 \qquad \text{Eq. (6)}$$

Tensile Matrix Mode

$$\left(\frac{\sigma_{22}}{{F_2}^{tu}}\right)^2 + \left(\frac{\tau_{12}}{{F_{12}}^{u}}\right)^2 = 1 \qquad for\ \sigma_{22} > 0 \qquad \text{Eq. (7)}$$

Compressive Matrix Mode

$$\left(\frac{\sigma_{22}}{2{F_{12}}^{u}}\right)^2 + \left[\left(\frac{{F_2}^{cu}}{2{F_{12}}^{u}}\right)^2 - 1\right]\frac{\sigma_{22}}{{F_2}^{cu}} + \left(\frac{\tau_{12}}{{F_{12}}^{u}}\right)^2 = 1 \quad for\ \sigma_{22} < 0 \qquad \text{Eq. (8)}$$

In 1987, Chang and Chang [58] augmented Hashin's failure criteria to have a fiber-matrix shearing term in place of the in-plane shear term as follows,

$$\bar{\tau} = \frac{({\tau_{12}}^2/2G_{12}) + \frac{3}{4}\alpha{\tau_{12}}^4}{(({F_{12}}^u)^2/2G_{12}) + \frac{3}{4}\alpha({F_{12}}^u)^4} \qquad \text{Eq. (9)}$$

where α is a nonlinear shear factor on the third-order term of the shear stress-strain elastic relation,

$$\varepsilon_{12} = \frac{1}{G_{12}}\tau_{12} + \alpha{\tau_{12}}^3 \qquad \text{Eq. (10)}$$

The Hashin failure criteria with Chang and Chang's augmentation will receive considerable attention in this paper, as these are the failure criteria used by the material model investigated in this body of research.

Another way to define mode-based lamina failure is to use phenomenological failure criteria, most notably Puck's criteria [59]. These types of models attempt to simulate the unique physical phenomena of different lamina failure modes and rely heavily on empirical data which requires specialized testing and curve fitting. Puck's criteria were evaluated in the WWFE, which reported a relatively positive performance in the exercise, however, it was also acknowledged

that the experimental requirement to define numerous fitting parameters of such phenomenological models is both burdensome and difficult to validate [60].

Finally, there is a category of interactive failure criteria which consider the failure of the entire ply rather than separating criteria into fiber and matrix modes. Orifici et al. [56] offer an interesting commentary on such criteria which are often criticized due to "their origins in theories originally proposed for metals." They continue, "however, interactive criteria have demonstrated accuracy comparable with leading theories in which the failure modes are considered, and continue to be commonly applied in industry and widely available in FE codes." One such failure criterion which is of interest for crash simulation is Wolfe's strain-energy based criterion [61]. Although it was not any more successful than any of the other simulation methods in the WWFE in predicting simple laminate loading conditions [62], it is suggested here that an energy based criterion could be useful in predicting the energy absorbing capability of composite structures in crash. Wolfe's criterion relies on the axial, transverse, and shear components of strain-energy as measured by the area under the material coupon-level stress-strain curves of the lamina. Each component is expressed as an integral of the stress in terms of strain, divided by its ultimate strain-energy value (as measured by coupon-level experiment), and raised by a power of m_i, a shape function. The sum of the three components become Wolfe's strain-energy failure criterion,

$$\left(\frac{\int_{\varepsilon_1} \sigma_1 d\varepsilon_1}{\int_{\varepsilon_1}^{u} \sigma_1 d\varepsilon_1}\right)^{m_1} + \left(\frac{\int_{\varepsilon_2} \sigma_2 d\varepsilon_2}{\int_{\varepsilon_2}^{u} \sigma_2 d\varepsilon_2}\right)^{m_2} + \left(\frac{\int_{\varepsilon_6} \sigma_6 d\varepsilon_6}{\int_{\varepsilon_6}^{u} \sigma_6 d\varepsilon_6}\right)^{m_6} = 1 \qquad \text{Eq. (11)}$$

The shape function values determine the shape of the failure surface in strain energy space, and are unique for every material system. These values have an upper bound of $m_i = 2$, and cannot be determined without curve fitting to biaxial test data. These values are suggested to be set

equal to 1 without such data, however it was shown during the WWFE that Wolfe's predictions required extensive updating after experimental data was made available. While several changes were made to improve the predicted results, for some cases the shape function values were each changed to a value of 2 such that the prediction better matched the experiment. The resulting improved model concluded that, in particular for non-linear behavior, "the strain energy based model generally predicts lower failure strengths than those from experimental testing," [62].

Following initial lamina failure, each composite material model must specify a damage model to degrade the performance of the material until ultimate failure is specified. There are two types of damage models for composites: continuum damage mechanics and progressive damage models [56]. In a continuum damage mechanics (CDM) model, material damage is defined using internal state variables contained in a set of equations which allow the material to remain a continuum with smooth, continuous field equations. The internal damage variables are incorporated into the material constitutive equations to degrade the material performance as damage progresses. Talreja [63] was one of the first to develop a CDM model, and more current examples of CDM models are given by Johnson et al. [64] and Sokolinsky et al. [65]. In each of these models, damage factors are introduced into the ply stress-strain equations which have an inverse relationship with the material constitutive properties. This has the effect of degrading the ply stresses following failure according to the damage evolution function defined by the material model. The analysis continues until the stress is degraded to zero, or until another condition specified for ultimate failure is satisfied.

In a progressive damage model, damage is simulated using a ply discount method where, when the failure criterion is violated in a ply specified constitutive properties in that ply are reduced (often stiffness is set to zero) and the analysis continues. This continues until all plies have

failed and the material is considered to have reached ultimate failure. Orifici et at. [56] report that the progressive damage approach is simple and that the binary reduction of constitutive properties is, "particularly suited to the quasi-brittle nature of fibre-reinforced composites, and numerous researchers have recorded significant success in applying this approach to represent ply damage mechanisms." A progressive damage model is used in the composite material model which is the main focus of this body of research, and is discussed at length in the main sections of this paper.

While material models which implement lamina-level failure criteria and damage models are computationally feasible and an appropriate choice for composites crash simulation, predictions often suffer from the over-simplification which arises as a consequence from modeling an anisotropic, heterogeneous material as a laminate of orthotropic, homogeneous layers [66]. The true physical nature and interaction of failure mechanisms occurring within the crush front cannot be directly modeled using such an approach, which consequently can impair the predictive capability of these models. This is an important feature of composite material models which requires a strategic approach to their use in crash simulation, which this body of research will directly address.

Crash simulation of composite structures

The state-of-the-art explicit FEA codes used to simulate the dynamic crushing deformation and damage of composite and metallic structures alike include LS-DYNA, ABAQUS Explicit, RADIOSS, and PAM-CRASH [1]. The crash simulation of metallic structures using these codes has matured into a reliable tool over the past decade in the automotive industry in particular [11]. Given the technical challenge presented by the ongoing development of composite material models, the use of such models in full-scale FEA crash simulations requires an intelligent approach and strategic implementation such that these advanced material models can be effective in providing useful results that are much needed as the use of composites in vehicle structures grows. Implementing the Building Block Approach (BBA) is the method which allows for the strategic use of composite damage material models in crash simulation.

The BBA is outlined in great detail in the CMH-17 handbook [1], and was developed to substantiate the design of composite structures using both analysis and testing in an optimized fashion. In addition to the CMH-17 handbook, in 2009 Feraboli [66] published a concise description of the use of the BBA in composite aircraft certification, while Rassaian and Davis [67] presented on the use of the BBA specifically for composites crashworthiness certification in 2012. These three resources are used to form the following discussion on the BBA.

The BBA uses experimental test data to support the development of the numerical model at increasing levels of structural complexity, as indicated in Figure 11, beginning with material coupons and progressing through structural elements, subcomponents, components, and finally the complete full-scale structure. Each level builds on knowledge gained in the previous, less complex levels. Progressing through the BBA, the specimen and experiment increase in both scale and complexity, but the number of test repetitions decreases. By combining testing and

analysis, analysis predictions are verified by experiment, test plans are guided by analysis needs, and the degree of knowledge, safety, and confidence in the design is increased.

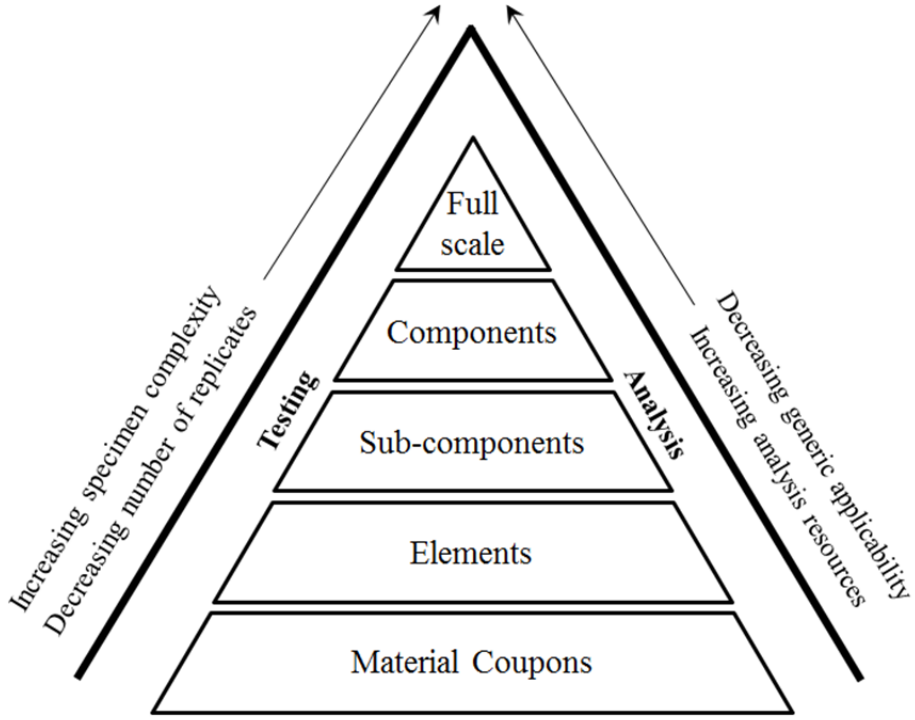

Figure 11. Building Block Approach for composite structural development.

At the lowest level of the building block, material coupon test data is directly input into the material model to form its initial definition. At this level, lots of coupon data is necessary to form design allowables data for the composite material system [66], while very little is done in the analysis other than to initialize the material model. In intermediate levels, experimental data supports the development of the analysis by calibrating simulated results against the test evidence. At the elements level of the BBA, testing includes the characterization of structural details such as bolted and bonded joints, radius details, stress concentrations, ect. Test data collected at this level can either be directly input into the material model or used to calibrate it, depending on the capability of the individual material model. The test matrix at the element

level is guided by the needs of the analysis model, such that it can be property calibrated to be used at the higher levels of the BBA.

At the sub-component and components level, tests are used almost exclusively to validate the analysis method previously calibrated. From Rassaian and Davis [67], an example of the sub-component test for a crashworthy structure is a 2-stanchion subfloor assembly from a fuselage section with the skin, stringers, stanchions, and cargo floor included. From Feraboli [66], component testing for an aircraft would include 3- and 5-stringer panels to characterize skin/stringer interactions, major bolted joint assemblies, and spar, stringer, and rib tests. The testing done at these level is used for validation of the analysis model, and to minimize the risks associated with the last level of the pyramid, full scale validation of the complete assembly. By the time the analysis model reaches the validation stage, the model is not calibrated further and must rely on the work done at lower levels. For this reason, the modeling strategy used for the full-scale final model must be the same as that used all the way down to the coupon-level. This means that heavily detailed composite material model that is not capable of scaling up to the full-scale analysis is not feasible.

While the BBA is widely acknowledged in the composites industry, most all of the development and expertise of its engineering application to composite crash modeling has been conducted in the private sector. One notable example of a publication on the topic of using the BBA for composite impact simulation comes from Feraboli et al. [68] in which a deep composite sandwich beam was impacted against a large pole, representative of a side-pole impact required for automotive crash certification. The event was simulated using an explicit analysis in LS-DYNA. In this effort, the model definitions for different parts of the sandwich structure were developed through tests and correlated analysis at lower levels of the BBA in order to build up to

the final model, which could be considered a sub-component model. The material model for the composite facesheets, MAT54, was calibrated from tests and simulation of 3-point bending tests. The material model for the aluminum honeycomb was calibrated from quasi-static crush tests and simulation of smaller honeycomb specimens. Finally, the adhesive between the facesheets and the honeycomb was calibrated from single lap shear tests and their simulation. These three calibrated components were then incorporated into the final model of the large honeycomb beam and validated against the experiment of the pole impact. By following the BBA, very good correlation between experiment and the validated simulation was shown, Figure 12.

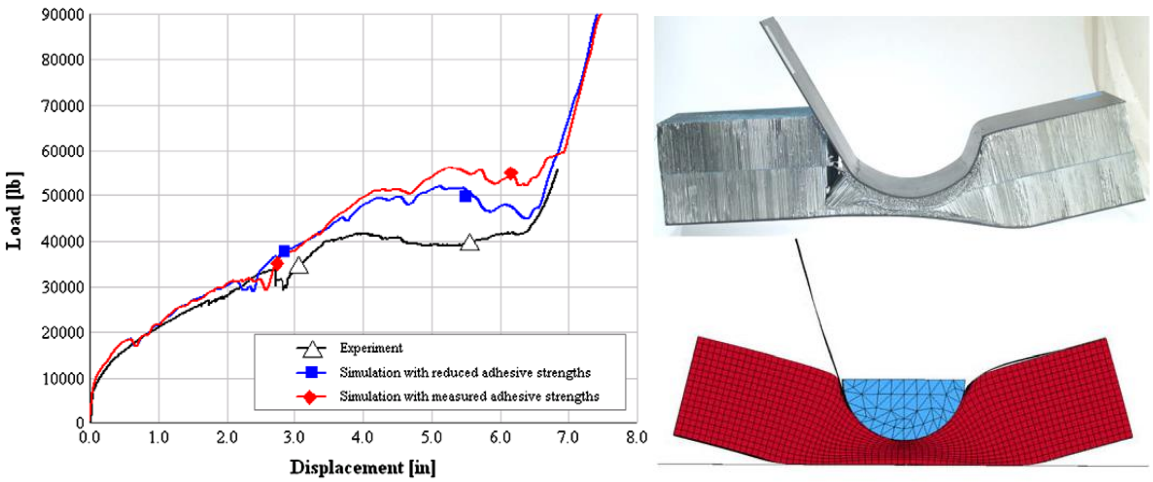

Figure 12. Successful test-analysis correlation from using the BBA to model a composite sandwich pole impact, from Feraboli et al. [68].

The other notable and most recent example of the use of the BBA for composites crash simulation comes from Heimbs et al. at DLR in 2013 [69]. In this study, a full-scale composite fuselage section subjected to crash conditions is simulated using Abaqus Explicit. In order to build up to this simulation, composite coupons are subjected to 3-point bend tests which are used to validate the elastic properties input into the material model from standardized coupon testing. The material model uses the Hashin failure criteria to determine failure initiation, similarly to the

LS-DYNA MAT54 model, and fracture energy criteria for damage modeling until ply erosion. The out-of-plane deflection of the test is also relevant to the skin bending failure mode expected of the fuselage section crash simulation. The minimum 0.2 in (5 mm) mesh size used is particularly large for the coupon simulations, but appropriate when scaled up to the full-scale fuselage section. Pull-through, single lap shear, and coach peel tests are performed at the coupon-level as well to fully characterize the performance of the bolted joints. The results from these tests were used to calibrate the beam elements used to simulate joints in Abaqus Explicit. At the element-level of the BBA, composite C-channels representative of the circumferential frames are subjected to 4-point bending tests. The analysis of this experiment proved to be difficult given the complicated experimental set-up. After a very detailed model of the entire test rig was complete, the corresponding load-displacement curve corresponded fairly well to the experiment, and the failure mode was exactly as it was observed in the experiment, Figure 13. The DLR study concludes that several features of the fuselage section model have been calibrated and validated for use at higher levels of the BBA.

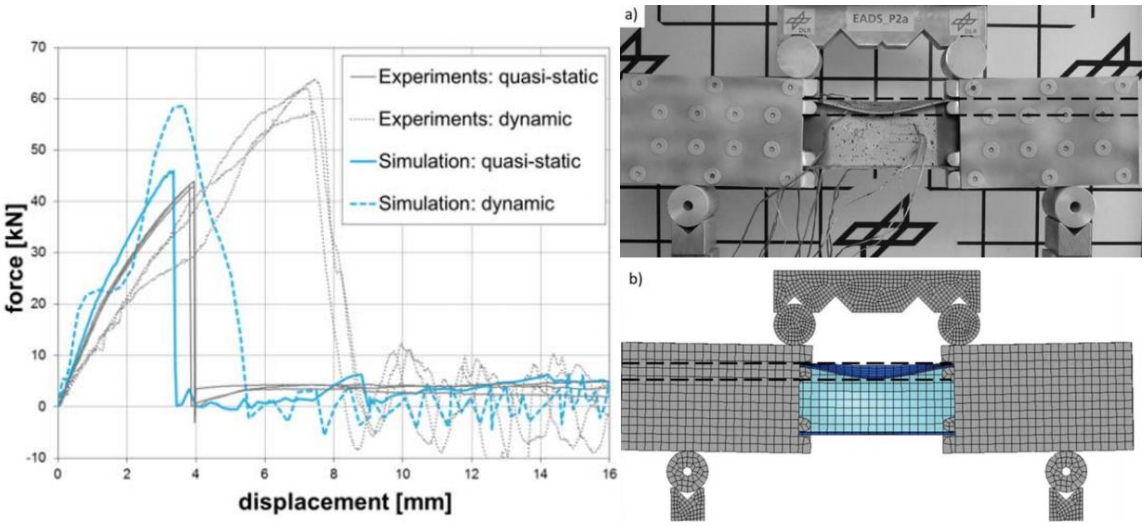

Figure 13. Successful test-analysis correlation from using the BBA to model a composite c-channel representative of a circumfrential frame, from Heimbs et al. [69].

Although the focus of this research effort lies within the lower levels of the BBA, the ultimate goal is to use this work to build up to the higher levels, and a review of the full-scale composite structure crashworthiness simulation efforts is briefly presented. These full-scale simulations are useful to review not only to provide a greater scope as to where the element-level testing and simulation efforts are heading, but also to define some limitations imposed by the large scale of the upper level simulations (i.e. mesh sizes, element types, general complexity, etc.) There are only a select number of large-scale composites crashworthiness simulation efforts available in the public domain which have all been generated from government sponsored research programs. These include investigations conducted at the NASA Langley Research Center (LaRC) over the past 15 years [70] [71] [72] and the European "Commercial Aircraft Design for Crash Survivability" (CRASURV) program [73].

The earliest work comes from the US Army, which initiated a research program in 1996 to evaluate the capabilities of commercial crash simulation codes for modeling the impact response of a composite helicopter drop tested at NASA LaRC [70]. While this is the first example available of a full-scale crash simulation of a composite structure, the crush failure of the composite material was not a focal point of this research effort. Instead, the correlation between experiment and the MSC.Dytran simulation focused on the energy absorption of the aluminum landing gear and overall deformation of the full structure. Failure criteria and post-failure material characteristics were only provided for the metallic material models, and the composite models were assumed to remain elastic. Similarly, an MSC.Dytran model of a composite fuselage concept drop tested at NASA LaRC in 2000 [74] did not contain a damage model for the carbon composite materials. The crash model instead focused on the simulation of foam block energy absorbers placed in the sub-floor of the fuselage section. Foam blocks were also

used in the drop test and analysis of the AGATE composite aircraft in 2002 [72]. In these early days, just over 10 years ago, only the elastic model of carbon composite material systems was used since damage models were not yet mature enough to be used in full-scale simulations.

One of the only examples of a large-scale composite structure crash simulation which uses a composite damage material model comes from the CRASURV program. The drop test of a prototype composite fuselage section in this program was performed and the simulation of the event was constructed using RADIOSS. The simulation built upon previous work within the CRASURV program to develop crashworthy composite subfloor designs of helicopters [8], which produced analysis data for the composite material model at lower levels of the BBA. Results from the fuselage section simulation were presented in 2004 by Delsart et al. [73]. The composite fuselage section drop tested used composite sinusoidal beams in the subfloor of the cargo bay as designed crash energy absorbers. The composite material model was calibrated using 0- and 90-direction coupon-level simulations in tension and compression, as well as +/-45 shear coupons of the UD composite. A critical parameter of the material model was determined to be "I_{off}" which prescribes a condition for element erosion following failure. This parameter was not able to be calibrated at lower levels. A section of the cargo beam, as well as the relevant joining plates, brackets, and frame it was attached to, was modeled separately as a sub-component model. Unfortunately there was no experimental data to validate these models, and the sub-component models served only to provide relative results of parametric trends of the modeling inputs and mesh sensitivity studies. The full fuselage section model was made up of shell and spring elements, with the finest elements used for the sinusoidal beams, using a shell mesh size of 0.16 in (4 mm). The critical parameter was shown to be the I_{off} element erosion parameter within the RADIOSS material model, and only after comparison of the full-scale drop

test results could appropriate values for this parameter in each section of the fuselage be determined. Delsart et al. conclude, "One can therefore estimate that the RADIOSS code may be used as a pre-design tool insofar it permits – if not to precisely predict the right structural behavior – to cover a realistic range of crash behaviors, by activating the rupture criteria I_{off} on the different components of the structure."

From each of these examples, certain similarities arise in the crash simulation model definitions which can be considered to be well established, and useful to know for the element-level simulations. For instance in all cases, crash simulation always uses an explicit formulation of the FEA solver which is conditionally stable, but computationally very expensive [47] [50] [64] [75]. For that reason, shell (2D) elements are preferred over the more onerous brick (3D) elements, and for composites the approach has been to use orthotropic 4-noded shell elements. In their review of FEA simulation of aircraft crashworthiness, Maia and de Oliveira [75] confirm that 4-noded Belytschko and Tsay shell elements are the basis of all crashworthiness simulations, and that the results obtained from "thousands" of crashworthiness simulations over the course of two decades have established the reliability and usefulness of such elements. These elements are remarkably efficient and rely on the local material coordinate system, which greatly reduces spurious stresses and strains when subjected to large deformations. To model a laminated composite material, the plies are grouped into a single shell element in which each lamina is represented by one or more integration points virtually existing through the thickness [68] [69]. This reduces the level of computational effort but prevents the simulation of interlaminar behavior. Models have been developed which use stacked shells to simulate groupings of plies in the laminate with tiebreak contacts in between the shell layers such that delamination modeling is possible [8] [48] [76]. The stacked shell element laminate, however, is too

computationally expensive to use in large-scale models, and material delamination modeling has not yet been directly implemented at the full-scale [77].

The current approach used in the aircraft industry requires adjustment and calibration of composite material models within the scope of the BBA in order to reach an agreement between experiment and crash simulation. As previously discussed, most all of the development and expertise of the engineering application of the BBA to composite crash modeling has been conducted in the private sector. The privatized localization of expertise is an impediment upon the broader use of composites in primary crashworthy structures. It has also presented a problem to regulatory agencies, such as the FAA, which ultimately must regulate the safety of all aircraft that are beginning to implement emerging composite technologies. For this reason, a coordinated cross-organizational effort within the Crashworthiness Working Group of the Composite Materials Handbook (CMH-17, formerly MIL-HDBK-17 [1]) was formed in 2005 by Feraboli and Rassaian [5]. This Working Group is comprised of representatives from the aerospace and automotive industries, academia, government laboratories, and regulatory agencies. Specifically to address crash simulation, in 2008 Dr. Rassaian launched a Numerical Round Robin (RR) exercise within the CMH-17 Crashworthiness Working Group with the goal to assess the predictive capability of commercially available FEA codes for composite crash simulation, and to provide numerical best practices guidelines. Participants of the RR are from the automotive and aerospace industries (Boeing Research & Technology, Ford Motor Company), numeric analysis tool developers (Altair Engineering, SIMULIA), government agencies (Federal Aviation Administration), and academia (University of Washington, University of Utah, Wichita State University). The research presented here was conducted within the context of the CMH-17 Crashworthiness Working Group.

Each participant of the RR developed a crash simulation strategy with its own solver, material model, contact definition, element type, and other modeling parameters specific to the individual strategy. The first two rounds of the RR exercise represent the first two levels of the Building Block, Figure 11, and will be officially coming to a close in 2014. Subsequent rounds will focus on higher levels of the Building Block, as represented in the RR roadmap in Figure 14. In Round I, participants were asked to make blind predictions of the result of an element-level crush experiment using their chosen modeling strategy. The objective of Round I was to evaluate whether any modeling strategy could be purely predictive of the composite crushing behavior given only standardized coupon-level material property input values. The result of Round I revealed that no such strategy existed, and that crush data was necessary to calibrate each material model. At the conclusion of Round I, participants were given the experimental data from the Round I crush element in order to calibrate their modeling strategy.

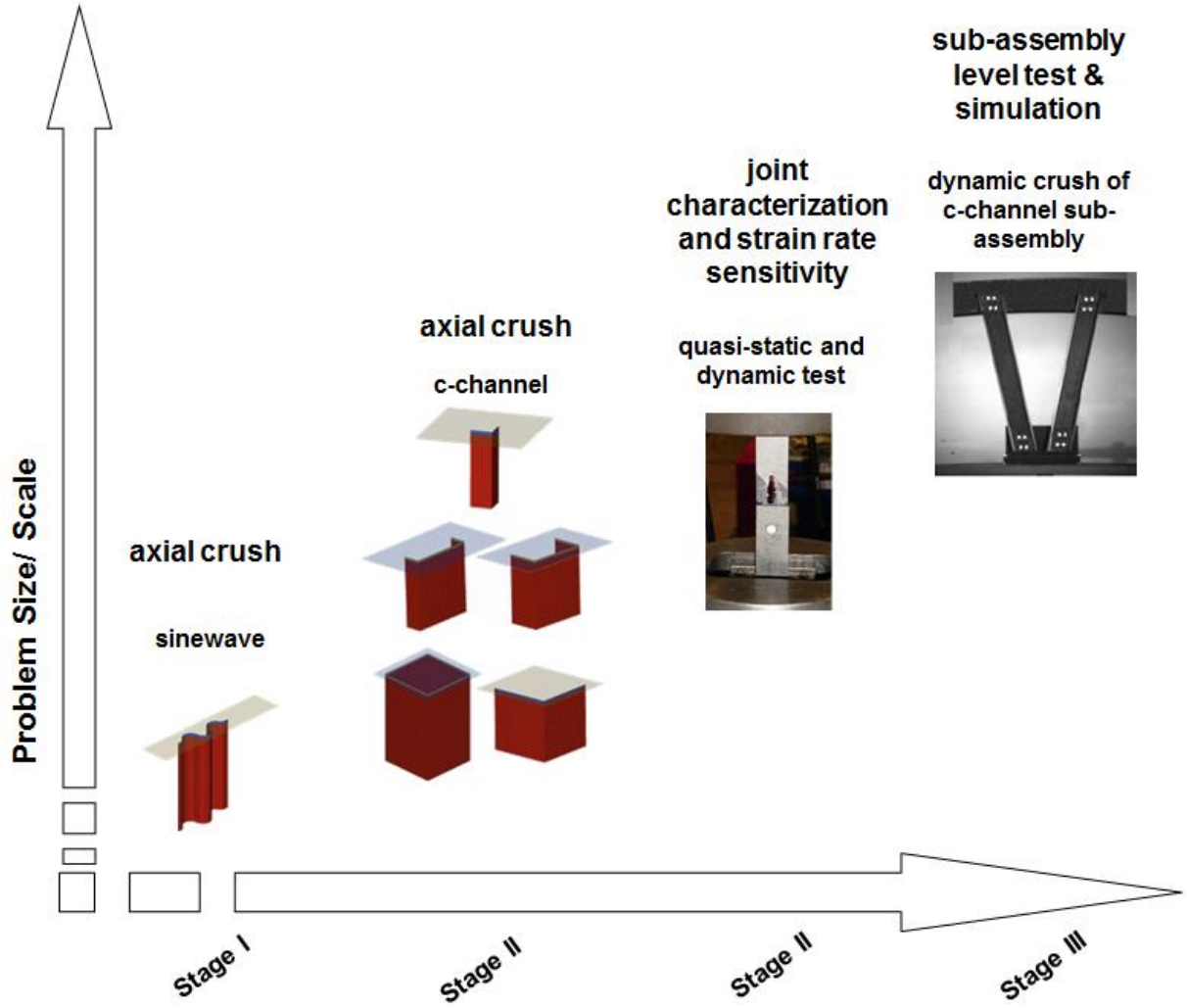

Figure 14. Roadmap of the CMH-17 Crashworthiness Working Group Numerical Round Robin Exercise [78].

In Round II, participants were challenged to make blind predictions of various element-level crush experiments based on their modeling strategy which had been calibrated using only the Round I experimental data. These predictions were not able to be made and as such it was revealed that the experimental SEA measured from each element-level test varied considerably even though the material system remained the same. The participants were then given all of the element-level experimental results from Round II and were challenged to calibrate their modeling strategy such that it produced results which matched the experiments well. The first

two rounds of the RR exercise represent the first two levels of the Building Block, Figure 11, and will be officially coming to a close in 2014. Subsequent rounds will focus on higher levels of the Building Block in order to test the predictive capability composite crash modeling strategies following their calibration at the element-level.

The crash modeling strategy developed by the author at the University of Washington with Boeing Research and Technology for the CMH-17 RR exercise uses the LS-DYNA built-in composite material model MAT54. Although several other codes are available, LS-DYNA has traditionally been considered the benchmark for composite crash simulations and is extensively used in the automotive and aerospace industries to perform explicit dynamic post-failure simulations [6] [79] [68] [80]. The LS-DYNA MAT54 material model is a great candidate for large, full-scale structural composite damage simulations because it is specifically meant for shell elements, for which all full-scale crash simulations are modeled with, and it relies on relatively few input parameters, most of which can be simply measured using standard material property testing. MAT54 therefore requires a reduced computational load that is appropriate for large-scale simulations, and was previously used in the BBA publication of Feraboli et al. [68].

Experimental

The primary goal of the experimental work is to characterize the energy absorbing capability of a composite material system such that this information can be used to calibrate the composite material model in a crash simulation within the construct of the Building Block Approach. The lack of a standardized method to measure energy absorption requires a scientific approach be taken to develop a way to characterize the energy absorption capability of a composite material system. In this study, only a single composite material system is of interest and enough experimental data must be generated such that the energy absorption capability of the material is fully characterized. Quasi-static crush experiments which feature various geometries are tested while keeping the material system, lay-up, manufacturing process, trigger mechanism, and all other testing parameters constant. From these experiments, the energy absorption capability of a composite material system will be fully described.

The material system selected for this study is carbon fiber/epoxy T700-2510 prepreg supplied by Toray Composites America (TCA). This material system has a 270º F cure resin (132º C) designated for a vacuum bag and oven cure only. Both the unidirectional (UD) and 12k tow, plain weave (PW), flat woven fabric forms of this composite material system were used, although the majority of the experimental crush testing uses the PW variety. This material is used extensively for general aviation primary structures, and its properties are well documented as part of the FAA-sponsored AGATE program [81] [82]. These properties are reproduced in Table 2. Idealized stress-strain curves in both the axial and transverse directions are generated for both material systems from the properties listed in Table 2. These curves are given in Figure 15.

One lay-up of each material system was considered, and these were a UD cross-ply $[0/90]_{3s}$ and a fabric $[(0/90)]_{8f}$, which yielded average cured laminate thicknesses of 0.065 in. (1.65 mm) and 0.073 in. (1.85 mm), respectively. For the UD cross-ply lay-up, additional material testing was necessary to supplement the published AGATE material data during the validation process of the numeric material model. The results from the standardized material property testing performed are presented in Appendix A: Additional experimental data.

Table 2. Material properties provided by the AGATE Design Allowables for T700GF 12k/2510 unidirectional (UD) tape [82] and T700SC 12k/2510 plain weave (PW) fabric [81].

	UD	**PW**
Density	1.51-1.57 g/cc	1.48-1.52 g/cc
$\mathbf{F_1^{tu}}$	319 ksi	132 ksi
$\mathbf{E_1^{t}}$	18.1 Msi	8.11 Msi
$\boldsymbol{\nu_{12}}$	0.309	0.043
$\mathbf{F_2^{tu}}$	7.09 ksi	112 ksi
$\mathbf{E_2^{t}}$	1.22 Msi	7.96 Msi
$\mathbf{F_1^{cu}}$	210 ksi	103 ksi
$\mathbf{E_1^{c}}$	16.3 Msi	8.09 Msi
$\mathbf{F_2^{cu}}$	28.8 ksi	102 ksi
$\mathbf{E_2^{c}}$	1.47 Msi	7.77 Msi
$\mathbf{F_{12}^{su}}$	22.4 ksi	19.0 ksi
$\mathbf{G_{12}^{s}}$	0.61 Msi	0.609 Msi

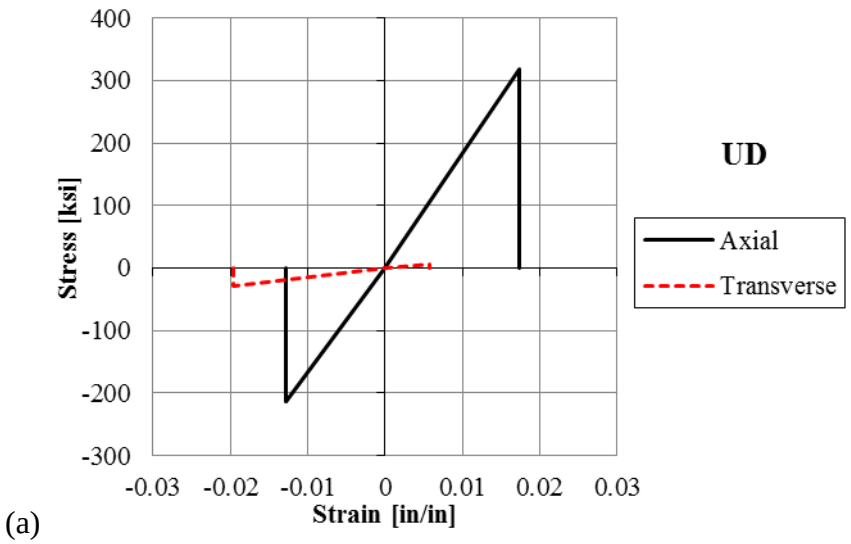

(a)

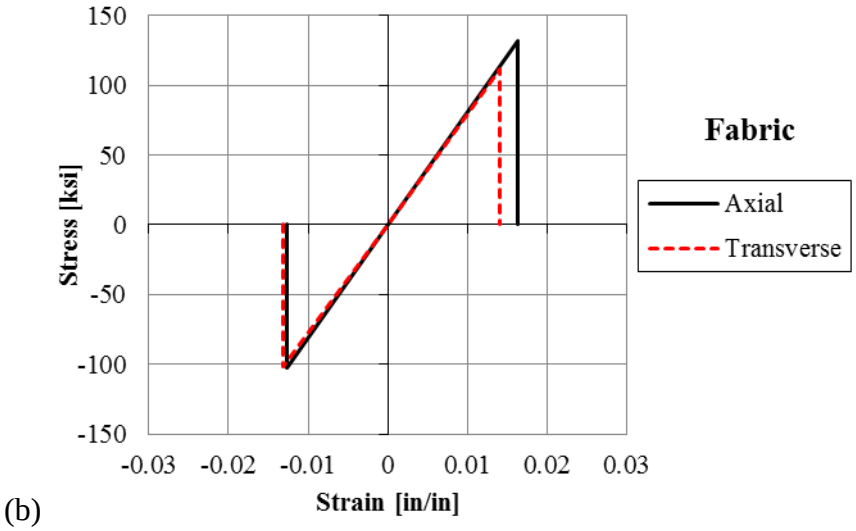

(b)

Figure 15. Idealized axial and transverse material stress-strain curves generated from published material properties for the (a) UD and (b) fabric material systems.

Flat CFRP coupon crush tests

The University of Washington flat coupon crush tests fixture, shown in Figure 7, was used to characterize the energy absorbing capability of flat AGATE fabric coupons. The flat crush coupon was 3.0 in. (76 mm) long and 2.0 in. (51 mm) wide with a 45-degree steeple machined along the bottom edge to initiate crushing behavior, as is common practice when crush testing composite coupons [83] [84]. The flat crush coupon, before and after testing, is shown in Figure 16. All tests were performed at a quasi-static rate of 2.0 in./min (50.8 mm/min), which is noticeably below any dynamic effect previously reported for modern systems [2], usually around 40 in./s (1 m/s) [16] [85]. For each unsupported distance, two specimens of AGATE material were tested as a part of the larger test program published by Feraboli in [12].

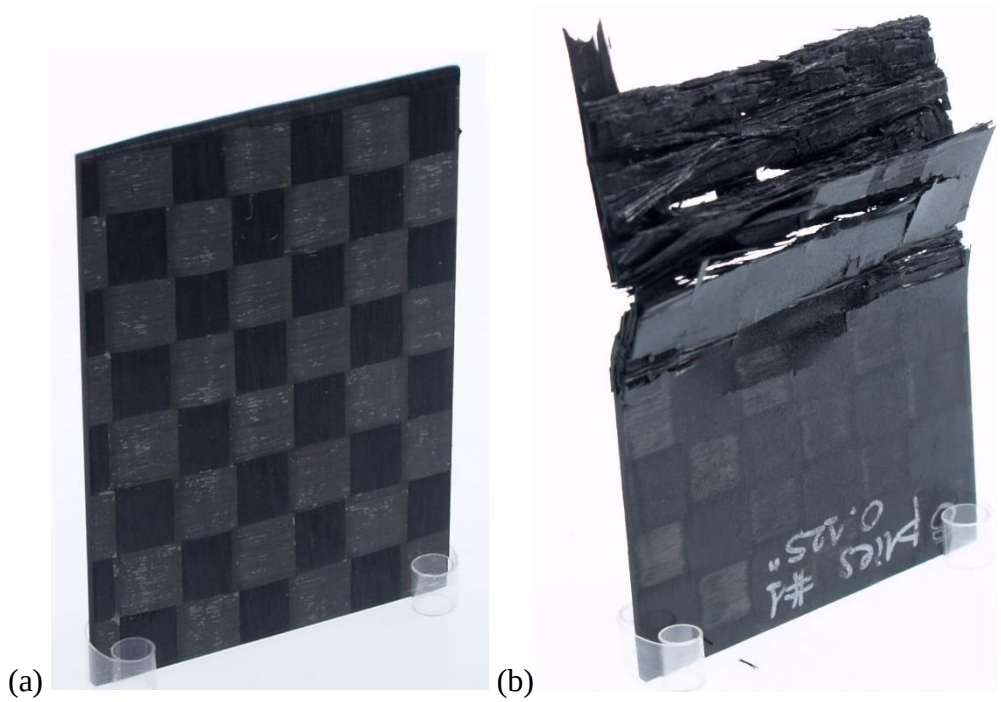

Figure 16. Flat crush coupons (a) tape lay-up before and (b) fabric lay-up after crush testing.

The unsupported height was found to only affect the experimental results at low values, Figure 17, for which the flat test coupons were over-constrained. The resulting average 'flat' SEA measurement for the fabric AGATE material system was 22.9 J/g. Limited testing was conducted using the flat test fixture due to the unknown effects of the fixture on the SEA measurement, as well as the challenge presented by modeling such a test using FEA, which is beyond the scope of this work. For these reasons, and many discussed in the Feraboli [12] results, the focus of SEA measurement during this scientific study was on self-supporting elements, and the results of the flat coupon experiments are used only as supplementary to the self-supporting experiments .

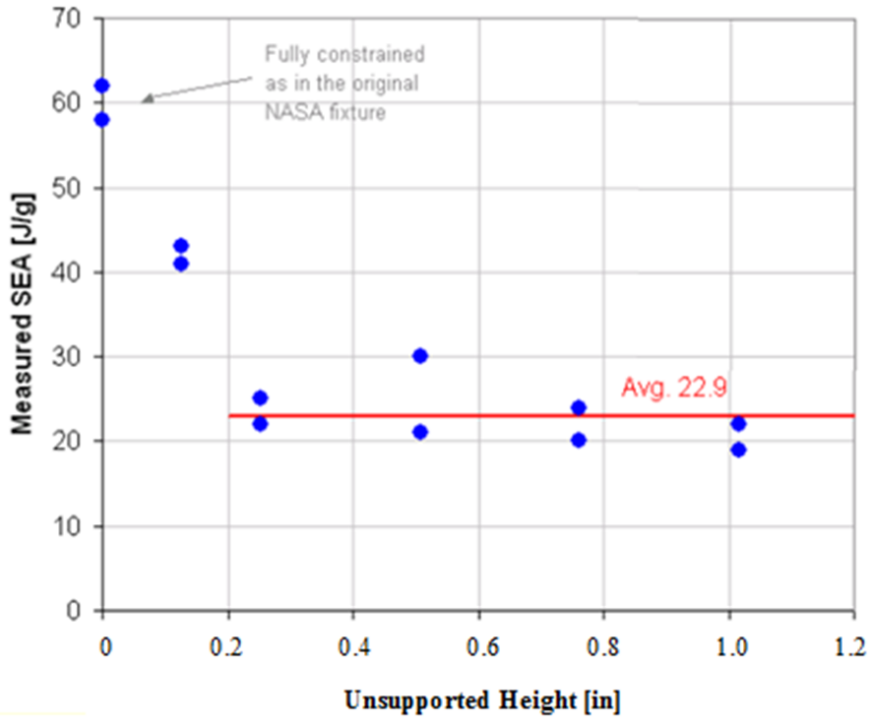

Figure 17. Effect of unsupported height on the measured SEA for the fabric AGATE material system.

Corrugated CFRP element crush tests

Three different corrugated web geometries were used in order to investigate how the degree and shape of the corrugation affect both stability and crush performance of the composite specimen. The design of the corrugated crush specimens comes from a previous experimental investigation which used various UD material systems, as published by Feraboli in [85]. Each corrugated geometry features three half-periods repeated on alternate sides of the mid-plane, and a short amount of flat material on either side of the corrugation for additional axial stability. The "low sine" geometry features a sinusoid function of amplitude 0.125 in. (3.2 mm) while the "high sine" geometry features a sinusoid function of amplitude 0.25 in. (6.4 mm). The "semi-circular" specimen features a semi-circular segment with radius 0.25 in. (6.4 mm) repeated three times on alternate sides of the mid-plane. Detailed dimensions of all three geometries are shown in Figure 18.

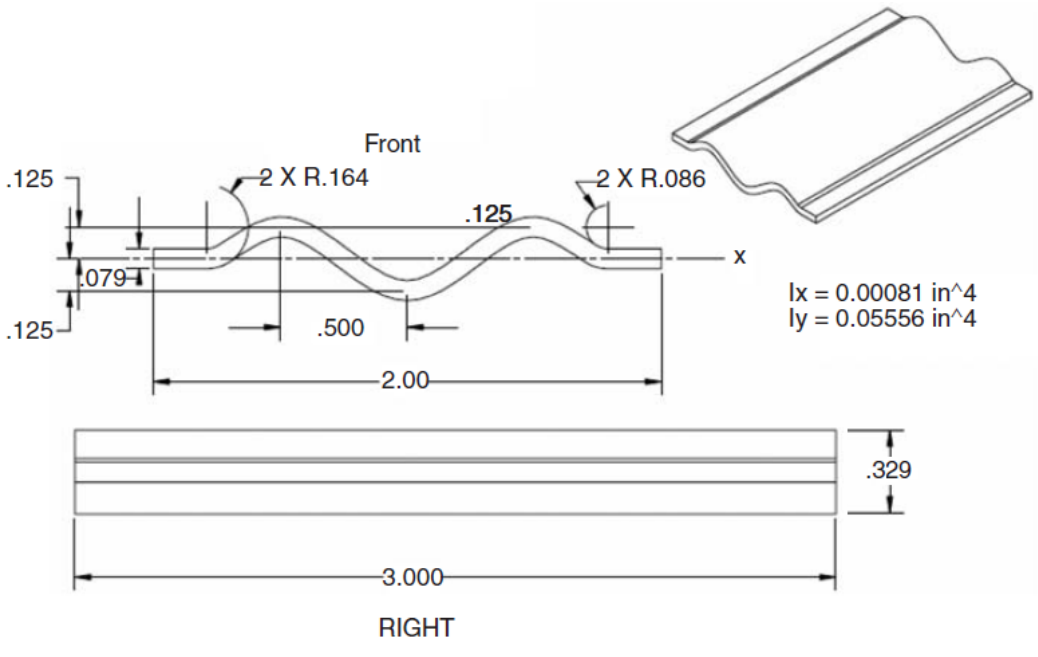

(a)

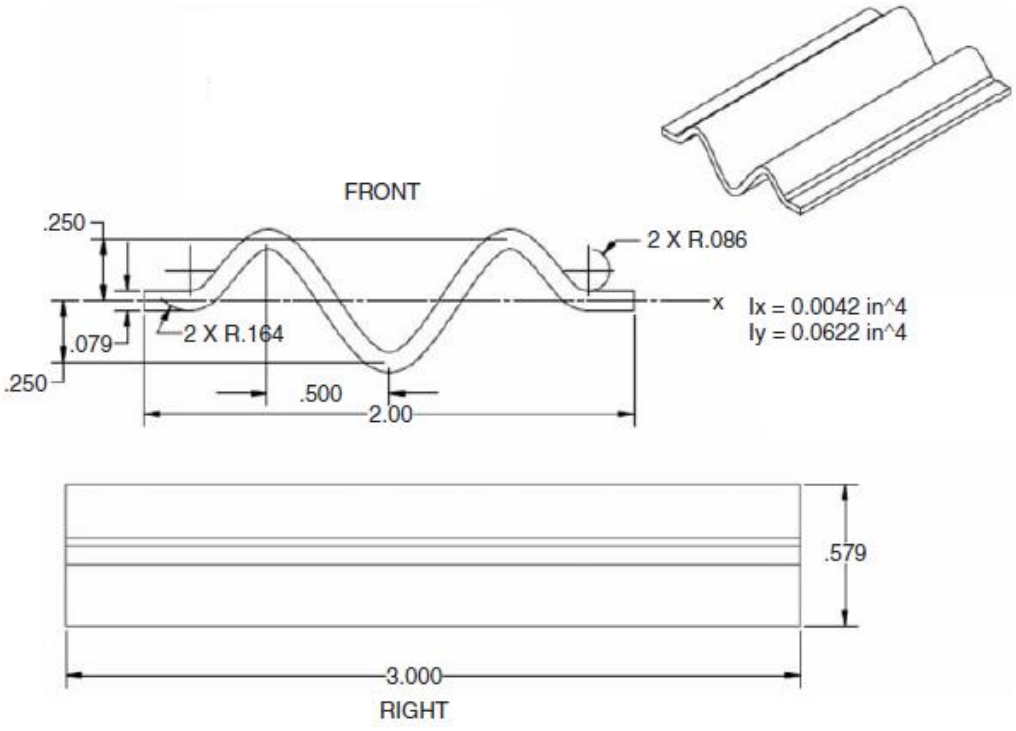

(b)

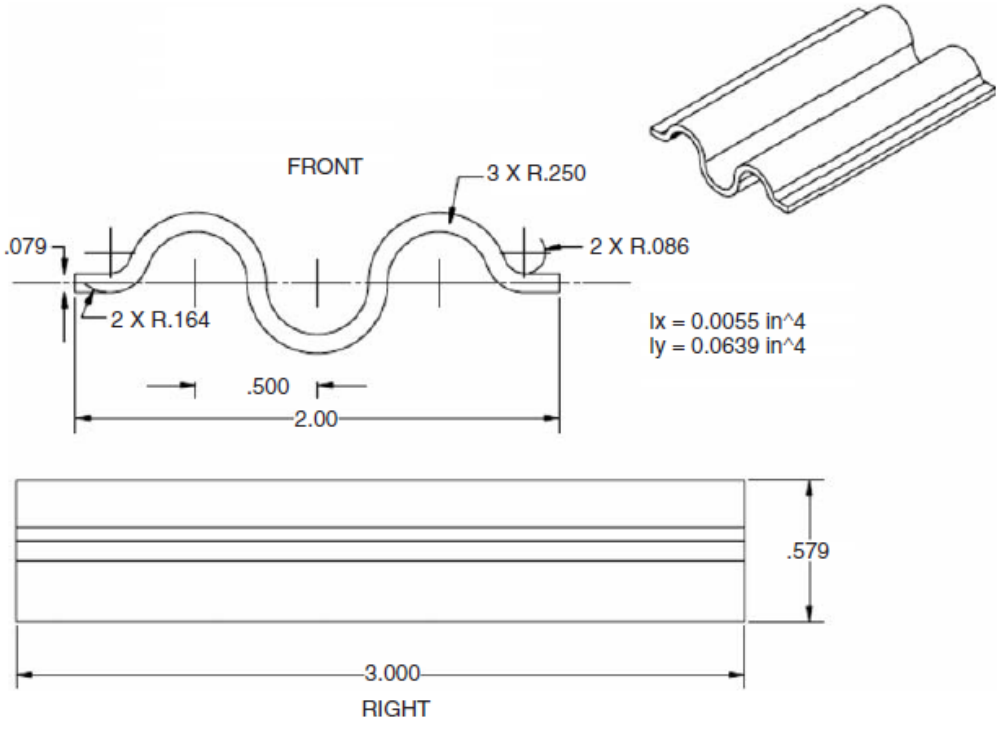

(c)

Figure 18. Three corrugated geometries and dimensions (all in inches) (a) low sine, (b) high sine, and (c) semi-circular.

Specimens were manufactured by press-molding through a set of aluminum matching tools, shown in Figure 19. All three corrugated specimens were used to characterize the energy absorbing capability of the AGATE fabric material system. Each specimen was trimmed to be 3.0 in. (76.2 mm) long with a 45-degree steeple machined along the bottom edge to initiate crushing behavior. Each specimen was mounted in 0.25 in. (6.4 mm) of potting resin to increase stability, reducing their effective length to 2.75 in. (69.8 mm). The three corrugated crush specimens, before and after crush tests, are shown in Figure 20. All tests were performed at a quasi-static rate of 2.0 in./min (50.8 mm/min). For each corrugated geometry and material combination, four specimens were tested.

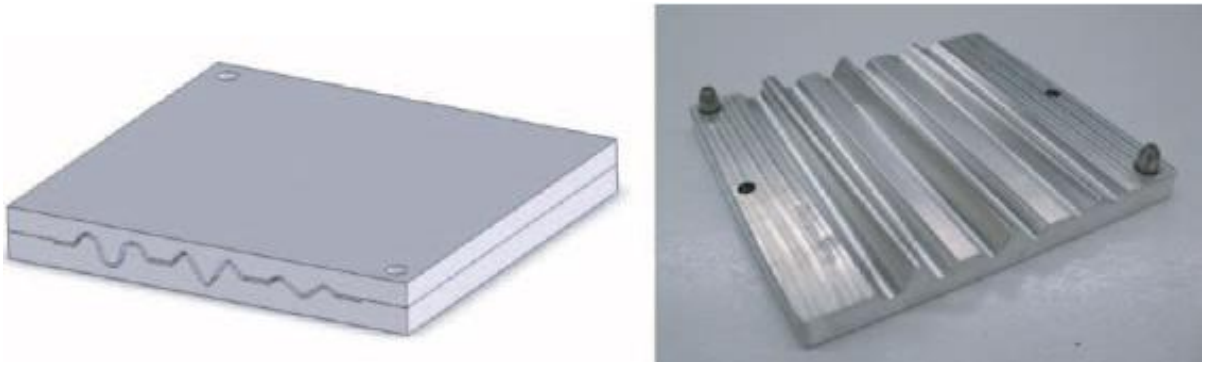

Figure 19. Aluminum tool used to make all three corrugated geometries.

(a)

(b)

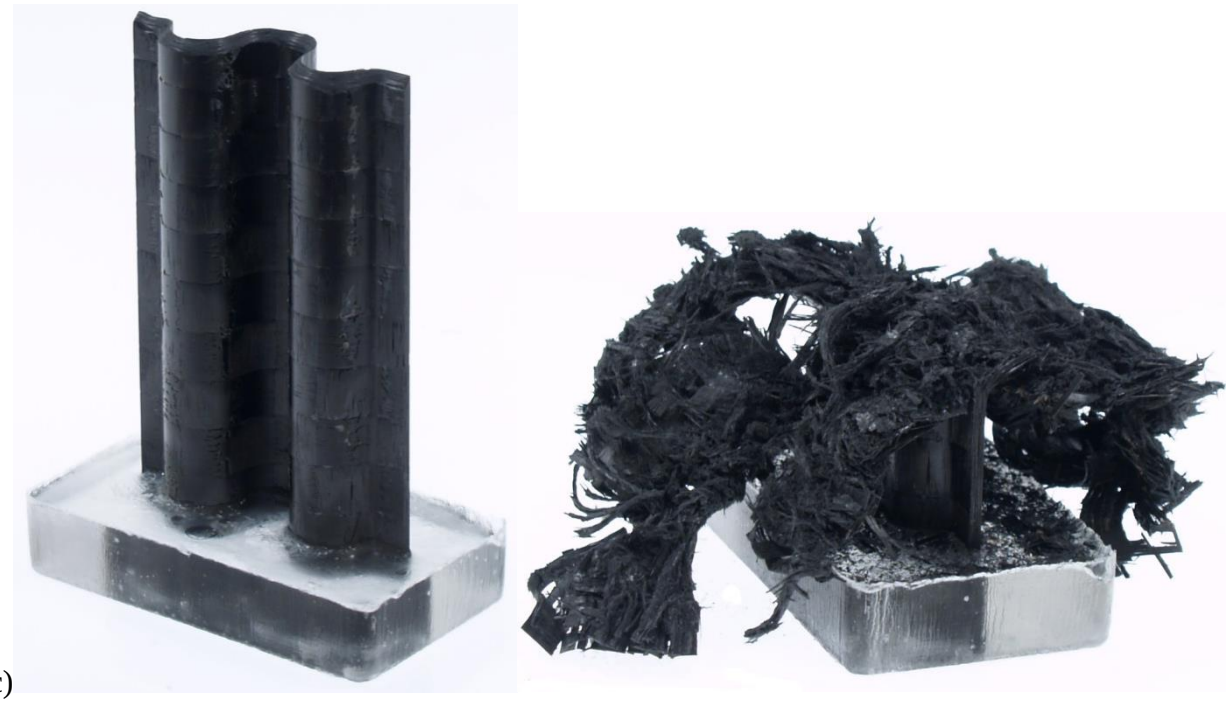

(c)

Figure 20. (a) Low sinusoid, (b) high sinusoid, and (c) semi-circular corrugated crush specimens before and after testing.

Prior to the work completed for this study, additional crush testing of the three corrugated elements took place at the University of Washington which investigated variations in material lay-up, material system, cure cycle, and crush speed. While these experimental variables are outside of the scope of this body of research, their results were published by Feraboli in [85]. One test from this published work used the UD AGATE cross-ply lay-up with the semi-circular sinusoid. The resulting crush curve from this representative test was used in this study strictly to provide data for the numerical analysis, and will not be discussed until the FEA analysis is introduced.

Experimental results from four repetitions of each the low, high, and semi-circular sinusoid specimens using the fabric material are shown in full in Figure 21-Figure 23. Important load and SEA data for each test specimen is presented in Table 3.

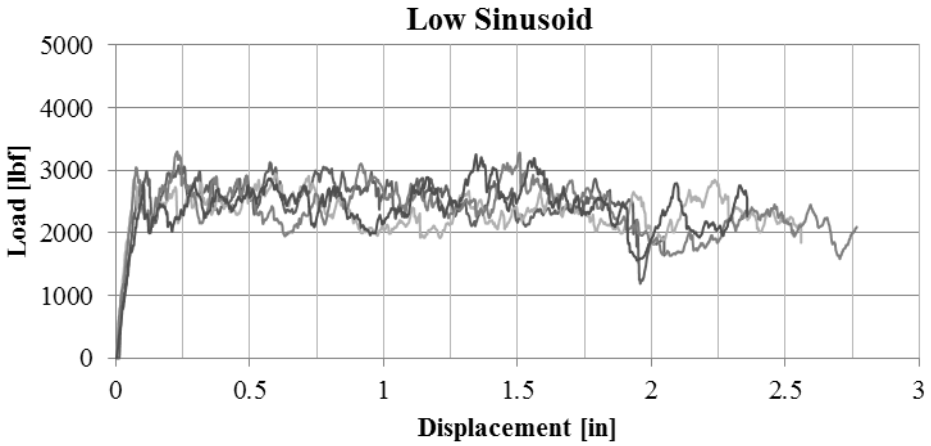

(a)

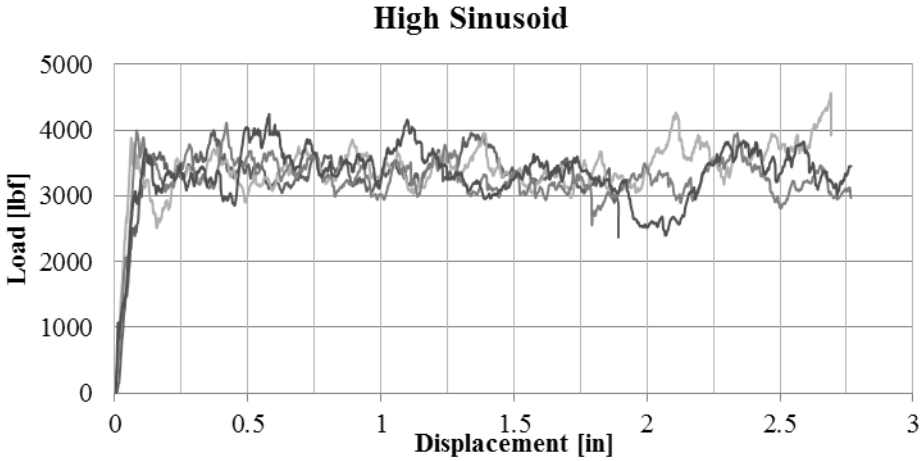

(b)

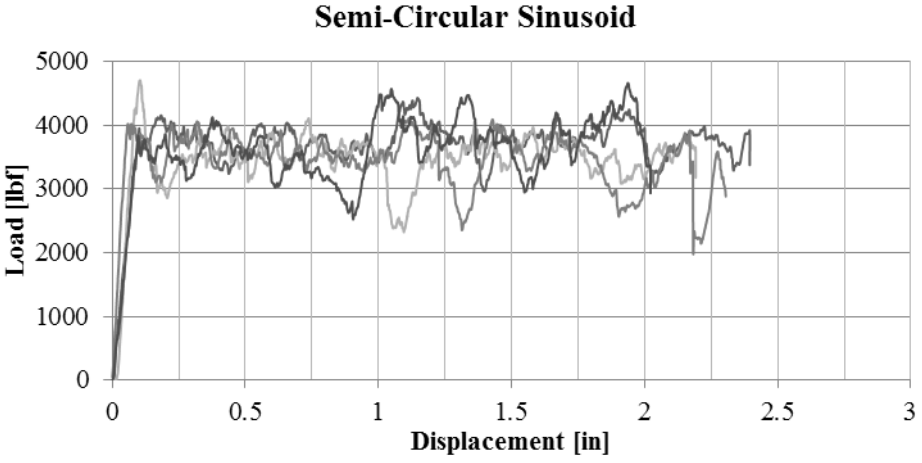

(c)

Figure 21. Load-displacement data from crush experiments of the (a) low, (b) high, and (c) semi-circular sinusoid elements made from the fabric material system.

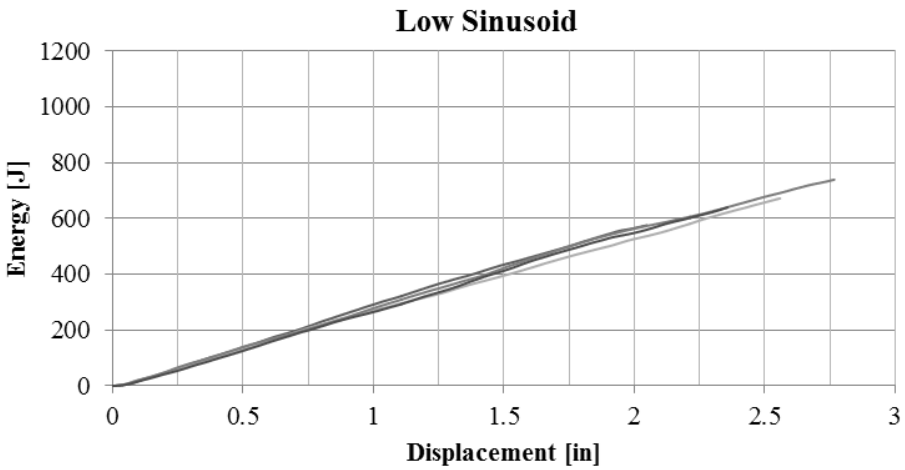

(a)

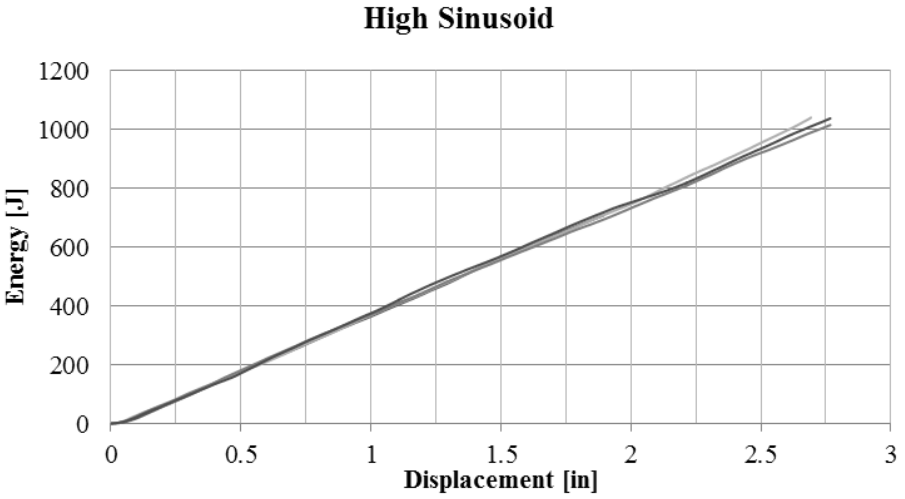

(b)

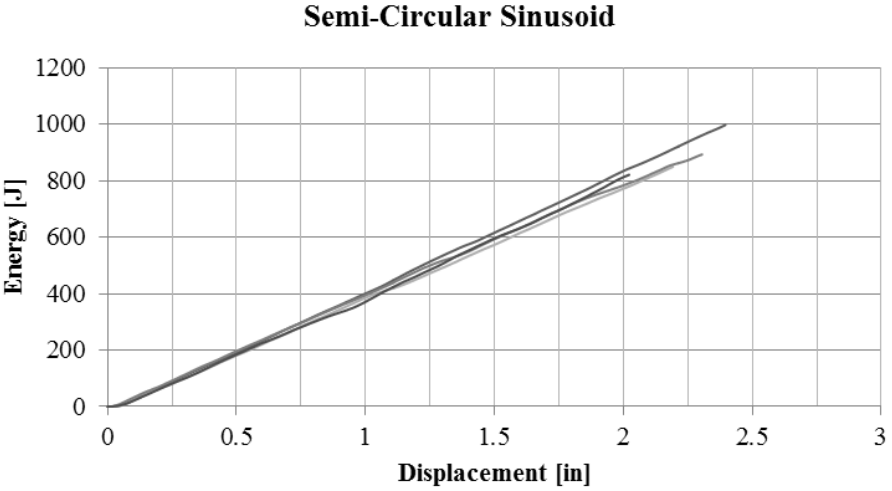

(c)

Figure 22. Energy absorbed vs. displacement data from crush experiments of the (a) low, (b) high, and (c) semi-circular sinusoid elements made from the fabric material system.

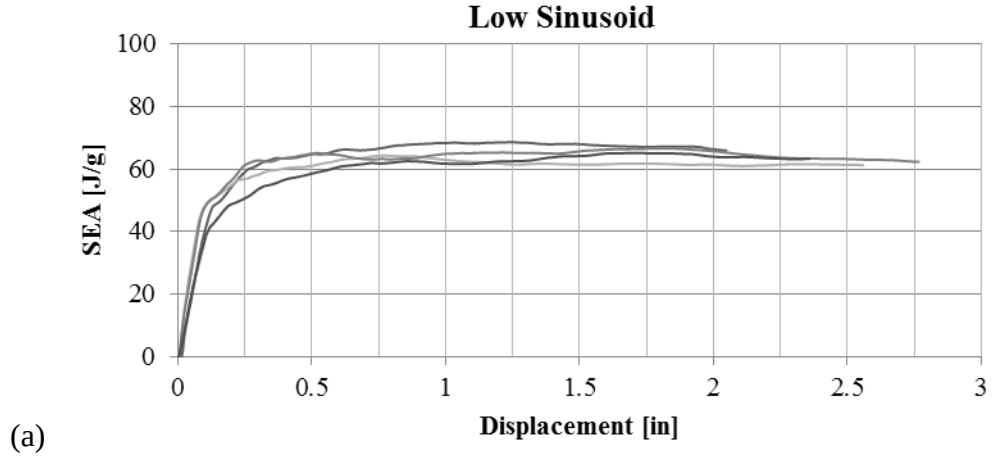

(a)

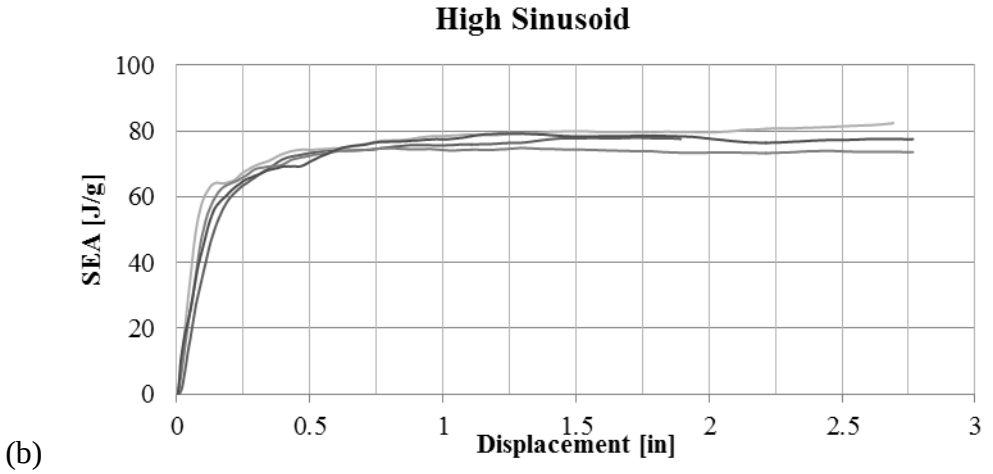

(b)

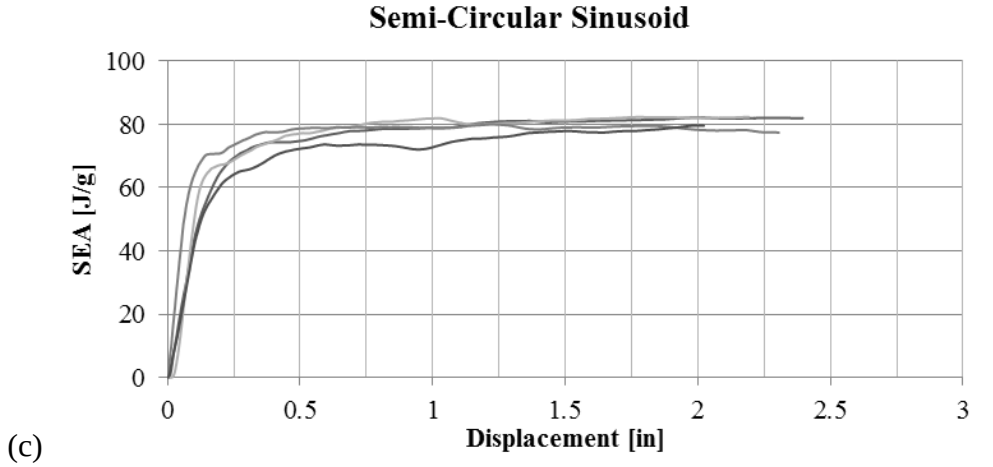

(c)

Figure 23. SEA vs. displacement data from crush experiments of the (a) low, (b) high, and (c) semi-circular sinusoid elements made from the fabric material system.

Table 3. Experimental load and SEA results from the sinusoid crush elements.

		Initial Peak *[lbf]*	**Average Crush Load** *[lbf]*	**SEA** *[J/g]*
Low Sinusoid	Specimen 1	2860	2346	61.5
	Specimen 2	3048	2391	64.3
	Specimen 3	2767	2446	62.4
	Specimen 4	2983	2584	66.6
	Average	2915	2442	63.7
	CoV	4%	4%	4%
High Sinusoid	Specimen 1	3883	3457	78.4
	Specimen 2	3997	3285	73.1
	Specimen 3	3624	3395	75.1
	Specimen 4	3713	3367	76.4
	Average	3804	3376	75.8
	CoV	4%	2%	3%
Semi-Circular Sinusoid	Specimen 1	4705	3483	79.5
	Specimen 2	4025	3399	77.8
	Specimen 3	3842	3681	74.7
	Specimen 4	3948	3761	79.2
	Average	4130	3581	77.8
	CoV	9%	5%	3%

The load-displacement curves, Figure 21, demonstrate the typical variability of experimental crush elements as the initial load peaks all fall within 4-9% of each other, and the average crushing load within 2-5%. These low variations are evident of stable and repeatable composite crush elements. The energy absorption data for the three sinusoid elements, Figure 22, confirms the test stability and repeatability. The rate of energy absorption is nearly constant within each family, with little variation between test specimens. In general, the semi-circular and high sinusoid specimens absorb more energy at a faster rate than the low sinusoid specimen, but all three families are very similar. Finally, the SEA data, Figure 23, also demonstrates a low variability between test specimens within each sinusoid family, however, the low sinusoid element achieved consistently lower SEA measurement than the high and semi-circular sinusoid

elements. With only a slight change in the specimen geometry, the average crush load and SEA measurements are clearly affected. Before drawing further conclusions, the dependence of the crush data on the specimen geometry is explored further by considering several new elements derived from a square tube.

Tubular CFRP element crush tests

Five tubular crush element geometries were tested in order to continue the study of the cross-sectional geometry effect on the overall crush behavior and energy absorption. Each specimen uses the same AGATE fabric material and lay-up such that the geometry was the only variable in the experiment. Several repetitions of each specimen were quasi-statically crush tested using the same test set-up as the corrugated specimens, and the energy absorption for each was measured. The findings from this experimental work were first presented in 2009 by the author [86], and published in 2009 by the author and her advisor in [87]; these results from the author were used in 2011 in [88].

The five new specimen geometries are derivatives of a common square composite tube with rounded corners: a small and a large c-channel, a small and a large corner, and the tube itself. Schematics for these geometries and their dimensions are shown in Figure 24.

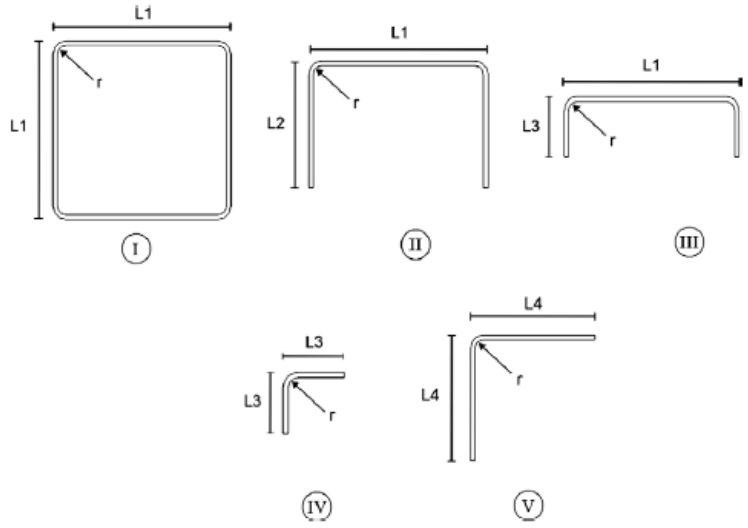

Dimension	Value	
L1	2.50 in.	(63.5 mm)
L2	1.75 in.	(44.5 mm)
L3	0.75 in.	(19.0 mm)
L4	2.00 in.	(50.8 mm)
r	0.175 in.	(4.45 mm)

Figure 24. Five channel geometries and dimensions I. Tube, II. Large c-channel, III. Small c-channel, IV. Small corner, and V. Large corner.

The experimental design motivation of the five channel-based crush geometries was that the square tube element is representative of tubular automotive crush structure elements, and the other four geometries could be manufactured as derivatives of the tube. Furthermore, c-channel geometries have been modern candidates in the design of subfloor stanchions in large commercial transport aircraft designed to provide energy absorption [89].

In order to make the channel specimens, portions of the square tube specimen were cut using a diamond-coated tile saw. With a single cut performed off-axis on the square cross section, the large and small c-channels were obtained (Figure 25 II and III, respectively). A second off-axis cut is performed on the small c-channel (Figure 25, IV), which isolates a single corner element whose dimensions are L3 x L3 (Figure 24, IV). The fifth channel specimen was obtained by performing two cuts on the original square tube section I (Figure 25, V), in the proximity of two opposing corners. The resulting is the large corner specimen with dimensions L4 x L4 (Figure 24, V).

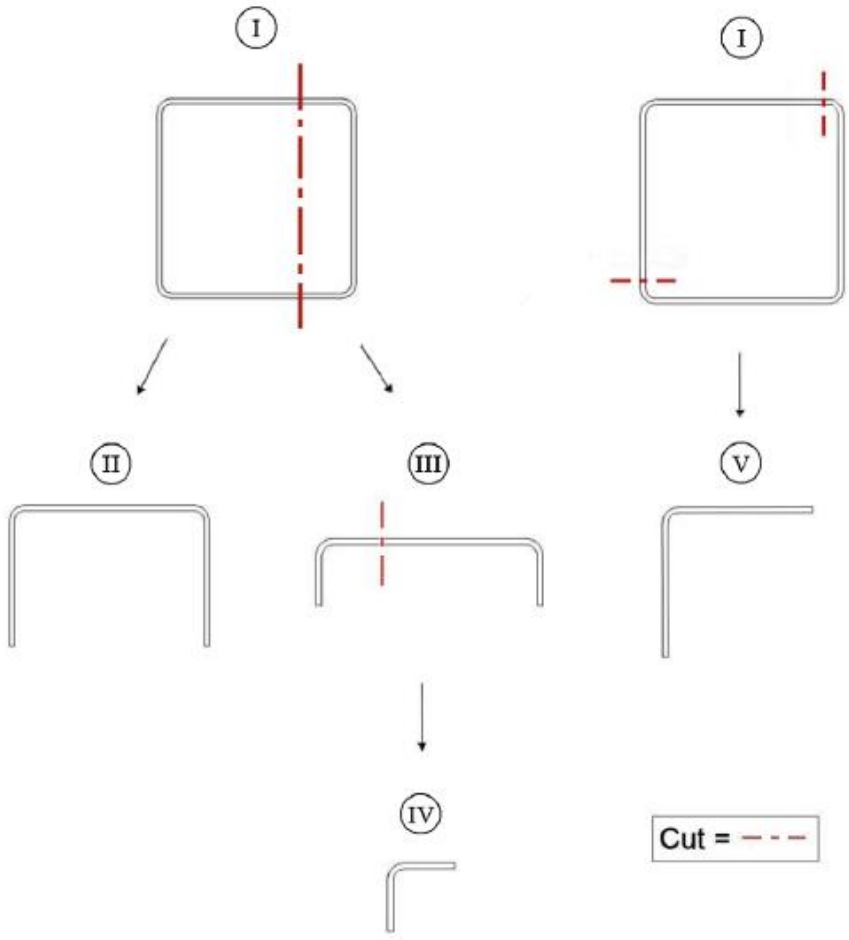

Figure 25. Schematic of machining operation performed to obtain channel test specimens II-V from the tubular specimen I.

The total section lengths, or perimeters, for each of the five channel section geometries are shown in Figure 26. Each of the five channel sections considered is comprised of one or more corner details, and additional segments of flat material. If the small corner geometry, specimen IV, is used as a repetitive unit, each cross-section can be subdivided into sections that are influenced by a single corner detail. These divisions are also shown in Figure 26.

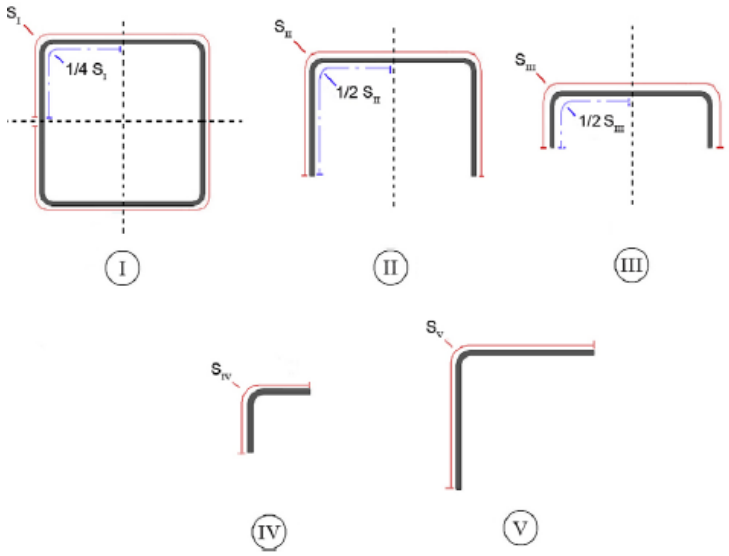

Perimeter	Value	
S_I	10.50 in.	(266.7 mm)
S_{II}	5.75 in.	(146.0 mm)
S_{III}	3.75 in.	(95.3 mm)
S_{IV}	1.25 in.	(31.75 mm)
S_V	4.50 in.	(114.3 mm)

Figure 26. Illustration of the total section length (perimeter) for each channel geometry considered, as well as the portion of each geometry influenced by a single corner detail.

The repeating corner unit is defined to be the small corner geometry (Figure 24, IV) and each cross-section is subdivided into sections that are influenced by that single corner detail plus additional flat segments. For instance, the square tube (Figure 24, I) is subdivided into a quarter-section, comprised of a single corner detail plus two additional flat segments on either side of the corner. This quarter section represents the portion of the square cross-section that is influenced by a single corner detail, since the double symmetry accounts for the other three corner elements. For the large and small c-channels, the half-section comprises the single corner detail plus additional flat segments. In the case of the small c-channel there is only one additional flat segment, since the length of the small c-channel flange is equal to the small corner detail flange. For the large c-channel, the longer flange means that there are additional flat segments on both sides of the corner detail. The large corner element is not subdivided since it is comprised of a single corner detail with longer flat segments on both sides. The subdivided sections for each geometry which represent the portion influenced by a single corner element are shown for each

of the five channel-type geometries in Figure 27, where S_{IV} is the perimeter length of the small corner element, and the ΔS', ΔS'', and ΔS''' quantities are the lengths of additional flat segments added for each geometry.

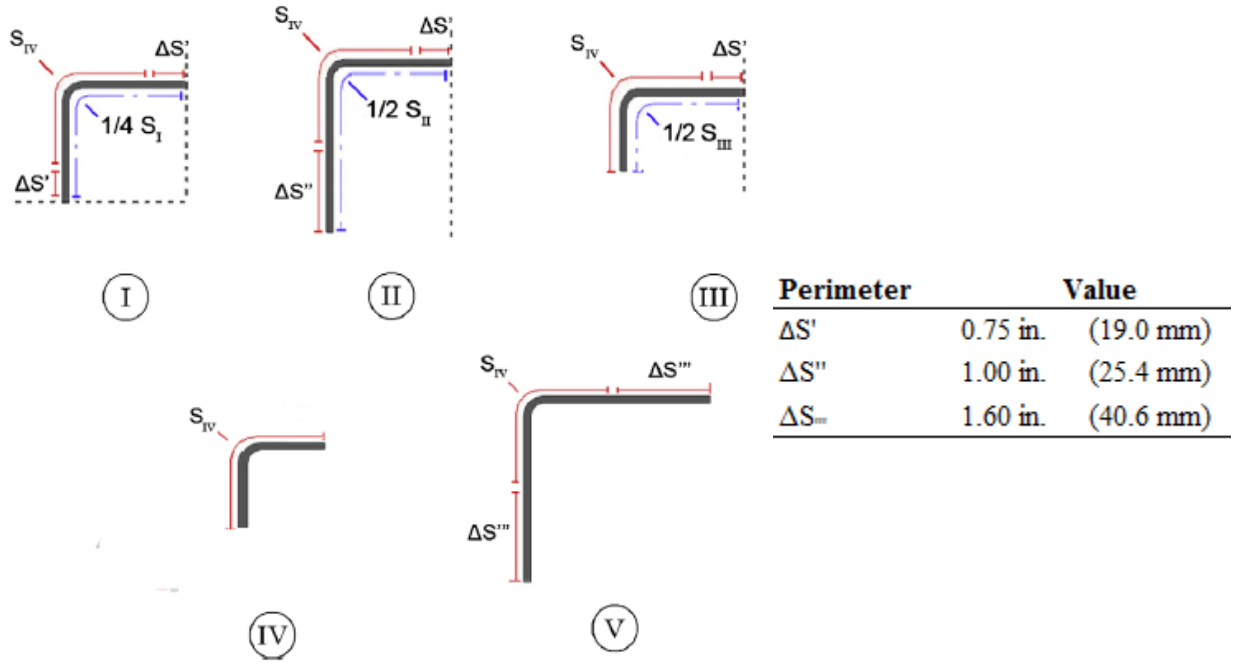

Perimeter	Value	
ΔS'	0.75 in.	(19.0 mm)
ΔS''	1.00 in.	(25.4 mm)
ΔS'''	1.60 in.	(40.6 mm)

Figure 27. Subdivision of section length into a corner detail, S_{IV}, and a portion of flat segments, ΔS, for each of the five channel-type cross-section geometries considered.

The purpose of this effort is to be able to measure the SEA and crush behavior of a stand-alone corner element, S_{IV}, and then extrapolate the actual in situ SEA and crush behavior of the flat sections, which is otherwise difficult to assess experimentally [19] [12] [90]. In this way, creating derivative geometries from the common square tube geometry is advantageous to determine the influence of the cross-sectional geometry on crush behavior. This specific exercise cannot be done with the three corrugated shapes since they do not contain the same corner element with strictly flat segments in the geometry.

The material system used for the tubular crush specimens was the AGATE fabric prepreg system, whose properties are given in Table 2. The lay-up considered was a $[(0/90)]_{4s}$, which yielded an average cured thickness of the tube of 0.065 in. (1.65 mm). The tubular specimens were manufactured on an aluminum square tubular mandrel with 0.175 in. (4.45 mm) radius rounded corners, Figure 28. After trimming, each specimen was 3.50 in. (88.9 mm) long. A single sided 45^{o} chamfer was machined on the upper end of every specimen to initiate crushing behavior during testing, as was done for the corrugated and flat crush specimens.

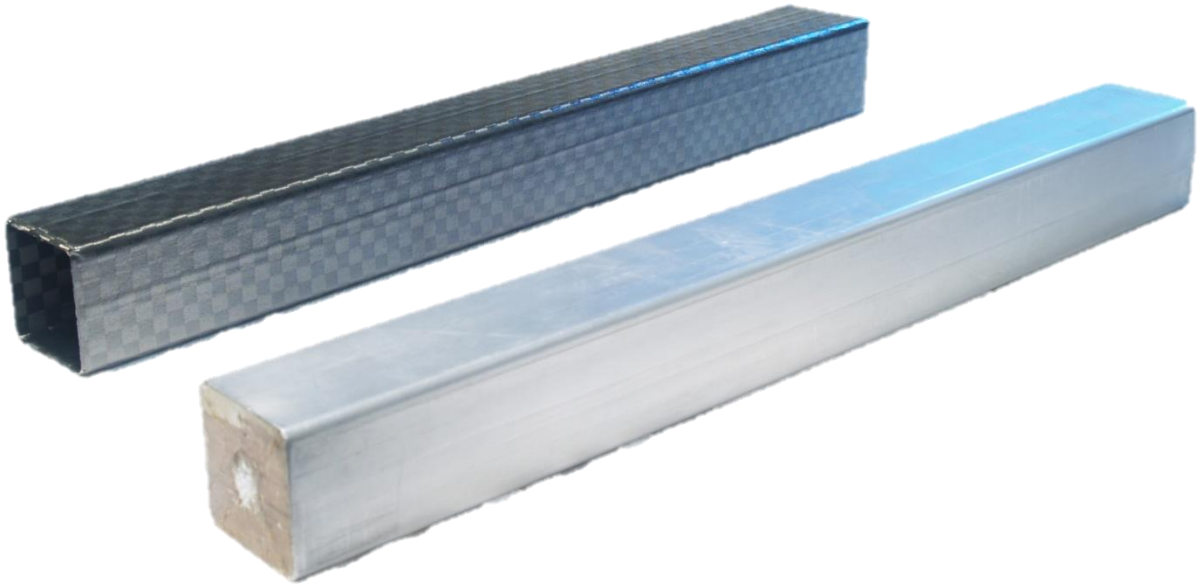

Figure 28. Square aluminum mandrel with carbon composite tube.

Specimens were crush tested between two aluminum plates with at least four repetitions for each geometry. The upper plate traveled at the same quasi-static rate of 2.0 in/min (50.8 mm/min) as used for the corrugated and flat crush specimens. All section specimens except for the square tube were potted into an epoxy resin base in order to provide stability during crushing; hence their effective length was reduced by at least 0.5 in. (12.5 mm). Pictures of the crush specimens

before and after crushing are shown in Figure 29-Figure 33. Each of the five tubular geometries was crush tested for a minimum of four repetitions.

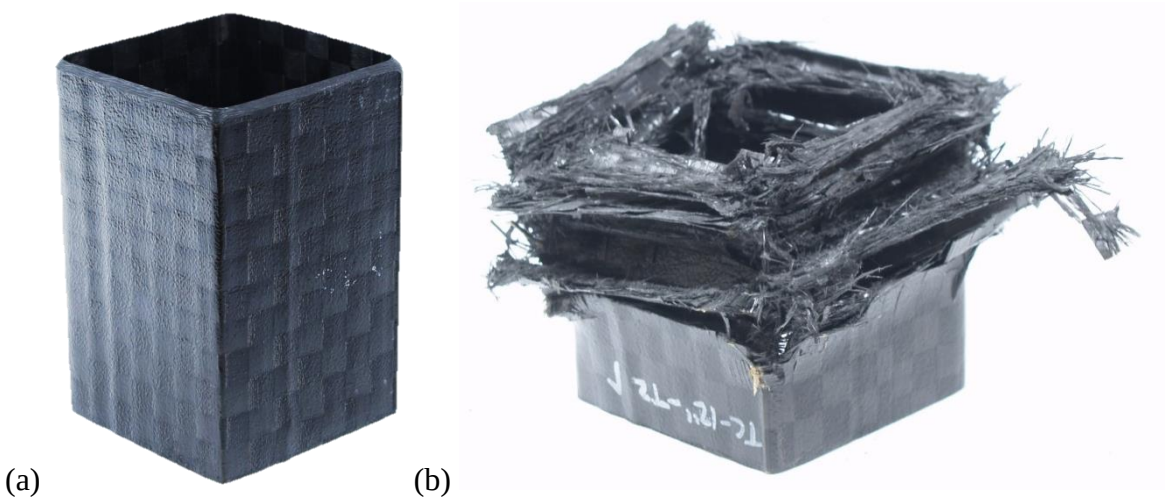

(a) (b)

Figure 29. Square tube, specimen I, (a) before and (b) after crush testing.

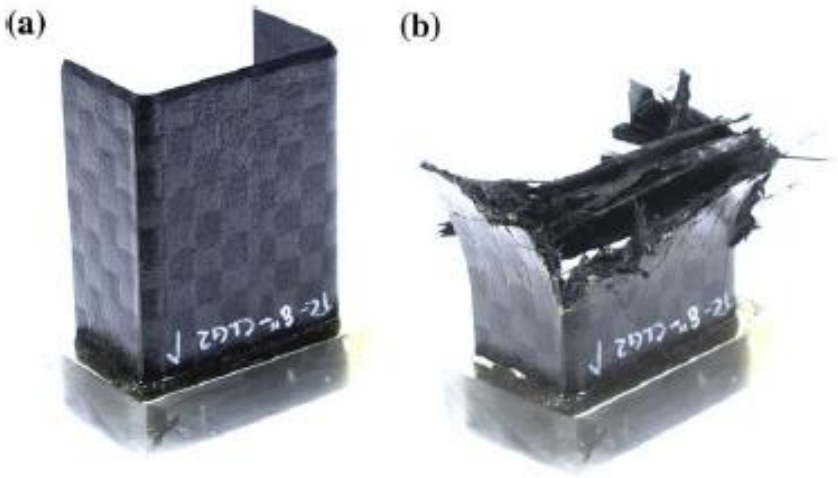

Figure 30. Large c-channel, specimen II, (a) before and (b) after crush testing.

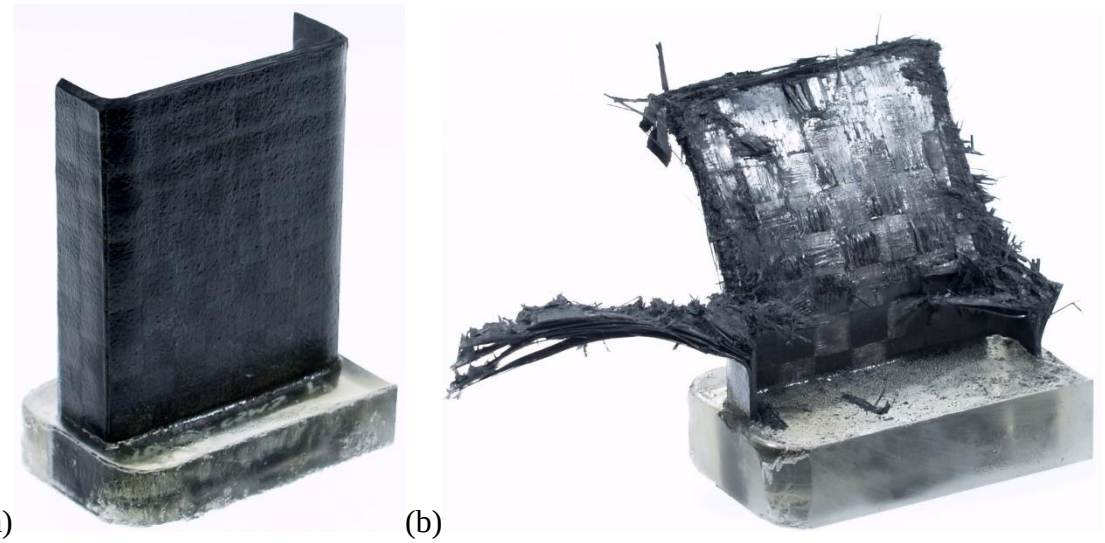

(a) (b)

Figure 31. Small c-channel, specimen III, (a) before and (b) after crush testing.

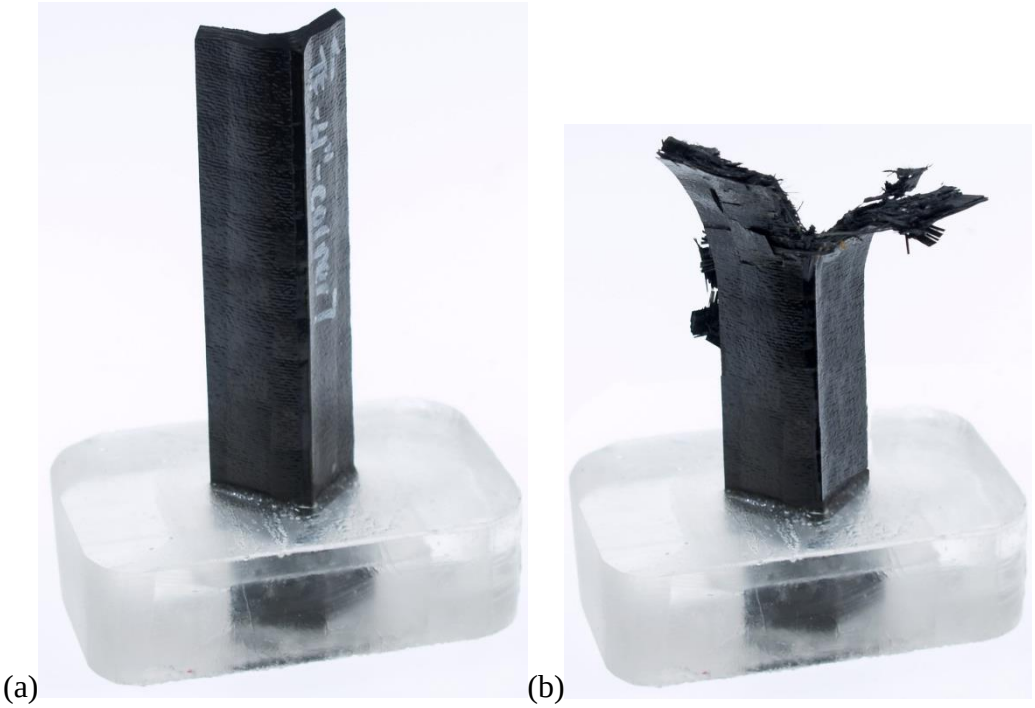

(a) (b)

Figure 32. Small corner, specimen IV, (a) before and (b) after crush testing.

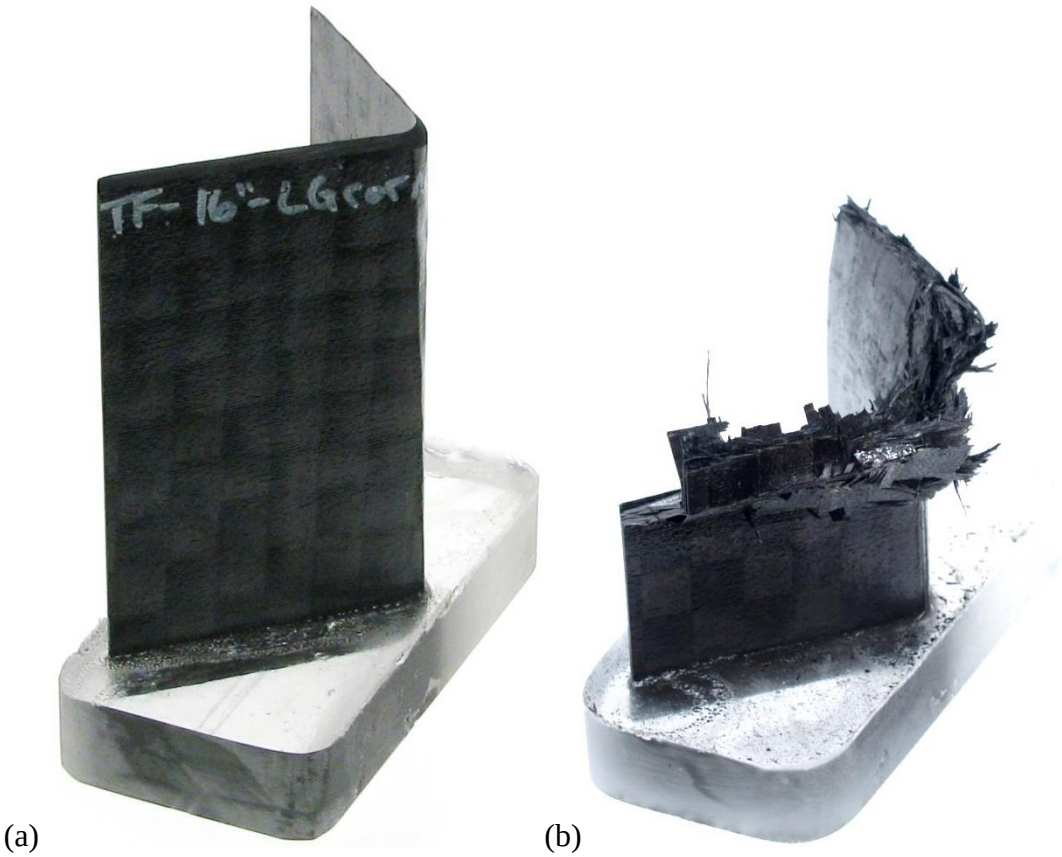

Figure 33. Large corner, specimen V, (a) before and (b) after crush testing.

All specimens presented in this study crushed in a stable manner. In general, greater variability was observed in the crush results from the tubular specimens than from the corrugated specimens, as best evidenced by the percent variability of the initial peak load, average crush loads, and SEA measurements provided in Table 4. The load, energy, and SEA crush curves from every stable repetition of the tubular specimens are given in Appendix A: Additional experimental data.

Table 4. Experimental load and SEA results from the tubular crush elements.

		Initial Peak *[lbf]*	**Average Crush Load** *[lbf]*	**SEA** *[J/g]*
Square Tube	Specimen 1	7655	5544	34.4
	Specimen 2	9122	5377	31.7
	Specimen 3	9325	5866	37.7
	Specimen 4	9414	5366	40.1
	Specimen 5	9037	4605	40.6
	Average	8911	5352	36.9
	CoV	8%	9%	10%
Large C-Channel	Specimen 1	4112	2616	34.5
	Specimen 2	3682	2604	32.4
	Specimen 3	4637	3126	39.9
	Specimen 4	4816	2940	39.0
	Specimen 5	5083	3312	38.7
	Average	4466	2920	36.9
	CoV	13%	11%	9%
Small C-Channel	Specimen 1	3283	2431	41.4
	Specimen 2	3780	2288	44.8
	Specimen 3	4277	2721	43.4
	Specimen 4	3837	2386	41.3
	Specimen 5	3993	2208	42.8
	Average	3834	2407	42.7
	CoV	9%	8%	3%
Small Corner	Specimen 1	1309	1067	63.3
	Specimen 2	1440	1067	52.8
	Specimen 3	981	1068	65.1
	Specimen 4	1360	1161	67.9
	Average	1272	1091	62.3
	CoV	16%	4%	11%
Large Corner	Specimen 1	3242	2241	30.7
	Specimen 2	3505	2283	33.3
	Specimen 3	2701	1818	28.2
	Specimen 4	2623	2133	34.1
	Average	3018	2119	31.6
	CoV	14%	10%	8%

In order to easily compare the results across the five different tubular and three corrugated crush specimen geometries, a representative load-displacement curve for each geometry is selected which best exemplifies the average peak load and crush load from each family. These curves are plotted in groups and are shown in Figure 34 and average SEA values from all stable repetitions are given in Table 5. These results have clearly demonstrated that the crush coupon geometry has a significant influence on SEA, and that for composite materials SEA is a structural property not a material property. For the composite material system investigated, the energy absorption capability lies within the range of 23 J/g (flat) to 78 J/g (corrugated).

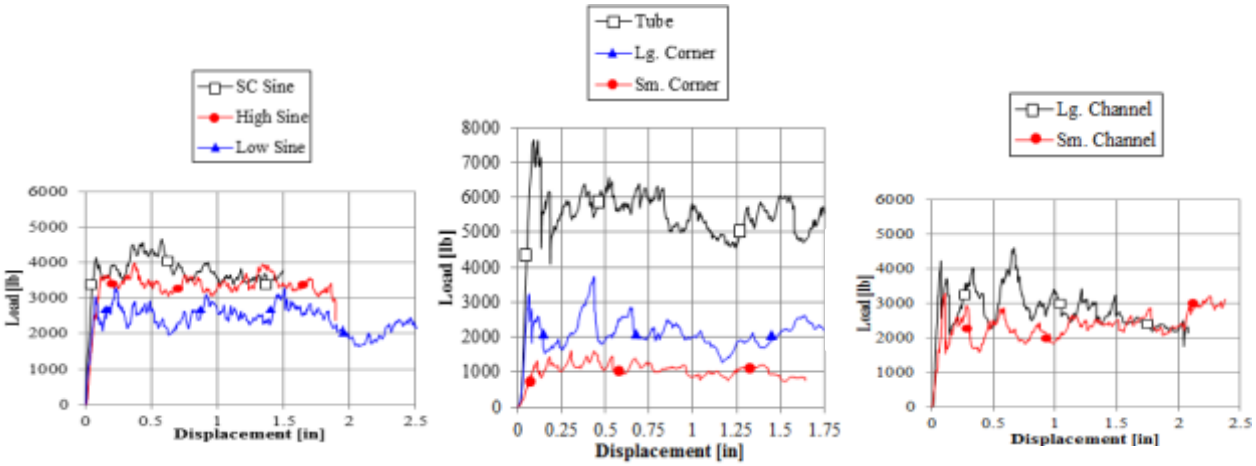

Figure 34. A sample load-displacement curve from crush tests of eight geometries

Table 5. SEA results from each of the nine geometries crush tested.

SC Sine	78 J/g	Tube	37 J/g	Lg. Channel	37 J/g
High Sine	76 J/g	Lg. Corner	32 J/g	Sm. Channel	43 J/g
Low Sine	70 J/g	Sm. Corner	62 J/g	Flat	23 J/g

Discussion of results

Given the clear influence of specimen geometry upon the resulting SEA measurement demonstrated in the crush experiments, a relationship which connects the geometric features of the crush specimens to the SEA is sought after and investigated. A further understanding of how the geometry influences the energy absorbing mechanisms occurring during crush failure is also desired and studied.

In order to relate the geometry to SEA, the geometry needs to be expressed in a mathematical form which can then be compared against SEA results. One way to describe the geometry in terms of mathematics which differentiates each crush specimen by a different value is to consider the amount of curvature of the cross-section relative to the total length, which can be expressed by a simple ratio. For the tubular specimens, the length of each curved section is equal to the length around one of the 90-degree corners, given by the quantity $(\pi/_2)r$. The degree of curvature ratio is therefore defined to be the arc length of one corner divided by the length of the cross-section influenced by that corner, as follows,

$$\varphi = \frac{(\pi/_2)r}{(S_i/_n)} \qquad \text{Eq. (12)}$$

Where r is the radius of the corner, S_i is the length of the cross-section (along the mid-plane), and n is the number of corners in the geometry. Because this value is a length scale divided by another length scale, it is a non-dimensional parameter. To calculate the degree of curvature of the corrugated geometries, the length of the corrugated portion of the section is divided by the total length, where the only flat portions of the cross-sections are the end flanges. The resulting degree of curvature values calculated for each geometry are given in Table 6.

Table 6. Degree of curvature, φ, values for each of the nine geometries crush tested.

SC Sine	0.895	Tube	0.105	Lg. Channel	0.096
High Sine	0.891	Lg. Corner	0.061	Sm. Channel	0.147
Low Sine	0.829	Sm. Corner	0.220	Flat	0.000

The SEA is plotted versus the degree of curvature for each geometry, which reveals a linear trend among the tubular shapes which have lower degrees of curvature, shown in Figure 35a. The corrugated shapes have a much higher degree of curvature, and at such values the SEA reaches a maximum threshold between 70-80 J/g for this material type, shown in Figure 35b.

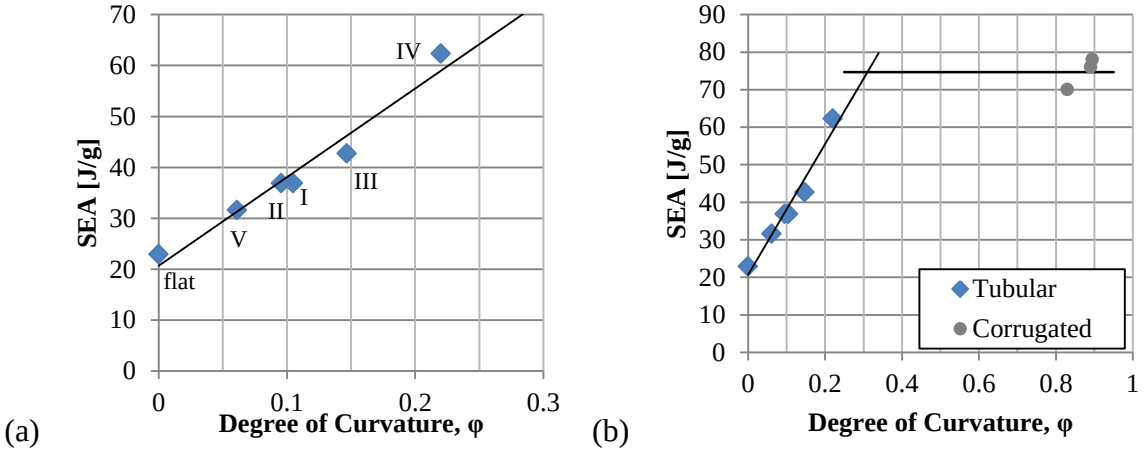

Figure 35. SEA vs. φ for different crush geometries: (a) tubular only (b) all geometries

This result shows that more curvature in the cross-sectional geometry provides a better efficiency in crushing, and that a threshold exists where increasing the amount of curvature of the geometry no longer contributes to raising the energy absorption capability. In order to better understand this phenomenon, a micrographic analysis of the crushed specimens is conducted to compare the higher SEA curve sections against the lower SEA flat sections. The analysis showed that the damaged region following the crush-front of curved sections was very small, and most of the specimen was intact and undamaged behind the crush-front. Micrographic analysis of flat

sections revealed long cracks which had propagated beyond the crush-front through material. A micrographic image from each a curved (from a semi-circular sinusoid specimen) and flat segment (from the web of a c-channel) in Figure 36 shows both of these failure mechanisms. In the flat segment shown, the damage had propagated over five times further past the crush-front than in the curved segment shown.

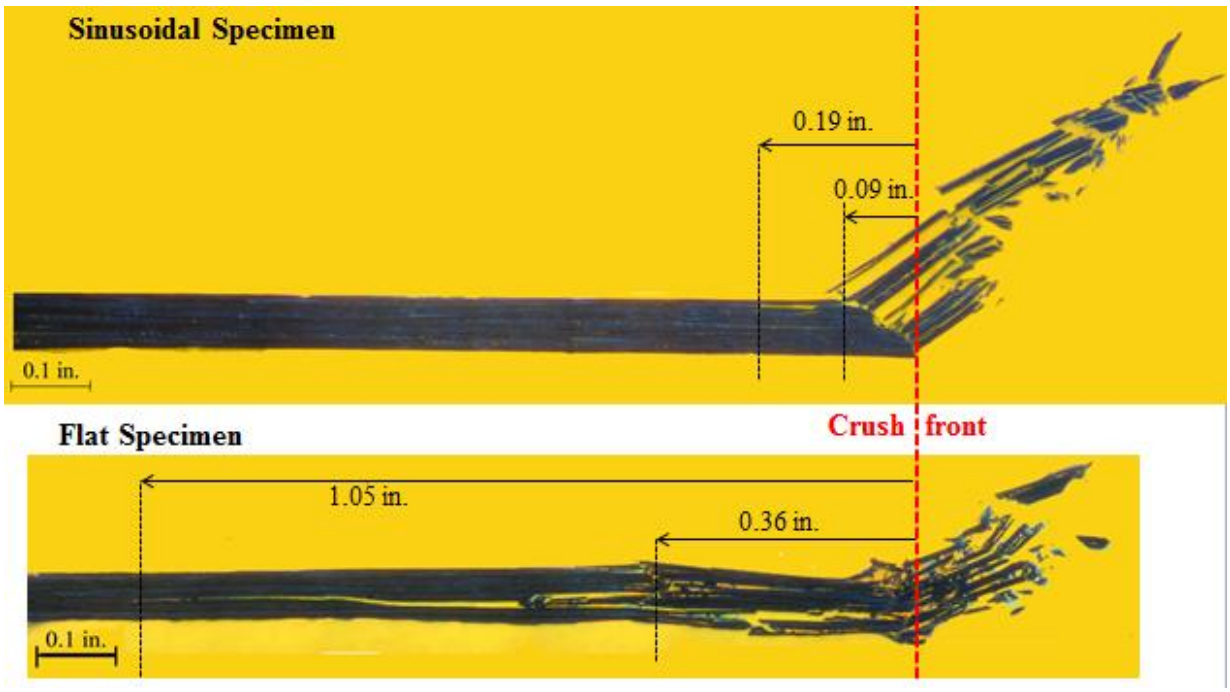

Figure 36. Micrographic analysis showing a short damage zone following tearing failure at the corners (top) and a large damage zone following ply splaying at the flat sections (bottom)

The key result is that the failure mechanisms of the curved and flat segments were observed to be very different. Referring to the energy absorbing mechanisms identified by Hull [9], the flat sections of the tubular geometries splayed open (Figure 31b) and allowed crack propagation deep down the interior of the material as indicated in the micrographic image of Figure 36. Material at the corners of the tubular sections (Figure 32b) and in the corrugated specimens (Figure 20) experienced abundant fragmentation and tearing.

The distinct failure mechanisms of the flat and curved segments each have a very different energy absorbing capacity. The delamination failure mode observed in the flat segment absorbed very little energy as most of the material remained intact while a large crack propagated between plies causing very little fiber breakage. The fragmentation observed at the corners, however, absorbed a lot of energy in the process of breaking up the material, both fiber and matrix, into pieces as small as dust particles. The greater the delamination suppression provided by a geometry is, the more fragmentation failure occurs and the higher the SEA. The amount of delamination suppression can be estimated by considering the degree of curvature of the geometry, given by Equation 12.

The estimation of SEA given by the degree of curvature must be considered with caution, however, as there is a material scale factor in terms of the specimen thickness and the local fiber buckling length which affects the favored failure mechanism in the material. For instance, a very large perfectly circular specimen with a large the diameter to thickness aspect ratio will have a geometric degree of curvature value $\phi = 1.0$ which would indicate a high SEA based on Figure 35. With a large enough diameter, this hypothetical circular specimen would locally have a flat geometry (to the limit, locally $\phi = 0.0$) and experience splaying and delamination failure mechanisms, which would result in a low SEA. In the case of the crush experiments presented here, the aspect ratio of length to thickness for all nine specimens was within similar values, and the material scale factor is not evident in the results. It would be appropriate to consider the geometric degree of curvature value ϕ a local phenomenon, for which the relevant scale factor must be determined for the material system tested.

Experimental conclusions

In the process of investigating experimental methods to characterize the energy absorption capability of composite material systems, several key findings were made. First, unlike isotropic materials, SEA is not a material property of a composite material system and SEA measurements vary significantly according to the geometry of the crush test element. This means that no single crush test can fully characterize the energy absorption capability of a composite material system, as several configurations must be tested that are each representative of geometric elements from the full structure in order for a range of SEA values to be collected. The underlying reason that there is a range of energy absorption capability in a single composite material system due to the variety of crush failure modes observed during crush testing which are each capable of absorbing different amounts of energy. These failure modes change according to the degree of curvature of the geometry of the crush test element.

Composite crush energy absorption mechanisms can be divided into two extreme behaviors, delamination/splaying and fragmentation, for which crush failure is a combination of varying degrees of both. In the delamination mode, little energy is expelled in splitting the material along an interlaminar crack front into two fronds, and the resulting SEA measurement is relatively low. This mode was observed for flat segments of the crush elements, where the geometry provides no delamination suppression and a crack front can easily propagate through the material. Fragmentation failure is a more comprehensively destructive failure mode which leaves little material intact and requires a lot of energy to break the material in such a manner, resulting in a high SEA measurement. Such failure occurs when crack propagation is suppressed by a highly curvaceous geometry.

As a result of these different crush failure modes, the energy absorbing capability of the single composite material system investigated varied from 23 J/g (flat) to 78 J/g (corrugated). From the nine crush geometries tested, a relationship between the SEA and the degree of curvature of the crush test element geometry was developed. This curve describes the energy absorption capability of the material according to the geometry of the crush element. This curve cannot be derived from a single test, and crush elements with different degrees of curvatures must be tested in order to develop such a curve for any other material, lay-up, thickness, etc. It is recommended that a flat coupon, low degree of curvature specimen (i.e. tube), and high degree of curvature specimen (i.e. corrugated) each be experimentally crush tested to develop this curve such that the material SEA is fully characterized. Such a comprehensive characterization of the energy absorbing capability of a composite material system is necessary such that the analysis material model can be calibrated to match the varying experimental results at the element-level (i.e. sinusoidal and tube specimens).

Analysis

LS-DYNA has traditionally been considered the benchmark for composite crash simulations and is extensively used in the automotive and aerospace industries to perform explicit dynamic post-failure simulations [6] [79] [68] [80]. The LS-DYNA MAT54 material model is a great candidate for large, full-scale structural composite damage simulations because it is specifically meant for shell elements, for which all full-scale crash simulations are modeled with, and it relies on relatively few input parameters, most of which can be simply measured using standard material property testing. MAT54 therefore requires a reduced computational load that is appropriate for large-scale simulations. The basic details of this material model can be found within the LS-DYNA User's Manual [91], reproduced in Appendix B. Unfortunately, its official documentation is brief, contains several small errors, and omits many details of the material model which are important for the complete understanding and proper implementation of this model. For these reasons, a portion of this research effort has been dedicated to the full characterization and documentation of this material model that is a good candidate for composites crash simulation. This was accomplished through single element studies, parametric studies of crush simulations, and the careful study and interpretation of the MAT54 source code generously provided by LSTC. The result of this effort is a more comprehensive description of MAT54, its parameters and governing equations, which is provided in Appendix C.

The results of the single element study are discussed first. The purpose of this study was to perform a thorough parametric investigation on the MAT54 input parameters to study their response to simple loading conditions in the most basic model of a single element. This study provided the necessary background of understanding the mechanics of MAT54 such that the crush simulation models could be developed. Following the single element study, the crush

simulation of the semi-circular sinusoid shape using a material model developed for the unidirectional tape composite is presented. In this investigation, the response of the MAT54 inputs to more complicated edge-on loading conditions representative of crushing are investigated, as well as other modeling definitions introduced for the crush simulation. The UD material system was chosen first as this is the type of material system that MAT54 was developed for. The purpose of this study was to focus on the initial development of a MAT54 crush simulation and study the effects of the basic model definitions, but this single simulation alone could not reveal feedback on the robustness or predictive capability of the model. The third investigation pursued was to change the material model definition from the UD material to that of the fabric material system, while maintaining the same semi-circular sinusoid crush model. In this way, the isolated effects of the material model definition in the crush element simulation could be studied. Already at this level, important findings were made regarding the robustness of the material model and its sensitivity in crush simulations which were investigated further. After establishing a solid understanding of the crush simulation using MAT54, the eight different geometries which were experimentally crush tested were modeled. From this comprehensive set of investigations using MAT54 to model a composite material undergoing crush failure, a detailed protocol describing the procedure to calibrate the MAT54 model for crush simulation, as well as a definition of the required experimental data necessary to achieve a calibrated material model, has been established.

Following this accomplishment, the source code of the material model has been edited and modified with the goal to improve its composite material simulation capability with an emphasis on crush simulation capability. The detailed interpretation of the source code and process of

modification is presented in Appendix E, and the results of the modification will be presented in the main text of this analysis discussion.

MAT54 single element studies

In order to properly utilize the MAT54 composite damage material model, a set of single element investigations were performed using MAT54 to simulate a carbon fiber/epoxy material system. This single element investigation was led by Morgan Osborne under the supervision of the author, and the results of which were first published in his Master's Thesis [92]. For the purpose of this discussion, a summarized table of all of the relevant MAT54 input parameters, their definition, and means of measurement is given in Table 7. The complete table and discussion of all MAT54 input parameters can be found in Appendix C.

MAT54 was used to simulate the same T700/2510 carbon fiber/epoxy prepreg material system used in the experimental portion of this research, for which material properties are given in Table 2. First, single elements with basic unidirectional (UD) lay-ups of $[0]_{12}$ and $[90]_{12}$ were investigated. Basic tensile and compressive loads were applied to the element, and a parametric study was performed on the user defined MAT54 input parameters in order to form a basic understanding of the material model. The results from these simulations were used to provide suggested modeling strategies to simulate UD composite laminates using MAT54. Following this study, single element parametric studies were performed on MAT54 when simulating a fabric material system with a $[(0/90)]_{8f}$ lay-up and a cross-ply laminate made from the UD material system with a $[0/90]_{3s}$ lay-up.

Table 7. Select MAT54 user-defined input definitions and required experimental data

Name	Definition	Type	Measurement
MID	Material identification number	Computational	N/A
RO	Mass per unit volume	Experimental	Density test
EA	Axial Young's modulus	Experimental	0-deg tension test
EB	Transverse Young's modulus	Experimental	90-deg tension test
PRBA	Minor Poisson's ratio ν_{21}	Experimental	0-deg tension test with biaxial strain measurement
GAB	Shear modulus G_{12}	Experimental	Shear test
ALPH	Elastic shear stress non-linear factor	Shear factor	**None; Default 0.1 recommended**
BETA	Shear factor in tensile axial failure criterion	Shear factor	**None; Default 0.5 recommended**
DFAILT	Axial tensile failure strain	Experimental	0-deg tension test
DFAILC	Axial compressive failure strain	Experimental	0-deg compression test
DFAILM	Transverse failure strain	Experimental	90-degree tension and compression tests; **May require adjustment for stability**
DFAILS	Shear failure strain	Experimental	Shear test
EFS	Effective failure strain	Optional	Combination of standard tests
TFAIL	Time step failure value	Computational	Derived from numeric time-step
FBRT	Axial tensile strength factor after 2-dir failure	Damage factor	**None; Default 0.5 recommended**
SOFT	Material strength factor after crushing failure	Damage factor	**None; Requires calibration**
YCFAC	Axial compressive strength factor after 2-dir failure	Damage factor	**None; Default 1.2 recommended**
XT	Axial tensile strength	Experimental	0-deg tension test
XC	Axial compressive strength	Experimental	0-deg compression test
YT	Transverse tensile strength	Experimental	90-degree tension test
YC	Transverse compressive strength	Experimental	90-degree compression test
SC	Shear strength	Experimental	Shear test

A single square element for each laminate was subjected to tension and compression loading in the axial direction, as shown by the schematic of loading and boundary conditions in Figure 37. The z-direction displacement on all nodes was constrained. For the $[90]_{12}$ laminate, the 'axial' direction was considered to be the local 90-degree direction. A constant loading rate of 2 in/s (51 mm/s) was applied to nodes 1 and 4 of the single element. The time step was chosen to be 50% of the critical time step, which is the maximum value determined by the Courant condition (given in Appendix C, Equation 34). The baseline time step was therefore 2.846E-7 seconds. It

was necessary to use a double precision solver for the single element simulations in order to avoid some instabilities.

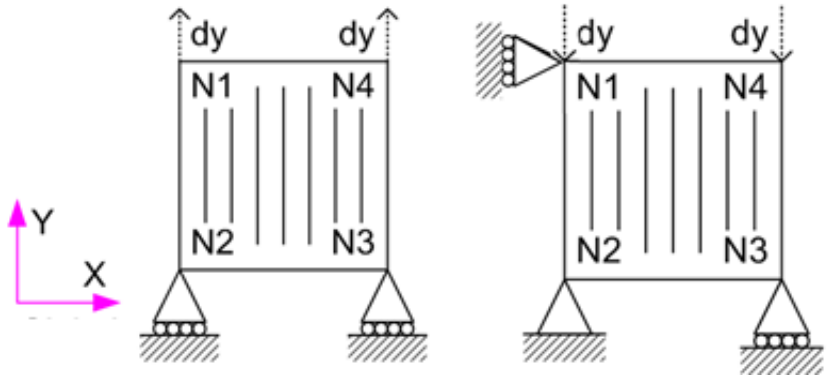

Figure 37. Schematic of the single element MAT54 simulations for tension (left) and compression (right) load cases.

Since all of the plies are in a single direction for these lay-ups, the ply response was the same as the laminate response, and first ply failure (FPF) corresponded to laminate failure. The average thickness of these laminates measured from experiments was 0.079 inches (2 mm). The ply angle and ply thickness at each integration point were defined in the *PART_COMPOSITE input deck. The element was a LS-DYNA Type 16 fully-integrated shell element with a mesh size of 0.1 inches (2.5 mm).

For each laminate and loading condition, parametric studies were performed by varying 20 of the MAT54 input parameters defined in Table 24. MAT54 parameters that are inactive or establish the local material orientation were not investigated. The baseline MAT54 input deck for the UD tape is given in Figure 168, for which parameter values were determined from the material properties as given in Table 2.

The design allowables report for this UD material system does not include strain to failure values [82]. Instead, it is suggested by the report to use simple one-dimensional linear stress-strain

relationships to obtain corresponding failure strain values. While for fiber-dominated laminates this is a valid approximation, for matrix-dominated laminates (such as $[90]_{12}$) a non-linear response is expected. Regardless, the design allowable guidelines were followed, and the MAT54 failure strain parameters were calculated by dividing the material strength by the appropriate modulus as follows:

$$DFAILT = \frac{XT}{EA} \quad \text{Eq. (13)}$$

$$DFAILC = \frac{XC}{EA} \quad \text{Eq. (14)}$$

$$DFAILM = \frac{YT}{EB} \quad or \quad DFAILM = \frac{YC}{EB} \quad \text{Eq. (15)}$$

where DFAILM can be defined using either the tensile or compressive matrix strengths. Since DFAILM defines the failure strain for both loading conditions, the higher of the two values from Equation 15 is recommended to define DFAILM, which often provides better stability.

Given the simplicity of the single element uniaxial loading conditions, many of the MAT54 parameters defined in Table 24 were found to have insignificant or no influence on the simulation outcome. These included shear parameters, ALPH, BETA, DFAILS, GAB, and SC, as well as parameters that require special loading conditions, SOFT, FBRT, and YCFAC. The Poisson's ratio, PRBA, had a negligible effect on the results. None of these parameters will be discussed in the results section. The investigation of the EFS and TFAIL input parameters found that these two deletion parameters were not uniquely influential among the single elements investigated, and that they provide a utility which can be applied to any laminate and loading condition. The parametric results for these two parameters will only be discussed in the $[0]_{12}$ results section.

As a part of this study, loading velocities from 1 in/min (25 mm/min) to 300 in/s (7.6 m/s) were simulated for every element, and results remained unchanged throughout the velocity range. Since MAT54 does not have any strain-rate sensitive parameters this result was expected, and will not be discussed further in the results section.

For all of the single element simulations, data was generated at three levels of scale: at the integration point (ply), at the node, and at the element (laminate). While data was recorded in all directions, for the purpose of this study only relevant data in the loading direction is reported. Data of interest at each integration point were the ply stresses and strains. Reaction forces at the boundary conditions on nodes 2 and 3 were recorded to generate the equivalent stress-strain data for the element and verify reported element results. Displacements and velocities were recorded on the free node, node 4, to monitor for unstable behavior. Finally, the total energy of the element was recorded. History variables which record violations of the Hashin failure criteria were monitored at the ply and element levels. Since these variables only report stress-based failures, the data was not found to be useful as many of the important MAT54 behaviors are strain-based.

Modeling parameters that were capable of significantly changing the stress-strain behavior, energy, or stability of the simulation are discussed in the results section. Each laminate was first simulated using the baseline MAT54 input values found in Figure 168. These initial simulations provided baseline numeric data against which data from the parametric studies were compared.

Unidirectional [0] and [90] laminates

Expected and experimental results

Given the material strengths and properties for the UD material system in Table 2, the expected stress-strain responses of the UD $[0]_{12}$ and UD $[90]_{12}$ elements were generated using the linear elastic equations (given in Appendix C, Equations 22-24), and the Hashin failure criteria (Equations 5-8), assuming no shear. The energy output was determined by calculating the area under the linear force-displacement curve. Force was calculated by multiplying the stress by the cross-sectional area of the element, and displacement was calculated by multiplying the strain by the element length.

The stress-strain results were compared against experimental coupon testing of the UD laminates. Results from the $[0]_{12}$ coupon tests, Figure 38a, align well with the expected linear elastic results. The $[90]_{12}$ experimental results, Figure 38b, deviate from the calculated linear stress-strain curve. Since nonlinear behavior is characteristic of matrix-dominated laminates, deviations from the linear-elastic assumption were anticipated. The expected strengths, failure strains, and output energies for the $[0]_{12}$ and $[90]_{12}$ laminates are given in

Table 8.

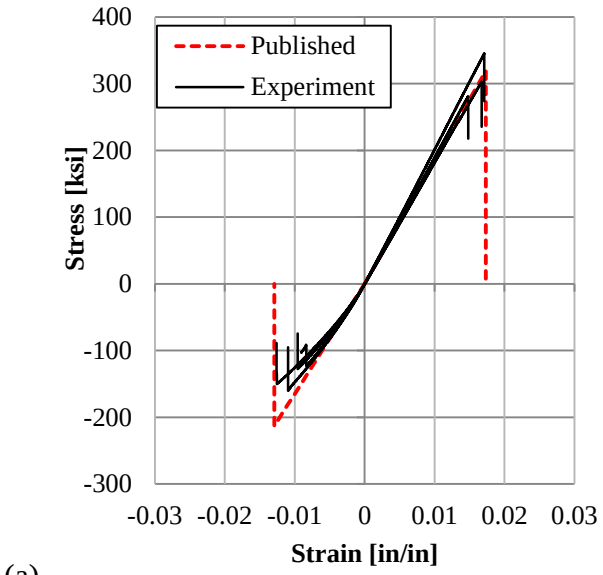

(a)

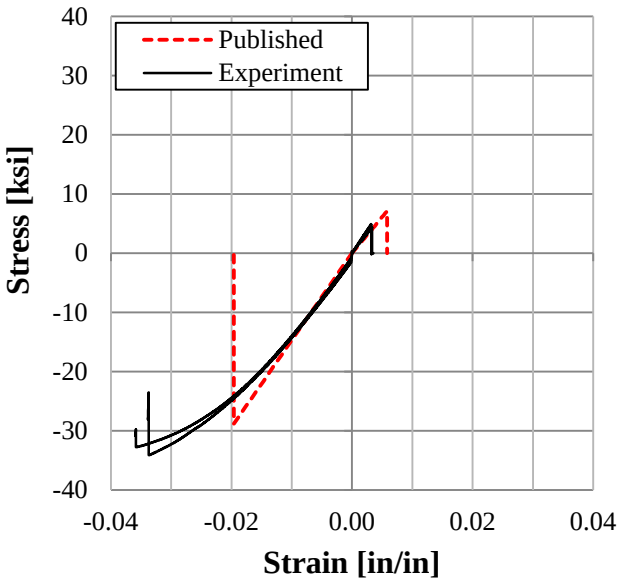

(b)

Figure 38. Stress-strain curves from (a) $[0]_{12}$ and (b) $[90]_{12}$ quasi-static coupon tests and the published material data from [18].

Table 8. Expected baseline strength, failure strain, and output energy values for the AGATE UD material system.

	Expected Result
$\mathbf{F_1^{tu}}$	319 ksi (2200 MPa)
$\mathbf{F_2^{tu}}$	7.09 ksi (48.9 MPa)
$\mathbf{F_1^{cu}}$	-213 ksi (-1466 MPa)
$\mathbf{F_2^{cu}}$	-28.8 ksi (-199 MPa)
$\boldsymbol{\varepsilon_1^{tu}}$	0.017337 in/in
$\boldsymbol{\varepsilon_2^{tu}}$	0.005811 in/in
$\boldsymbol{\varepsilon_1^{cu}}$	-0.011576 in/in
$\boldsymbol{\varepsilon_2^{cu}}$	-0.023607 in/in
$\mathbf{Energy_1^t}$	0.24682 J
$\mathbf{Energy_1^c}$	0.11004 J
$\mathbf{Energy_2^t}$	0.00184 J
$\mathbf{Energy_2^c}$	0.03034 J

Baseline simulation results

The UD single element loaded along the fiber direction produced the stress-strain curve shown in Figure 39a. These results correlated perfectly with the expected linear elastic curve with zero error. Parabolic behavior was observed in the output energy plot, Figure 39b, with a total energy result of 0.25 J without any error.

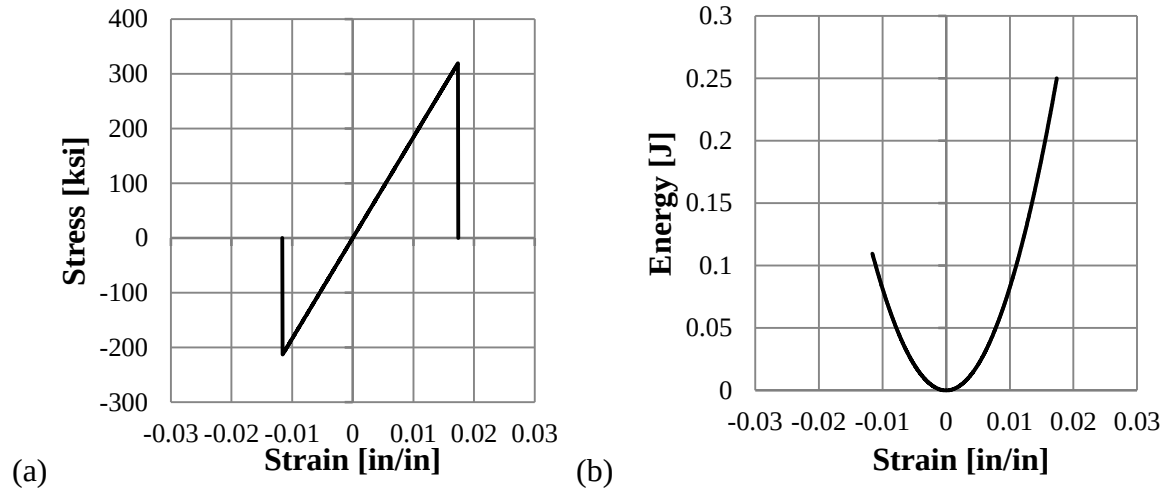

Figure 39. Laminate (a) stress-strain and (b) output energy curves for the baseline $[0]_{12}$ single element simulation.

Predictions for the simulation of the UD laminate loaded in the matrix direction were not as successful. Simulation results in compression correlated very well with expected results, both for stress and energy, but in tension the MAT54 results did not match expectations. Figure 40a shows the unexpected perfectly plastic region following the linear elastic behavior in tension. This plastic region was a consequence of the way MAT54 computes the element stresses after failure by adding the new stress from the current time-step to the stress calculated in the previous time-step. This calculation is shown in Appendix C, Equation 29, and illustrated in Figure 169. Recall that there is only one modulus and one failure strain parameter in the matrix direction, meaning the tensile and compressive values cannot be independently defined. As a consequence, only one strength value can satisfy the linear elastic relationship between stress and strain, but there are two matrix strength parameters (for tension and compression). Since these strengths are different and the matrix failure strain was determined using the compressive strength value in Equation 15, the tensile loading case will not satisfy the linear elastic stress-strain relationship. Thus, the simulation reached the tensile strength before the matrix failure strain and continued to plastically strain and carry stress until the failure strain was reached, 0.024 in/in. This strain value was over four times greater than the expected strain at failure, 0.0058 in/in. The plasticity caused the energy to increase linearly, Figure 40b, which added a significant amount of energy to the output of the baseline simulation, more than seven times what was expected. The MAT54 simulation of the UD matrix in tension did not agree with the expected behavior.

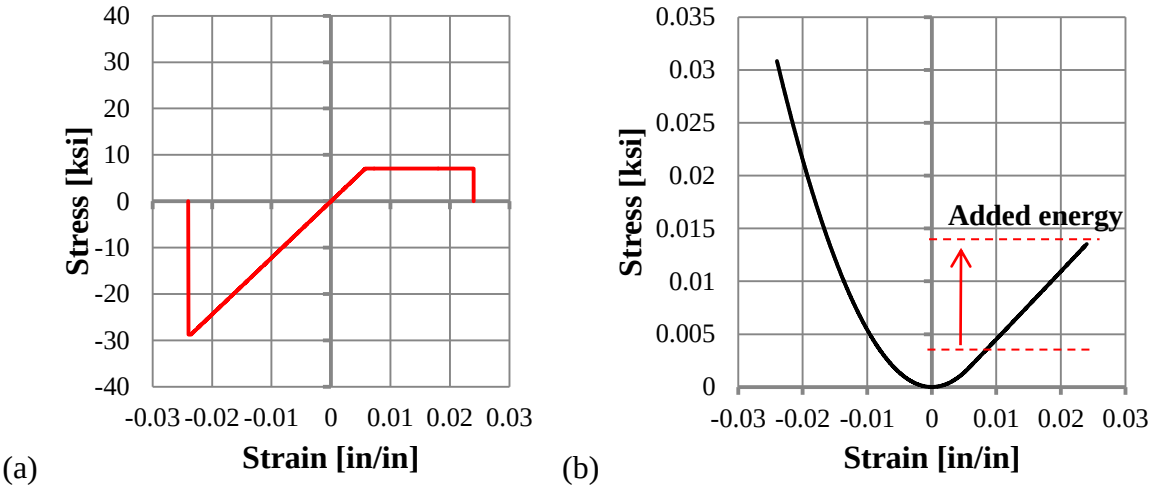

Figure 40. (a) MAT54 results for baseline $[90]_{12}$ laminate (a) stress-strain and (b) energy, with added energy highlighted.

Results from the $[0]_{12}$ laminate parametric study

The test matrix for the study of MAT54 parameters using the $[0]_{12}$ UD laminate is given in Table 9. The parameters which exclusively influenced the matrix direction, such as EB, DFAILM, YC and YT, were found to have no influence on the $[0]_{12}$ simulations in the loading direction and are therefore omitted from this report.

Table 9. Parametric test matrix for the MAT54 $[0]_{12}$ lay-up, baseline and parametric values.

Variable	Baseline value	Parametric values			
EA	1.81E+7	0	9.2E+7	3.7E+8	
XT	314000	0	200000	400000	
XC	210000	0	50000	100000	200000	300000
DFAILT	0.0174	0	0.01	0.03	
DFAILC	-0.0116	0	-0.005	-0.01	-0.02	-0.03
EFS	0	0.001	0.01	0.017821	
TFAIL	1.153E-9	2.835E-7	2.840E-7	2.846E-7	

Changing the fiber modulus, EA, affected the single element both in tension and compression since MAT54 does not distinguish compressive and tensile moduli. As one would expect, larger values of EA produced a stiffer stress response from the single element and lower EA values produced a softer response, Figure 41. The failure strain remained the same when changing EA, causing the element with a low modulus to fail at a lower stress value. For the high modulus case, the stress stopped increasing at the strength value and continued to plastically deform until the failure strain was reached and the element was deleted. Since this was a fiber-dominated laminate, the plastic response from the high modulus case was not expected and is not physically meaningful.

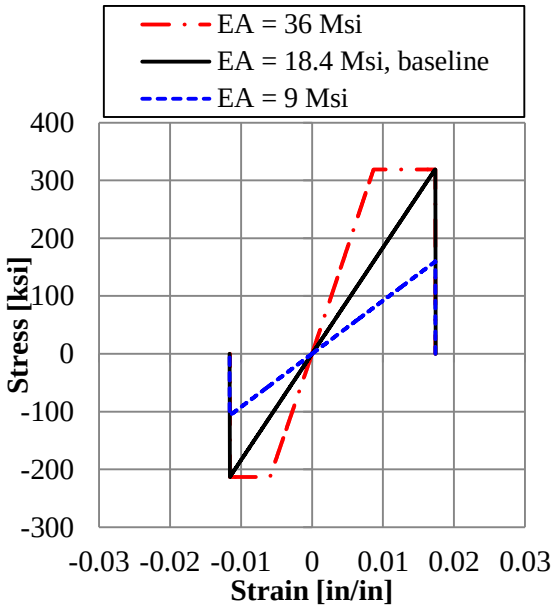

Figure 41. Stress-strain results from changing the fiber modulus, EA.

Changing the fiber strengths, XT for tension and XC for compression, changed the peak stress limits of the $[0]_{12}$ single element simulation. Element stress-strain plots for parametric studies of XT and XC are shown in Figure 42. Increasing strength values larger than the baseline values changed the results by less than 0.1% from the baseline. For these simulations, the element

reached the failure strain before the strength, which caused element deletion at the same strain as the baseline. Material strengths set to zero were considered by MAT54 to be numerically infinite, which produced the same results as simulations with increased strengths. Lowering the fiber strength below the baseline value caused the stress to remain constant at the strength magnitude until the element was deleted at the given failure strain. Because a MAT54 element is not eroded until the failure strain is reached, raising the strength without also changing the failure strain to match alters the shape of the nominally brittle linear elastic stress-strain material curve such that plasticity is introduced.

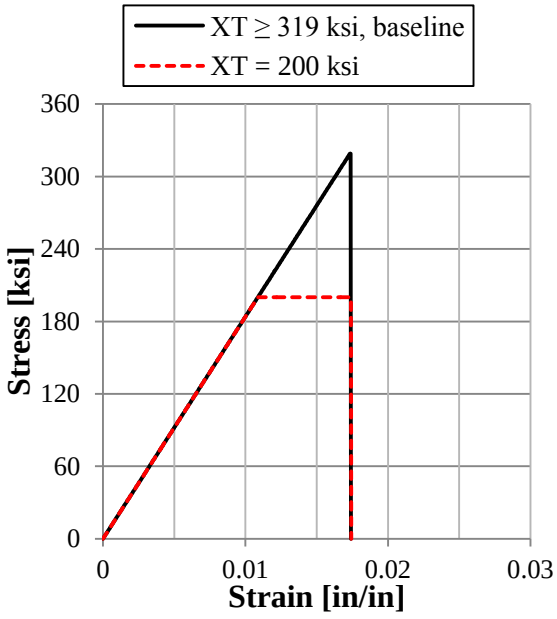

(a)

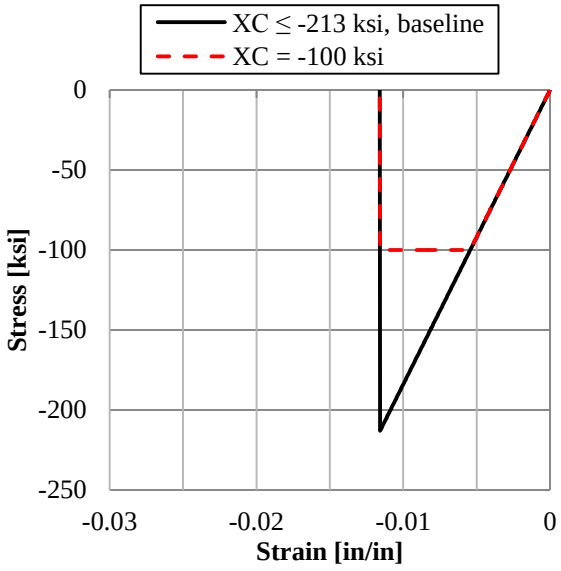

(b)

Figure 42. Stress-strain curves resulting from changing the MAT54 parameters for fiber strength in (a) tension, XT, and (b) compression, XC.

To demonstrate the great difference between expected results and the results given by MAT54 when plasticity is present, a simulation with plasticity in both tension and compression was generated by lowering the XT and XC strengths by approximately 100 ksi (690 MPa). The resulting laminate stress-strain curve with plasticity is plotted in Figure 43a, along with the baseline curve and the expected brittle stress-strain result. In Figure 43b, the total energy outputs from these three cases are plotted. Following stress failure and in the plasticity region, energy increased linearly until the failure strain was reached. From this plastic energy growth, a laminate with a 100 ksi (690 MPa) strength reduction only had an 18% loss in energy. The MAT54 energy output was over two times greater than what was expected.

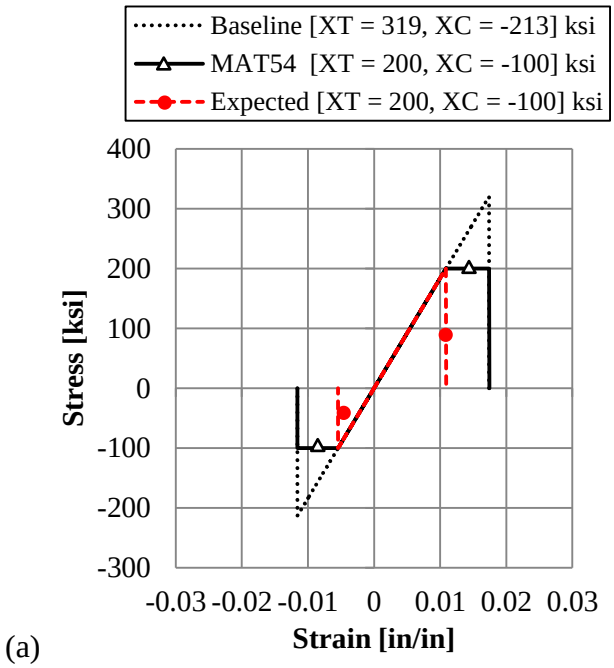

(a)

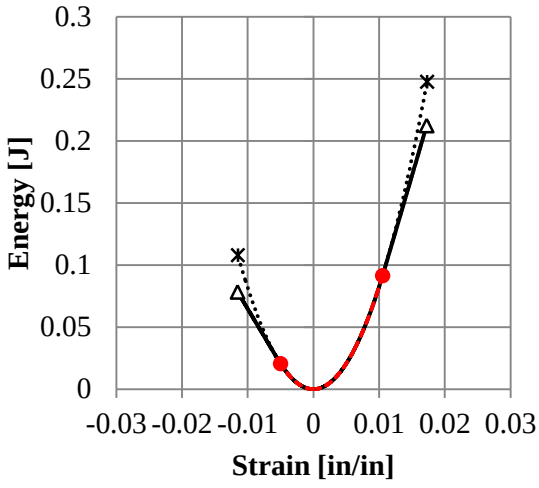

(b)

Figure 43. Expected and MAT54 results when the strength is reduced by 100 ksi: (a) stress-strain and (b) output energy.

The influence of varying strength parameters was similar when changing failure strains, DFAILT and DFAILC. Increasing these values larger than the baseline caused plasticity until the increased failure strain value was reached, shown in Figure 44. Decreasing the failure strains caused early element deletion before the material strength was reached. For simulations with

especially large plastic zones, such as DFAILC = -0.03 in/in, it was necessary to decrease the time step in order simulate the large deformation and avoid minor instabilities.

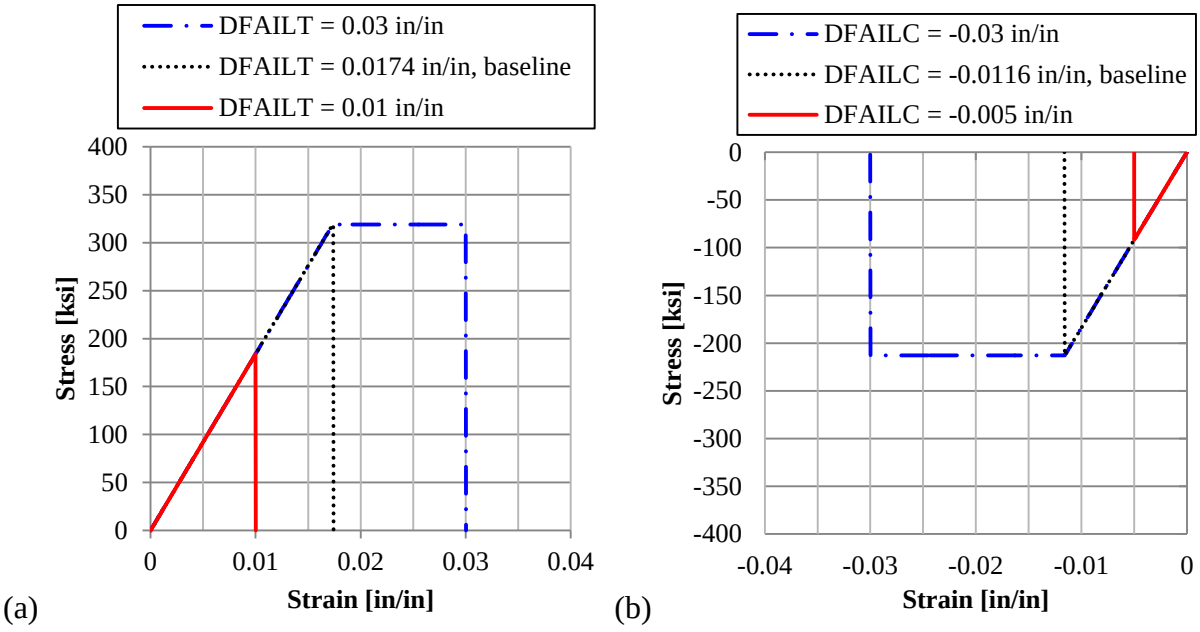

Figure 44. Stress-strain curves resulting from changing the MAT54 parameters for fiber failure strain in (a) tension, DFAILT, and (b) compression, DFAILC.

A simulation with plasticity in both tension and compression was generated by using failure strains of ±0.03 in/in. The resulting laminate stress-strain and energy curves are shown along with the expected linear elastic curves in Figure 45. When the failure strain was increased, the simulated MAT54 energy was three times the total energy expected from linear elastic behavior. While the effect on the shape of the stress-strain curve from changing the failure strains resembled that from changing the material strengths, the plasticity caused by varying failure strains produced a greater error in energy. With decreased strengths, the magnitude of the energy added was relatively lower because the added plasticity occurred at a value below the material strength. Adding plasticity by increasing the failure strain, however, added energy at a greater rate since the added plasticity occurred at the material strength.

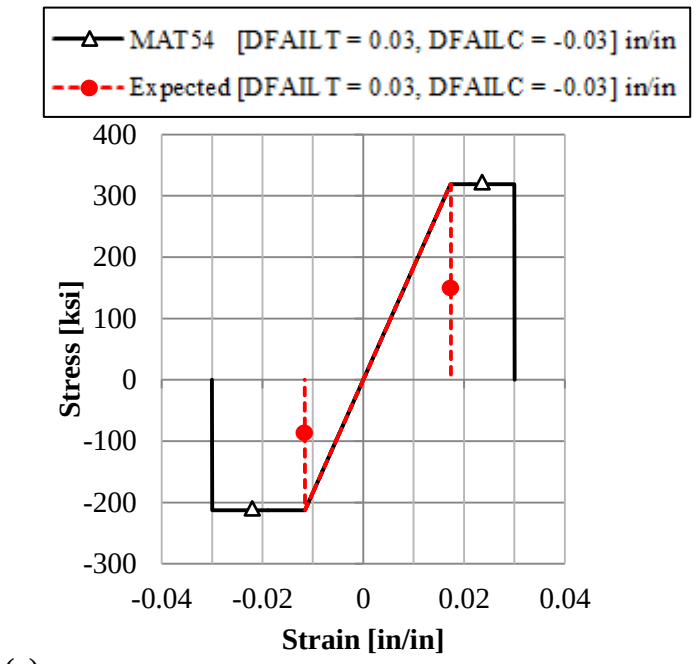

(a)

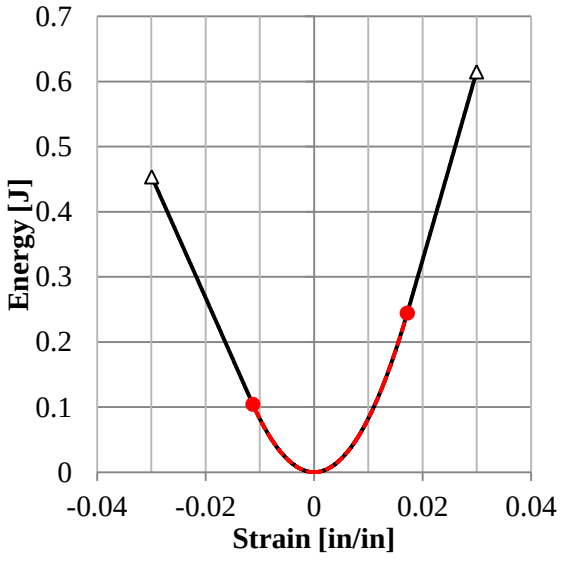

(b)

Figure 45. Expected and MAT54 results when the failure strain is increased to ±0.03 in/in: (a) stress-strain and (b) output energy.

A special case arose when DFAILT was set to zero. Without the fiber tension failure strain to determine element deletion, the fiber tensile strength, XT, determined deletion. When the element failed in the fiber tension mode, MAT54 implemented a special degradation scheme for the ply stresses which reached zero in exactly 100 time steps and the element was deleted. The

stress-strain plot showing the degradation of the element stress when DFAILT = 0 is given in Figure 46. This special case was only applicable to DFAILT and did not work for DFAILC or DFAILM. For instance, using DFAILC ≥ 0 immediately terminated the simulation since the maximum failure strain was violated upon initiation of the simulation. Furthermore, when DFAILT was set to zero but the loading case was not tension in the fiber direction (e.g. fiber compression, matrix tension, matrix compression) the special case shown in Figure 46 did not apply.

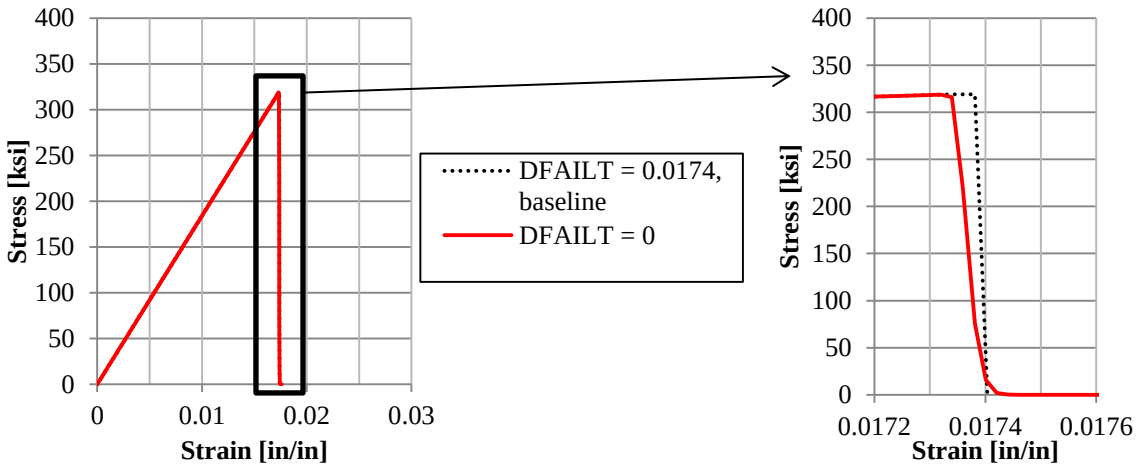

Figure 46. Stress-strain results showing stress degradation when DFAILT = 0 for the tension loading case of the $[0]_{12}$ laminate.

Determining the effect of the EFS parameter required that the critical EFS value for this material system be determined. This was done by using the 1- 2- and 12-strains at failure in Equation 33. The resulting critical EFS value was 0.0178 in/in, which was the effective strain at failure. Using an EFS value less than the critical value caused the element to be deleted at a lower strain as shown in Figure 47. Values higher than the critical value did not change the results. The default value of EFS is zero, which MAT54 considers as numerically infinite. The critical EFS can be determined for any simulation by calculating the EFS at the point of failure. Only EFS values below critical will influence simulation results.

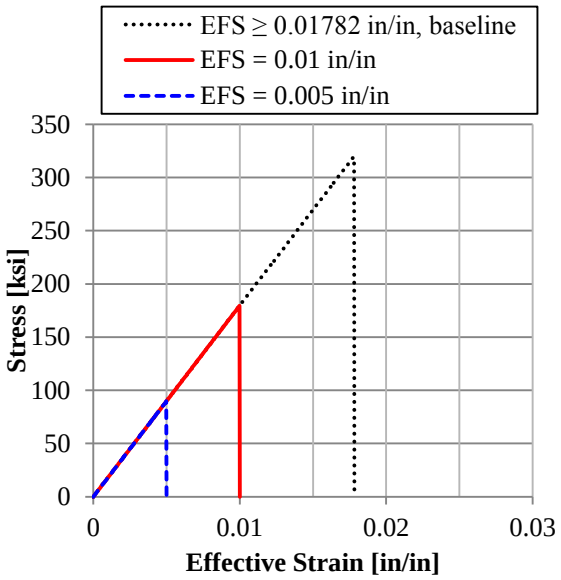

Figure 47. Stress vs. effective strain results from the EFS parameter study.

Finally, altering TFAIL such that it was greater than the element time step caused early element deletion. This effect can only be seen by using TFAIL values slightly larger than the element time step, Figure 48. Implementing values larger than this eliminated the element at the onset of the simulation. The critical value of TFAIL is the element time step, and a value that was two orders of magnitude smaller than this was chosen for the baseline in order to prevent errors.

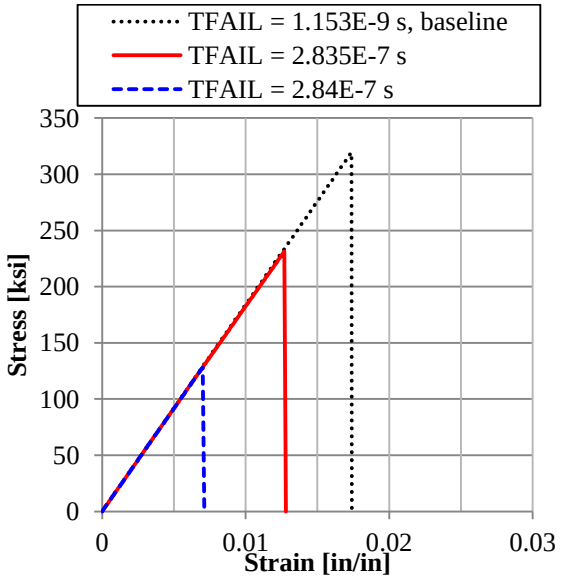

Figure 48. Stress vs. strain results from the TFAIL parameter study.

Results from the $[90]_{12}$ laminate parametric study

The test matrix for the UD $[90]_{12}$ parametric study is given in Table 10. The test matrix was reduced by excluding parameters which exclusively influence the fiber direction, such as EA, DFAILT, DFAILC, XT, and XC, none of which were observed to affect the $[90]_{12}$ simulations in the loading direction.

Table 10. Parametric test matrix for the MAT54 $[90]_{12}$ lay-up, baseline and parametric values.

Variable	Baseline value	Parametric values					
EB	1.22E+6	0	6.1E+5	1.83E+7			
YT	7090	0	3545	25000	29280	40000	
YC	28800	0	14400	21600	40000		
DFAILM	0.024	0	0.00291	0.00581	0.012	0.02361	0.035

Changing the matrix modulus, EB, had the same effect on the $[90]_{12}$ laminate as changing the fiber modulus in the $[0]_{12}$ laminate. Raising EB caused a stiffer stress response and lowering it caused a softer response, both in tension and compression, Figure 49.

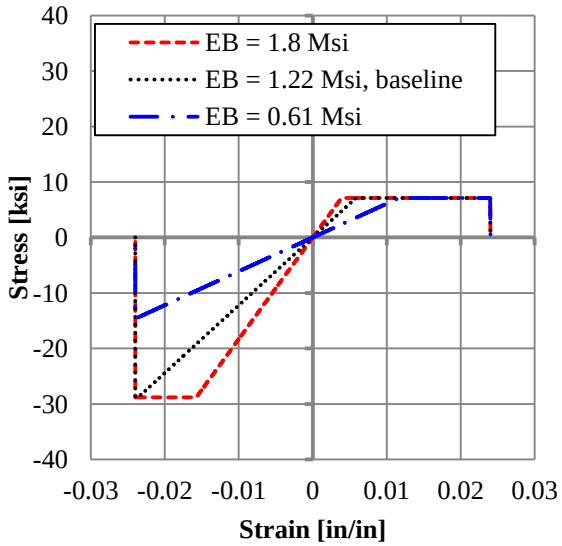

Figure 49. Stress-strain result from changing the matrix modulus parameter, EB.

The matrix strengths, YT for tension and YC for compression, determined the peak stress limits of the $[90]_{12}$ single element, and the effect of these strengths was similar to the effect of the fiber strengths in the previous section. Strength values greater than or equal to 28.8 ksi (199 MPa) for both YT and YC caused perfectly linear elastic stress-strain behavior. This strength threshold was determined from using the compressive strength value, YC, in Equation 15. As shown in Figure 50, strength values less than 28.8 ksi (199 MPa) caused failure followed by a region of constant stress until the failure strain was reached and the element deleted. A zero value for either strength parameter was considered by MAT54 to be numerically infinite.

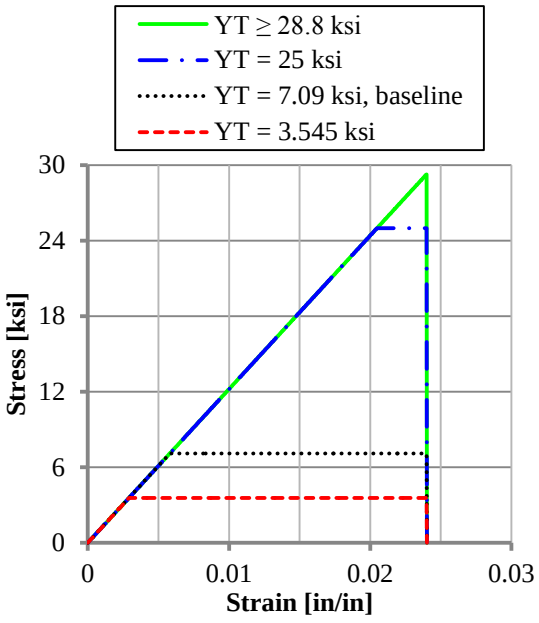

(a)

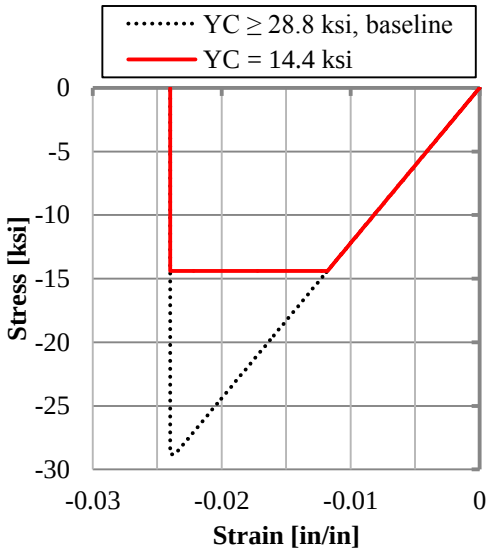

(b)

Figure 50. Stress-strain curves resulting from changing the MAT54 parameters for matrix strength in (a) tension, YT, and (b) compression, YC.

Changes in DFAILM had a very strong influence on the matrix single element model as the fiber failure strains had in the previous section. Lower values underestimated the compressive matrix strength, shown in Figure 51, while increasing DFAILM such that it was larger than the baseline caused an elongation of the plasticity region in tension, and the introduction of one in compression. Choosing a zero value for DFAILM caused MAT54 to consider it to be numerically infinite and the element loaded purely in the transverse direction was eventually only deleted by the violation of the minimum time step, TFAIL. By using the default TFAIL value, element deletion occurred at unfeasibly high strain values, 1 in/in in tension and -4 in/in in compression.

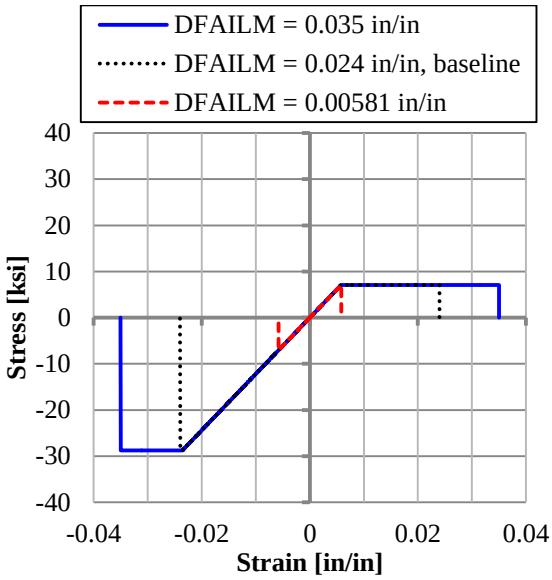

Figure 51. Stress-strain curve resulting from changing the matrix failure strain parameter, DFAILM.

The strong influence of DFAILM in MAT54 consequently makes the choice of defining DFAILM based on either the tensile or compressive load case influential on the material model. The stress-strain plot in Figure 52a illustrates the difference between defining DFAILM based on the tensile load case (DFAILM = 0.00581 in/in) and the compressive load case (DFAILM = 0.024 in/in), against the expected result in which the stress-strain curve is linearly elastic in both tension and compression. The energy outputs from these three cases are plotted in Figure 52b. The great loss of energy from using the tensile DFAILM, and gain of energy from using the compressive DFAILM is evidenced in the curves, and the corresponding energy values in Table 11. Unfortunately, the DFAILM parameter cannot be tailored to give ideal results like DFAILT and DFAILC, and will always cause some error. This must be taken into account when using MAT54 to model a composite material system.

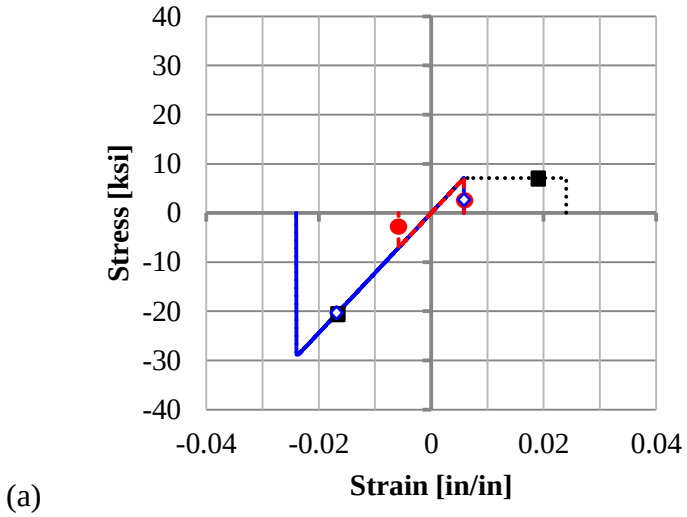

(a)

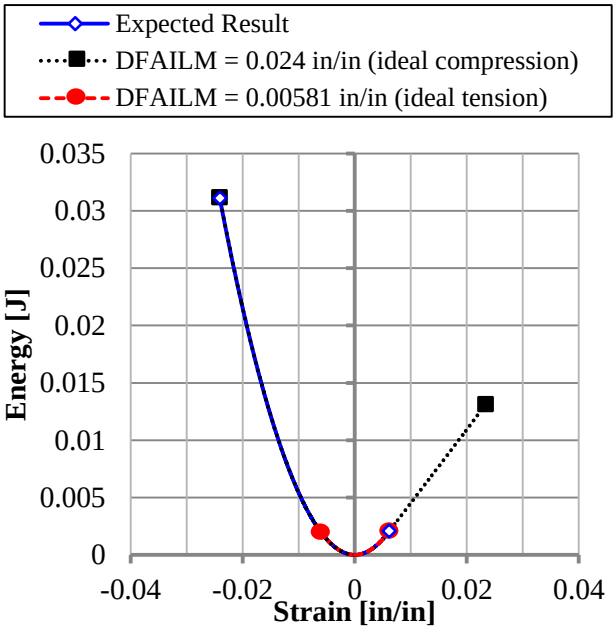

(b)

Figure 52. Expected and simulated (a) stress-strain and (b) output energy curves from using the two possible baseline DFAILM values.

Table 11. Energy output values from ideal DFAILM simulations in Figure 52.

	DFAILM	Compression	Tension	Total	Error
Linear Elastic	-	0.0308 J	0.0018 J	0.0327 J	-

Ideal tension	0.0058 in/in	**0.0018 J**	0.0018 J	0.0037 J	-89%
Ideal compression	0.0240 in/in	0.0308 J	**0.0135 J**	0.0443 J	+36%

Fabric $[(0/90)]_f$ & cross-ply [0/90] laminates

Expected results for the baseline simulations

The expected elastic response of the $[(0/90)]_{8f}$ fabric laminate is generated from the experimentally measured nominal material properties given in Table 2. The Hashin failure criteria are used to determine the expected failure as it would occur in MAT54, Figure 53. Generated the expected response of the $[0/90]_{3s}$ cross-ply laminate required considering individual ply stresses and progressive ply failure. It was expected that the 90-degree plies would fail before the 0-degree plies. CLT was used with the MAT54 failure criteria (Appendix C, Equations 25-28), and the resulting stress-strain response is also shown in Figure 53. The expected stress-strain response of the fabric and the cross-ply laminates are very similar in strength and stiffness.

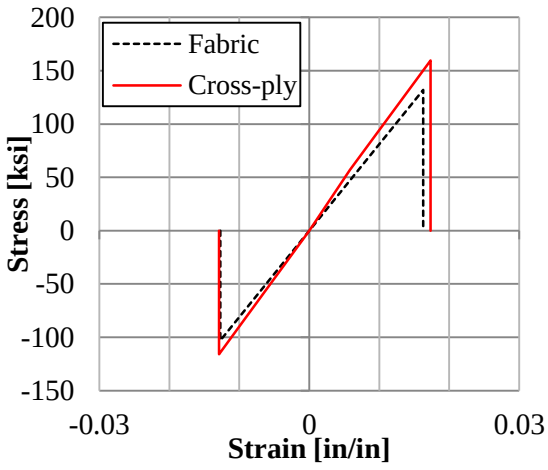

Figure 53. Expected results of the fabric and cross-ply laminates as determined using the published material property data.

Baseline simulation results

The baseline fabric single element produced ply stresses and strains which were equal in each ply because of its uniform $[0]_8$ lay-up. The laminate stress-strain curve and output energy are shown in Figure 54, both of which correlated very well with the expected linear elastic stress results as determined by the fabric material properties. Peak stress, strain, and energy values for the baseline simulation are given in Table 12, where the expected energy output was determined by calculating the area under the expected linear force-displacement curve. The fabric baseline was also simulated using a $[90]_8$ lay-up to test the transverse properties of the material system. A comparison of the longitudinal (0-degree) and transverse (90-degree) stress-strain curves generated by MAT54, Figure 55, demonstrates the similarity of the two fabric directions.

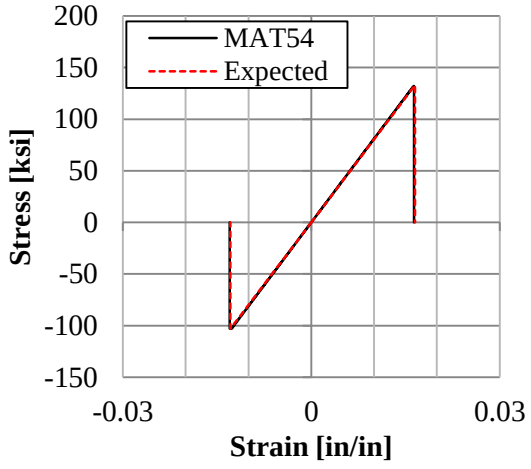

(a)

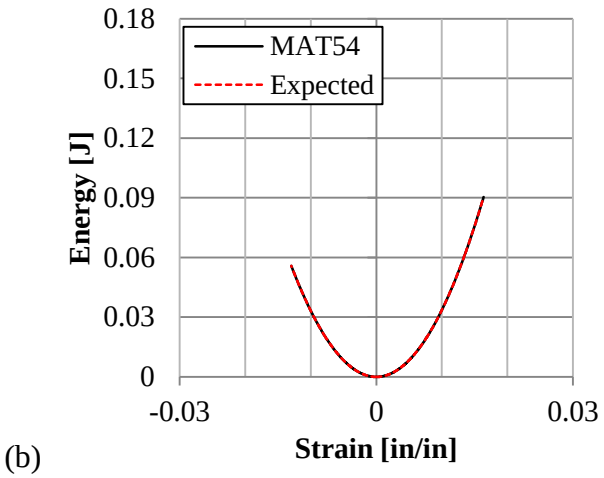

(b)

Figure 54. Laminate (a) stress-strain and (b) output energy curves for the baseline fabric single element simulation.

Table 12. Expected and simulated peak stress, strain, and energy values for the baseline $[(0/90)]_{8f}$ fabric single element with error values.

	Expected	MAT54	Error
$\mathbf{F_1^{tu}}$	132 ksi	131.98 ksi	0.0%
$\mathbf{F_1^{cu}}$	-103 ksi	-103.00 ksi	0.0%
$\boldsymbol{\varepsilon_1^{tu}}$	0.0164 in/in	0.01638 in/in	-0.2%
$\boldsymbol{\varepsilon_1^{cu}}$	-0.0130 in/in	-0.01300 in/in	-0.1%
Energy^{tu}	0.09661 J	0.09046 J	-6.4%
Energy^{cu}	0.05976 J	0.05583 J	-6.6%

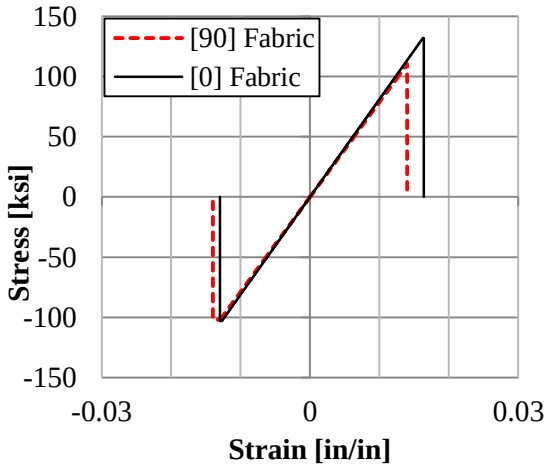

Figure 55. Baseline fabric single element simulated using MAT54 in the [0] and [90] directions.

In the elastic region of the stress-strain curve of the baseline cross-ply simulation, Figure 56, the simulated curve was identical to that which was expected. After failure, however, the simulation continued at a low stress level to plastically strain until the failure strain parameter, DFAILM, was reached. The shape of the simulated curve in Figure 56 does not have a meaningful physical interpretation, as the plastic straining was a consequence of the way MAT54 determines element failure from strain parameters. While MAT54 successfully predicted first ply failure (there was a change of slope when the 90-degree plies failed), ultimate laminate failure was incorrect. To understand how MAT54 generated the cross-ply laminate curve, the 0- and 90-degree ply stresses are shown separately in Figure 57. The greater magnitude of the 0-degree ply stresses shows that these plies carried the majority of the stress in the laminate. For a balanced cross-ply laminate, the laminate stress can be determined by averaging the 0- and 90-degree ply stresses. The ply stresses of the 0- and 90-degree plies are superimposed with the laminate stress, shown in Figure 58 in terms of MAT54 user input parameters. From this plot, the influence of each parameter on the cross-ply element can be anticipated, for instance, changes in XT can be expected to affect the first stress peak in tension of the laminate. This schematic will be useful during the parametric studies of the cross-ply element.

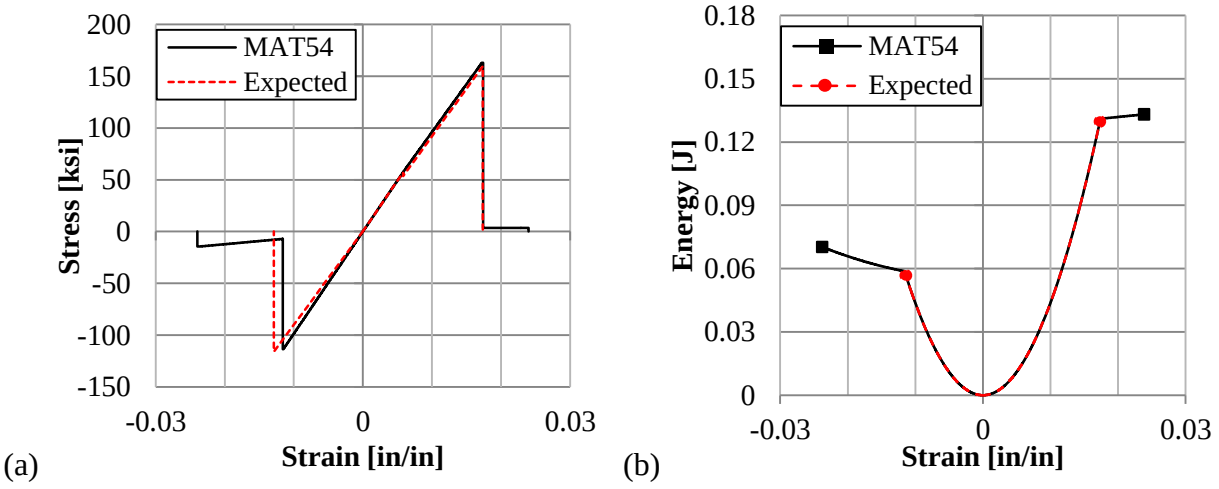

Figure 56. Simulated baseline cross-ply (a) stress-strain and (b) output energy compared against expected results.

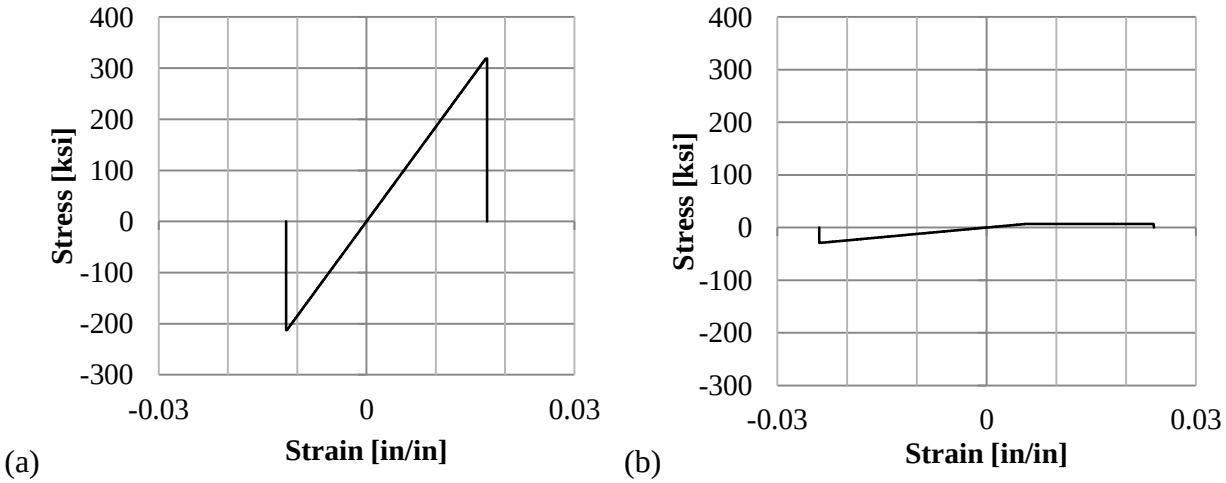

Figure 57. Ply stresses of the (a) 0-degree and (b) 90-degree plies in the cross-ply laminate.

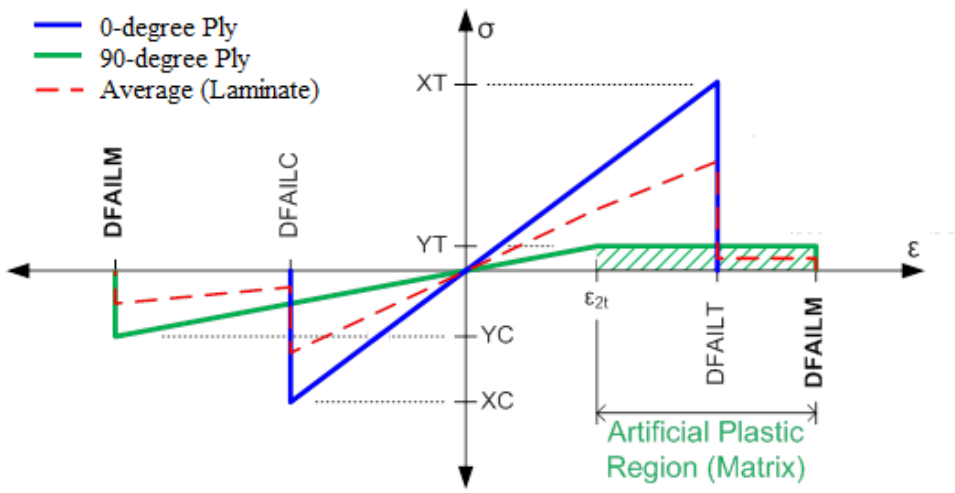

Figure 58. The 0-degree ply, 90-degree ply, and laminate (average) stress-strain curves of the cross-ply single element shown in terms of MAT54 input parameters.

Considering the cross-ply laminate stress, the element was not deleted after the 0-degree plies failed. Instead, element deletion only occurred once the 90-degree plies were deleted due to DFAILM. This result once again suggests the importance of the DFAILM parameter in MAT54. The additional stress in the element after failure contributes 7.4% additional energy to the simulation that was not expected to be there. Peak stress, strain, and energy values for the baseline simulation are given in Table 13, along with the error of these values against the expected results. The failure strains had the highest error of these parameters due to the plastic straining caused by DFAILM in the simulation.

Table 13. Expected and simulated peak stress, strain, and energy values for the baseline $(0/90)_{3s}$ cross-ply single element with error values

	Expected	**MAT54**	**Error**
$\mathbf{F_1^{tu}}$	163.0 ksi	160.0 ksi	-1.8%
$\mathbf{F_1^{cu}}$	-120.9 ksi	-113.5 ksi	-6.1%
$\boldsymbol{\varepsilon_1^{tu}}$	0.0174 in/in	0.024 in/in	38%
$\boldsymbol{\varepsilon_1^{cu}}$	-0.0129 in/in	-0.024 in/in	86%
Energy^{tu}	0.13106 J	0.13318 J	1.6%
Energy^{cu}	0.05855 J	0.07053 J	21%

Recall that the experimental stress-strain results from these two laminates were comparable. A comparison of the simulations results from these two laminates also showed similarity, Figure 59, except the error of the failure strains in the UD cross-ply laminate. When choosing between using a [0] lay-up given fabric lamina properties versus a [0/90] dispersed lay-up with UD lamina properties, the modeler should be aware of these differences.

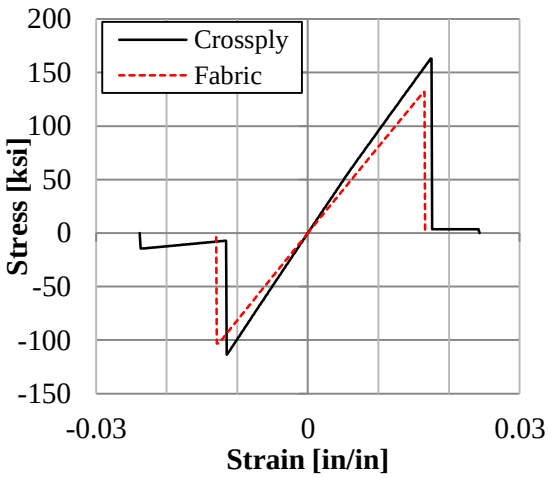

Figure 59. Stress-strain curves from the baseline single element simulations of the MAT54 models for the fabric and cross-ply laminates.

Results from the parametric study

$[(0/90)]_8$ fabric laminate

The test matrix for the study of the influence of MAT54 parameters upon the fabric single element laminate is given in Table 14. The parameters which exclusively influenced the transverse direction, such as EB, DFAILM, YC and YT, were found to have no influence on the fabric simulations in the axial direction. Given the uniform lay-up of the fabric element, it was expected that the trends from the parametric study would be the same as those in the UD single element. Simulations of the fabric single element confirmed this expectation.

Table 14. Parametric test matrix for the MAT54 model of the fabric material, baseline and parametric values.

Variable	Baseline value	Parametric values		
XT	132000	0	75000	320000
XC	103000	0	50000	200000
DFAILT	0.0164	0	0.01	0.03
DFAILC	-0.0130	0	-0.005	-0.024
DFAILM	0.0140	0.005	0.0129	0.024

Changing the fiber modulus, EA, directly affected the stiffness of the stress-strain curve, both in tension and compression, Figure 60. Higher EA values caused the element to achieve the strength before the failure strain, and plastic straining followed. Changing the fiber strengths, XT and XC, changed the peak stress limits, Figure 61a. Larger values did not change results since achieving the failure strain deleted the element before it could reach a higher stress. Considering smaller strength values, one would expect that the element would fail at a lower strength. In the simulation, however, using smaller strength values caused plasticity upon reaching the material strength. This produced energy which was more than 1.5 times higher than what was expected for the low strength simulation, Figure 61b. Although these nonlinear behaviors are not physically correct for this fiber-dominated laminate, the fabric single element simulation showed the same trends as the UD single element.

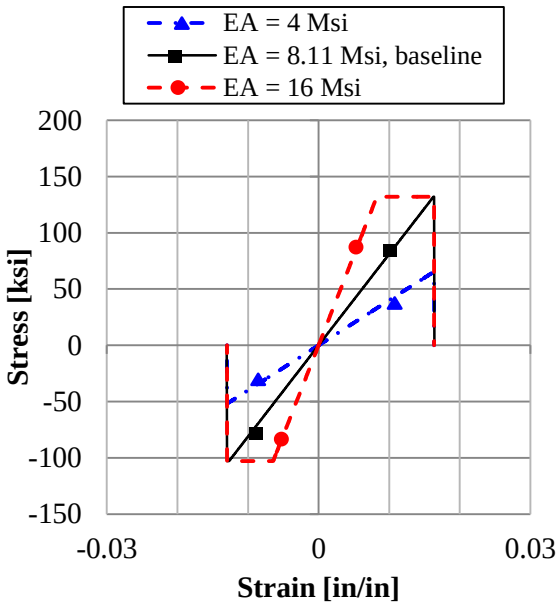

Figure 60. Effect of changing the fiber modulus, EA, on the fabric single element.

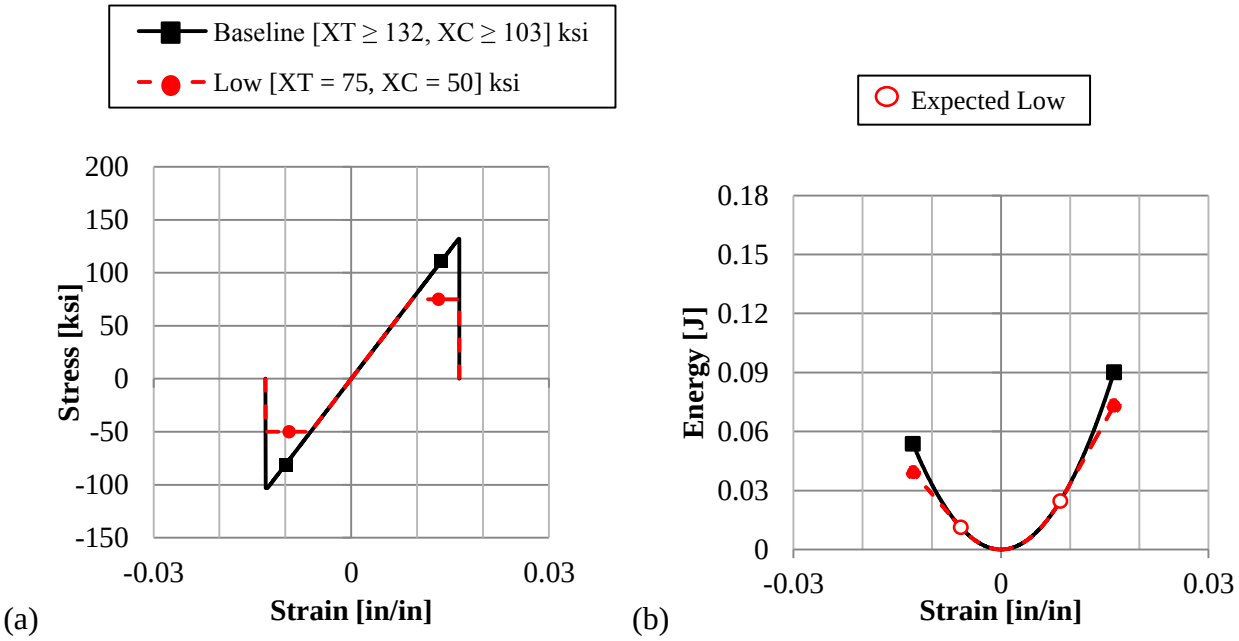

Figure 61. Parametric (a) stress-strain and (b) output energy results from varying axial material strengths, XT and XC, on the fabric single element.

Varying the axial failure strain parameters, DFAILT and DFAILC, also produced the same trends demonstrated by the UD single element. Failure strains larger than the baseline caused plasticity until the new failure strain was reached while decreasing failure strains below the baseline value caused deletion of the element before the material strength was reached, Figure 62a. These failure strain parameters greatly influenced the energy output by the element, producing values that were 96% above and 91% below the baseline value, Figure 62b.

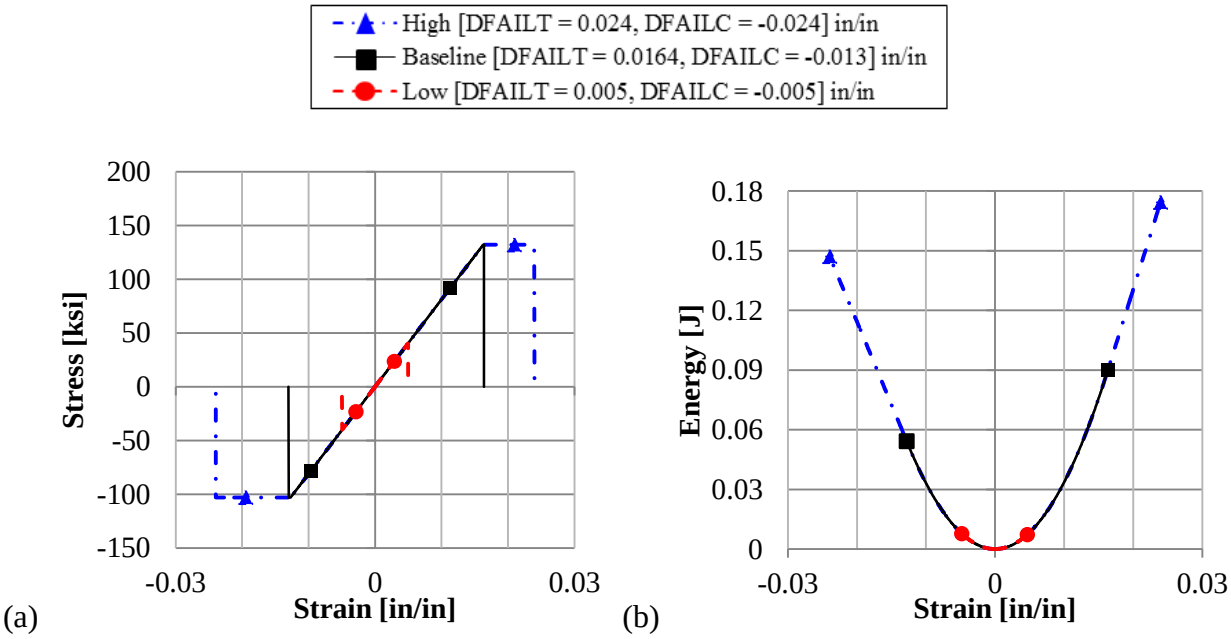

Figure 62. Parametric (a) stress-strain and (b) output energy results from varying axial strains-to-failure, DFAILT and DFAILC, on the fabric single element.

Simulations of the fabric element in the transverse direction yielded the same parametric trends as observed for the [90] UD single element, where transverse parameters such as EB, YT, YC, and DFAILM had a great influence on the stress-strain and energy results.

$[0/90]_{3s}$ cross-ply laminate

The test matrix for the study of the influence of MAT54 parameters upon the UD cross-ply single element laminate is given in Table 15. For the cross-ply study it was important to consider ply stresses as well as laminate stresses to monitor progressive ply failure.

Table 15. Parametric test matrix for the MAT54 UD cross-ply lay-up, baseline and parametric values.

Variable	Baseline value	Parametric values				
XT	319000	2000	5000	7000	160000	479000
XC	213000	1000	106500	234300		
YT	7090	1000	3000	28800	29300	
YC	28800	1000	14400	31680	57600	
DFAILT	0.0174	0.0087	0.024	0.025		
DFAILC	-0.0116	-0.0058	-0.0087	-0.01276	-0.0174	-0.024
DFAILM	0.0240	0.0058	0.0087	0.0174	0.0264	

The fiber modulus, EA, defines the material stiffness along the 0-direction. As the majority of the stress in this cross-ply laminate was carried in the 0-degree plies, changing the modulus in this direction greatly altered the stiffness of the whole element until the 0-degree plies failed, Figure 63a. After 0-degree ply failure, the simulation with varying EA values does not change from the baseline. The 0- and 90-degree ply stresses, Figure 63b-c, show that EA greatly affected the 0-degree plies but had no effect on the 90-degree plies. On the other hand, changing the matrix modulus, EB, altered the stiffness of the 90-degree plies, but not the 0-degree plies, Figure 64. Since the 90-degree plies had only a small influence over the element stress response, varying EB only slightly changed the laminate stress-strain curve.

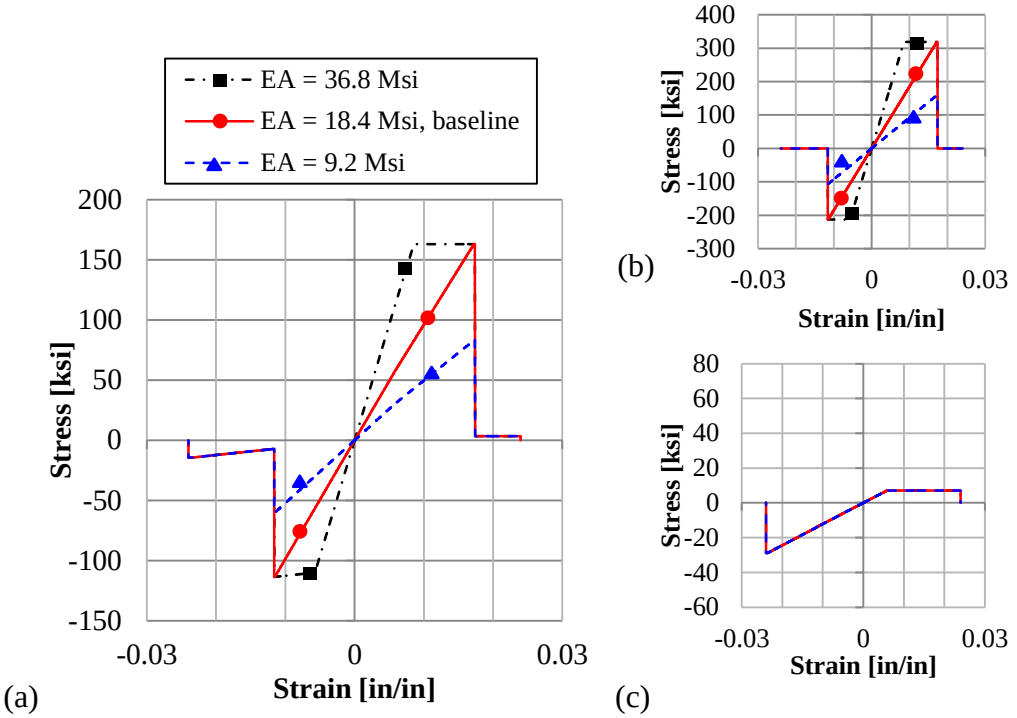

Figure 63. Stress-strain results from changing EA on the (a) whole element, (b) 0-degree plies, and (c) 90-degree plies

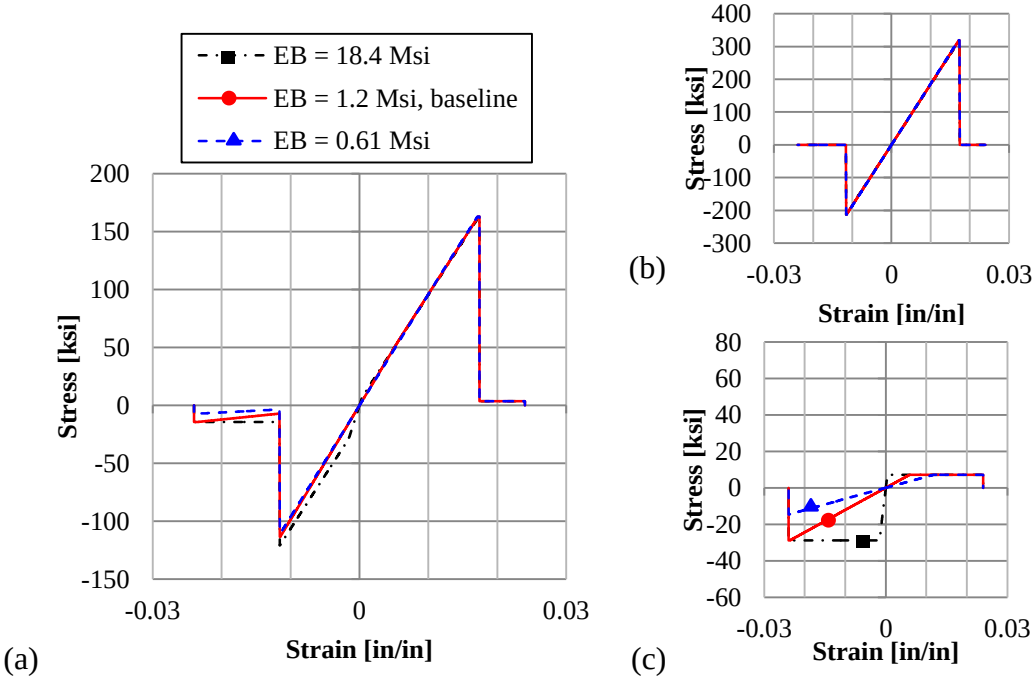

Figure 64. Effect of changing EB on the cross-ply single element (a) laminate, (b) 0-degree plies, and (c) 90-degree plies.

Changing the fiber strength parameters only affected the stress in the loading direction of the 0-degree plies. Changing XT altered the peak stress limit of the 0-degree plies in tension, while changing XC altered the peak stress limit of these plies in compression. Varying XT and XC greatly altered the total laminate response, Figure 65, where larger strength values did not change results, but smaller values caused plasticity. The energy losses associated with reduced strength values, Figure 66, were not as severe as would be physically expected since the plasticity provided additional energy that would have otherwise been lost.

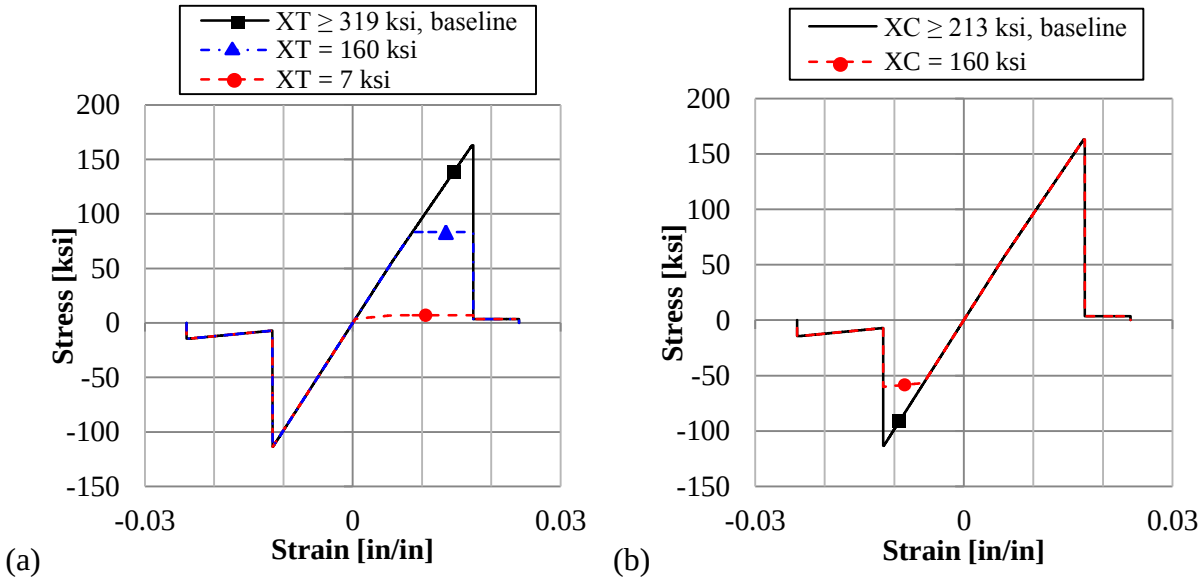

Figure 65. Effect of (a) XT and (b) XC on the stress-strain curve of the cross-ply single element laminate.

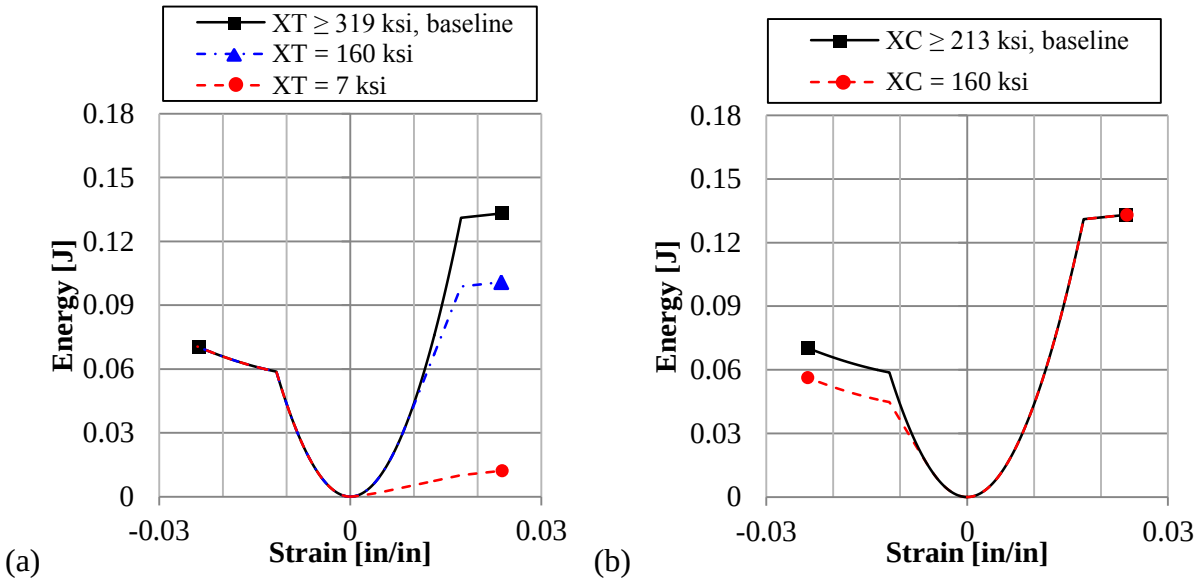

Figure 66. Effect of (a) XT and (b) XC on the laminate output energy of the cross-ply single element.

The matrix strength parameters, YT and YC, have a similar effect on the 90-degree plies that the XT and XC parameters had on the 0-degree plies. The effect upon the laminate stress response is inconsequential, however, since the 90-degree plies carry little the stress in the laminate. Changing YT had only a very slight effect on the laminate stress in tension, Figure 67a. The only noticeable change regards the stress in the 90-degree plies, shown in Figure 67b. Here, higher values of YT increased the stress value at which plasticity occurs, and lower values decreased this stress limit. The overall energy increase in the laminate was only 7% in the case where YT was increased over four times above the baseline value. In compression, changing YC only had noticeable effects on the 90-degree plies as well, while the laminate stress was only very slightly affected, Figure 68. Halving YC only resulted in an energy decrease in the laminate of 6% below the baseline. For this material system, transverse strength values are not critical MAT54 parameters in a laminate which has fiber-dominance in the two principle directions.

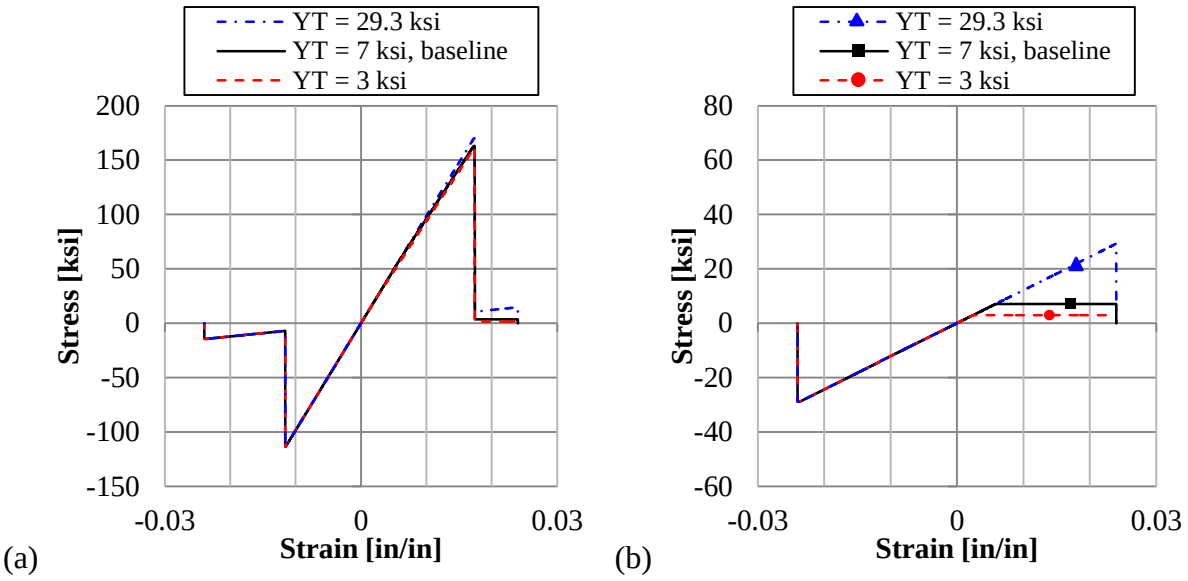

Figure 67. Effect of YT on the cross-ply single element (a) laminate stress and (b) 90-degree ply stresses.

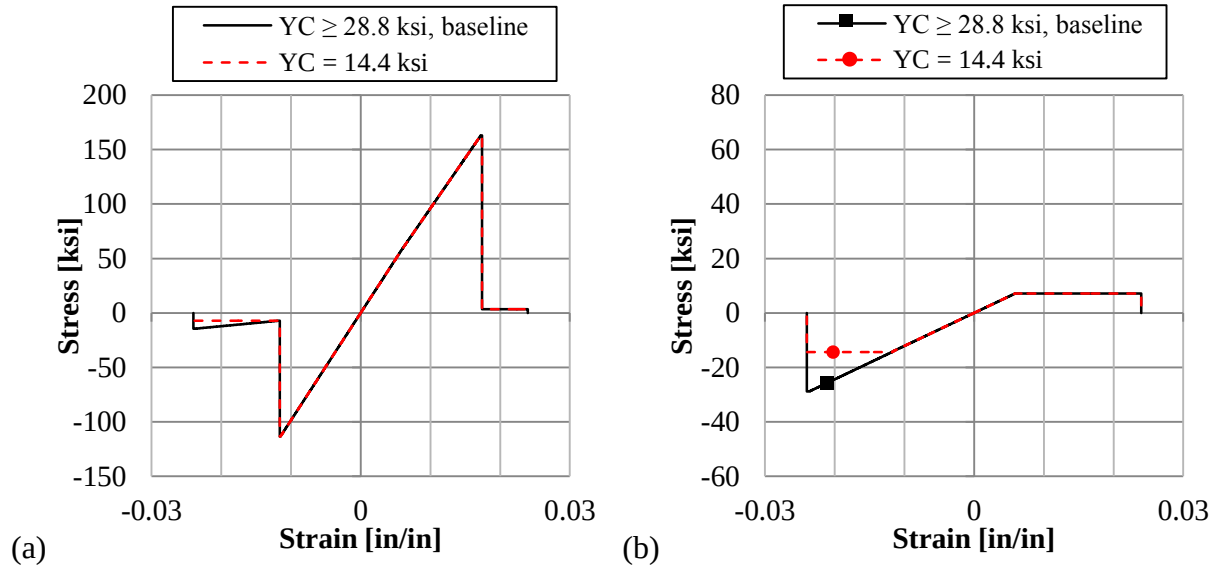

Figure 68. Effect of YC on the cross-ply single element (a) laminate stress and (b) 90-degree ply stresses.

Changes in the fiber failure strains, DFAILT in tension and DFAILC in compression, significantly changed the cross-ply laminate stress results, Figure 69, since these parameters controlled the deletion of the 0-degree plies. Smaller values reduced the peak stress magnitude

since the 0-degree plies would be deleted prior to reaching the material strength. Larger values created plasticity at the peak stress value until 0-degree ply deletion. These variations greatly impacted the energy of the simulations, as shown in Figure 70. In the case of the DFAILT value 44% greater than the baseline (DFAILT = 0.025 in/in), the energy increases 83% above the baseline value.

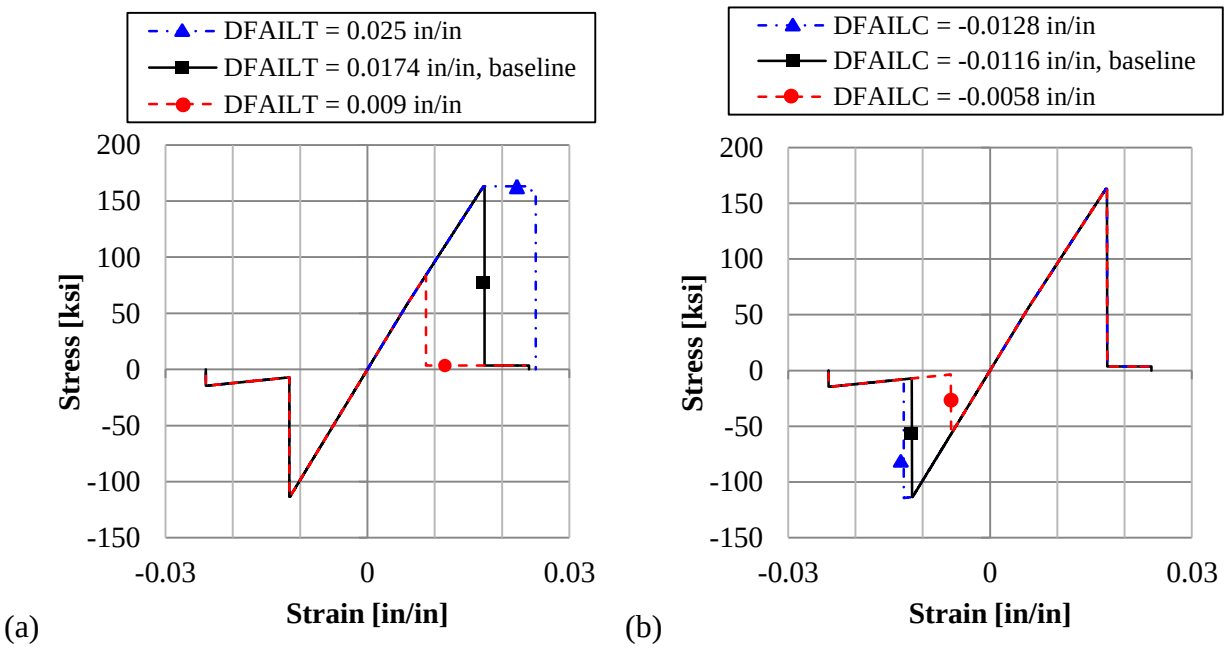

Figure 69. Effect of (a) DFAILT and (b) DFAILC on the stress-strain curve of the cross-ply single element laminate.

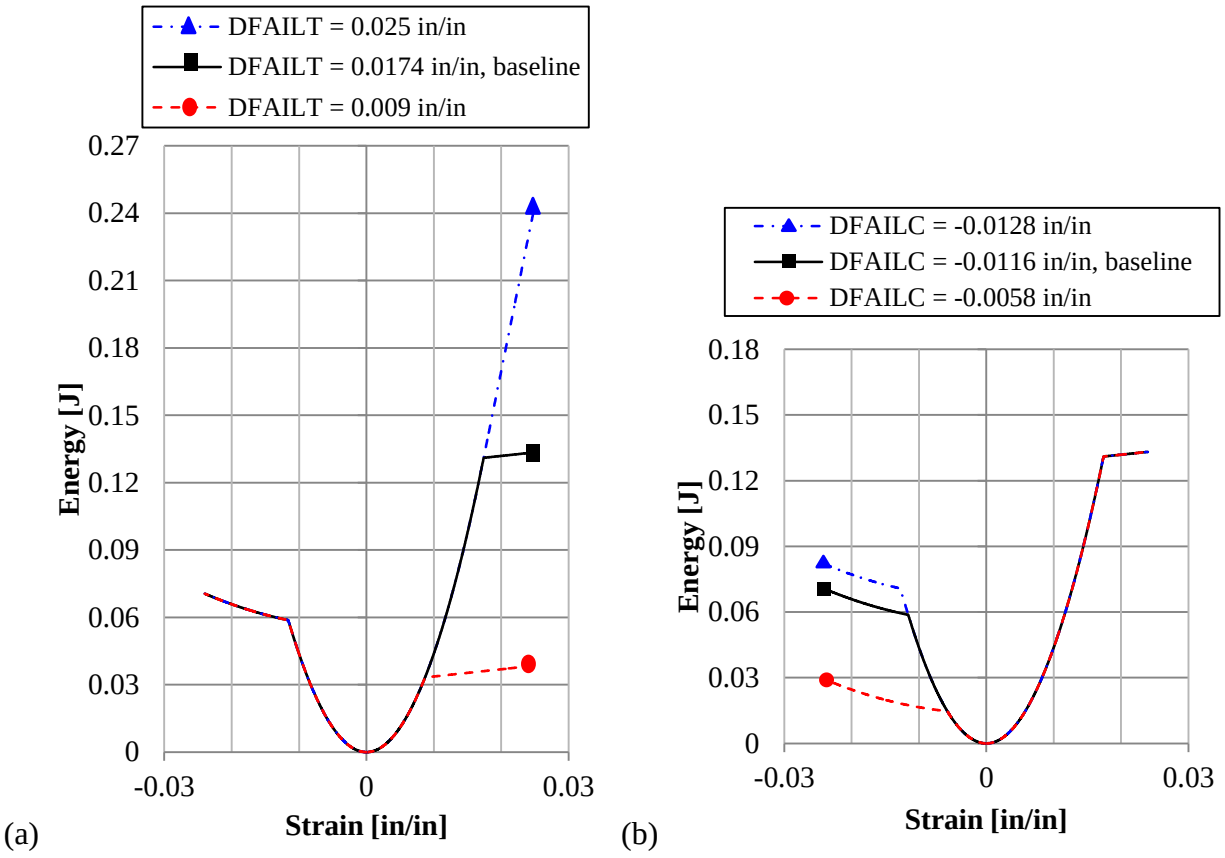

Figure 70. Effect of (a) DFAILT and (b) DFAILC on the energy output of the cross-ply single element laminate

The deletion of the 90-degree plies depended on the matrix failure strain DFAILM. Since the element was only deleted once all of the plies had been deleted, DFAILM also directly affected the deletion of the element. Lowering DFAILM lowered the strain to failure of the element and shortened the plasticity region in tension, Figure 71a, while raising DFAILM had the opposite effect. Since the 90-degree plies had so little influence on the overall laminate response, changes in DFAILM were relatively inconsequential to the element stress-strain response. This is important since DFAILM can only be linearly elastic in one loading case, depending on the determination of DFAILM by Equation 15. This limits the MAT54 user to defining the 90-

degree failure strain perfectly in either tension or compression, never both. While the effect upon the stress-strain of changing DFAILM was small, the resulting difference in energy was slightly more significant. Considering the two perfectly linear elastic values, DFAILM = 0.024 in/in in compression and DFAILM = 0.0058 in/in in tension, Figure 71b shows the -5.3% in tension and -21% in compression energy loss associated with using the smaller DFAILM value.

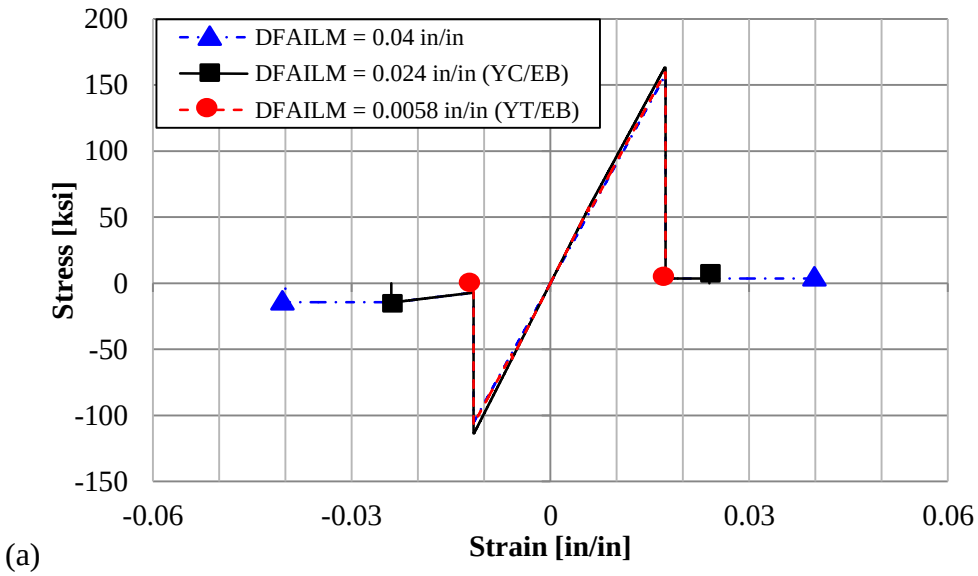

(a)

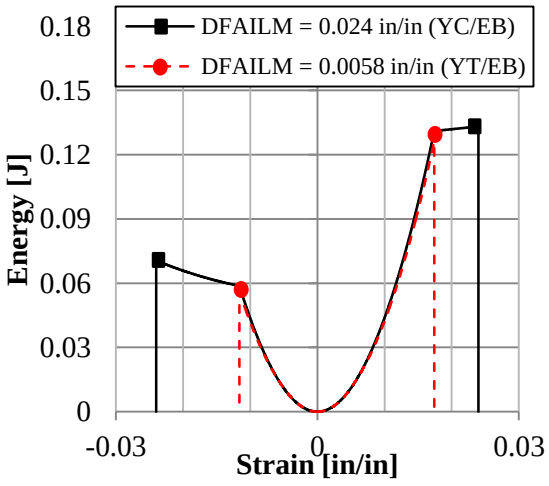

(b)

Figure 71. Effect of changing DFAILM in the cross-ply single element on the (a) laminate stress and (b) energy output.

Conclusions

The LS-DYNA MAT54 material model has been shown to be capable of modeling basic single element behaviors for a plain-weave fabric material system and a unidirectional tape material system with a dispersed, cross-ply lay-up. Experimentally these two laminates were shown to be similar as they were made from the same carbon fiber and epoxy constituents. The baseline simulations for these laminates were also similar, except for a significant error in the strain-to-failure values of the cross-ply laminate which were grossly overestimated. This error primarily affected the deletion of the element, and the stress-carrying 0-degree plies failed as expected resulting in only a moderate error in energy. Due to this error, however, the shape of the stress-strain curve for the cross-ply laminate was not physically accurate.

The concern of using the Hashin failure criteria, meant for matrix materials, to determine the compressive failure of the fiber-dominated fabric in the transverse directions was addressed. Opting to use the Maximum Stress failure criterion in place Hashin had minimal effects on the failure stress, however, the shear-free single element model is likely to have over-simplified the problem. The loading conditions upon the simulated single element were free of shear stresses, which have a large role in the Hashin failure criteria. It is expected that, given more complex loading, the differences between using Hashin and Maximum Stress for the fabric material system could be significant.

Just as the UD single element, the sensitivity of the fabric laminate towards the MAT54 parameters was dependent on the direction of the applied load. Axial loads were only sensitive to 'fiber' properties EA, XT, XC, DFAILT, and DFAILC, and transverse loads were only sensitive to 'matrix' properties EB, YT, YC, and DFAILM. This meant that critical properties, such as strains-to-failure, were critical in one direction, and entirely insignificant in the

perpendicular direction. One way to remedy this condition would be to give the fabric material system a dispersed lay-up. This would reduce the influence of any one parameter, such as DFAILM, and allow for more flexibility in their definition.

The UD cross-ply element was mostly sensitive to fiber properties, and not matrix properties. For this laminate, loading direction is completely inconsequential since the number of 0- and 90-degree plies in the lay-up was exactly the same axially and transversely, and the stress response was the same regardless of the loading direction. This lay-up was also strongly influenced by the fiber failure strain parameters, but a significantly less so for the matrix failure strain, DFAILM, given that the 90-degree plies were minor contributors to the laminate. The influence of DFAILM was very different from that of the fabric element, for which all of the failure strains were strongly influential depending on the loading direction. If artificial plasticity is desired in a MAT54 element for greater stability, it can be implemented relatively inconsequentially by raising DFAILM in the cross-ply element. This would require a higher strain to delete the element without adding significant stress, and may provide additional stability. This method cannot be applied to the fabric simulation unless its plies were also dispersed.

Simulation of unidirectional tape sinusoid crush specimen

The quasi-static crushing of a composite specimen, consisting of a semi-circular sinusoid and manufactured with carbon fiber/ epoxy unidirectional prepreg tape, is modeled using the progressive failure material model MAT54. Details of the composite specimen design, manufacturing, and testing procedure have been reviewed in the experimental portion of this research. The unidirectional tape material system was not central to the experimental portion of this research effort, but the analysis requires experimental results against which simulation results must be compared. For this reason, a single experimental crush curve was chosen which is representative of the average results obtained from several UD sinusoid crush elements which were tested as part of a separate research effort, published by Feraboli in [85]. The representative experimental load-displacement curve for which all simulation results in this section will be compared against is given in Figure 72. The primary focus of the remainder of this discussion is centered on the analysis approach and the sensitivity of the model to parametric variations. The results from this investigation were published in 2011 by the author and her advisor in [93], as well as in 2013 within an FAA Technical Report by the author and her advisor, [94]. Some of the images from the 2011 publication were also presented in [88], and a disclaimer which outlines the work performed on this topic is given in Appendix H.

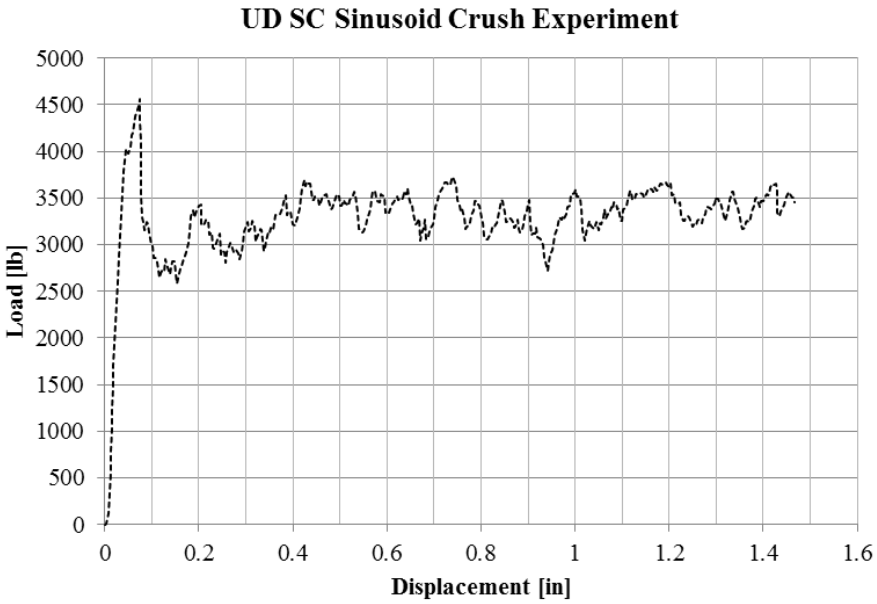

Figure 72. Representative experimental load-displacement curve from the crush testing of a unidirectional tape semi-circular sinusoid crush element.

The LS-DYNA model is represented in Figure 73 and shows the loading plate, the composite specimen and the trigger row of elements. The geometry is imported into LS-DYNA and meshed using a fully integrated linear shell element (formulation 16) of 0.1 in. x 0.1 in. (2.54 mm x 2.54 mm) square element size. Since the laminate thickness is 0.079 in. (2.0 mm), the aspect ratio of the element is 0.079/ 0.1 = 0.79. For the 12-ply corrugated specimen, there are 12 integration points (NIP=12 in the LS-DYNA shell element definition). Each ply is defined by 1 integration point through the thickness, with the prescribed orientation. The specimen is modeled with a total of 840 elements, having constant thickness of 0.079 in. (2.0 mm).

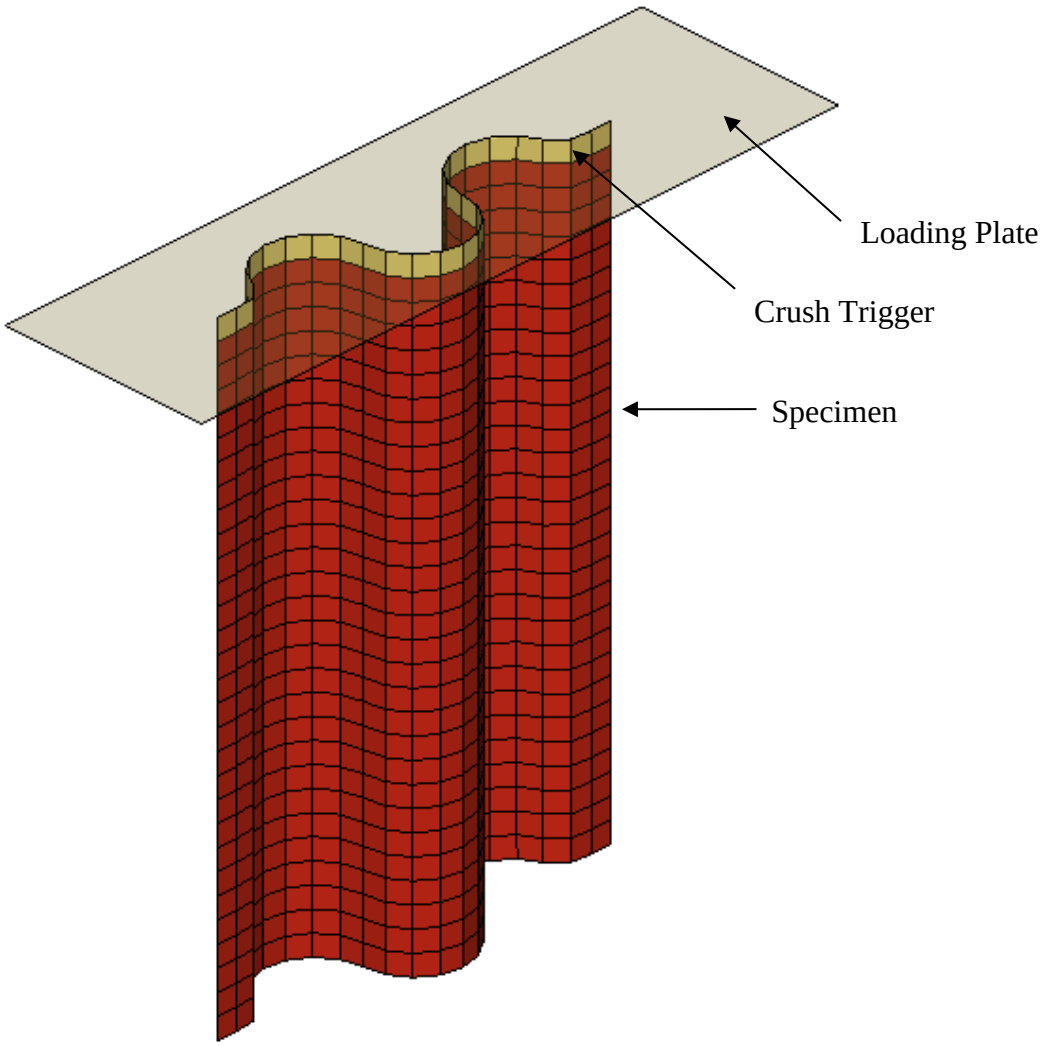

Figure 73. LS-DYNA model of the corrugated composite specimen, crush trigger, and loading plate.

The material properties of the UD material system as measured from experiment, Table 2, are used as input parameters for the MAT54 material deck. It should be noted that for English units, the material density input RO must be converted from pound-weight to pound-mass by dividing by a gravity factor of 386.4 in/s^2. The value of 1.5E-4 lbf/in^3 (1.52 g/cm^3) is input into MAT54 as 0.05/386.4 = 1.5E-4 lbm/in^3. The input deck for the baseline MAT54 UD material model is given in Table 16. The meaning of all parameters, including the inactive ones that are indicated with a strikethrough, is given in Appendix C, Table 24.

Table 16. MAT54 baseline model input deck for the unidirectional material model. (strikethrough parameters are not used).

*MAT_054 (ENHANCED_COMPOSITE_DAMAGE)							
mid	**ro**	**ea**	**eb**	~~**ec**~~	**prba**	~~**prca**~~	~~**prcb**~~
1	1.50E-4	1.84E+7	1.22E+6	0.0	0.02049	0.0	0.0
gab	~~**gbc**~~	~~**gca**~~	~~**kf**~~	**aopt**			
6.10E+5	6.10E+5	6.10E+5	0.0	0.0			
xp	**yp**	**zp**	**a1**	**a2**	**a3**	**mangle**	
0.0	0.0	0.0	0.0	0.0	0.0	0.000	
v1	**v2**	**v3**	**d1**	**d2**	**d3**	**dfailm**	**dfails**
0.0	0.0	0.0	0.0	0.0	0.0	0.024	0.03
tfail	**alph**	**soft**	**fbrt**	**ycfac**	**dfailt**	**dfailc**	**efs**
1.1530E-9	0.1	0.57	0.5	1.2	0.0174	-0.0116	0.0
xc	**xt**	**yc**	**yt**	**sc**	**crit**	**beta**	
213000	319000	28800	7090	22400	54	0.5	

The trigger is modeled as a single row of reduced thickness (0.01 in. or 0.25 mm) elements at the crush front of the specimen. In order to apply different element properties to the trigger row such as the element thickness, the trigger must be modeled as a separate part from the corrugated coupon. The trigger is then merged to the rest of the specimen in a part set, and the two parts act as one. The specimen is kept at rest by constraining all degrees of freedom using a nodal single point constraint (SPC) boundary condition on the bottom row of nodes opposite the crush trigger. A large single shell element perpendicular to the specimen crush front is used to model the loading plate.

A contact definition between the loading plate and the specimen is necessary for the two parts to properly interact. LS-DYNA offers a variety of built-in contact algorithms, which can be divided in three categories: the kinematic constraint method for contact and release, the penalty method for prolonged contact, and the distributed parameter method for sliding contact. For crash analysis, standard penalty formulation methods are used [68] [50]. These methods place

springs normal to the surface between all penetrating nodes and the contact surface in order to facilitate a reaction force upon contact. The stiffness of the springs is determined directly from the value of the penalty stiffness parameter used by the specific contact algorithm. The reaction force due to contact is a function of the normal distance between two parts multiplied by a constant penalty factor, which acts as the spring stiffness constant. For the MAT54 material model, a continuous load-penetration (LP) curve is necessary to employ in place of the constant penalty factor. This curve defines the reaction normal force applied to each node as a function of the distance the node has penetrated through the surface that is contacting. The LP curve influences the initial slope of the numeric crush curve, as well as the overall stability of the simulation since it dictates how gradually the load is introduced into the row of elements at the crush front. The LP curve constitutes the most critical characteristic for a given contact type. Further discussion will be given in the parametric analysis section that follows. The contact interface between the loading plate and the specimen is defined using the contact type "Entity" for the baseline simulation. This contact type is relatively simple to implement since it requires a reduced set of parameter definitions relative to other standard penalty formulation contact types, and it produces stable results. The master part for Entity is a rigid body geometry, the loading plate in this case. Three alternative contact types have been attempted: "Rigid Nodes to Rigid Body", "Eroding Surface to Surface", and "Automatic Surface to Surface". Reasonable results are obtained from using the "Rigid Nodes to Rigid Body" contact type, however the model is very unstable with regards to slight changes in parameters, and requires constant re-calibration of the trigger thickness and of the load-penetration curve. The other two contact types investigated, "Eroding Surface to Surface" and "Automatic Surface to Surface", do not work well for this kind of load-specimen configuration. As soon as a row of elements comes into contact with the

loading plate, it generates a sharp impulse load, which immediately deletes the element row. This peak is followed by zero load until the next row is loaded, thus preventing the load to ever achieve a stable crush value.

Typically, contact type Entity defines a virtual geometry as the master part in the contact. For the crush coupon simulation, there is a physical part that contacts the specimen; hence the master part is the loading plate itself. This substitution may only be made with a shell mesh within the contact type Entity; therefore the element formulation for the loading plate is the default shell element formulation for explicit calculations (formulation 2), with no integration points through the thickness. The material system of the loading plate is defined using the rigid body material model MAT20, which attributes non-deformable characteristics to the plate, with steel material properties.

Solution time takes 96 seconds using a workstation with a 2.26 GHz dual Quadcore (8 processors) 64-bit 16 GB RAM computer. The velocity of the plate is 150 in/sec. (3.81 m/sec), and is defined by a linear load curve imposed on the nodes of the loading plate. The effect of using a simulation crush velocity that is much higher than the experimental one is discussed in the following section.

The time progression of the baseline simulation, Figure 74, reveals that failure advances in an even and stable fashion, through the element deletion at the crush front. When the first ply in an element fails, the element remains in the straight position and does not exhibit a different morphology. Once all plies have failed, the element is immediately deleted. Once an element is deleted, the entire row of elements is also deleted. Therefore crush progresses with a progressive deletion of the crush front row of elements without any other graphic indication. It is an unfortunate characteristic of MAT54 to not allow for elements to bend forming fronds,

regardless of what actually happens in the physical world (Figure 20). It should be noted that this is a peculiar behavior of axial crush simulations, which are governed by the SOFT crush front parameter. Other simulations [68] have shown that MAT54 can exhibit a limited degree of damage morphology if not loaded in axial behavior, as in the case of flexure loading or indentation of a flat plate.

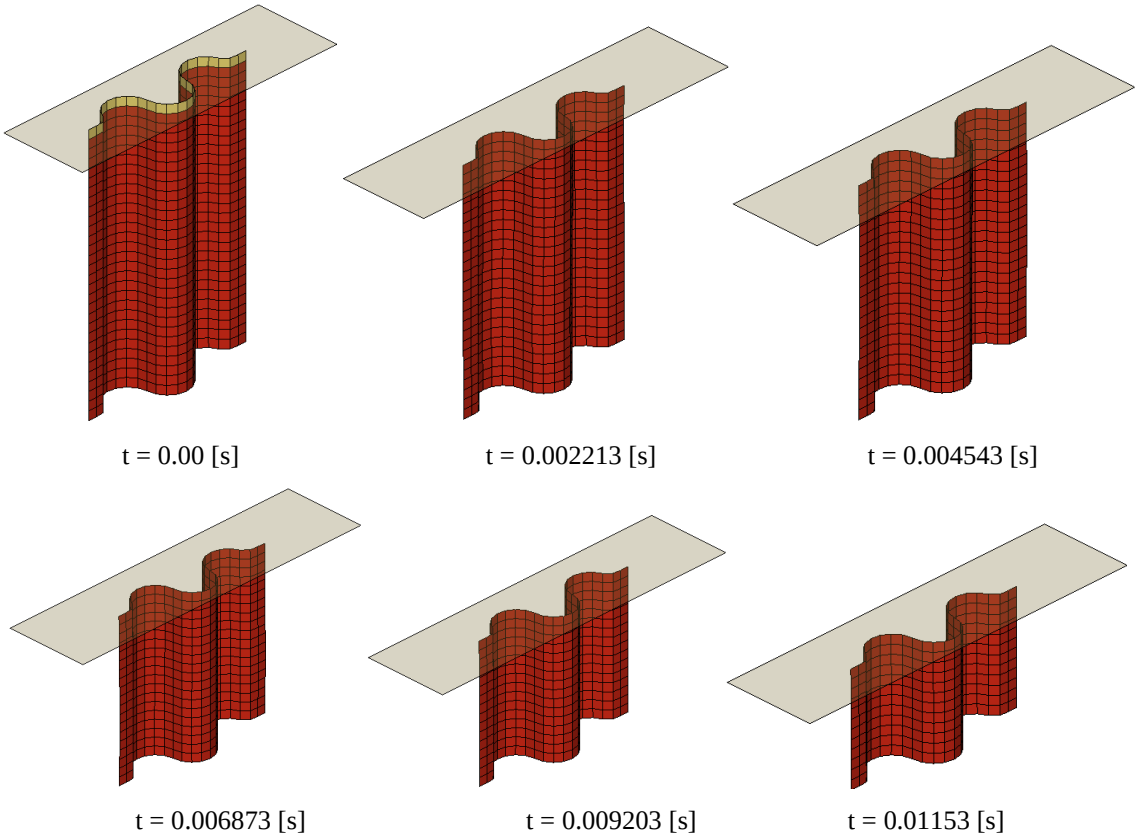

Figure 74. Time progression of the baseline UD sinusoid crush simulation showing stable element row deletion.

The load-displacement curve obtained from the model is shown in Figure 75 in its raw and filtered state. The raw curve is characterized by an alternating series of sharp peaks and valleys, giving it a saw tooth look. This feature is a typical result of the mathematical model, which is linear up to failure at the peak, then drops to zero upon deletion of the current row of elements, until the next row of elements picks up the load again. It is common practice to filter the

numeric results using a low-pass digital filter (CFC 600 Hz) during post-processing. The practice of filtering impact data was standardized by the SAE in 1974 for experimental testing [95]. The SAE developed a standardized set of Channel Frequency Class (CFC) low-pass Butterworth (maximally flat) filters for use in impact testing such that high-frequency noise due to the internal mechanical motions and resonances of the test frame could be filtered out from the data, leaving only data that is representative of a real world impact. One paper from SAE [96] recommends using a CFC 600 Hz filter for the analysis of impact data of structural components, which is the baseline filter frequency used for the sinusoid crush specimen. In crash and impact analysis, high frequency data typically seen in analytical time-histories for a particular node must also be filtered using the same low-pass filter as used in experiment such that data is kept consistent. Due to the quasi-static speeds of the experimental sinusoid data, application of the same CFC 600 Hz filter does not change the experimental result since there is no high frequency data. Filtering in this way is common practice, as recommended by NASA in 2002 [50], and used for all numeric crush simulations submitted for the CMH-17 Crashworthiness Numeric RR [97].

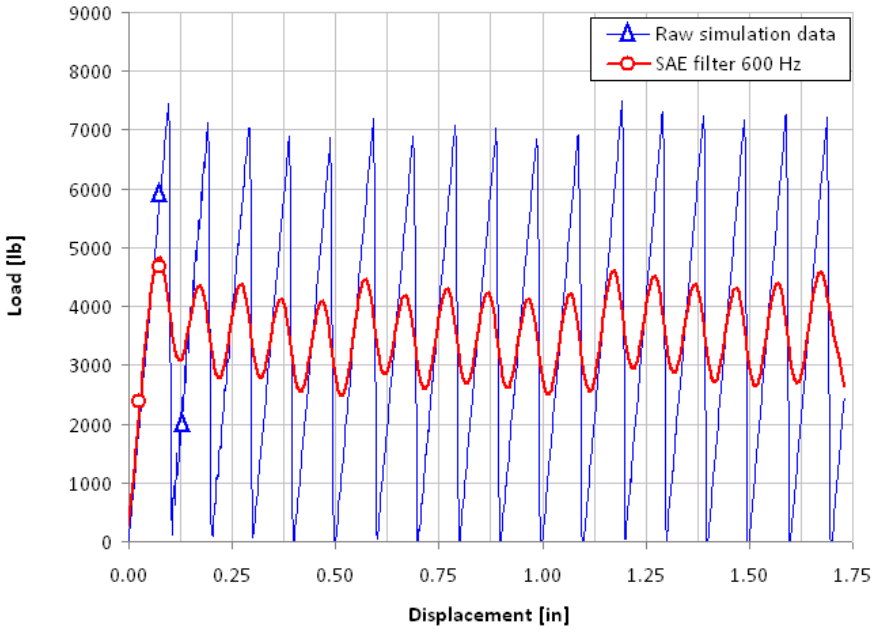

Figure 75. Filtered versus raw numeric load-displacement crush data from the baseline UD sinusoid crush simulation.

Through filtering, the average crush load remains unchanged, but the peaks and valleys are smoothed, Figure 75. The curve oscillates about the average crush load without large variations in local peak values, indicating that the simulation is stable. The effect of the filter upon the crush simulation results was studied and will be discussed in the parametric study results section. The filtered crush curve from the baseline simulation is compared with the experimental curve in Figure 76. The simulation captures all key characteristics of the experimental curve: initial slope, peak load, and average crush load, which in turn is used to compare the SEA value of the simulation to the experimentally measured SEA value. The predicted value is 64.1 J/g, compared to the experimental 67.06 J/g, the difference being – 4.4%.

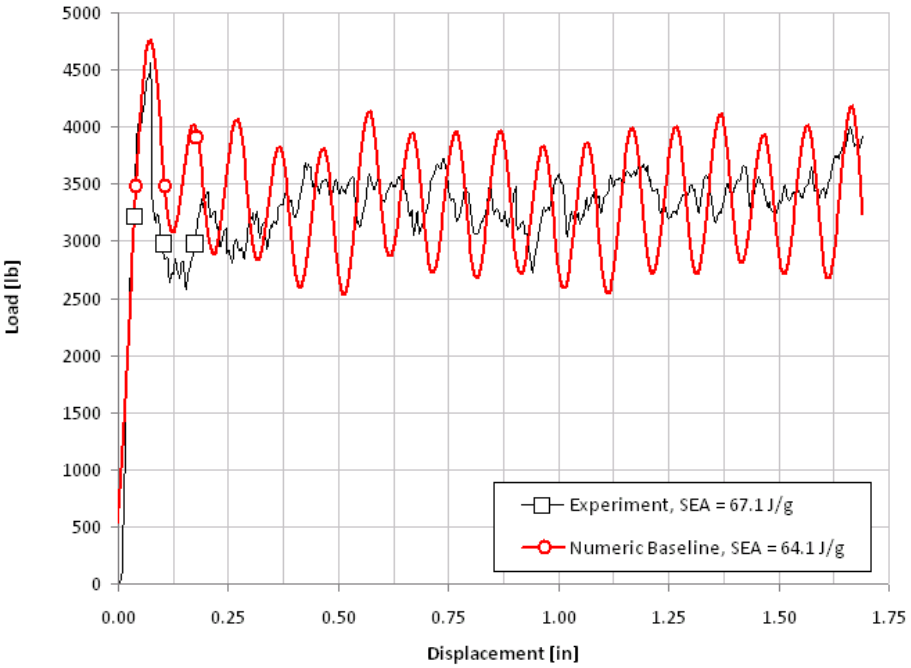

Figure 76. Experimental and simulation baseline load-displacement curves for the crushing of the UD sinusoid element.

In this section it was shown how material model MAT54 can be used to generate a model that closely approximates the experiment and captures all of its significant features. In the following two sections the sensitivity of the model to variations in the MAT54 input parameters is investigated. A summary of the MAT54 input parameters varied and their values is reported in Table 17, which also lists the corresponding Figure in the text.

Table 17. Summary of the parametric studies performed on the UD material model (units not shown for clarity).

Parameter	Baseline Value	Parametric Variation	Figure
MAT54: XT	319000	0, 5000, 50000, 150000, 250000, 300000, 350000, 370000, 400000, 500000, 640000	-
MAT54: XC	-213000	0, -100000, -150000, -200000, -230000, -250000, -265000, -275000, -300000	Figure 77
MAT54: SC	22400	1, 10000, 15000, 175000, 18000, 19000, 20000, 30000, 35000, 50000	Figure 78
MAT54: YT	7090	0, 3000, 6800, 7500, 10000, 50000, 500000	-
MAT54: YC	-28800	0, -5000, -15000, -25000, -30000, -35000, -70000, -200000, -288000, -320000, -400000, -500000	-
MAT54: DFAILT	0.0174	0, 0.005, 0.00625, 0.00688, 0.0075, 0.01, 0.015, 0.04, 0.08	Figure 79
MAT54: DFAILC	-0.0116	0, -0.005, -0.0075, -0.00813, -0.00875, -0.01, -0.012, -0.015, -0.02, -0.0225, -0.025, -0.03, -0.1	Figure 80
MAT54: DFAILM	0.024	0, 0.01, 0.015, 0.0163, 0.0165, 0.018, 0.02, 0.03, 0.06	Figure 81
MAT54: DFAILS	0.03	0, 0.006, 0.01, 0.037, 0.05, 0.1	-
MAT54: EFS	0	0.01, 0.5, 1	-
MAT54: ALPH	0.1	0, 1.0E-14, 1.0E-6, 1.0E-4, 1.0E-3, 0.03, 0.3, 0.9, 1	-
MAT54: BETA	0.5	0, 1	-
MAT54: FBRT	0.5	0, 0.1, 0.95, 1	-
MAT54: YCFAC	1.2	0, 0.5, 2, 4, 7.396, 9	-
MAT54: TFAIL	0.115E-08	0, 1E-07, 0.05, 0.11	-
MAT54: SOFT	0.57	-0.5, 0, 0.05, 0.4, 0.55, 0.565, 0.575, 0.6, 0.8, 2	Figure 82
SAE Filter frequency	600	180, 1000	Figure 84
Crush Speed	150	1.5, 15, 50	Figure 85
Contact Load-Penetration Curve	PCWL	PCWL Stiff, PCWL Soft, Linear	Figure 87-Figure 90
Mesh Size	0.1	0.05, 0.15, 0.2	Figure 91-Figure 92
Trigger Thickness	0.01	0.005, 0.015, 0.020, 0.025 0.030, 0.035, 0.040, 0.045, 0.047, 0.050, 0.060, 0.079	Figure 93
Trigger Geometry	Constant thickness	Tapered thickness	Figure 94

Sensitivity of MAT54 to material properties

An effective model needs to be sufficiently robust to tolerate small variations in material property input data, in order to accommodate small errors in measured strength and stiffness data, and yet sensitive enough to capture more significant variations, which translates in being able to capture different behaviors for different input material properties. The sensitivity of the model to variations in strengths (XT, XC, SC, YT, and YC) and strains-to-failure (DFAILT, DFAILT, DFAILM, DFAILS and EFS) is shown below.

Varying fiber tensile strength XT above or below the baseline value does not affect the outcome of the simulation, except for extreme cases where XT $\leq$ 5 ksi (34.47 MPa), which is not physically meaningful. This observation seems to suggest that fiber tension strength is not a primary failure driver for the given specimen geometry-material combination.

On the other hand, varying fiber compressive strength XC has a great effect on the resulting load-displacement curve. Small increments in XC (making it less negative) significantly lower the average crush load, while small decreases of XC (making it more negative) raise significantly the average crush load, at least until a stability threshold is reached and the model becomes unstable, Figure 77. This instability occurs at XC = -275 ksi (-1,896 MPa). The model's strong dependence on XC would suggest that the dominant failure mode occurring during these crush simulations is the compressive fiber mode.

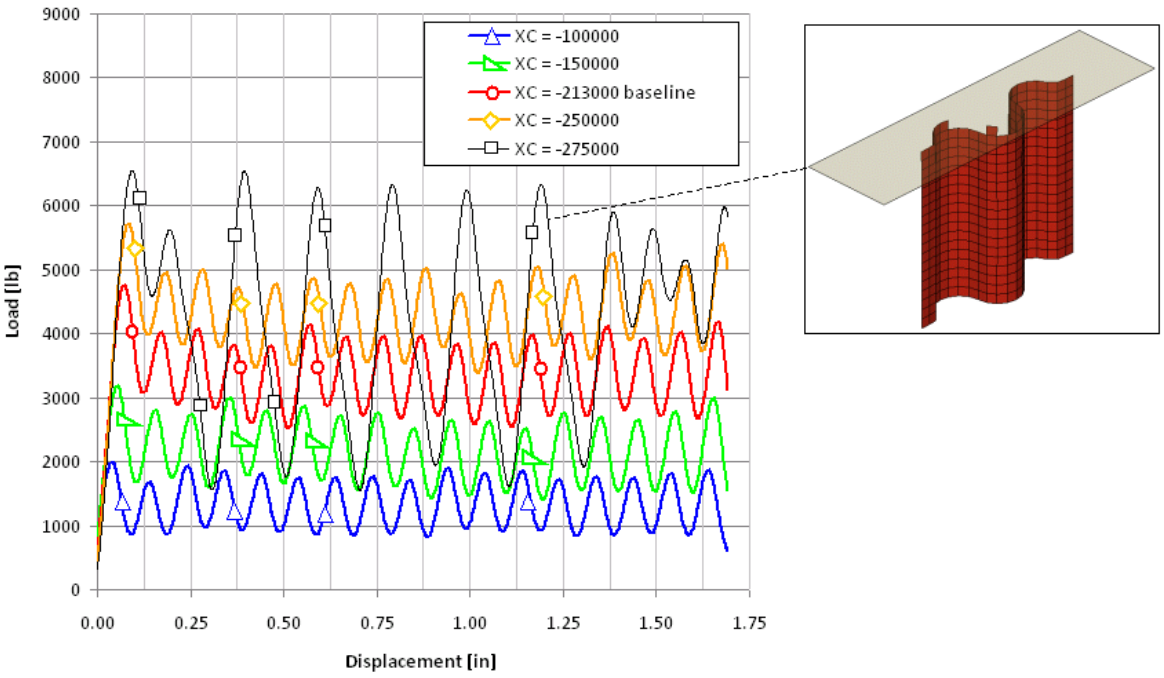

Figure 77. Effect of varying compression strength, XC, on the baseline model, showing that small changes to XC lead to large changes in the simulation results.

Shear strength SC has an unexpectedly strong and peculiar influence on the stability of the model. Increasing SC above the baseline value does not affect the results, even up to values that are twice the experimental strength of the material. On the other hand, decreasing SC by even small amounts (approximately 15% of the experimentally measured value) creates instabilities in the model, Figure 78. Increasingly lower values of SC cause greater instabilities in the crush curve. Interestingly, MAT54 does not have a failure criterion dedicated to shear strength, but SC appears as an interactive term in three of the failure modes, Equations 25, 27, and 28, in the tensile fiber (through the parameter BETA if nonzero), tensile matrix, and compressive matrix failure modes. By decreasing SC, the contribution due to the shear term in the three equations increases, combining with the other stress, to the point that it causes premature ply and element failure. The results indicate that shear strength is a fundamental parameter for the stability of the specimen during crushing. The deviation between the baseline value (22.4 ksi or 154.4 MPa)

and the partially unstable simulation value (19 ksi or 131 MPa) is 12%, which is above the expected experimental error of a thorough material property testing protocol. For a small-scale test program of a high variability material system, however, a 12% deviation may lie within experimental error of a shear strength test. Care should therefore be taken while examining the results of the material property testing for shear strength for input into MAT54.

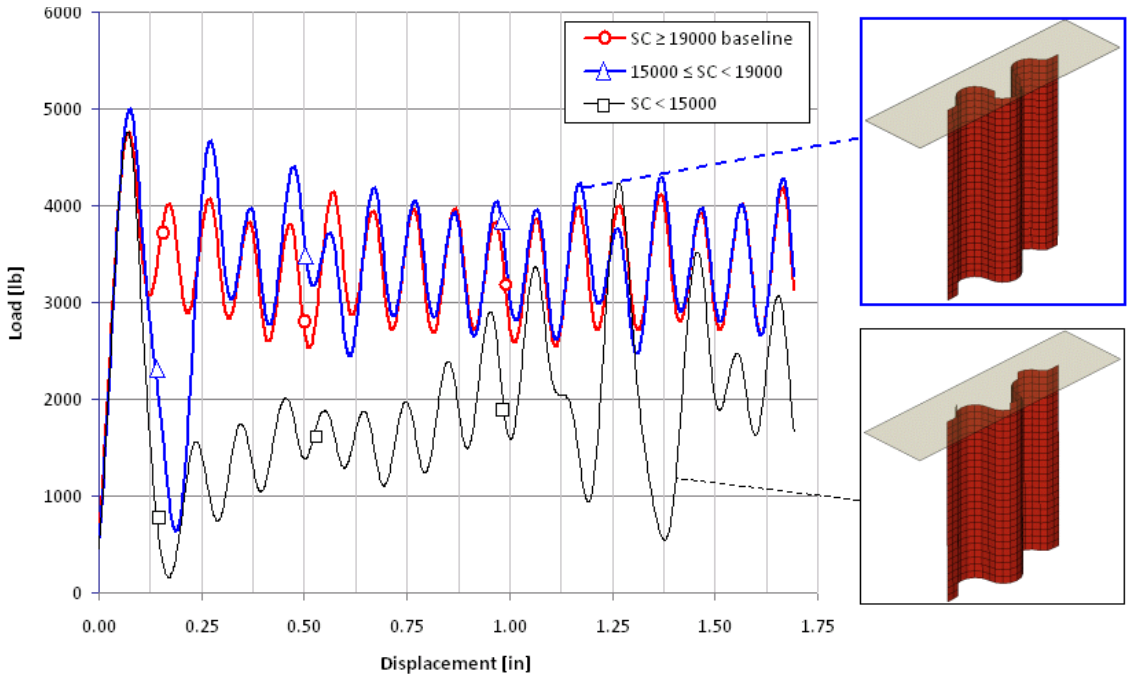

Figure 78. Effect of varying shear strength, SC, on the baseline model, showing an unexpected influence of shear strength on the stability of the crush model.

Altering the matrix tensile strength YT, found in the failure criterion for the tensile matrix mode only (Equation 27), from 0 to 300 ksi (2,068 MPa), with the baseline value being 7.09 ksi (48.9 MPa), does not affect the results: the load-displacement curve remains stable and the average crush load does not change.

Varying the matrix compressive strength YC, found in the failure criterion for the compressive matrix mode only (Equation 28), does not change the results of the crush simulation. However, for exceptionally high values, such as 200 ksi (1,379 MPa), the crush curve is approximately

10% lower than the baseline curve. Since this value is not realistic for unidirectional tape, it can be neglected. Matrix (transverse) tension and compression are therefore not failure driving mechanisms for this geometry/ material combination under crush loading.

For the tensile strain-to-failure in the fiber direction, DFAILT, the simulation results remain unchanged from the baseline, which uses a value of +0.0174, for values as high as +0.070 and as low as +0.0075. This suggests that allowing for a virtual plasticity in the positive direction does not affect the simulation, Figure 79. However, if the strain-to-failure is further reduced, below +0.0075, instabilities start to manifest, with non-uniform element failure at both ends of the specimen. For values as low as a +0.005, immediate buckling occurs without any stable crushing. This observation seems to suggest that fiber tension strain to failure is not a primary failure mode for the given specimen geometry-material combination, as long as the strain to failure is sufficiently large to inhibit secondary failures.

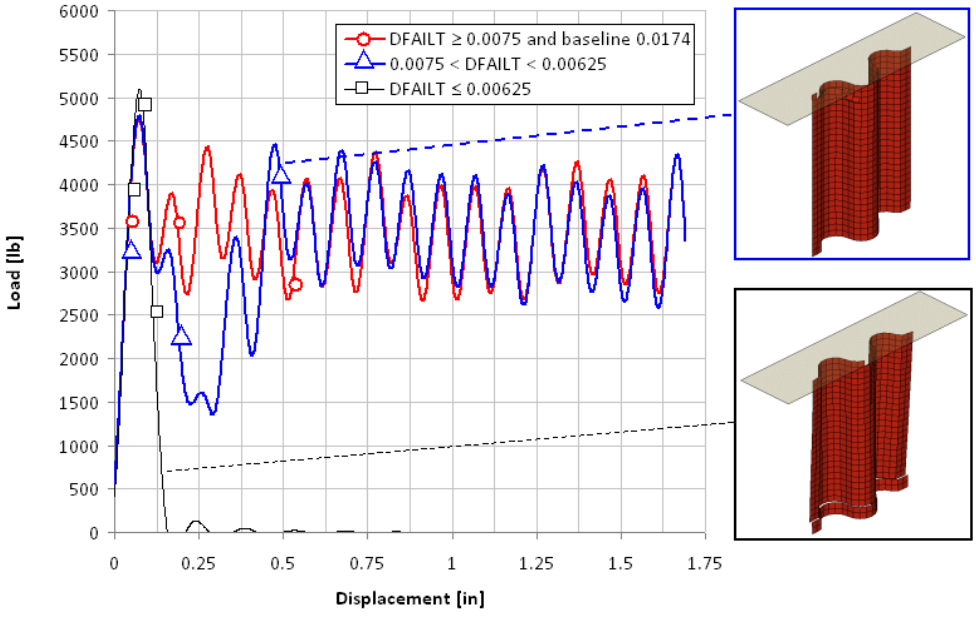

Figure 79. Effect of varying the tension strain-to-failure parameter, DFAILT; only very low values of DFAILT lead to non-uniform element deletion at the crush front (unstable crushing) and global buckling.

The compressive strain-to-failure in the fiber direction, DFAILC, has a deeper effect on the results of the simulation. Within the range [-0.2, -0.0081], around the baseline value of -0.0116, changing DFAILC changes the average crushing load, Figure 80. Reducing DFAILC (making it more negative) increases the average crush load, while increasing DFAILC (making it less negative) decreases the average load value. Lowering DFAILC below -0.02 however leads to non-uniform element deletion at the crush front, Figure 80. Adding virtual plasticity [87] has a detrimental effect on the simulation results. On the other hand, if DFAILC is increased up to -0.0081, global buckling occurs immediately. Based on these results, compressive strain to failure is a primary failure mode for the given specimen geometry-material combination, and therefore a critical parameter for achieving successful simulation results.

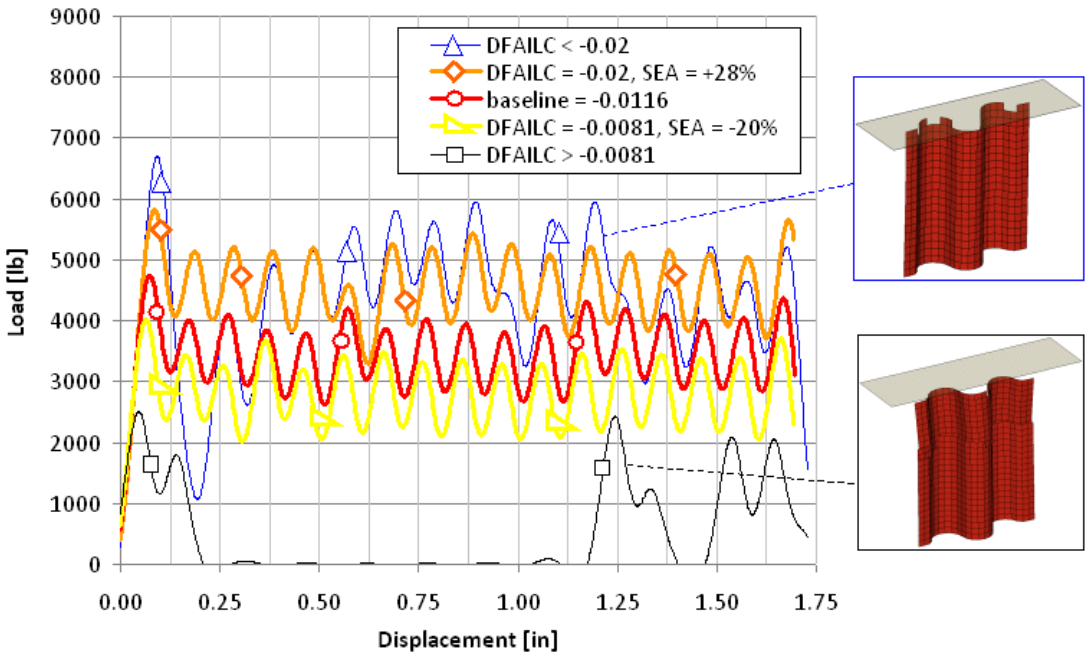

Figure 80. Effect of varying the compression strain-to-failure parameter, DFAILC; small changes to DFAILC have a dramatic influence on the simulation results.

In the transverse direction, the positive and negative failure strains are both defined by a single parameter, DFAILM. Since from experiment the compressive strength of the matrix is greater

than its tensile strength (Table 2), it is not easy to define a single strain-to-failure value for both directions using only one parameter. As such, this is a limitation of the MAT54 material model. For the baseline model, DFAILM is set to be the compressive strain-to-failure $|0.0240|$, which automatically imposes a plateau of virtual plasticity in tension, Figure 40a. As it turns out, the simulation is unaffected for absolute values of DFAILM as low as $|0.0165|$ and as high as $|0.0500|$, Figure 81. However, values smaller than $|0.0165|$ causes unstable crushing and element deletion is non-uniform, resulting in great load fluctuations, Figure 81. In the extreme, setting DFAILM to zero causes severe element distortion, element detachment without deletion, and non-uniform deletion.

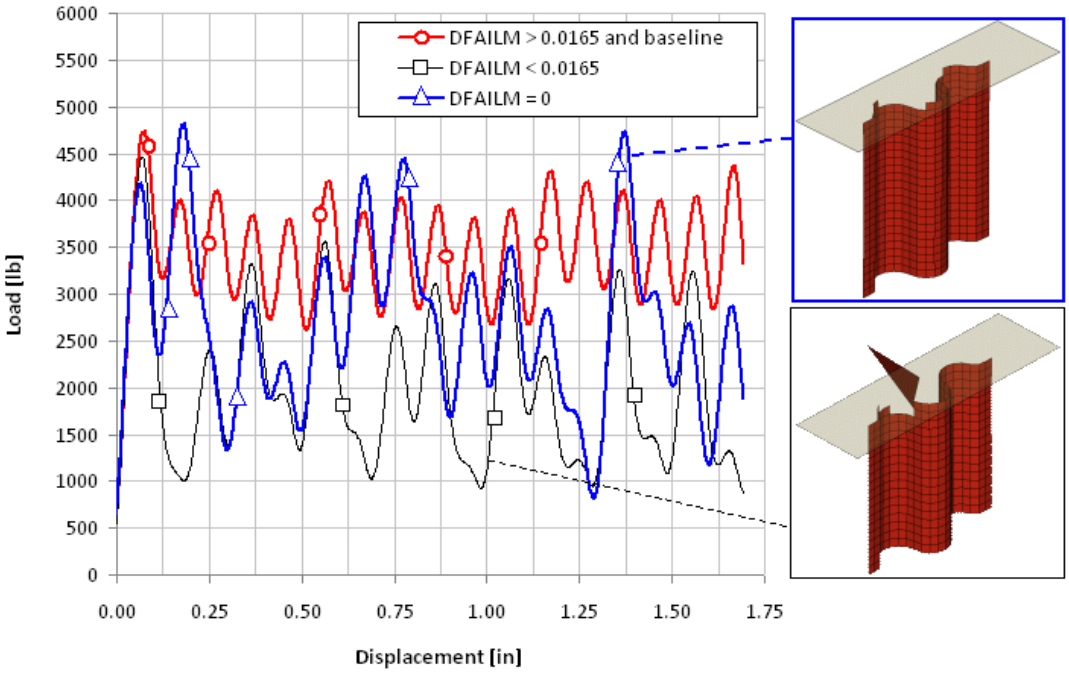

Figure 81. Effect of varying the matrix strain-to-failure parameter, DFAILM; this parameter has a significant role in the stability of the crush simulation.

From the baseline value of DFAILS = 0.03, the shear strain-to-failure is varied in the range [0, 0.10]. It is found that the crush load-displacement curve remains unaltered from the baseline, thus suggesting that either shear is not a dominant failure mechanism for this crush problem, or

that the model is not able to capture shear-related phenomena. While MAT54 allows the element to fail if the strain exceeds DFAILT, DFAILC or DFAILM, it should be noted that there is no explicit criterion for failure associated with DFAILS.

The EFS parameter is a measure of a general strain to failure in the absence of the individual values of DFAILT, DFAILC, and DFAILM. If these values are defined, the model neglects the value of EFS, and it is found that indeed altering the EFS between [0, 1] does not change the simulation results at all. However, if DFAILT, DFAILC and DFAILM are set to zero and EFS is utilized, the model encounters errors and does not run at all for any value of EFS. Therefore, for this type of crush simulation, it is recommended to always utilize the experimental measured strains to failure for the unidirectional lamina and not rely on an arbitrary value of EFS.

From these results, it appears that compressive strength XC and compressive strain-to-failure DFAILC are the dominant parameters leading to element failure, and therefore have the stronger influence on simulation results.

Sensitivity of MAT54 to other model-specific parameters

This section focuses on the effect of parameters that are specific to the MAT54 material model, and are necessary for the simulation to progress in a stable fashion. These parameters either have no immediate significance in the physical world or cannot be measured experimentally, and hence have to be calibrated by trial and error. These quantities include the ALPH, BETA, FBRT, YCFAC, SOFT and TFAIL parameters.

The ALPH and BETA parameters, which appear in Equations 24 and 25 respectively, are shear stress weighing factors that may hold values between [0, 1]. Parametric studies reveal that using any value of ALPH or BETA in the admissible range does not influence in any way the baseline

simulation, both in terms of load-displacement curve and SEA. The independence of the BETA term suggests that shear stress has no effect on the fiber failure, which in turn signifies that the failure criterion used for tensile fiber failure (Equation 25), whether Hashin (BETA = 1) or Maximum Stress (BETA = 0), is not critical for the outcome of the simulation. This observation, in conjunction with the previous observations for XT and DFAILT, seems to confirm that fiber tension failure is not a primary damage mechanism. On the other hand, the insensitive nature of this model to the value of the ALPH parameter, which adds the third-order shear term in Equation 24, seems to suggest that the shear stress-strain relation can be simplified to a first-order equation for this material/ geometry/ loading combination.

The strength reduction factors FBRT and YCFAC were arbitrarily selected to be equal to 0.5 and 1.2 respectively for the baseline simulation. Both the FBRT and YCFAC terms are fiber strength reduction factors (for XT and XC respectively) for elements that have already experienced damage, and appear in Equations 30 and 31, respectively. They are used to degrade the fiber strength properties of the element following the first-ply (matrix) failure. These are varied systematically in the range [0, 1] for FBRT and [0, 7.4] for YCFAC. Results show that the simulation is unaffected by the fiber strength degradation scheme. These factors have negligible effect on the results of the simulation.

As for TFAIL, the simulation runs unaffected for small values of TFAIL, such as [1E-08, 1E-05]. Using TFAIL = 0 leads to immediate global buckling because of the SOFT condition violation discussed earlier. Using large TFAIL values in the range [0.001, 0.1] should be avoided, since the time-step of the simulation is smaller and elements are deleted before being loaded. It should be emphasized that LS-DYNA assigns the time-step automatically to ensure

that the Courant condition is satisfied [98] [99] [100]. In this case the default time-step is 2.44219 E-7 [101].

The sensitivity of the model to variations in the SOFT parameter is investigated within the admissible range [0,1]. Values >1 are confirmed to yield the same curve as if SOFT were set to 0. Results show that SOFT has a dramatic effect on the simulation and is perhaps the single most influential parameter in the entire input deck, Figure 82. By itself, it is capable to dictate whether the simulation is stable or unstable. It can also shift the average crush load above or below the baseline by at least 30% from the baseline value of 64.12 J/g (for SOFT = 0.57). The results are shown in Figure 11, along with the average SEA values. Increasing the SOFT value has the effect of increasing the average crush load and SEA of the simulation. For SOFT = 0.6, SEA = 75.8 J/g (+13%), for SOFT = 0.8, SEA = 87.1 J/g (+30%) and partial instability occurs halfway in the simulation. Further increasing the SOFT to 0.95 the specimen is too stiff and buckles immediately. Lowering the SOFT value has the effect of lowering the average crush load and SEA value of the simulation. For SOFT = 0.4, SEA = 48.8 J/g (-27%), and it could go even lower for lower values of the SOFT (for SOFT = 0.05, SEA = 2.74 J/g or –96%).

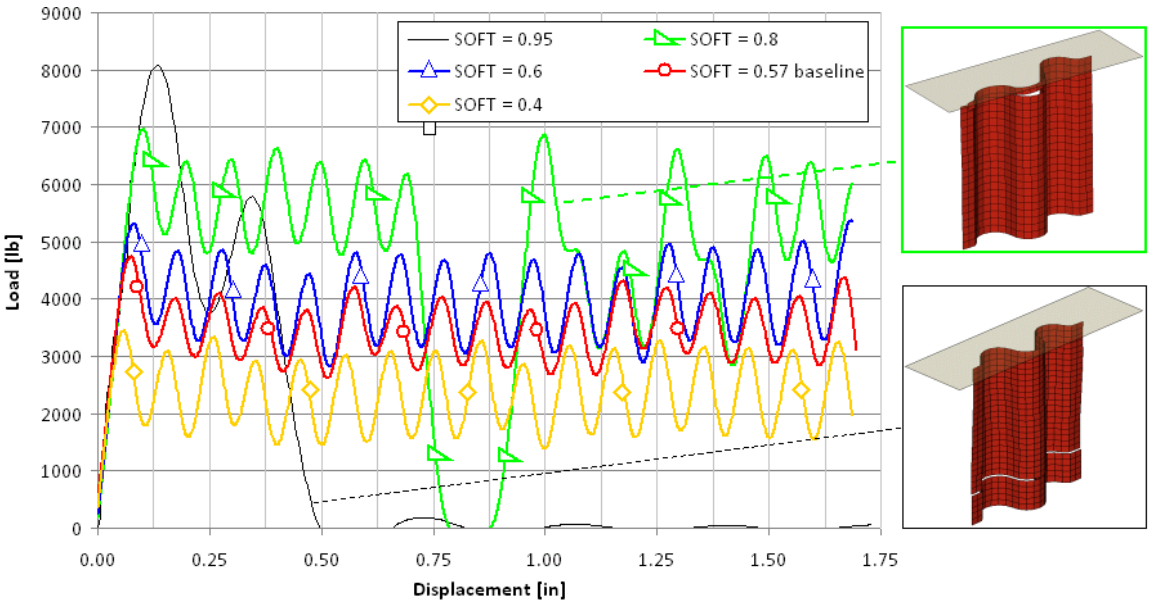

Figure 82. Effect of the SOFT parameter on the simulated load-displacement curve shows that this parameter is the most critical and influential parameter for the results of the crush simulation.

It should be recalled that the meaning of the SOFT parameter is to artificially reduce all of the material strengths of the row of elements immediately ahead of the active crush front, as indicated in Figure 83. This parameter is a mathematical expedient to avoid global buckling of the specimen, which would occur if the peak load were transferred instantaneously upon deletion from the active crush front to the row of elements immediately ahead of the crush front. In the physical world one could perhaps interpret the SOFT as a damage zone (comprised of delaminations and cracks) ahead of the crush front that reduces the strength of the material. When that material undergoes crushing, it has a strength lower than its pristine value. Determining the correct SOFT value is a challenging task, since it cannot be measured experimentally, but it has to be found by trial and error until the load-displacement curve of the simulation matches the experimental result. Unless the right value of the SOFT parameter is found and utilized, it is not possible to obtain a successful simulation. The most important

consequence of this observation is that the MAT54 material model is by all means not a true predictive tool since the SOFT parameter needs to be calibrated to the experiment.

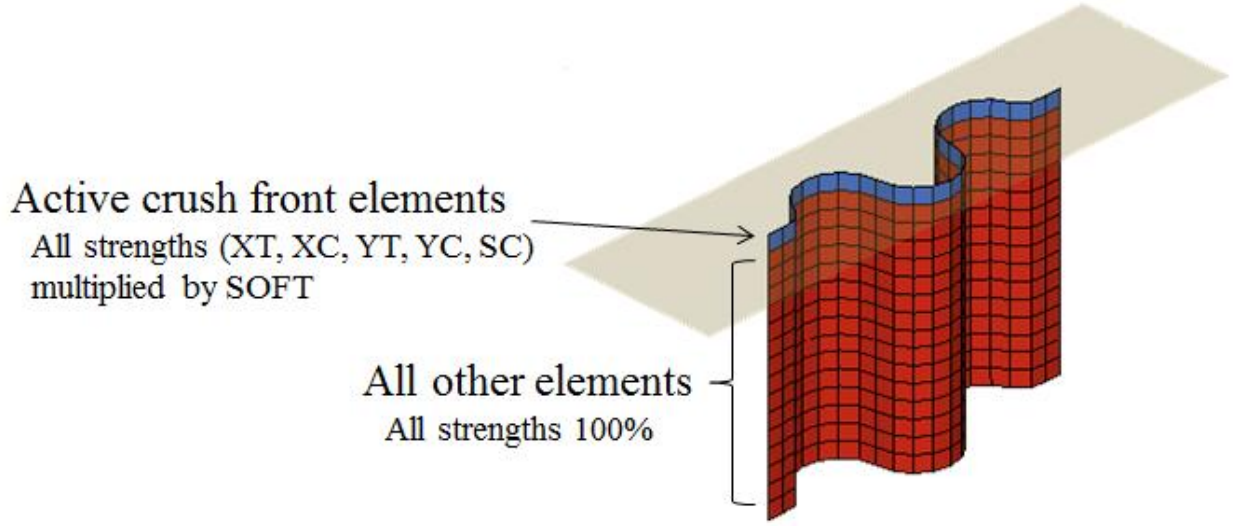

Figure 83. Schematic of the crush-front elements and the strength input parameters which the SOFT parameter effects on the sinusoid crush element during the crush simulation.

Sensitivity to other modeling parameters

In this section, the influence of parameters that are not specific to the material model itself but are particularly influential for the simulation is discussed. These include filtering, crush speed, contact type, load-penetration (LP) curve, mesh size, trigger thickness and trigger shape.

The choice of frequency for the filter can significantly change the behavior of the crush curve. Low-pass filter frequencies are useful to damp large variations in load, however can also mask out important physical information such as the initial slope and peak load. It is desirable to use a frequency that is high enough to capture the initial slope and peak, while sufficiently attenuating (smoothing) the load-displacement curve. Typically, the correct low-pass filtering frequency is determined by measuring the duration of the acceleration pulse from accelerometer data recorded during impact. Since this data is not available for a coupon level test, frequencies from the SAE

CFC for vehicle impact are investigated to find the appropriate filtering frequency. One paper from SAE [96] recommends using a CFC 600 Hz filter for the analysis of impact data of structural components, which is the baseline filter frequency used for the sinusoid crush specimen. Varying the CFC frequencies of 180 and 1000 Hz from the baseline value of 600 Hz produces the curves shown in Figure 84. The 600 Hz filter has the lowest frequency which maintains the initial slope of the curve. Using a 180 Hz frequency filter causes loss of both the initial slope and load peak, while the 1000 Hz filter retains large load peaks that mask the initial physical peak and the stable crush load. The resulting SEA value changes only a few percent, but the overall load-displacement curve loses significance. The result shown in Figure 84 from varying the filter frequency demonstrates the same trend as reported by NASA in the 2002 Best Practices for Crash Modeling report [50]. A known effect associated with filtering, regardless of the frequency used, is the shift of the load-displacment curve to the left, causing the initial load in the filtered curve to be nonzero. This phenomenon, which is purely mathematical and not physical, can be seen dramatically in Figure 84 for the 600 and 180 Hz filters, and is also reported in the 2002 NASA report. Filtering causes an initial load at time zero to be close to 2,000 lb (8.896 kN) using these filters.

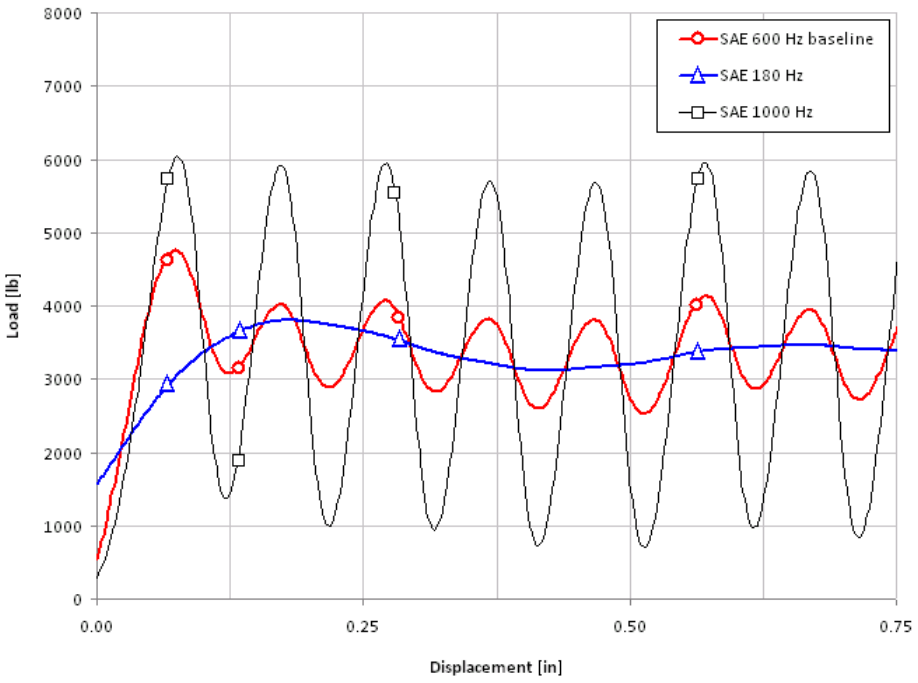

Figure 84. Effect of SAE filter frequency on the baseline sinusoid crush simulation.

Although the true experimental crush loading rate is 1.0 in./ min. (25.4 mm/min), simulations are performed using a crush velocity of 150 in./sec (3,810 mm/sec) because of computational runtime limitations. Since all material properties were measured with quasi-static tests, no strain-rate dependent material properties were defined in the material input deck, hence the model cannot assume strain-rate behavior. Nonetheless, inertial effect may arise, which could lead to different global response for the specimen. To verify the validity of the assumption, two simulations are carried out at simulation speeds of 15 in./sec (381 mm/sec) and 1.5 in./sec (38.1 mm/sec), which are both well below any dynamic threshold reported in the literature [16] [15] [97]. These simulations have runtimes of 16 minutes and 164 minutes respectively, compared to the runtime of 96 seconds of the baseline model, and are hence very impractical with the available computational power. Reduced crush speeds do not change significantly the results from the baseline simulation, Figure 85.

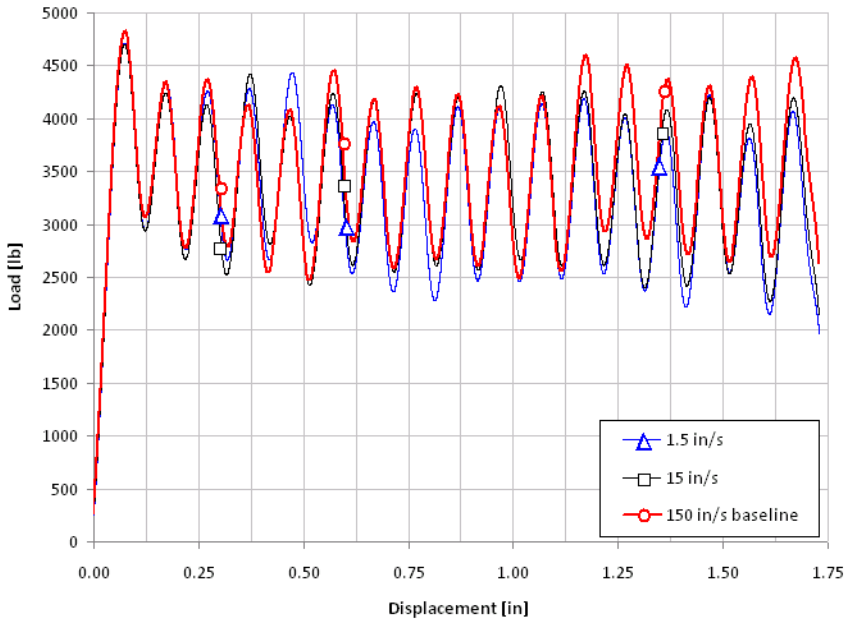

Figure 85. Effect of crush velocity on the baseline sinusoid crush simulation results.

Several different contact definitions to describe the contact interface between the loading plate and the sinusoid composite specimen were tried, with limited success. Most contact types are incompatible with MAT54, and transfer forces too suddenly to the MAT54 elements, causing pulses of load in the resulting crush curve. A contact which provides a more gradual transfer of forces is necessary, and this requires the use of a load-penetration curve such that the user can explicitly define the loads transferred as a function of contact displacement. Only two such contacts exist, Entity and Rigid_Nodes_to_Rigid_Body. Results from using an automatic and an eroding type contacts are shown in Figure 86, along with the baseline Entity contact which employs an LP curve. Similar results have recently been reported by Krishnamoorthy et al. [102], where only an Entity type contact was reported to be compatible with MAT54 in a crush element simulation.

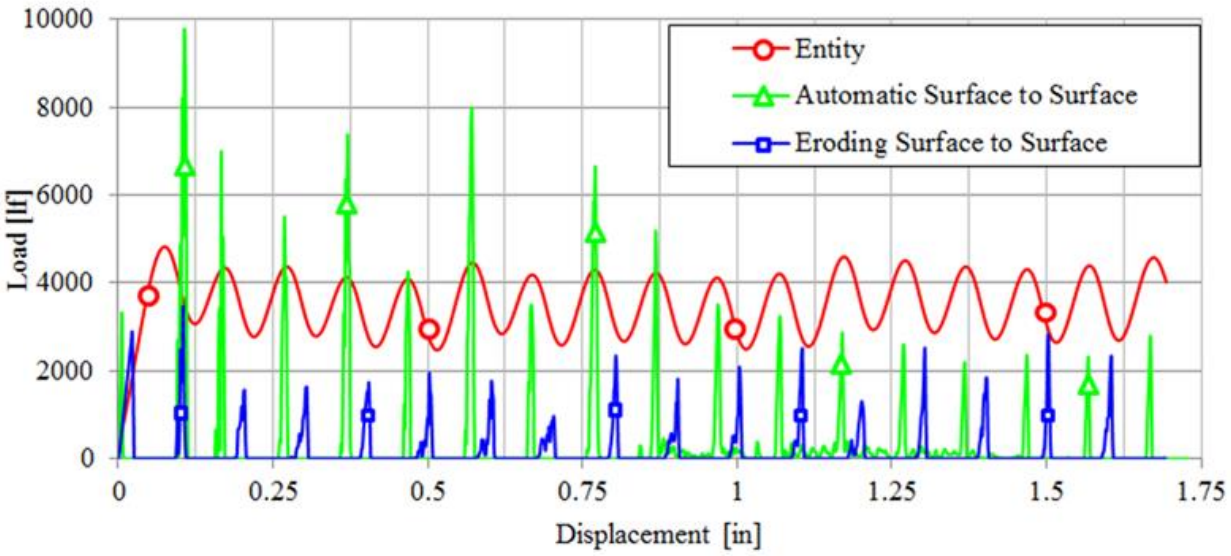

Figure 86. Effect of using different contact definitions in the UD sinusoid crush simulation.

Varying the LP curve has a deep effect on the stability of the model, yet there is no way of knowing in advance or determining experimentally the correct shape this curve needs to have for the specific material/ geometry/ loading combination. Definition of the LP curve takes place by trial and error. The baseline LP curve is a piecewise linear (PCWL) function, Figure 87, which introduces the load in a gradual fashion into the element. If the stiffness of the PCWL function is varied above and below that of the baseline, the LP curves take the shape of Figure 87 (stiff and soft respectively). A stiff LP curve introduces the load into the coupon less gradually, while a soft LP curve introduces the load even more gradually. It should be expected that using a stiff LP curve would increase the reaction forces on the elements, which in turn would increase the slope of the load-displacement curve (i.e. the load raises faster to its plateau) and the magnitude of the peak load oscillations, thus raising the average crush force. The opposite should be expected for a soft LP curve. However, filtered results show that the stiff LP curve leads to a greater stiffness as predicted, but lower peak load and lower average crush load, while the soft LP curve generates lower initial stiffness, but higher peak load and average crush load than the

baseline (Figure 88). This counterintuitive result is a deception of the analysis due to the filtering scheme. If the raw load-displacement curves for the baseline and stiff LP curves are plotted (Figure 89 shows only these for clarity), it can be seen that indeed the stiff LP curve generates higher peak loads than the baseline curve. However, it also leads to element failure and deletion well before the loading plate reaches the next row of elements. This results in greater positive/negative oscillations and long periods where zero-load exists before the next row of elements contacts the plate. The higher oscillations and zero load regions in between element rows decrease the average crush load as calculated by the SAE filter. To the extreme, if an aggressive linear LP curve is used (Figure 87), which leads to the same final load value as the PCWL LP curve of the baseline but at a much faster rate, the filtered load-displacement curve shows a higher initial stiffness but an even lower average crush load than the stiff PCWL LP curve, Figure 88. The raw load-displacement curves for all four types of LP curves are shown in Figure 90, where for clarity only the early portion of the curve is reported. It can be seen that the linear LP curve has the highest initial stiffness and the most variation between positive and negative amplitudes, while the soft PCWL LP curve leads to the lowest initial stiffness and most moderate oscillations. Using a softer LP curve leads to lower peak values, which in turn leads to element deletion only when the next row of element is already contacting the plate. Thus the load never drops to zero, and the SAE filter interprets it as a higher average crush load.

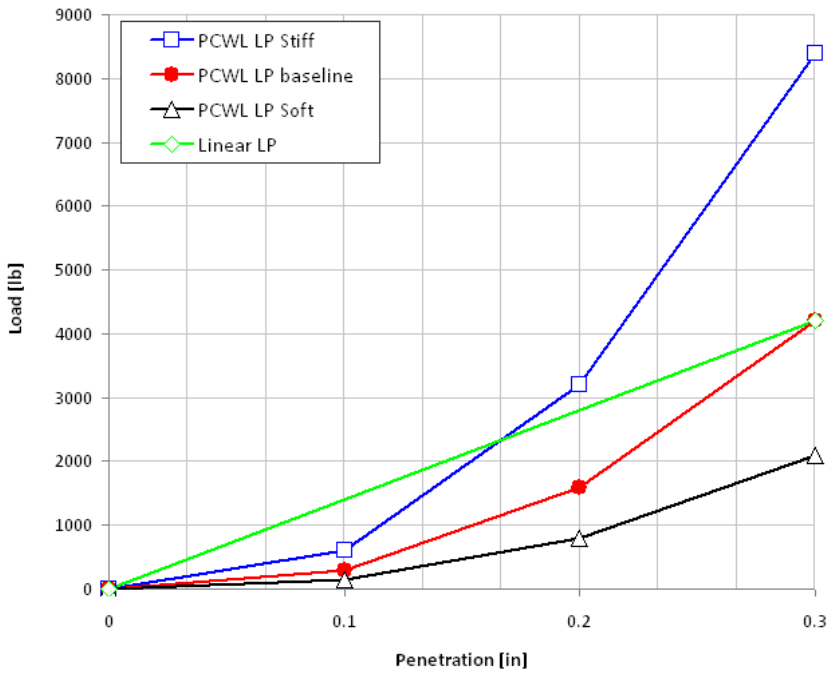

Figure 87. Four load-penetration curves investigated in the contact definition of the baseline crush simulation.

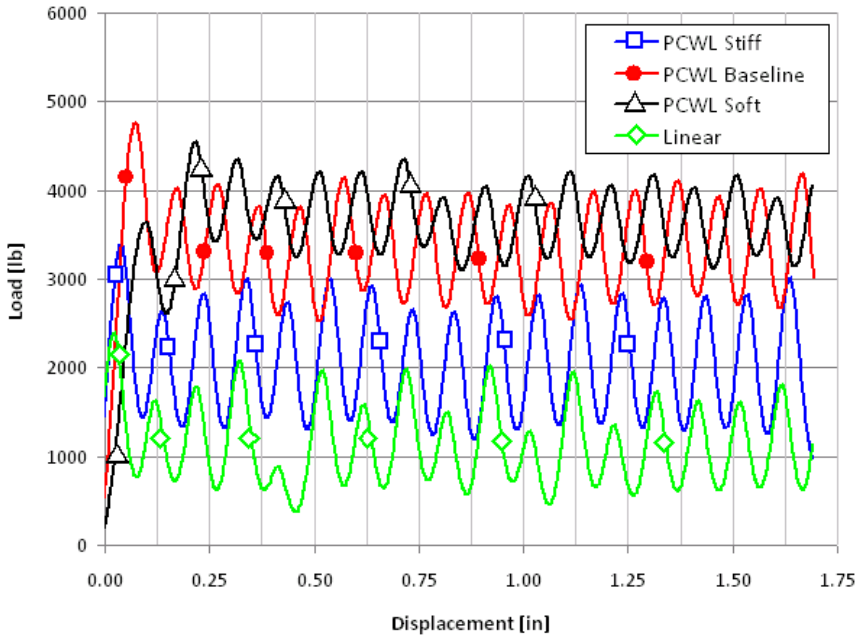

Figure 88. Effect of the four different load-penetration curves (from Figure 87) on the filtered load-displacement curves.

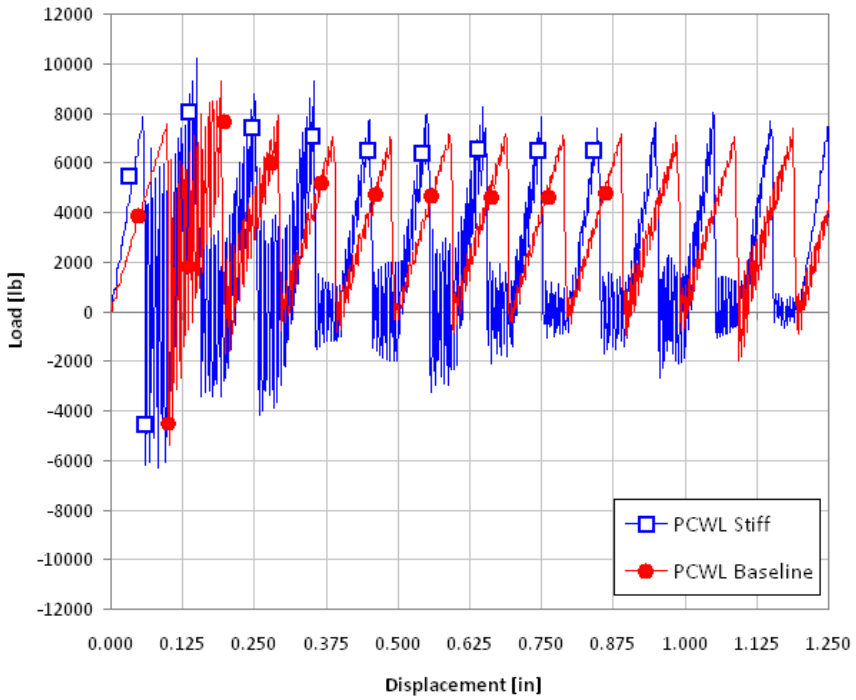

Figure 89. Two unfiltered load-displacement curves from Figure 88.

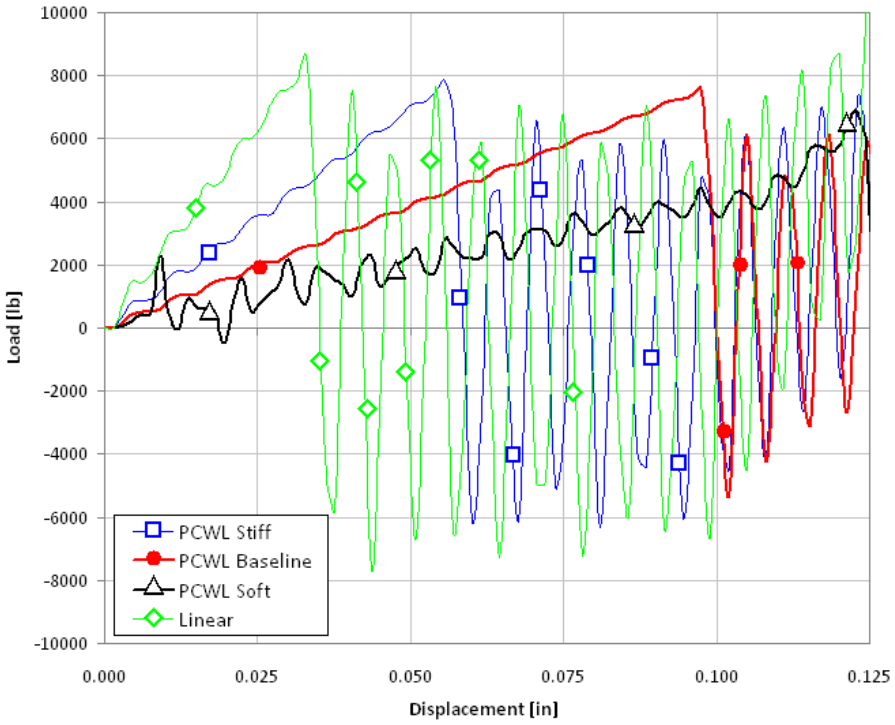

Figure 90. Details of the influence of the four load-penetration curves on the initial time-steps of the unfiltered load-displacement crush curves.

Explicit FEA codes are known to be particularly mesh-sensitive, and while it is desirable to always use the finest mesh size, computational costs become particularly demanding. From the baseline value of 0.1 in. (2.54 mm), the mesh size is varied down to 0.05 in. and up to 0.2 in. (1.27 mm and 5.08 mm respectively). All other parameters are left unchanged from the baseline model. While the runtime for the baseline mesh size is 96 seconds, the run times for the finer mesh is 7 minutes 19 seconds, while for the coarser mesh it is 43 seconds. The filtered load-displacement curve for the coarse mesh, Figure 91, shows that the initial load and slope are very close to the baseline, but the curve never achieves a stable crush load. The filtered curve oscillates with greater amplitude than the baseline, and the reason for this behavior can be found by looking at the raw curve. Once a row of elements fail, there is a large gap with zero load before the next row of elements comes into contact with the loading plate, similarly to the case of the stiff LP curve. Intuitively, softening the LP curve would correct this behavior, however trials show that sustained crushing without zero loading cannot be achieved no matter how soft the LP curve is. Softening the LP curve also reduces the initial peak load and slope, and the average crush load is overall lower than the baseline due to the presence of the zero-load sections. Attempts to raise the curve have been made by increasing the SOFT parameter, which increases the peak loads, however it is not sufficient to increase the average crush load. The coarse mesh size appears to be too coarse to capture the relevant behaviors. Another observation that supports this conclusion is that the element formulation 16 in LS-DYNA is a linear shell element, and therefore it cannot be curved or bent to conform to a curved geometry. For the sinusoid specimen, characterized by continuous curvature with a radius of 0.25 in. (6.4 mm), the coarse meshes will approximate the sinusoid geometry too roughly, Figure 91 right. Quadratic shell elements are not currently available in LS-DYNA.

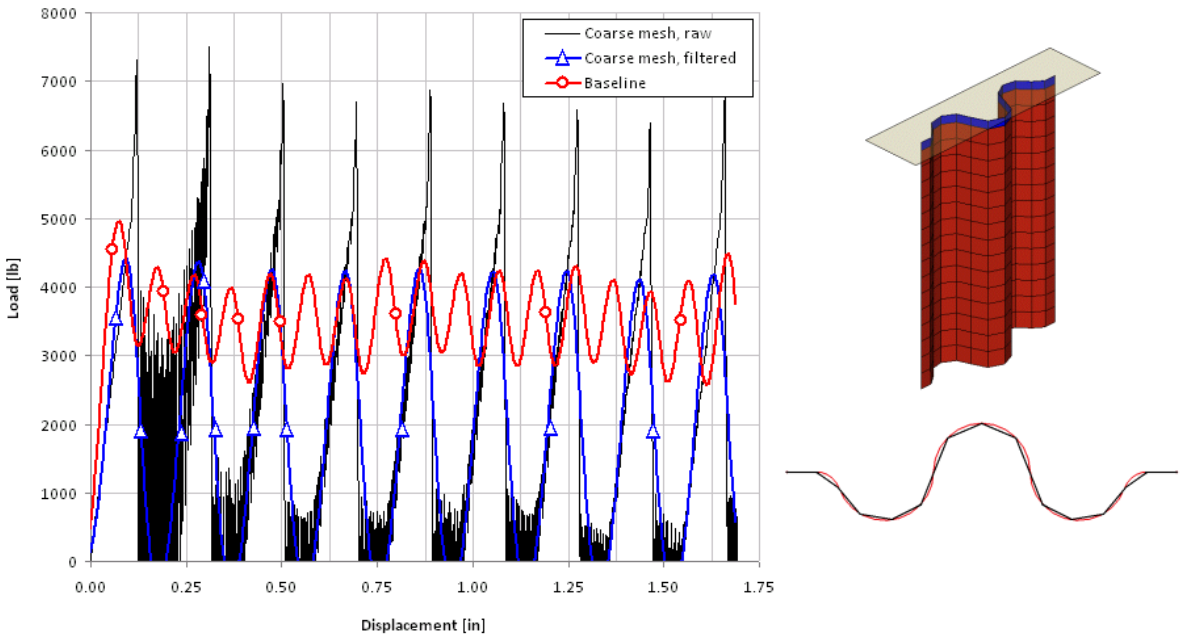

Figure 91. Effect of a coarse mesh size on the baseline load-displacement crush curve, both filtered and unfiltered.

The finer mesh yields the load-displacement curve of Figure 92. Without changing any other parameters, the load has a larger initial slope and peak value, which is followed by some instability and large oscillations, and eventually undergoes global buckling. In this case, by reducing the SOFT parameter (from 0.57 to 0.50), the finer mesh simulation acieves sustained crushing, with only some instability at the beginning of the simulation, as seen in the stable crush curve of Figure 92. Attempts to stabilize the model by modifying the LP curve yield even more unstable results. The oscillations for the modified fine-mesh model have higher frequency and amplitude as a result of the doubled number of element rows, but overall the finer mesh model matches the experimental data well.

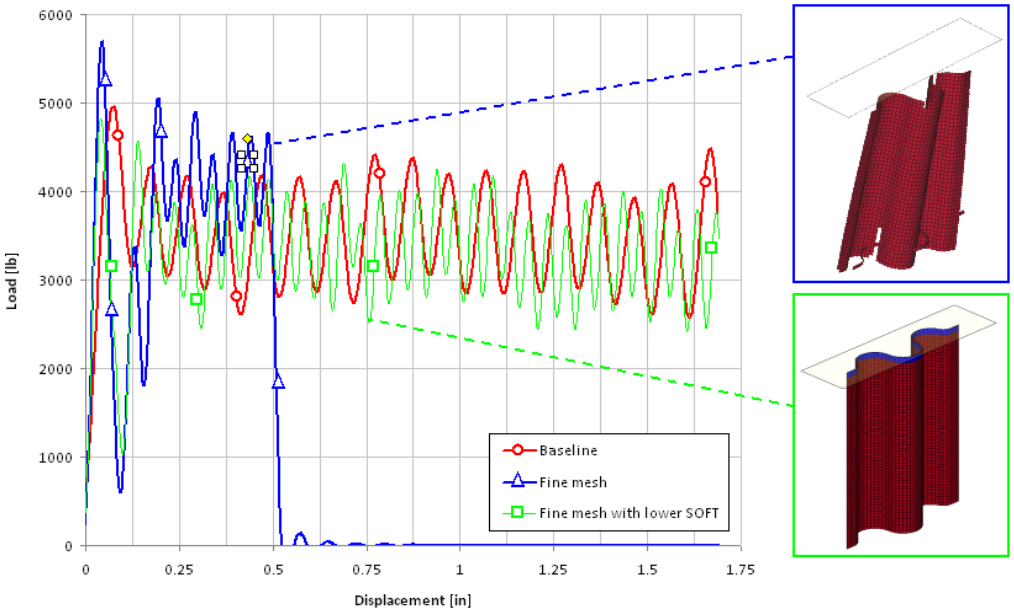

Figure 92. Effect of a fine mesh size on the filtered load-displacement crush curve, with the baseline and a reduced SOFT parameter.

The crush trigger determines the initial behavior of crushing, directly influences the initial peak load value, and can also influence crush stability. The baseline trigger geometry is a single row of constant reduced thickness elements (0.01 in. or 0.25 mm). The thickness is varied between 0.001 and 0.5 in. (0.025 mm and 12.7 mm) and it is found that increasing trigger thickness up to a thickness of 0.047 in. (1.19 mm) leads to lower initial peak load than thinner triggers, Figure 93. However, similar to the previous discussion on the LP curve, this is an apparent phenomenon associated with filtering. The raw data shows that early instabilities during crushing can cause the second row of elements to be deleted simultaneously with the trigger row, leading to near zero load, which the filter then interprets that as a lower initial peak load. Increasing the thickness to 0.05 in. and above (12.7 mm) leads to immediate global instability, which causes the specimen to buckle, Figure 93. Since the trigger is at the contact interface of the loading plate, the choice of contact formulation affects the sensitivity of the trigger thickness to the simulation results. For the Entity contact, a thin trigger row of elements is capable of

initiating stable crushing and produces the best results for the crush simulation. An alternate trigger geometry is investigated, consisting of a single row of elements having tapered thickness, which varies linearly from 0 to 0.079 in. (2 mm, the full thickness of the specimen). This trigger more closely resembles the geometry of the physical trigger. The tapered trigger has a slightly lower initial peak load than the constant-thickness trigger, however the global response and average crush load are nearly identical, Figure 94.

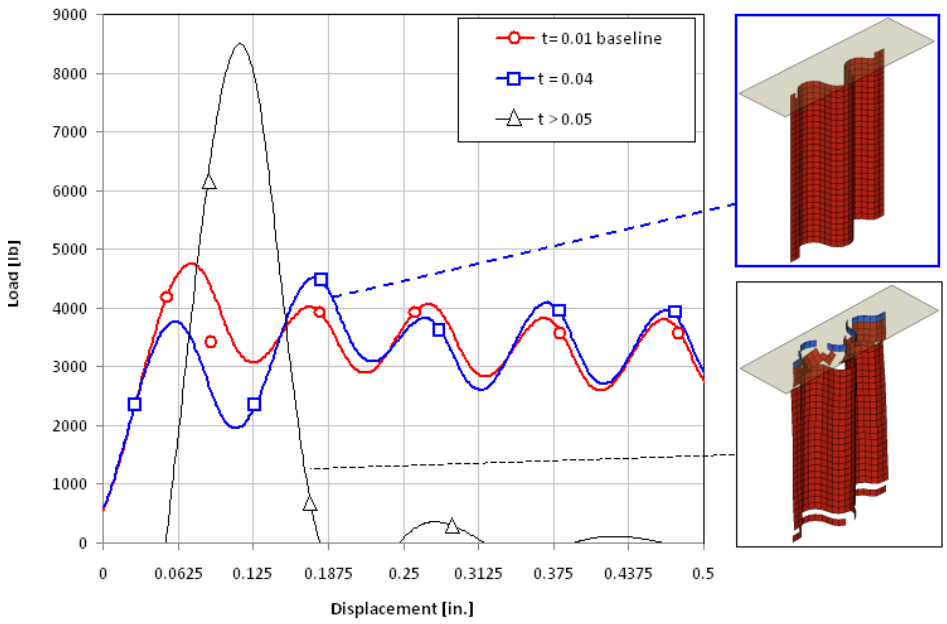

Figure 93. The effect of the trigger thickness on the initial peak load and stability of the load-displacement crush curve.

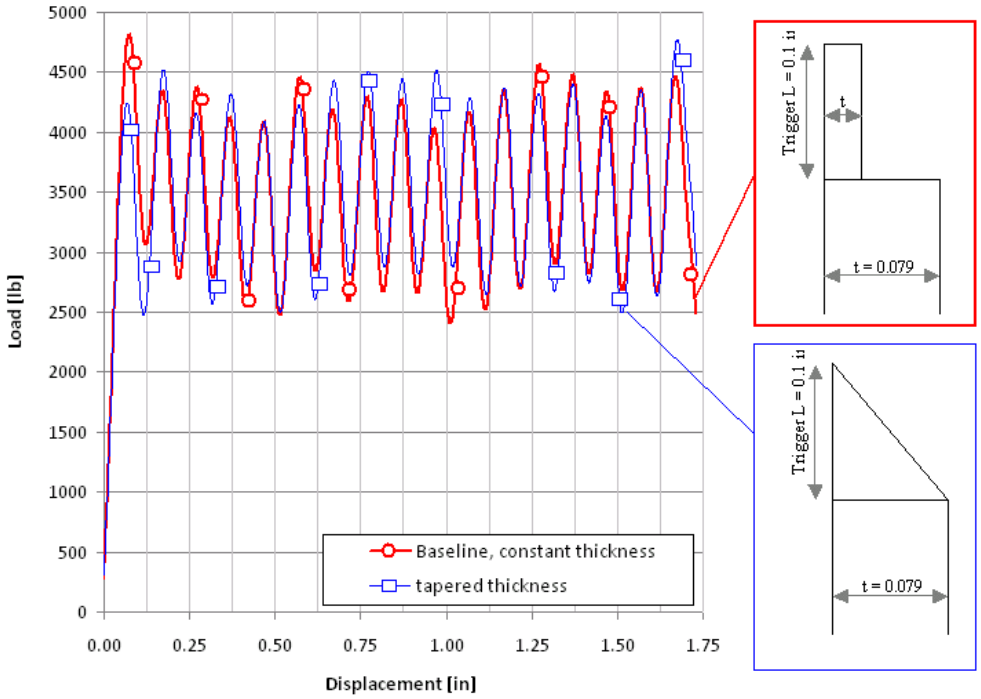

Figure 94. Two different crush trigger geometries, one of reduced constant thickness (baseline) and one with a tapered thickness (similar to the physical trigger) produce very similar results.

From the sensitivity studies performed, it becomes clear that there may be more than one way to obtain a "baseline" simulation. Mesh size and contact formulation have a dramatic effect on the simulation, and it is possible adjust these to obtain multiple baselines. Furthermore, for a given mesh size and contact formulation, it is possible to obtain a good match to the experimental data using multiple combinations of MAT54 parameters, in particular the SOFT parameter, XC and DFAILC, which have the most influence on the simulation results. The combinations of these parameters for five equivalent baseline simulations are summarized in Table 18. If DFAILC is reduced from the baseline value, the load-displacement curve tends to exhibit higher average crush load, Figure 80. However, if the SOFT parameter is reduced, the load-displacement curve tends to exhibit lower average crush load, Figure 82. If both are varied at the same time, the two effects counteract each other and the resulting load-displacement (baseline 2 in Figure 95) curve

matches the experimental one as well as original baseline 1 (Table 18). Similarly, if DFAILC and SOFT are simultaneously increased, the resulting load-displacement curve also matches the experimental data, baseline 3 in Figure 95 and Table 18. Similar trends can be obtained by varying XC and SOFT by a small amount, to obtain nearly identical crush load-displacement curves (baselines 4 and 5). Therefore, DFAILC, XC and SOFT can be adjusted simultaneously to yield multiple combinations that generate accurate results. It is therefore important to ensure that the correct experimental material properties are used, and that the analyst is fully aware of the sensitivity of the model to variations in these parameters.

Table 18. Summary of the numeric baselines for the unidirectional tape sinusoid crush element.

Baseline	Contact Type	LP Curve	Mesh size	SOFT	DFAILC	XC	SEA [J/g]	% Error
1	Entity	PCWL baseline	0.1	0.57	-0.0116	-213,000	64.12	-4.4 %
2				0.48	-0.0175	-213,000	67.32	+0.4 %
3				0.615	-0.0100	-213,000	67.80	+1.1 %
4				0.62	-0.0116	-200,000	66.39	-1.0%
5				0.54	-0.0116	-230,000	66.49	-0.9%

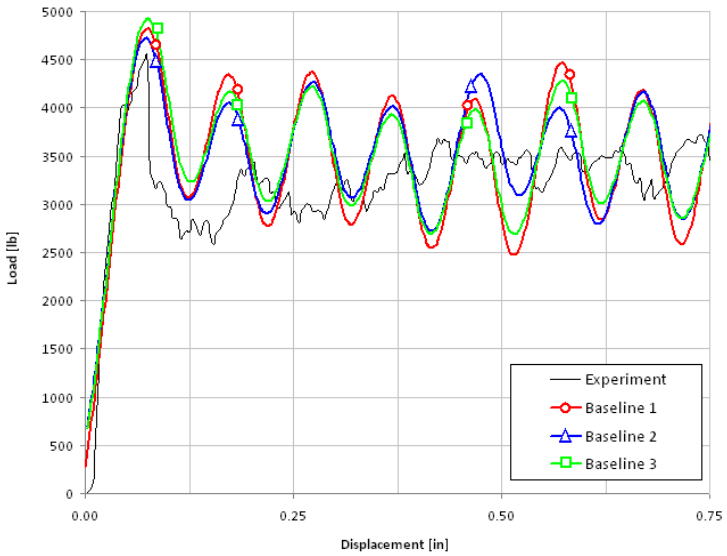

Figure 95. Multiple baselines (1 to 3 in Table 18) obtained by varying simultaneously DFAILC and SOFT.

Conclusions

Dynamic failure analysis is a complex effort that requires a deep understanding of the sensitivity of the model to input parameters. LS-DYNA material model MAT54 can be used to successfully simulate the behavior of a unidirectional tape composite material system applied to a sinusoidal crush element undergoing axial crushing. The model exhibits stable and progressive element failure and deletion, and is capable of capturing with accuracy the peak and average crush loads, as well as the overall load-displacement response. Through a sensitivity study, it has been shown that the fiber compression strength XC and strain-to-failure DFAILC are the primary material parameters leading to element failure and deletion, and each directly have a limited influence on the average crushing load response of the model. The SOFT crush front parameter, however, is the single most influential parameter for determining the success of the simulation. Through a careful calibration by trial-and-error, the right value for the SOFT parameter can be identified, but there is no way of determining it *a priori* or measuring it experimentally except to use the experimental crush curve to find the correct SOFT value. Furthermore, by adjusting the SOFT parameter in conjunction with XC or DFAILC, it is possible to obtain multiple combinations that yield similar simulation results, which match the experimental ones. Unlike SOFT, however, XC and DFAILC are both directly measured from material property testing, so changing their values to change the result of the crush simulation is cautioned against. Other complexities of the model discovered include the selection of the contact definition between the specimen and the crush plate (such as the contact type, load-penetration curve and trigger thickness), mesh size, and filtering scheme. For these reasons, this modeling approach is considered to be not truly predictive, and requires calibration against the crush element experiment using the building block approach before scaling up to higher levels of complexity.

Simulation of fabric sinusoid crush specimen

Following the development of the MAT54 model for the UD material system subjected to crush loading, the influence of the entire material model definition in a crush simulation is investigated. To do so, the material system modeled is changed from the UD to the fabric material system used in the experimental crush element investigation. The fundamental modeling definition developed for the semi-circular crush model in the previous section was maintained while only changing the fabric model. Two small upgrades from the original approach were made and applied retroactively to the UD baseline model. First, the LS-DYNA solver was updated from the single precision R4.2.1 to the double precision R5.1.1. This update did not change the simulation results, Figure 96a. This change was implemented since double precision solvers were found to be more stable for the MAT54 material model than single precision solvers, as demonstrated during the single element studies.

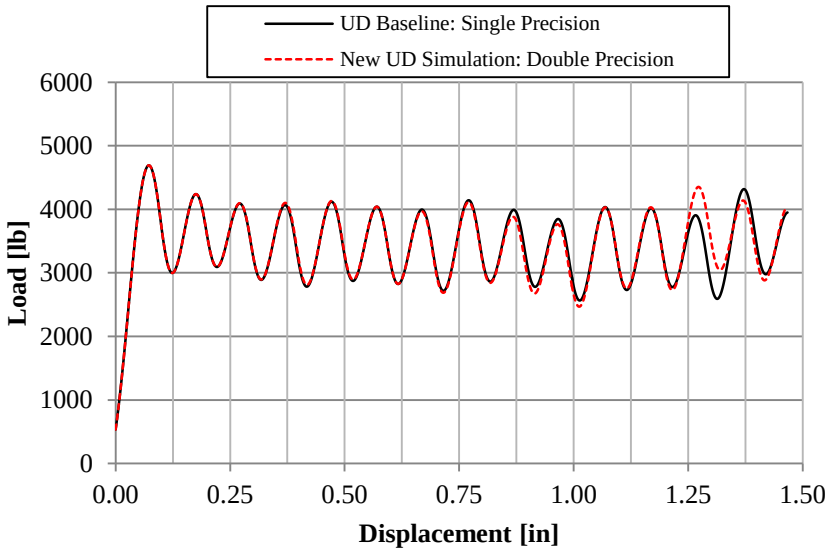

(a)

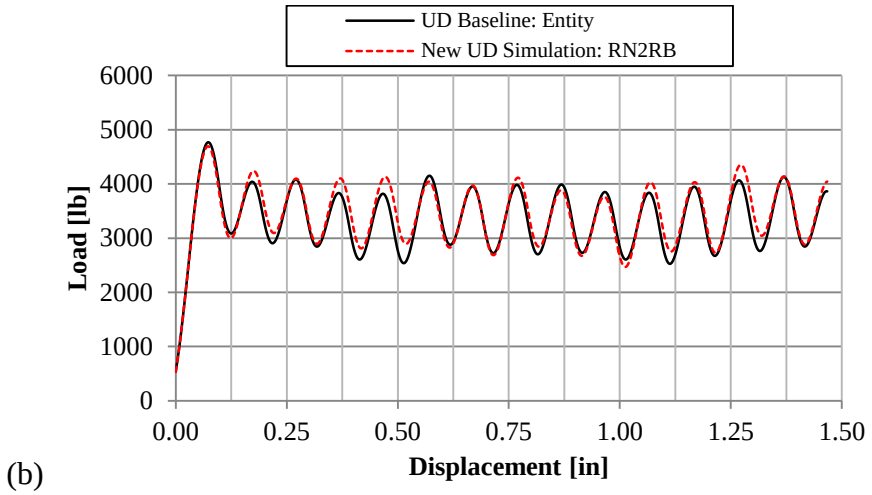

(b)

Figure 96. Load-displacement crush curves generated from changing the UD baseline by (a) using a double precision solver rather than single precision and (b) using the RN2RB contact rather than Entity.

Second, an alternate crush simulation baseline was developed which used the Rigid Nodes to Rigid Body (RN2RB) contact type instead of the Entity contact type. RN2RB uses a standard penalty formulation and a load-penetration (LP) curve to define the reaction forces at the contact just like Entity. Replacing Entity for RN2RB in the baseline UD simulation requires that only the thickness of the trigger row of elements be adjusted to produce stable and accurate results, Figure 96b. The trigger thickness in the RN2RB model directly affected the initial load of the crush curve, and allows direct calibration of the initial load peak by adjustment of the trigger thickness, as shown in Figure 97. The Entity contact type was not sensitive to changes in trigger thickness. All of the rest of the parametric trends observed when using Entity were also observed using RN2RB. For both the UD and the fabric material systems, both the Entity and the RN2RB contact types were simulated using the baseline MAT54 material deck. The baseline simulation considered for the extensive MAT54 parametric study, however, is that of the fabric material system using the RN2RB contact.

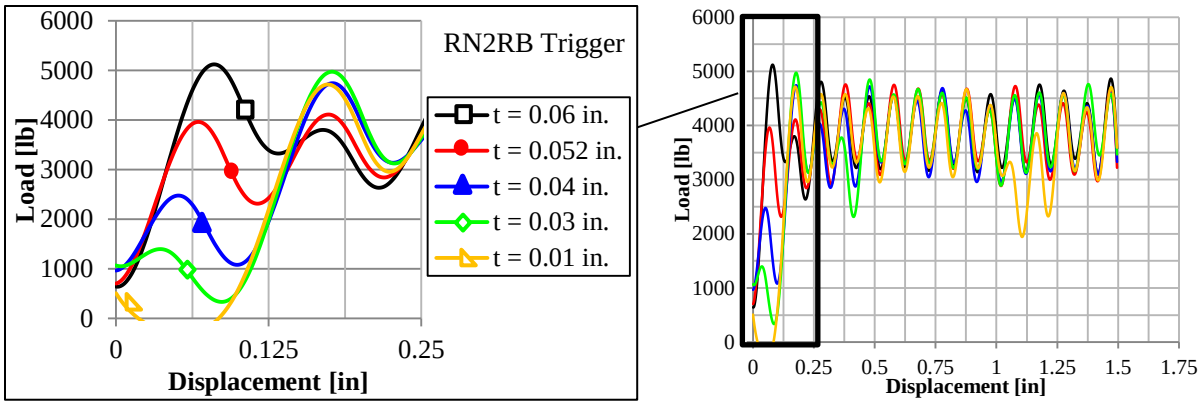

Figure 97. Effect of changing the trigger thickness on the initial load peak of the sinusoid crush curve when using the RN2RB contact type, which is different from the observed effect of the trigger thickness on the Entity contact type.

Generating the baseline fabric MAT54 model

The baseline MAT54 UD Entity crush model was modified to have the material properties and lay-up of the fabric laminate as given in Table 2. The baseline MAT54 input deck for the fabric material model is given in Figure 98, and the definition for each MAT54 input parameter is given in Table 24. The fabric model was identical to the UD model with respect to the appearance and mesh of the loading plate, composite sinusoid, and crush trigger, Figure 73. For the 8-ply fabric sinusoidal specimen, there were 8 integration points through the thickness of each element. The specimen was modeled with a total of 840 elements measuring 0.1 x 0.1 in. (2.54 x 2.54 mm) with a constant thickness of 0.07286 in. (1.85 mm) except at the trigger row, which for the Entity models is equal to 0.01 in. (0.254 mm), and for the RN2RB models equal to 0.052 in. (1.32 mm).

*MAT_054 (ENHANCED_COMPOSITE_DAMAGE)							
mid	**ro**	**ea**	**eb**	**ec**	**prba**	**prca**	**prcb**
1	1.50E-4	8.11E+6	7.89E+6	0.0	0.043	0.0	0.0
gab	**gbc**	**gca**	**kf**	**aopt**			
6.09E+5	6.09E+5	6.09E+5	0.0	0.0			
xp	**yp**	**zp**	**a1**	**a2**	**a3**	**mangle**	
0.0	0.0	0.0	0.0	0.0	0.0	0.000	
v1	**v2**	**v3**	**d1**	**d2**	**d3**	**dfailm**	**dfails**
0.0	0.0	0.0	0.0	0.0	0.0	0.06	0.03
tfail	**alph**	**soft**	**fbrt**	**ycfac**	**dfailt**	**dfailc**	**efs**
1.1530E-9	0.1	0.73	0.5	1.2	0.0164	-0.013	0.0
xc	**xt**	**yc**	**yt**	**sc**	**crit**	**beta**	
103000	132000	102000	112000	19000	54	0.5	

Figure 98. Baseline MAT54 input deck for the fabric material model with DFAILM and SOFT values calibrated to generate a good match with the crush experiment of the sinusoid.

By simply changing the material properties and stacking sequence to those of the fabric laminate, an unstable crush curve with a low average crush load was generated, Figure 99. The SEA of the simulated sinusoid crush had an error of -32% from the experiment. The MAT54 SOFT parameter was recalibrated, from 0.57 to 0.72, in order to increase the crushing load. The resulting crush curve exhibited a higher average crush load but was very unstable, Figure 100. To stabilize the fabric model, DFAILM was raised from 0.0141 in/in to 0.06 in/in. The resulting model was the baseline fabric Entity model, which crushed in a stable manner and simulated the experiment well except at the initial load peak.

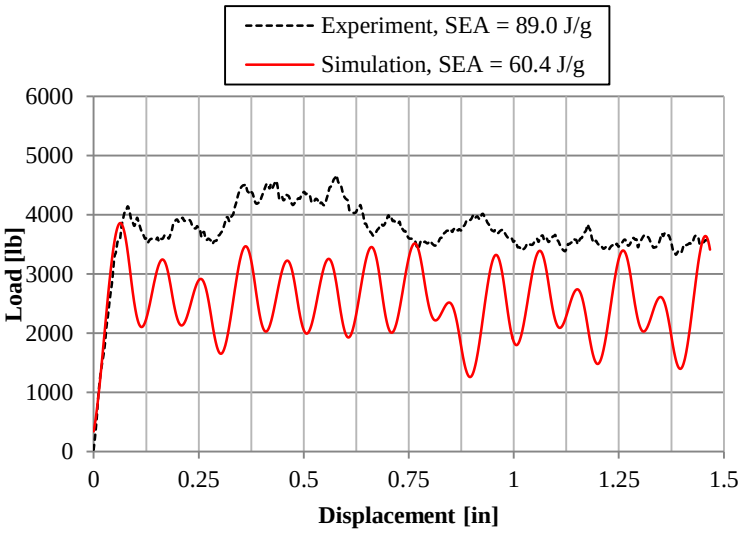

Figure 99. Load-displacement crush curve from replacing the UD material system in the baseline simulation with the fabric material system without further adjustments.

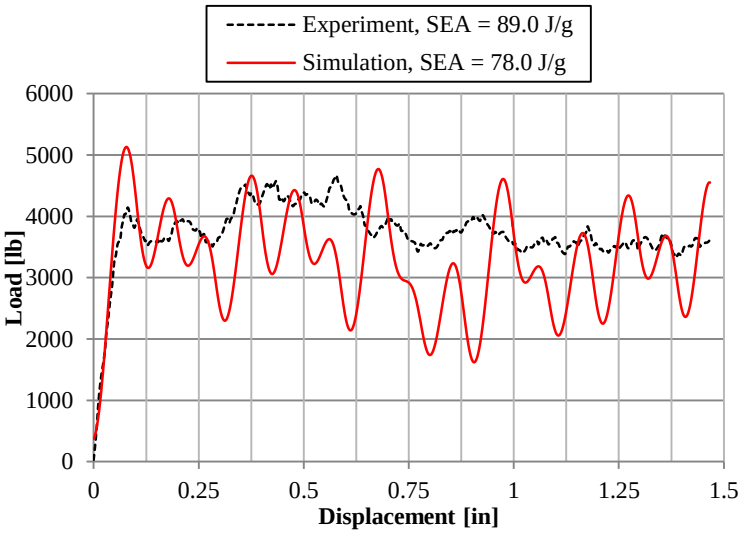

Figure 100. Load-displacement crush curve from calibrating SOFT parameter in simulation shown in Figure 99.

The raw and filtered load-displacement data generated by the model are shown in Figure 101a, while the filtered data is compared against the experimental data in Figure 101b. The raw data is collected at the fixed boundary condition at the end of the fabric sinusoid crush element opposite of the loading plate rather than at the loading plate itself as it was in the simulation of the UD

sinusoid crush element, Figure 75, and for this reason the two sets of raw data appear very different. This change was made to better represent the forces being transmitted into the crush specimen, and only affects the raw data as the filtered data remains the same regardless of which end of the crush element it is collected from. The SEA-displacement plot of the simulation showed a poor match of the initial load peak when compared with the experimental data, Figure 101c, and there is significant error in SEA during the first 0.5 in. of displacement. The crushing SEA of the fabric Entity baseline was 90.2 J/g which had an error of +0.1% from the experiment. Solution time took 84 s using a workstation with 2.26 GHz dual Quadcore 64-bit computer.

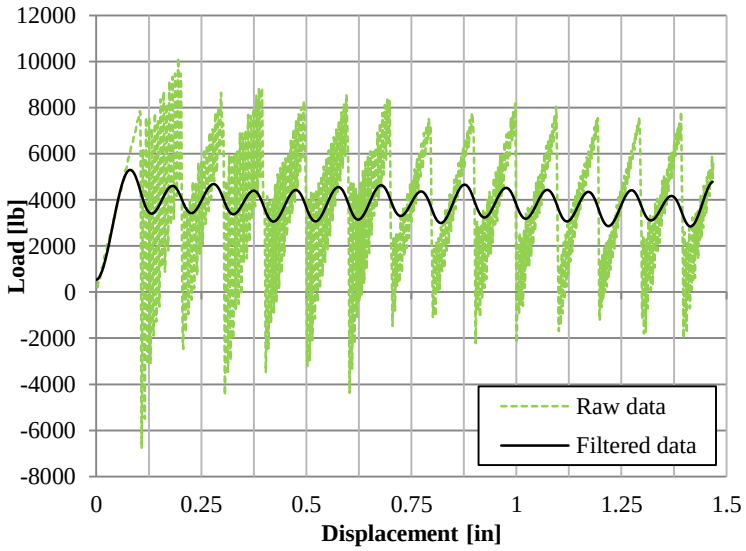

(a)

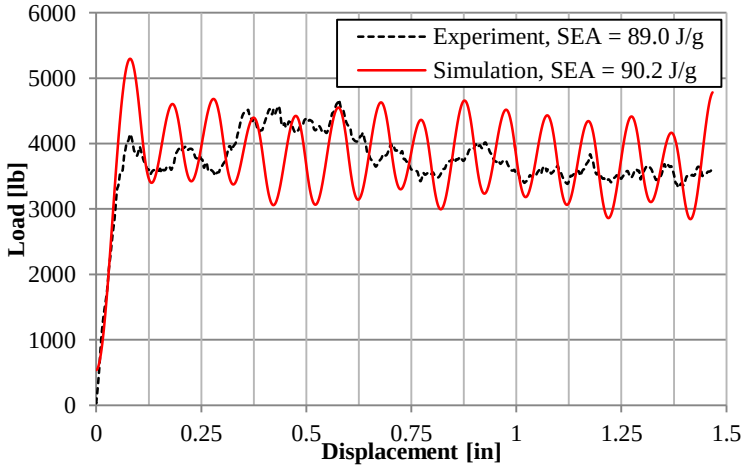

(b)

(c)

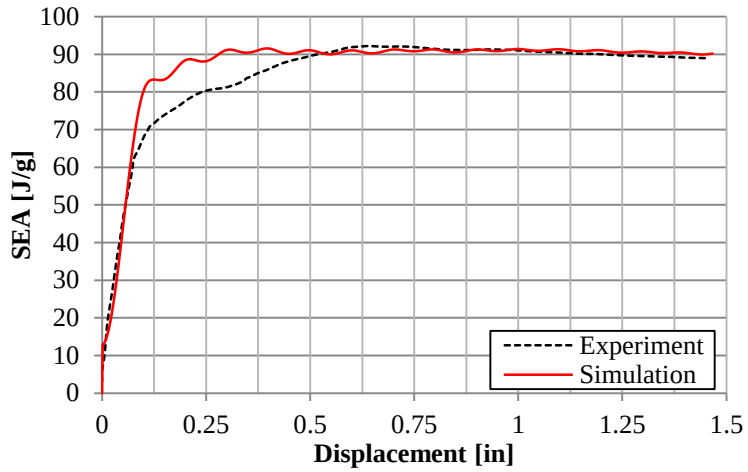

Figure 101. Baseline simulation for the fabric sinusoid crush using Entity (a) raw and filtered load-displacement curve, and (b) load and (c) specific energy absorption compared with the experiment.

To generate the baseline RN2RB fabric sinusoid simulation, only the material properties and lay-up of the UD RN2RB baseline were changed to simulate the fabric laminate. Without changing any other parameters, the resulting simulation captured the initial peak load but had a low average crush load, Figure 102. In order to raise the load, the SOFT was recalibrated from 0.57 to 0.73, from which a very unstable simulation resulted, Figure 103. DFAILM was raised to 0.06 in/in to stabilize the model and the resulting simulation was the fabric RN2RB baseline simulation. The raw and filtered load-displacement data generated by the model are shown in Figure 104a. The crush and SEA-displacement curves match the experiment very well, Figure 104b-c. The SEA of the RN2RB fabric baseline simulation was 88.90 J/g, yielding an error of -0.1% from the experiment. Solution time for this model took 75 s.

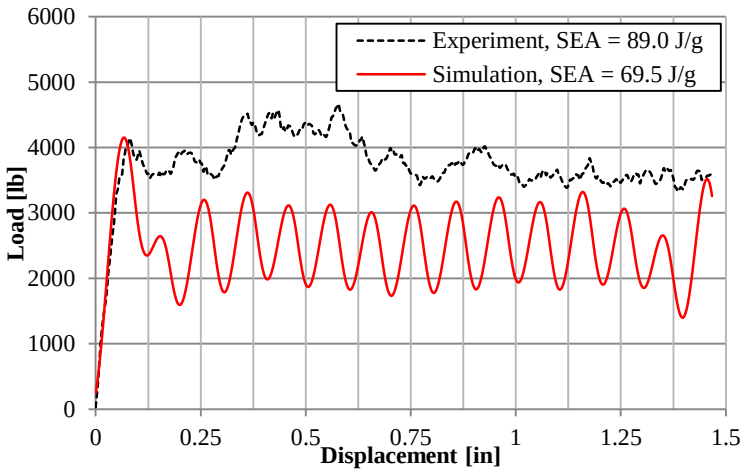

Figure 102. Load-displacement crush curve generated from replacing the UD RN2RB baseline simulation with the fabric material system without further adjustments.

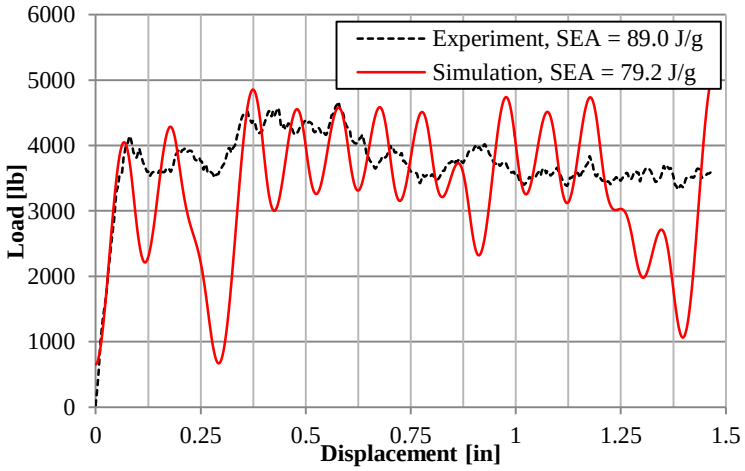

Figure 103. Load-displacement crush curve from calibrating SOFT parameter in simulation shown in Figure 102.

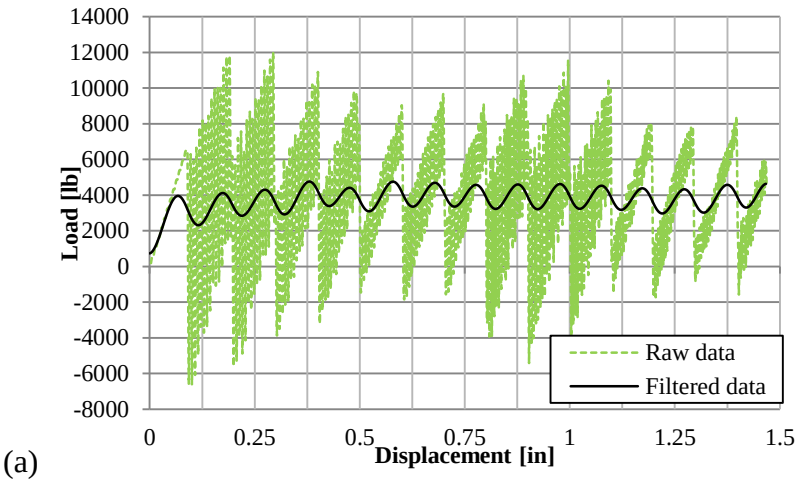

(a)

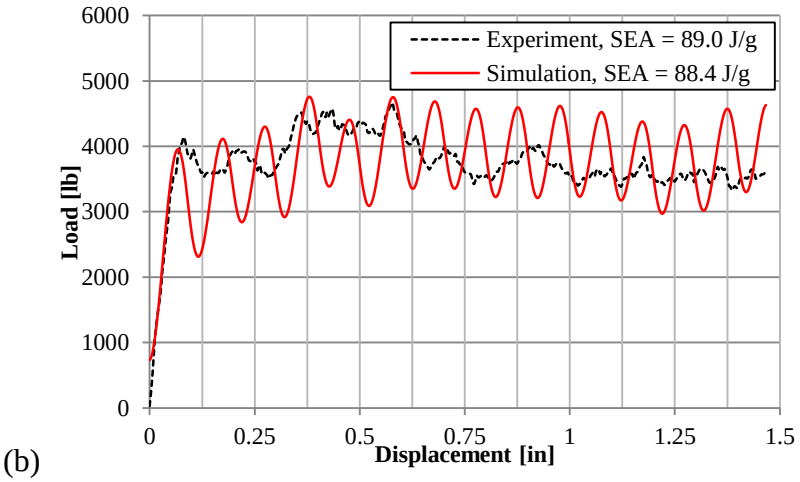

(b)

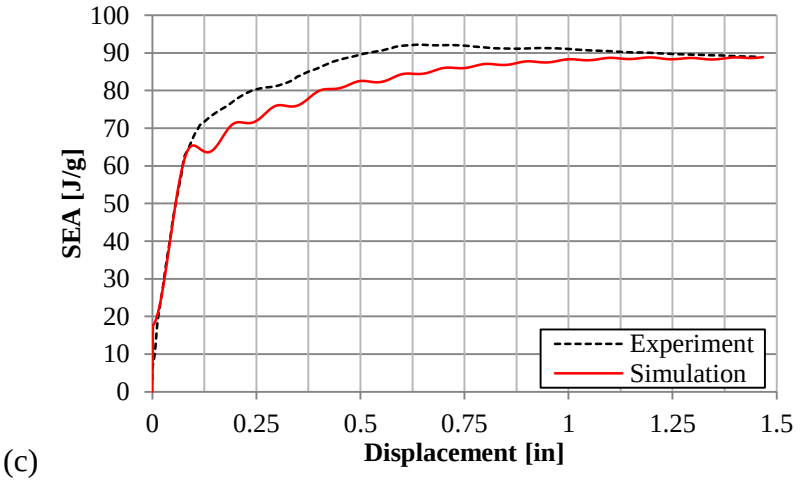

(c)

Figure 104. Baseline simulation for the fabric sinusoid crush element using RN2RB (a) raw and filtered load-displacement curve, and (b) load and (c) specific energy absorption compared with the experiment.

Since the transverse failure strain was modified for the fabric material system in simulations using both contact types, the nominal transverse material properties shown in Figure 15b no longer accurately represent the MAT54 model defined in the baseline simulations. The adjusted material property stress-strain curves used in the baseline fabric MAT54 material model are shown in Figure 105, which illustrates that the curves in the axial and transverse directions are no longer similar and that the failure strain in the transverse direction is significantly greater.

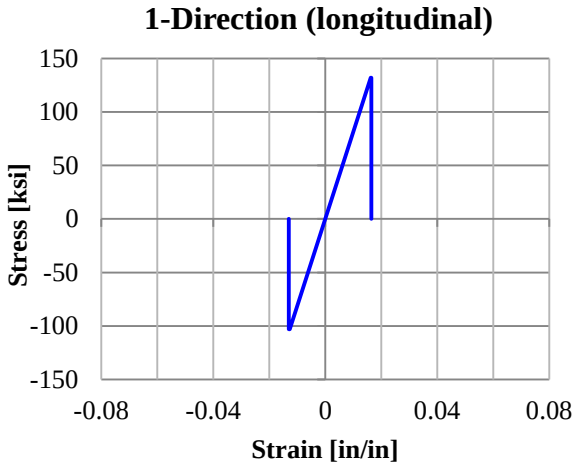

(a)

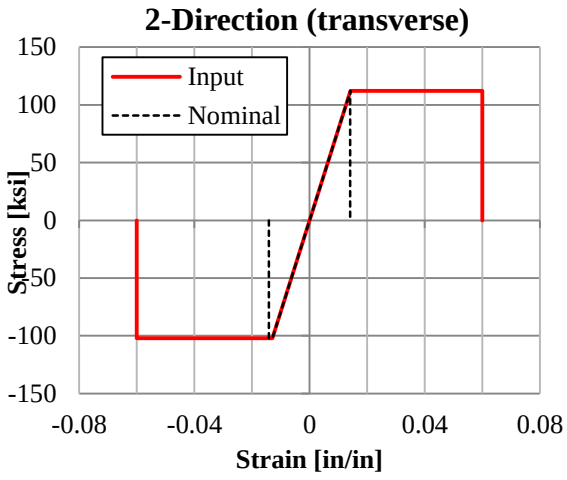

(b)

Figure 105. Stress-strain curve inputs of the material model MAT54 for the baseline fabric crush models.

Four baseline sinusoid crush simulations using MAT54 to model both a UD tape and a fabric material system have been successfully generated using two different contact types with minimal adjustments necessary between them. For this specific material system, to modify a UD model to simulate a fabric, the SOFT and DFAILM parameters must be recalibrated, both increasing in value for the fabric material system. To change the contact definition from Entity and RN2RB contact types, only the trigger thickness must be recalibrated. The adjustments necessary to model the four baseline sinusoidal crush simulations using the AGATE material system are summarized in Figure 106. The MAT54 parametric study for the fabric material system used only the RN2RB contact type.

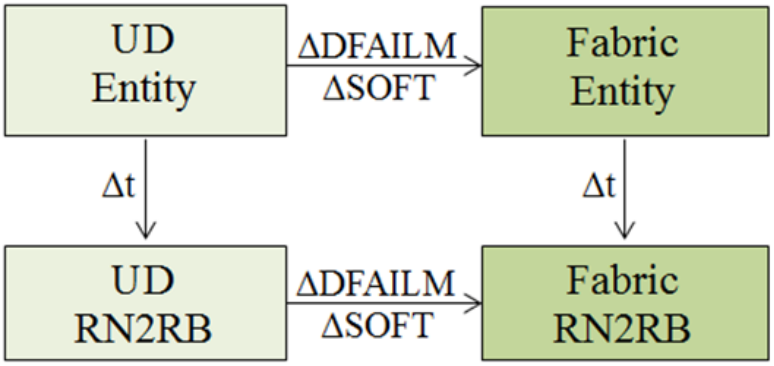

Figure 106. Summary of the parametric changes necessary to model the four UD and fabric sinusoid crush baselines using either the Entity or RN2RB contact type.

Sensitivity of the fabric MAT54 model to material properties

An effective material model needs to be sufficiently robust to tolerate small variations in material property input data, in order to accommodate for small errors in measured strength and stiffness. Yet, it should also be sensitive enough to capture different behaviors for different input material properties. The sensitivity of the model to variations in strengths (XT, XC, YT, YC, and SC)

and strains-to-failure (DFAILT, DFAILC, DFAILM, and DFAILS) is discussed in this section of the paper. A summary of the parametric study performed on the fabric material model is given in Table 19. The comparison between the capability of MAT54 to model a UD versus a fabric material system with regards to these parametric changes will also be discussed.

Table 19. Summary of the parametric studies performed on the fabric material model (units not shown for clarity).

Parameter	Baseline Value	Parametric Variation	Figure
MAT54: XT	132000	50000, 100000, 2500000	-
MAT54: XC	-103000	-50000, -75000, -90000, -95000, -105000, -150000	Figure 107
MAT54: SC	19000	10000, 12000, 13000, 25000	Figure 108
MAT54: YT	112000	5000, 50000, 75000, 150000	Figure 109
MAT54: YC	-102000	-5000, -30000, -50000, -75000, -90000, -120000, -130000, -140000, -150000, -200000	Figure 110
MAT54: DFAILT	0.0164	0, 0.01, 0.011, 0.02, 0.05	-
MAT54: DFAILC	-0.013	-0.011, -0.012, -0.025, -0.03, -0.05	Figure 111
MAT54: DFAILM	0.06	0, 0.01, 0.014, 0.0141, 0.025, 0.027, 0.028, 0.03, 0.035, 0.038, 0.04, 0.05	Figure 112
MAT54: DFAILS	0.03	0.005, 0.015, 0.02, 0.05	Figure 113
MAT54: ALPH	0.1	0, 1.0E-14, 0.3, 1.0	-
MAT54: BETA	0.5	0, 0.01, 0.05, 0.1, 1.0	Figure 114
MAT54: FBRT	0.5	0, 0.1, 0.95, 1	-
MAT54: YCFAC	1.2	0, 0.25, 0.5, 0.75, 1.0	Figure 115
MAT54: SOFT	0.73	0.3, 0.5, 0.57, 0.6, 0.72, 0.8	Figure 116
Crush Speed	150	1.5, 15, 50	Figure 117
Contact Load-Penetration Curve	PCWL	PCWL Stiff, PCWL Soft, PCWL Soft 2, Linear	Figure 118-Figure 119
Mesh Size	0.1	0.05, 0.15, 0.2	Figure 120-Figure 121
Trigger Thickness	0.052	0.01, 0.03, 0.04, 0.06	Figure 97

Varying the fiber tensile strength XT above or below the baseline value did not affect the outcome of the simulation, except for cases where XT was particularly low like XT $\leq$ 50 ksi. As was the case for the UD material system, the axial tensile strength does not appear to be a

primary failure driver for the given specimen geometry-material combination. The axial compressive strength XC directly influenced the average crush load for the fabric model, as it did for the UD model. Small increments in XC (making it less negative) significantly lowered the average crush load, and slight decreases in XC (making it more negative) significantly raised the average crush load. This was true within an envelope of stable values, beyond which the model became unstable, Figure 107. Finally, the influence of the shear strength parameter, SC, was not strong. Increasing SC did not affect results, but decreasing it by 32% to 10 ksi causes the model to mildly destabilize, Figure 108. Low values of SC such as this are not realistically within the boundaries of experimental error when measuring shear strength. SC is therefore not considered a sensitive MAT54 parameter for the fabric material, unlike the UD material model where smaller changes in SC caused great instability. The fabric model appeared to be more robust to changes in SC than the UD model.

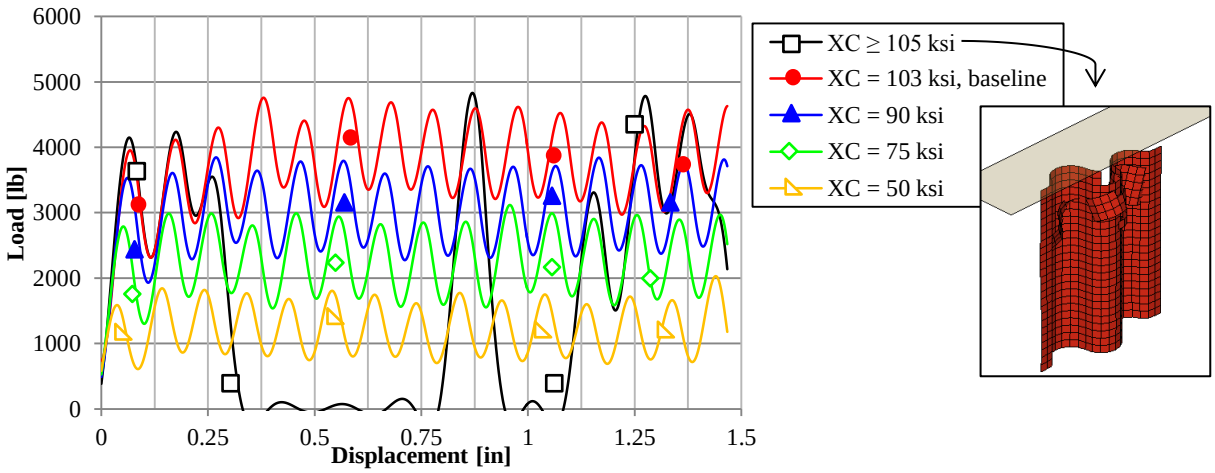

Figure 107. Effect of varying compression strength XC on the baseline fabric sinusoid model, showing that small changes in XC result in large changes in the simulation.

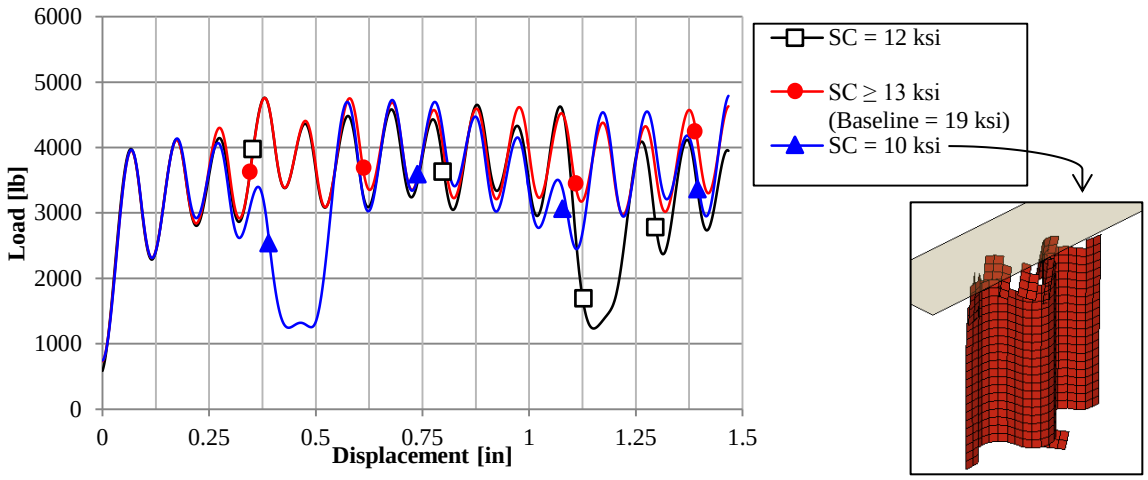

Figure 108. Effect of varying shear strength SC on the baseline fabric sinusoid model showing that particularly smaller values destabilize the crush load-displacement curve.

Raising the tensile transverse strength parameter YT did not affect the crush model, but low values near 5 ksi caused early failure and a great reduction of load in the crush curve, Figure 109. This low magnitude of tensile strength is not feasible for a fabric material and YT is not a significant parameter for the fabric material model. The compressive transverse strength, however, had a great effect on the stability of the fabric crush model. Only values of YC within a certain range produced stable results, Figure 110. The baseline fabric YC value lies within the stable range of 90 to 130 ksi, however this stable range is slim. The YC parameter appears only in the compressive matrix failure criterion, Equation 28, which is the only failure criterion in MAT54 designed specifically to simulate a matrix material. This failure criterion is not appropriate for a fabric material system, and as such it was not expected that transverse compressive failure would be properly simulated. While for this particular fabric material system the baseline YC value worked well, it may be acceptable to adjust this parameter had it not produced stable results when a fabric material system is being modeled. This cannot be said about the other strength parameters since the other failure criteria, Equations 25-27, are appropriate for fiber-dominated laminates such as the fabric material system.

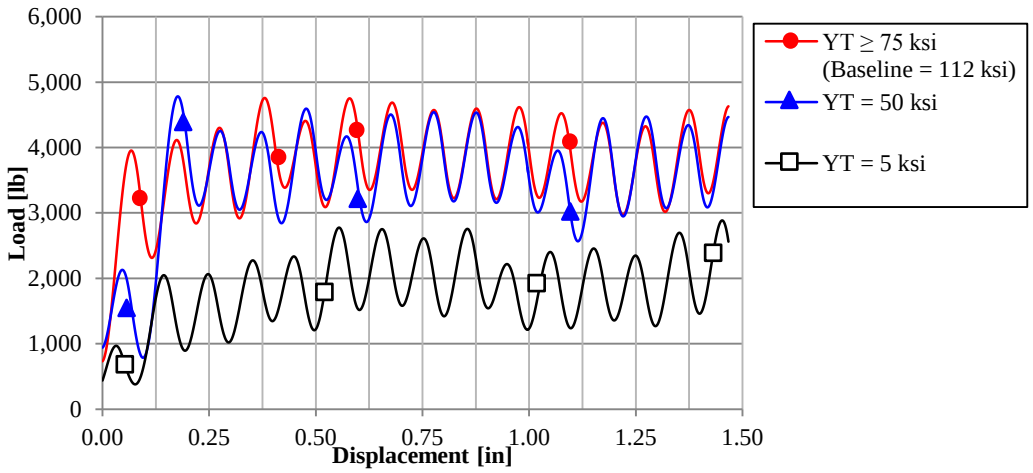

Figure 109. Effect of varying transverse tensile strength YT on the baseline fabric sinusoid model showing that very small values lower the crush load-displacement curve.

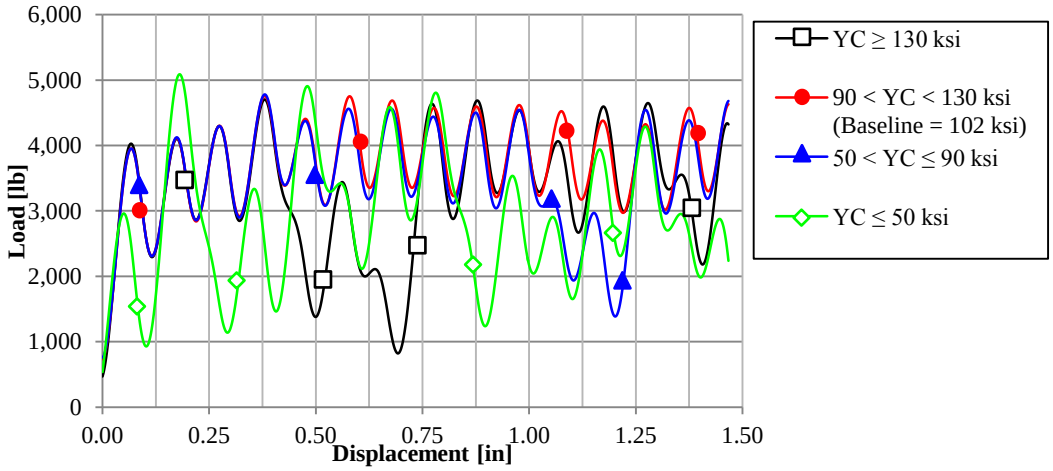

Figure 110. Effect of varying transverse compressive strength YC on the baseline fabric sinusoid model showing its effect on the overall stability of the crush load-displacement curve.

Changes of the tensile strain-to-failure in the axial direction, DFAILT, were inconsequential for both the UD and fabric crush simulations, which allowed for a virtual plasticity in the positive axial direction that did not affect the simulation. Changes in the compressive strain-to-failure in the axial direction, DFAILC, greatly affected the average crush load, Figure 111. The upper bound of DFAILC at which the fabric crush simulation became unstable was only 15% higher than the baseline value which does not leave sufficient room for experimental error.

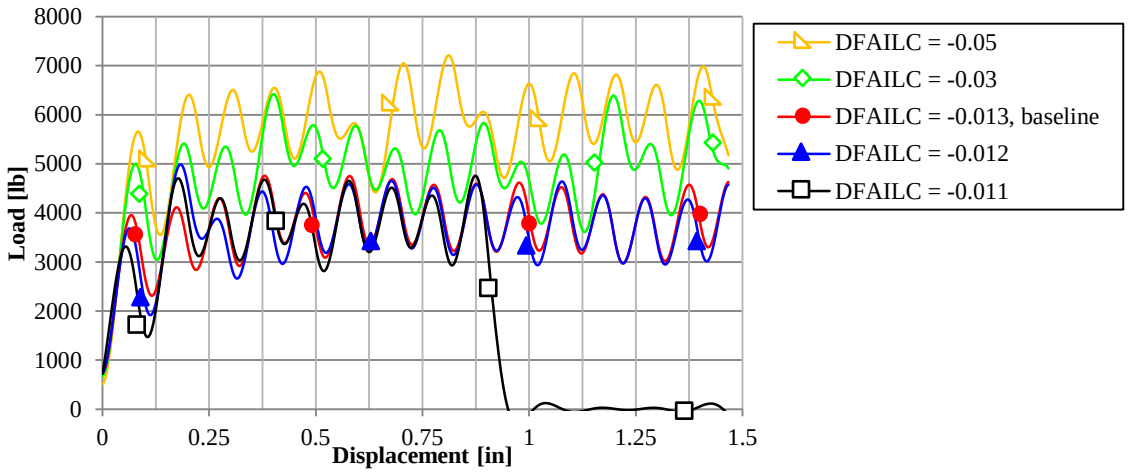

Figure 111. Effect of varying the axial compressive strain-to-failure DFAILC on the baseline fabric sinusoid model showing that small changes can lead to greater loads and less stability.

Changes to the transverse strain-to-failure, DFAILM, caused instabilities in both the UD and fabric models. For the fabric, the nominal DFAILM was too small and caused instabilities, Figure 112. The baseline simulation featured a much larger DFAILM value and a virtual plasticity in the transverse direction which was necessary for stability. Lower values of DFAILM allow for stable results, as low as 0.028 in/in, however the model was only conditionally stable and often destabilized with other parametric changes. For this reason, a large amount of virtual plasticity was added to the baseline simulation.

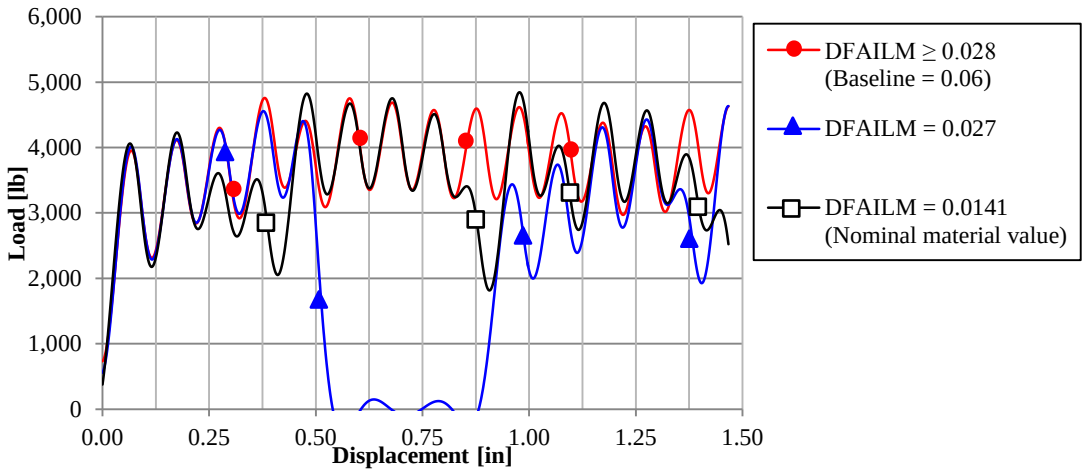

Figure 112. Effect of varying the transverse strain-to-failure DFAILM on the baseline fabric sinusoid model showing that an enlarged value is necessary for stability.

The shear strain-to-failure, DFAILS, was one parameter which exhibited very different behavior between the UD and the fabric crush simulations. While varying DFAILS by any amount in the UD material model had no effect on the results, lowering DFAILS by more than 30% destabilized the fabric crush model, Figure 113. The low DFAILS values which destabilized the model are not physically significant, however, as it is often recommended to assume a shear failure strain value of 3-5% for a carbon fiber-epoxy composite material model [1] [81].

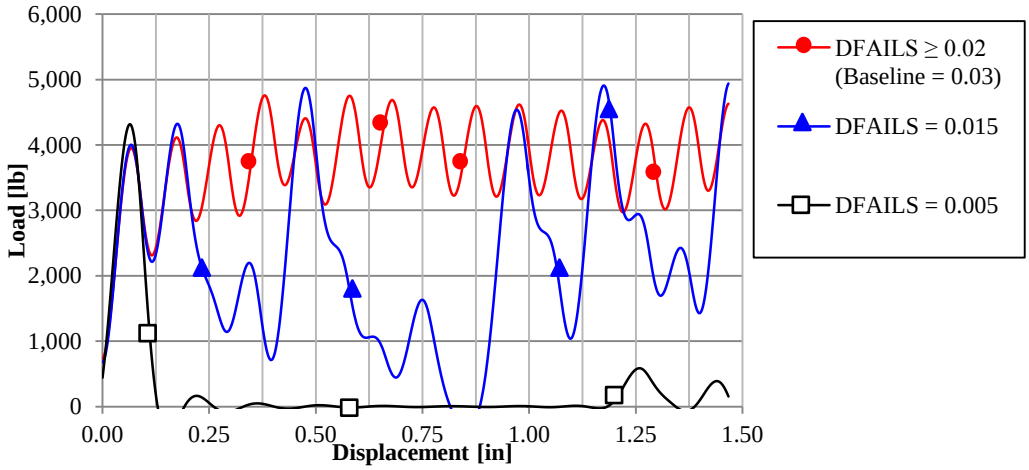

Figure 113. Effect of varying the shear strain-to-failure DFAILS on the baseline fabric sinusoid model showing its significant impact on the stability of the model.

Sensitivity of the fabric MAT54 model to other model-specific parameters

This section focuses on the effect of parameters that are specific to the MAT54 material model, and that are necessary for the simulation to run. These parameters either have no immediate physical significance or cannot be measured experimentally and hence have to be calibrated by trial and error. These quantities include the ALPH, BETA, FBRT, YCFAC, and SOFT parameters.

Parametric changes to the shear stress weighing factors, ALPH and BETA, did not influence the results of either the UD or fabric material models, except for very low values of BETA. While the UD material model was completely independent from changes in BETA, the fabric material can successfully be modeled using any value of BETA above 0.05, Figure 114. This indicates that the Maximum Stress failure criterion (BETA = 0) for the tensile axial mode, Equation 25, cannot be used and that at least some shear stress is necessary to prevent the axial tensile failure from being the dominant mode when modeling the fabric material system. This was not the case for the UD material system.

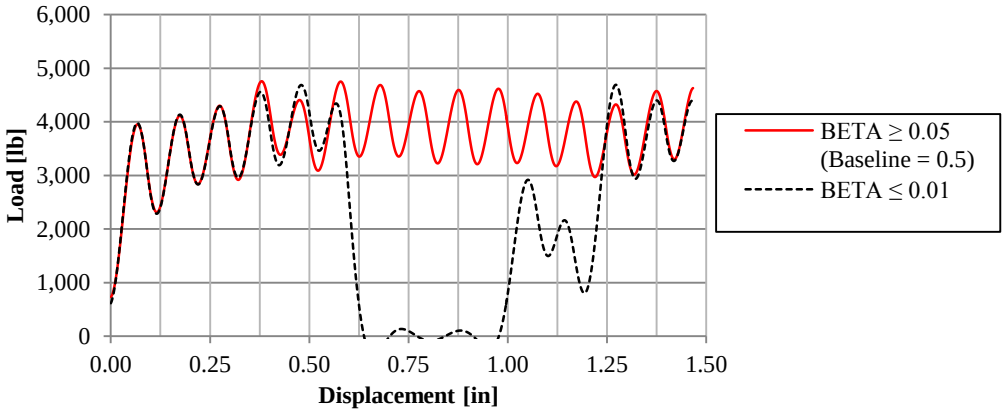

Figure 114. Effect of using very low values of BETA on the baseline fabric sinusoid model.

Both the FBRT and YCFAC terms are fiber strength reduction factors (for XT and XC respectively) used to degrade the fiber strength properties of the element following the first-ply (transverse, matrix) failure. Parametric changes of the FBRT parameter do not affect the simulation results for both the UD and fabric material models. While the YCFAC parameter was not an influence for the UD material system, YCFAC is important for crushing stability of the fabric model, Figure 115. This suggests that there is transverse damage occurring in the fabric elements which activates YCFAC in order to reduce the effective compressive fiber strength, XC. Greater reductions in XC following damage (i.e. lower values of YCFAC) cause instabilities as crush front elements are deleted at a lower stress threshold.

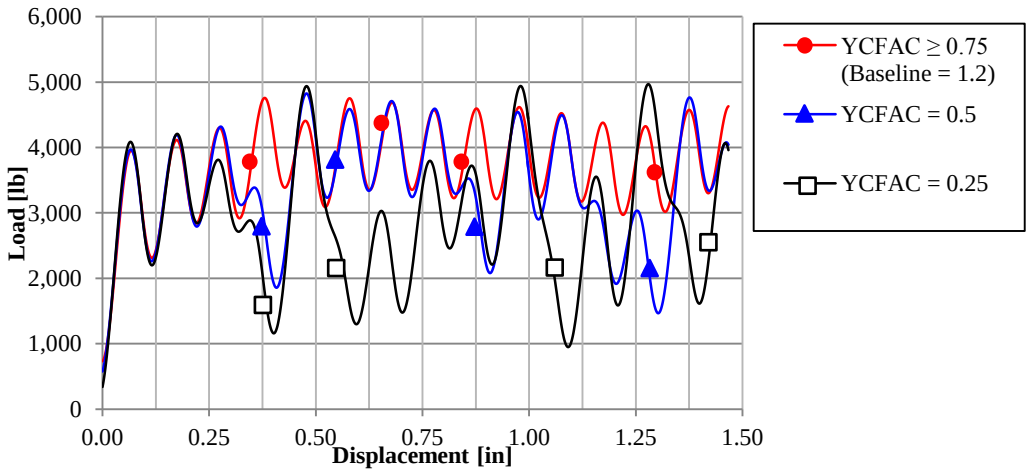

Figure 115. Effect of varying the transverse compressive strength knock-down factor, YCFAC, on the baseline fabric sinusoid model showing its influence on crush stability.

The UD parametric study found the SOFT parameter to be the most influential MAT54 parameter for crush simulations. The purpose of the SOFT parameter is to artificially reduce the strength of the elements immediately ahead of an active crush front. In the physical world one could interpret the SOFT parameter as a damage zone (comprised of delaminations and cracks) ahead of the crush front that reduces the strength of the material. By itself, the SOFT was

capable of dictating whether the simulation was stable or unstable. It could also shift the average crush load above or below the baseline by at least 40% from the baseline value of 88.90 J/g (for SOFT = 0.72), as shown in Figure 116. The SOFT value could not be increased much larger than the baseline value, and for SOFT = 0.8 the simulated sinusoid buckled during crushing. Lowering the SOFT parameter had the effect of lowering the average crush load and SEA value of the simulation. For SOFT = 0.5, SEA = 51.77 J/g (-42%), and it could go even lower for lower values of SOFT. Determining the correct value of the SOFT parameter is a challenging task, since it cannot be measured experimentally, but it has to be found by trial and error until the load–displacement curve of the simulation matches the experimental result. Unless the right value of the SOFT parameter is found and utilized, it is not possible to obtain a successful simulation. The most important consequence of this observation is that the MAT54 material model is not a true predictive tool since the SOFT parameter needs to be calibrated to the experiment.

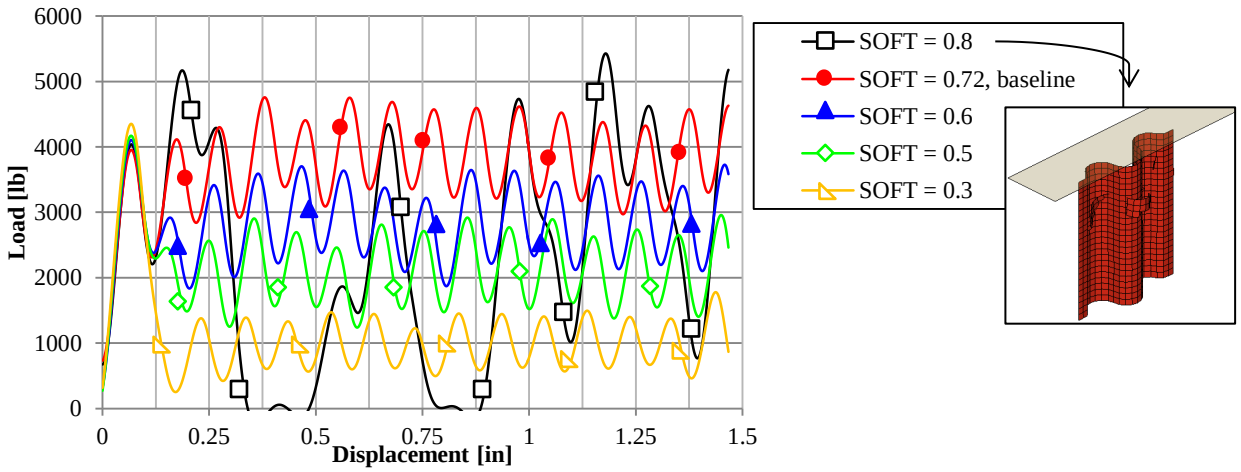

Figure 116. Effect of varying the SOFT crush-front parameter on the baseline fabric sinusoid model showing its strong influence on the results of the crush load-displacement curve.

Sensitivity of the fabric MAT54 material model to other model parameters

In this section, the influence of parameters that are not specific to the material model itself but are particularly influential for the execution of the simulation is discussed. These include crush velocity, the load-penetration (LP) curve of the contact definition, the mesh size, and the trigger element thickness. The effect of the trigger thickness on the sinusoidal crush model using the RN2RB contact type has already been shown in Figure 97. In the case of the Entity contact, the trigger thickness did not significantly affect the simulation, as demonstrated in the UD model.

Although the true experimental crush loading rate was 1.0 in./min. (25.4 mm/min), simulations were performed using a crush velocity of 150 in./s (3810 mm/s) due to computational limitations. Since all material properties were measured with quasi-static tests, no strain-rate dependent material properties were defined in the material deck, hence the material model cannot assume strain-rate behavior. Nonetheless, inertial effects may arise, which could lead to different global response for the specimen. To verify the validity of the assumption, three simulations were carried out at simulation speeds of 50 in./s (1270 mm/s), 15 in./s. (381 mm/s) and 1.5 in./s (38 mm/s) which are well below any dynamic threshold reported in the literature [16] [15] [97]. These simulations have runtimes of 230 s, 29 min, and 4 hr 48 min respectively, and are less practical to use with the available computational power. Reducing the crush velocity did not significantly change the results from the baseline simulation except for a slight change at the initial load peak, Figure 117. The trigger thickness could be recalibrated to achieve better matching results at initiation.

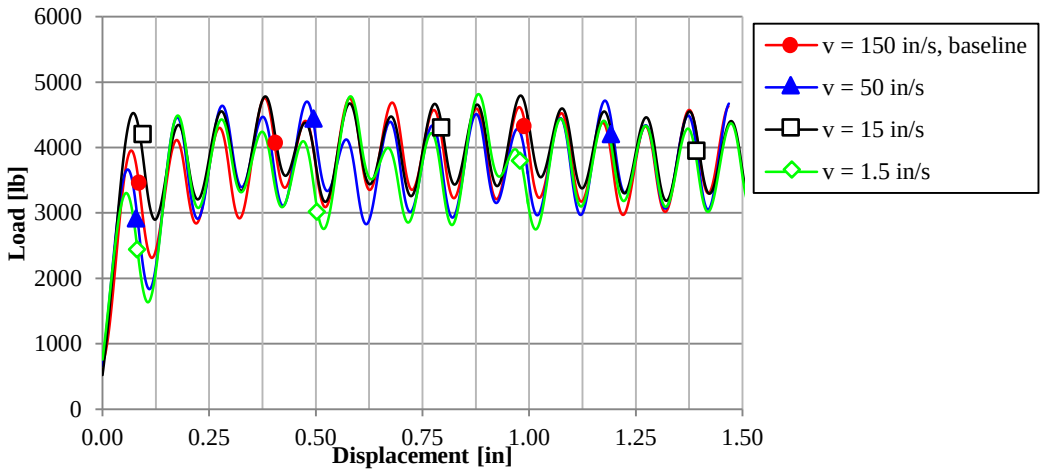

Figure 117. Effect of varying loading velocity on the baseline fabric sinusoid simulation.

The LP curve defines the reaction forces at the contact interface for both the Entity and RN2RB contact types. Such a curve is necessary in the contact definition when using the MAT54 material model. Varying the LP curve has an important effect on the stability of the model, yet there is no way of knowing *a priori* or determining experimentally the correct shape this curve needs to have for the specific material/geometry/loading combination. Four LP curves which differ from the baseline piecewise linear (PCWL) curve were used to study the effect of the LP curve, Figure 118a. The baseline LP curve introduced the load in a gradual fashion into the coupon, the stiff LP curve introduced the load into the coupon more suddenly, and the two soft LP curves introduced the load more gradually. The fourth LP curve was linear, and introduced the load into the coupon quickly. Without changing any other parameters, many of the alternative LP curves introduced instabilities and caused global buckling of the sinusoid element, Figure 118b. In some cases, buckling results from the greater forces acting at the contact, such as with the stiff and linear LP curves, while in the case of the Soft 2 LP curve the forces at the contact surface are not introduced quickly enough and the contact interface is allowed to fully pass through the element in contact, and stable crushing cannot be properly established. As was

done in the parametric study of LP curves in the UD sinusoid crush element, the SOFT parameter is recalibrated for unstable simulations to enable stability, and the stabilized LP parametric results agree with those discovered and explained in the UD study, Figure 119.

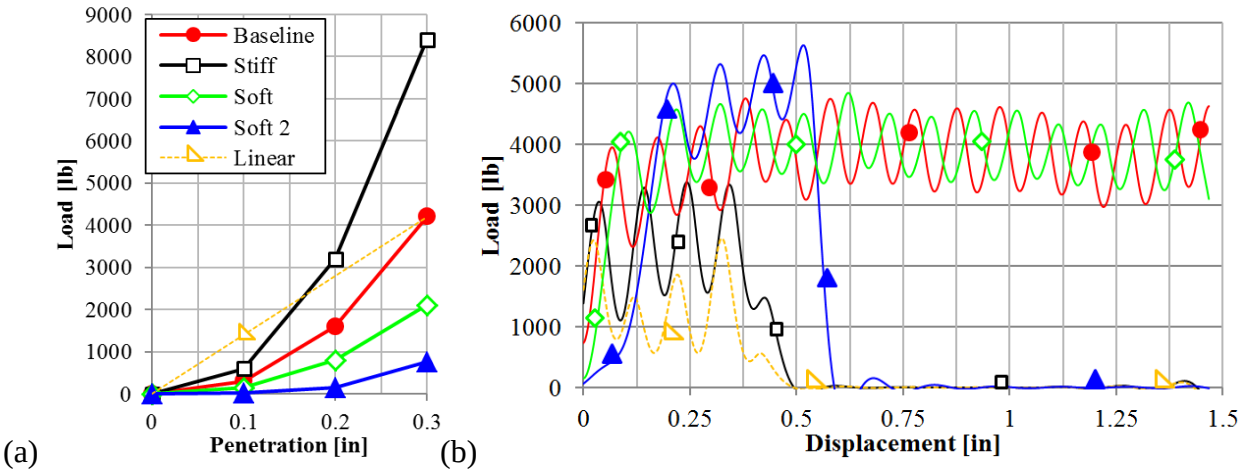

Figure 118. (a) Five different load-penetration curves investigated in the contact definition and (b) their influence on the fabric sinusoid crush simulation load-displacement curves.

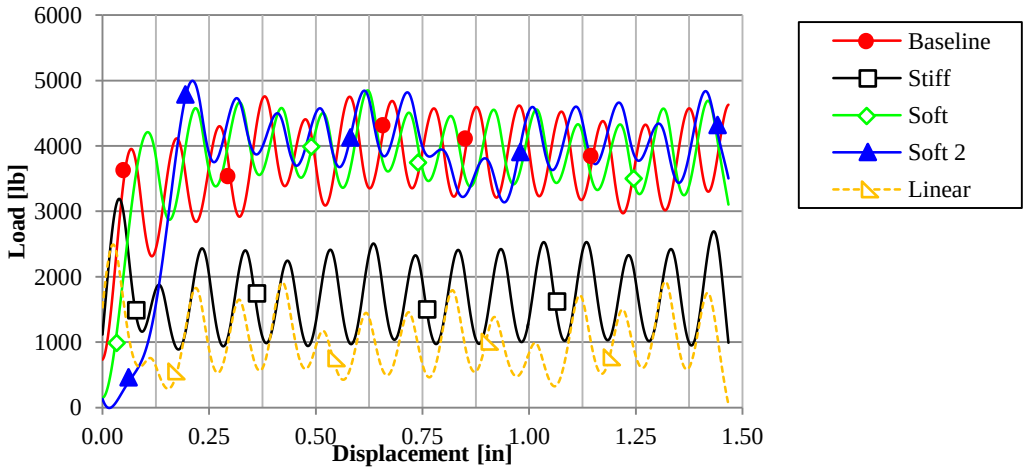

Figure 119. Effect on the baseline fabric sinusoid model load-displacement crush curve using various LP curves and recalibrating the SOFT parameter to provide stability.

Explicit FEA codes are known to be particularly mesh-sensitive, and while it is desirable to always use the finest mesh size, computational costs become particularly demanding. The

sinusoidal geometry used in this crush study was shown to be incompatible with mesh sizes larger than the baseline size of 0.1 in. (2.54 mm). The mesh size was therefore only varied by reducing it to 0.05 in. (1.27 mm) for the parametric study. The run time for the finer mesh was 17 min 42 s. The finer mesh produced the load–displacement curve which experienced two oscillations before global buckling, Figure 120 (black). To address this, the SOFT was recalibrated (from 0.73 to 0.60) to stabilize the smaller elements from the load pulses. Stable crushing initiates but global buckling still occurs, Figure 120 (blue). The fine mesh requires further stabilization, which is accomplished by increasing DFAILC (from 0.013 to 0.02 in/in). This was one of the MAT54 parameters that had a baseline value at the edge of its stability threshold for the fabric material system. The resulting simulation demonstrates stable crushing behavior, and matches the baseline simulation well, Figure 121. This fabric material crush model was mesh sensitive, but it was possible to make empirical adjustments to the material deck in order to stabilize it using different a mesh size.

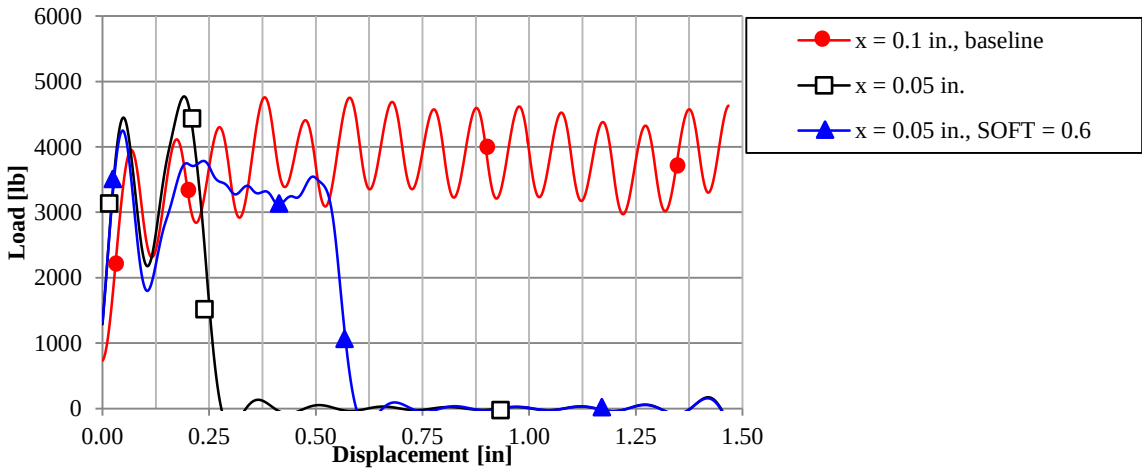

Figure 120. Effect of using a smaller mesh size without changing any parameters (black) and after recalibration of the SOFT (blue) which shows unstable behavior for both.

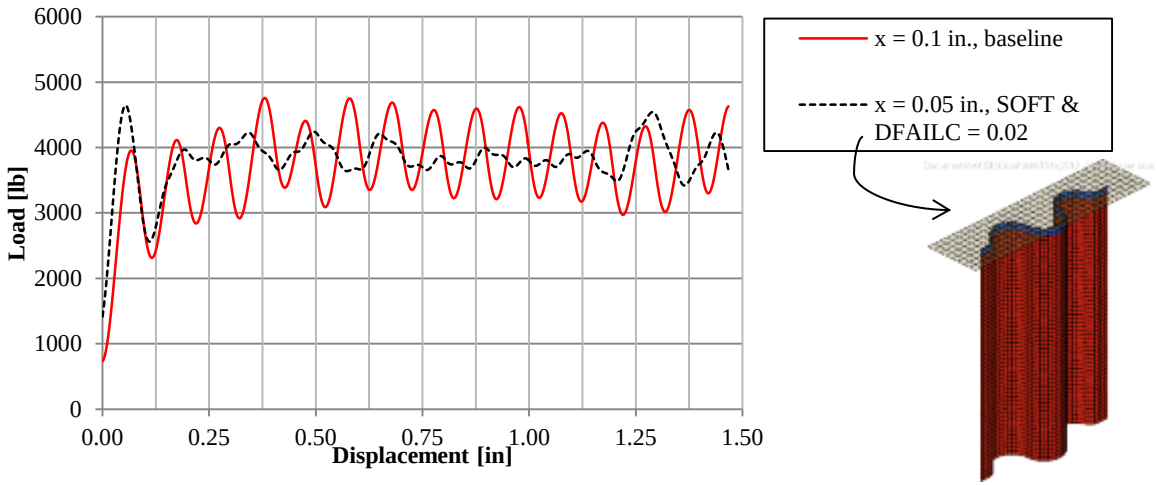

Figure 121. Load-displacement crush curves from using two different mesh sizes in the fabric sinusoid crush simulation, and recalibrating SOFT and DFAILC parameters for the smaller mesh.

Comparison of MAT54 parametric trends of the fabric and UD models

Many of the parametric trends observed for the crush simulation of the UD material system modeled using MAT54 were also observed for the fabric. The critical MAT54 parameters which most affected the stability and SEA of the UD crush simulation, XC, DFAILC, and SOFT; also greatly influenced the crush simulations modeling the fabric composite. The fabric material model, however, was also influenced by transverse compressive parameters YC (and consequently YCFAC) and DFAILM, which was not observed for the UD system. The compressive transverse mode is not suitable to simulate a fabric material system due to the Hashin failure criterion. Given this, it is sensible that the transverse compressive strength parameter, YC, could be empirical for a fabric material system. Similarly, the transverse failure strain, DFAILM, is meant to model matrix materials which have a higher strain-to-failure value than fibers.

One of the biggest differences between the two material models is that the true material properties of the UD yield stable results which match the experiment, while the fabric material model must use artificial plasticity in the transverse direction to achieve stable results. Furthermore, there are parameters such as XC and DFAILC which have material property values that are 2% and 15% away from causing instability in the fabric model. The fabric MAT54 model is not as robust as the UD model, and sensitive material parameters may require adjustment when features such as mesh size and velocity are changed.

Based on these observations, the proposed modeling approach is considered to be non-predictive for both material systems at this level of structural complexity (i.e. at this level of the BBA), since it is not possible to simulate crushing behavior with a sufficient level of confidence based solely on the material properties derived from tension, compression and shear coupon level tests. For these reasons, the sinusoidal specimen crush test should be interpreted as an element-level test, from which the analysis model can be successfully calibrated for each material system individually. Following the calibration at the element level of structural complexity, it is expected that the simulations will become predictive. However, it is imperative that the structural assembly be comprised of elements having the same geometry as the sinusoidal elements tested. It is expected that if the elements were to exhibit differences in thickness or degree of curvature, even while maintaining material and manufacturing process unchanged, the analysis model will lose its predictive capability, and additional element-level testing and model calibration will need to be performed.

Conclusions

The LS-DYNA material model MAT54 has been successfully shown to model both a unidirectional and a fabric material system in the simulation of a sinusoidal specimen undergoing

axial crushing. The performance of the UD and fabric models within the crush simulation shared many similar trends, such as the sensitivity of the model to the fiber compression strength XC and strain-to-failure DFAILC parameters. Regardless of the material system modeled, these parameters are the primary material parameters which ultimately determine energy absorption in a crush simulation by determining element failure and deletion. The single most influential MAT54 input parameter for energy absorption and determining the success of a crush simulation remains the SOFT parameter. Using a systematic calibration against the crush experiment, the appropriate value for the SOFT parameter can be identified. Some differences between the UD and fabric material systems were identified, such as the influence of the transverse tensile strength YC and strain-to-failure DFAILM which both significantly influence the stability of the fabric model, but not the UD model. Both of these parameters are measured from experiment, and while the experimental value of the YC parameter yielded a stable simulation, DFAILM required artificial increase for a stable simulation. This increase provides transverse plasticity in the model following failure, a feature noted in impact simulations to be necessary for composite modeling [68]. This has also been noted to be a similar to the stress unloading following failure featured in simulations of composite materials involving stress concentrations and linear elastic fracture [103]. If a stable crush simulation of a MAT54 UD material model has already been defined, a change of material properties followed by a calibration of the DFAILM and SOFT parameters has been shown to achieve a successful crush simulation. This modeling approach is not yet considered to be predictive for this level of structural complexity, and instead is classified as a calibration of the model using experimental data within the scope of the building block approach, building towards a full-scale crash simulation.

Simulation of other fabric crush specimens

Following the parametric investigations of the sinusoid crush element simulations, for which material models for both the UD and fabric material systems were investigated, several new crush elements are simulated using the MAT54 fabric material model. The new crush elements are the seven geometries, five channel variants and two additional sinusoids, which were experimentally crush tested. The eight geometry models (including the baseline semi-circular sinusoid) are shown in Figure 122. The modeling strategy developed for the fabric semi-circular sinusoid crush element, including mesh size, contact definition, boundary conditions, material card, etc.; is used as a template to model the seven new geometries. The nominal dimensions for the sinusoidal and channel specimens are given in Figure 18 and Figure 24, respectively.

Recall that the experimental investigation of the different crush elements revealed that the cross-sectional geometry of the crush element greatly influences its energy absorbing capability, indicating that SEA is not a constant of the material system. The difference in SEA is attributed to the different failure mechanisms exhibited by each crush element. In particular, elements with more curvature exhibited greater delamination suppression, which encourages material fragmentation, a highly energy absorbent failure mechanism. The variation in SEA measured from the different crush elements is directly dependent upon the different failure mechanisms experienced, and it is the goal of this numerical investigation to determine the best way to represent such changes in the simulated crush models.

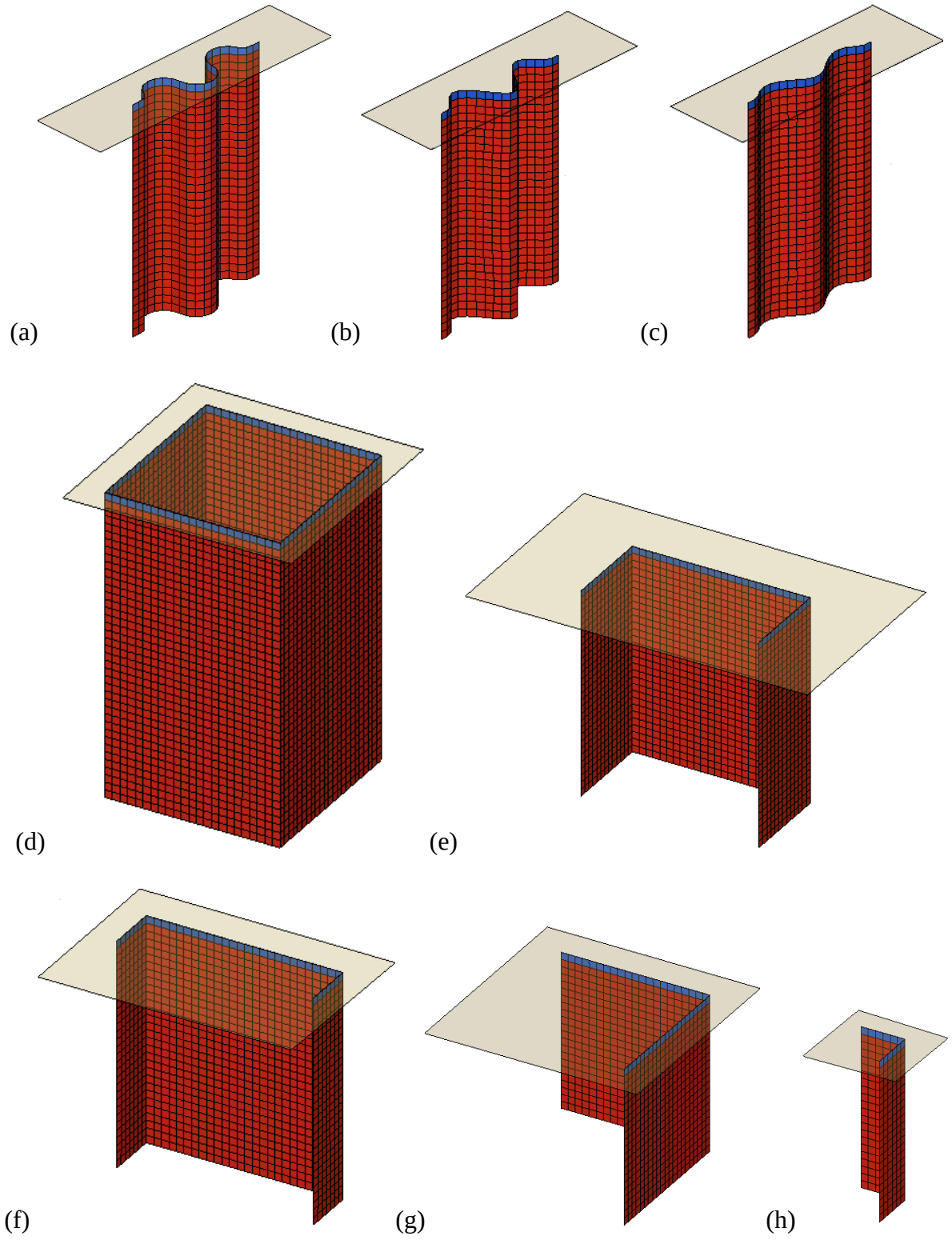

Figure 122. Eight LS-DYNA crush specimen models with different geometries: (a) semi-circular sinusoid, (b) high sinusoid, (c) low sinusoid, (d) tube, (e) large c-channel, (f) small c-channel, (g) large corner, and (h) small corner.

Unfortunately, the very failure mechanisms which differentiate the energy absorbing capability of the different crush elements (e.g. delamination) cannot be directly simulated using the single shell element approach developed for the sinusoid crush simulations. Without the capability to simulate delamination, it is expected that simulating different geometries requires changes in the material model itself even though the material remains constant throughout this investigation. This investigation will determine what changes are necessary in the model in order to simulate the crush elements with various geometries which were previously crush tested.

The baseline MAT54 input deck for the fabric material model is given in Figure 98. The baseline MAT54 parameter values were derived from the material properties of the fabric material system given in Table 2, with the exception of the DFAILM parameter which was artificially increased for stability of the sinusoid crush model. From the sinusoid crush model all modeling definitions remained the same and only the geometry was changed. For the square tube element, the change of geometry caused a failure at crush initiation where several elements were eroded away from the crush front at very high loads, which directly led to global buckling, Figure 123. Similar results were obtained from modeling each of the other seven geometries directly from the baseline sinusoid model, as given in Appendix D: Additional crush element simulation results. By simply changing the geometry, the crush simulations of the new shapes are not successful; however this result is not unexpected since the different energy absorbing failure mechanisms cannot be individually modeled using the current approach. The continued systematic investigation is focused to discover the best method to simulate the change in SEA due to change in geometry using the modeling parameters that most influence stability and SEA, as discovered in the parametric studies of the crush model.

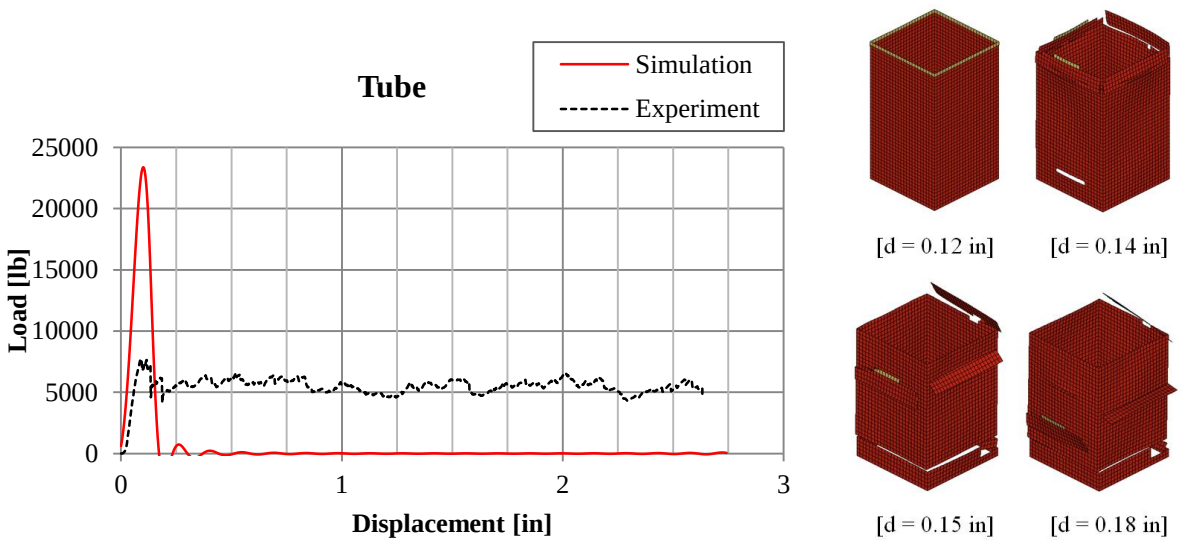

Figure 123. Simulated load-displacement crush curve and simulation morphology from changing only the specimen geometry from the sinusoid baseline to that of the tube element.

First, the modeling parameters which influence SEA are investigated to discover if the crushing loads can be reduced enough to achieve stability and the correct simulated SEA. With the intent to reduce the crush loads, the MAT54 parameters SOFT, DFAILC, and XC are reduced, without acceptable success. It is observed that the crush models of all of the tubular, channel, and corner geometries are too unstable to appropriately alter the crushing load without experiencing global failures, such as those shown in Figure 123. Next, parameters which influence stability are investigated with the goal to reduce variability and promote stability such that changes can be made to lower the crushing load. To promote stability, DFAILS, SC, and YCFAC are raised, in conjunction with lowering the SEA-influencing parameters DFAILC, XC, and SOFT. All such efforts which have contained changes within the MAT54 card are unable to provide a significant improvement in the model stability. Finally, the LP curve at the contact is altered in order to promote stability. A softer contact LP curve, Figure 124, was used to soften the introduction of the reaction forces transmitted into the crush specimens. This is the same LP curve as was featured in the fabric sinusoid crush parametric study, labeled “PCWL Soft 2” in Figure 119.

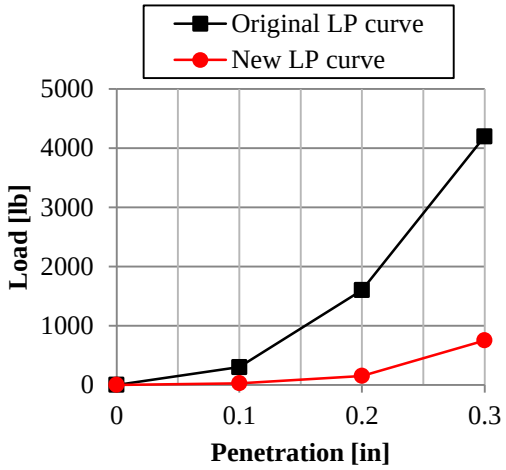

Figure 124. Original and new Load-Penetration curves defined in the contact deck.

Implementing only this change in the contact definition LP curve and applying the baseline sinusoid material model to the seven geometries did not yield immediate success, as shown in Figure 125.

(a)

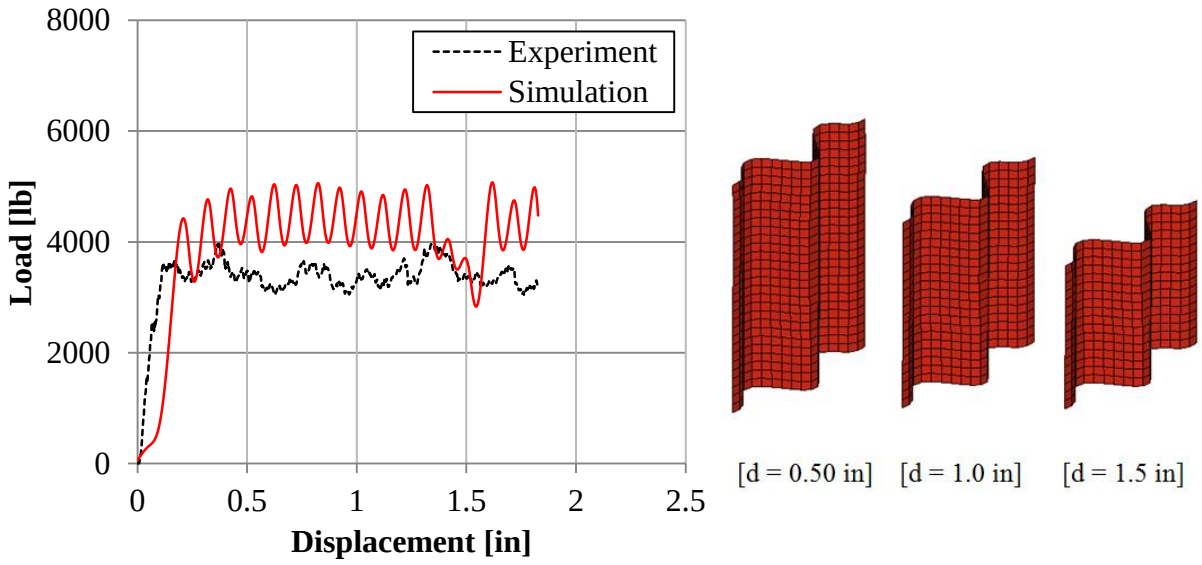

(b)

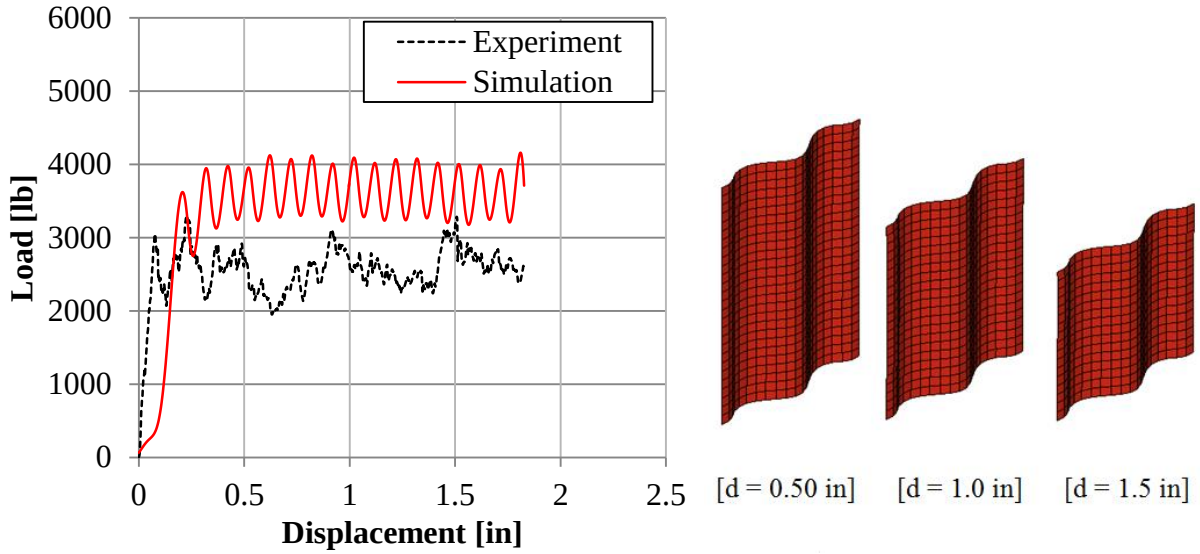
Experiment
Simulation
Load [lb]
Displacement [in]
0
1000
2000
3000
4000
5000
6000
0
0.5
1
1.5
2
2.5
[d = 0.50 in]
[d = 1.0 in]
[d = 1.5 in]

(c)

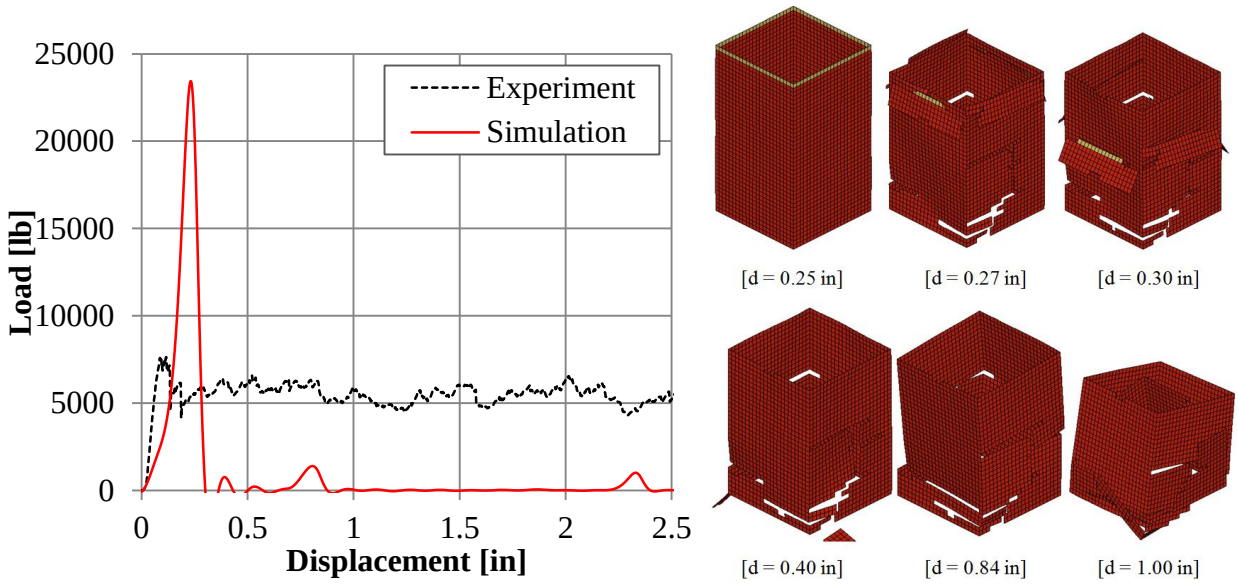
Experiment
Simulation
Load [lb]
Displacement [in]
0
5000
10000
15000
20000
25000
0
0.5
1
1.5
2
2.5
[d = 0.25 in]
[d = 0.27 in]
[d = 0.30 in]
[d = 0.40 in]
[d = 0.84 in]
[d = 1.00 in]

(d)

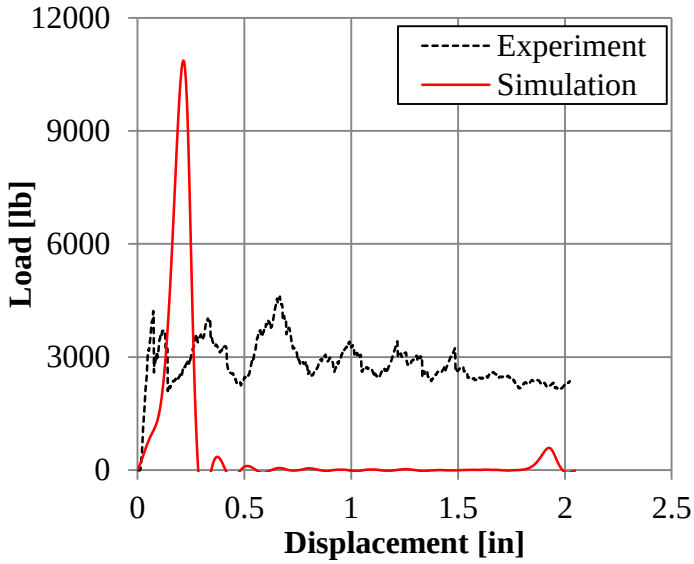
12000
9000
6000
3000
0
Load [lb]
0
0.5
1
1.5
2
2.5
Displacement [in]
Experiment
Simulation

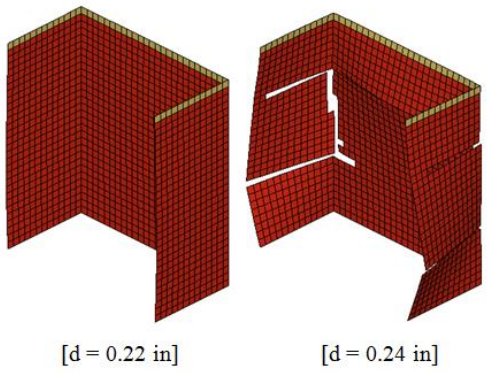
[d = 0.22 in]
[d = 0.24 in]

(e)

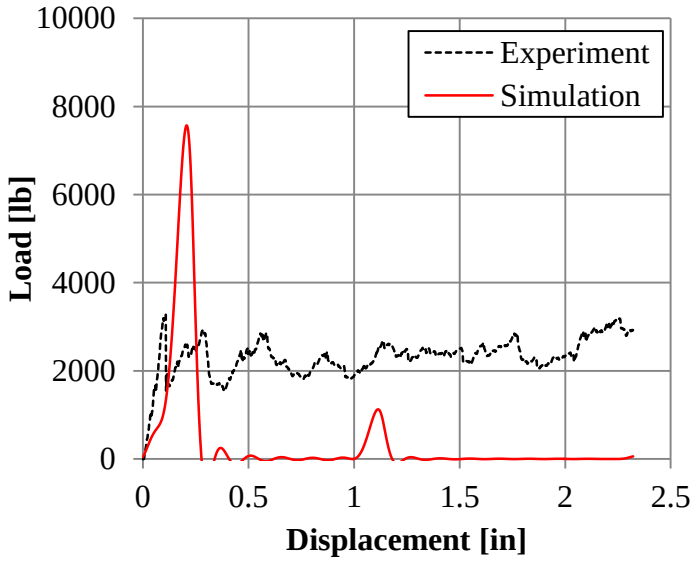
10000
8000
6000
4000
2000
0
Load [lb]
0
0.5
1
1.5
2
2.5
Displacement [in]
Experiment
Simulation

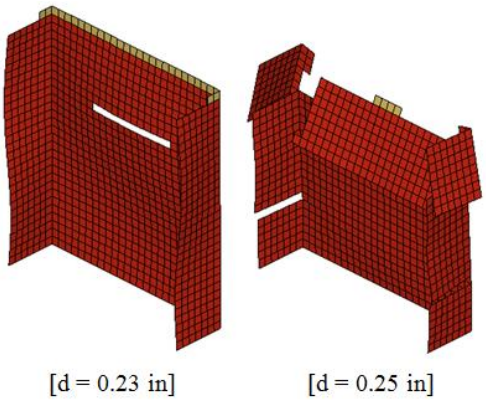
[d = 0.23 in]
[d = 0.25 in]

(f)

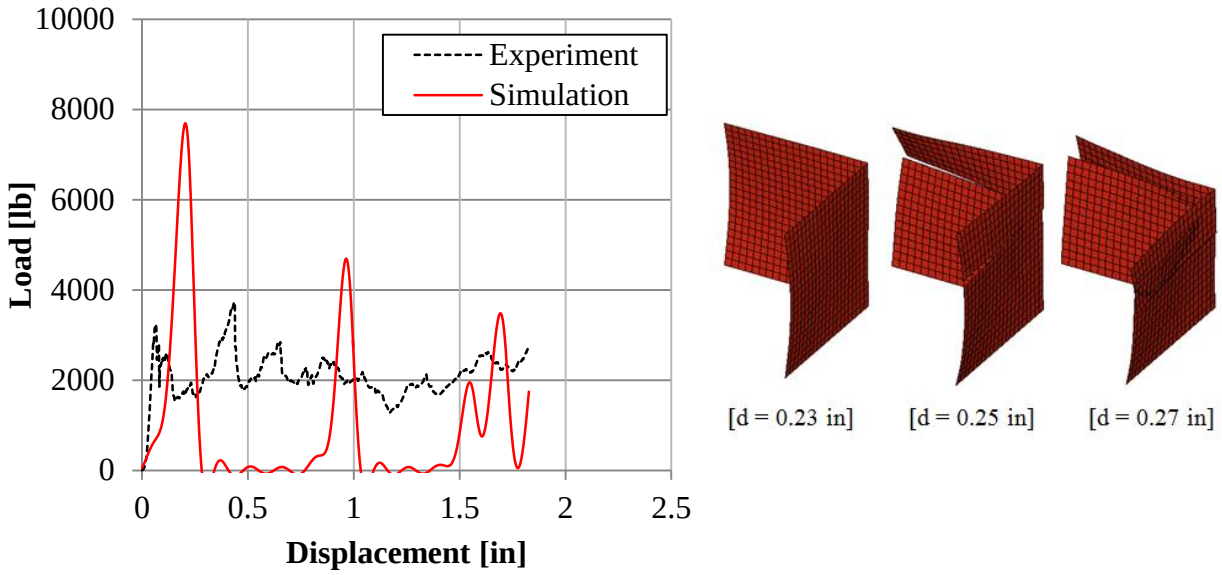

(g)

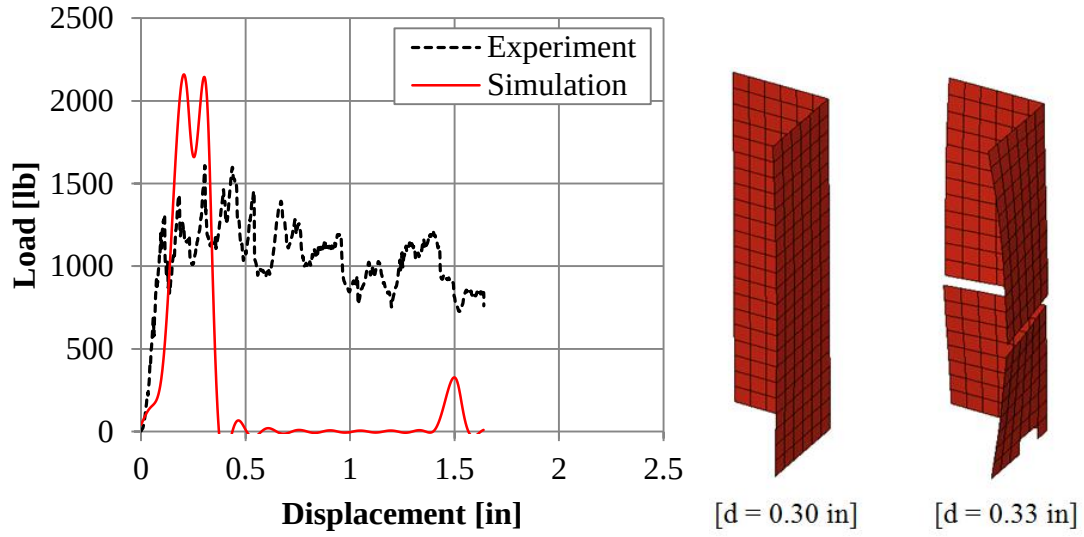

Figure 125. Undesired crush simulation results compared against the experimental curve when only the geometry is changed from the semi-circular sinusoid baseline model: (a) high sinusoid, (b) low sinusoid, (c) square tube, (d) large c-channel, (e) small c-channel, (f) large corner, and (e) small corner elements.

While initial results were unstable, changes to the SOFT parameter and the trigger thickness in combination with the new LP curve generated positive results. Noting from Figure 123c that failure of the square tube occurs at the initial load peak, the trigger thickness in this simulation was reduced to 0.011 in. (0.28 mm) to prevent early failure and enable crush initiation. With a softer LP curve and a lower trigger thickness, the SOFT parameter was calibrated to a value of 0.145 such that the average crush load matched that of the experiment, shown in Figure 126**.** The trigger thickness was then calibrated to a value of 0.015 in. (0.38 mm) to match the initial load peak of the experimental curve, Figure 127. The shape of the resulting load-displacement curve, initial peak load value, crush load value, and SEA value matched the experimental results well, Figure 128, the tube crush baseline simulation. The crush progression, Figure 129, was smooth as elements were deleted simultaneously row by row at the crush front.

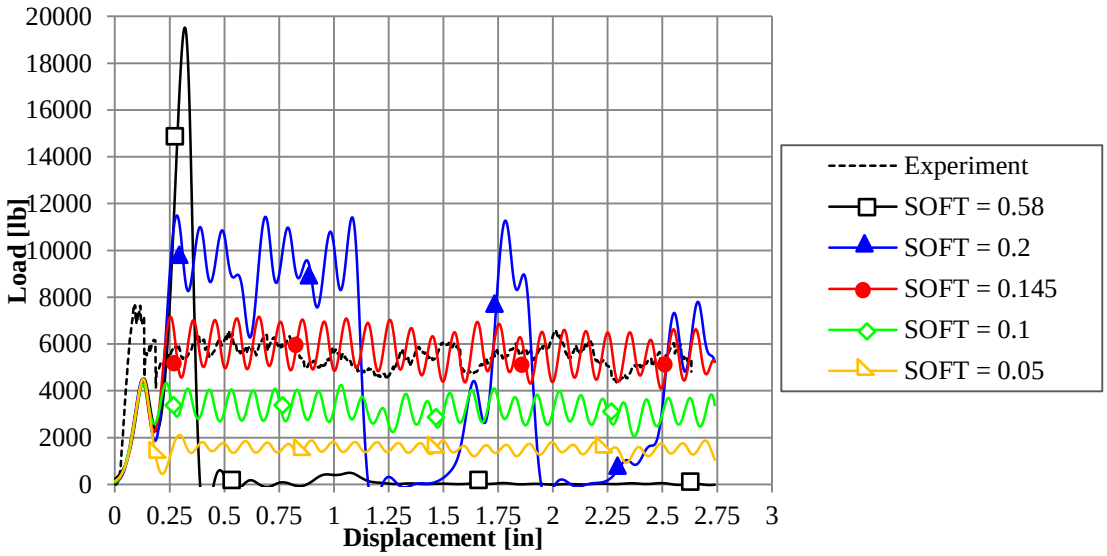

Figure 126. SOFT parameter calibration of the tube simulation using new contact LP curve.

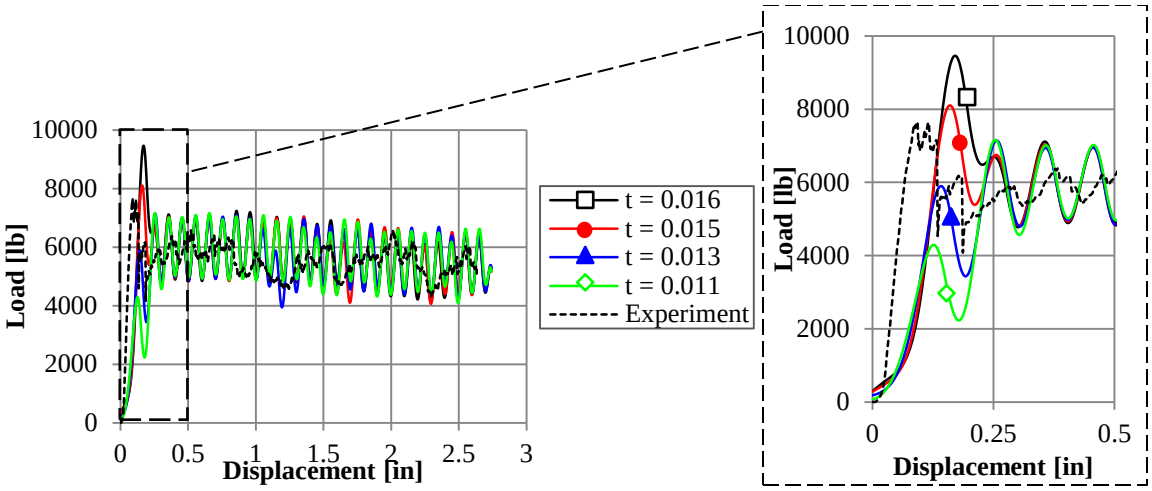

Figure 127. Trigger thickness calibration of the tube simulation using new contact LP curve.

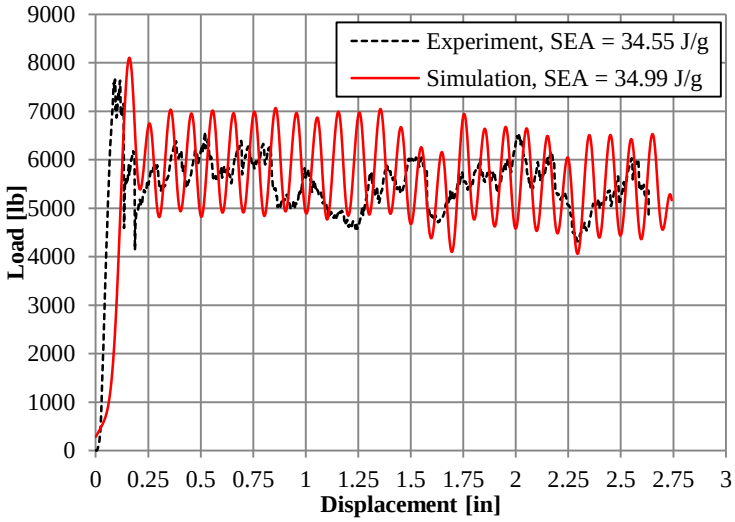

Figure 128. Load-displacement curves from simulation and experiment of the tube crush specimen.

From the development of the square tube crush simulation, three parameters required adjustment when changing the geometry of the crush specimen from the sinusoid to the tube: the LP curve for stability, the SOFT value to calibrate the crush load and SEA, and the trigger thickness to calibrate the initial load peak value. Rather than calibrate the LP curve for each new geometry, the soft LP curve was used for all of the crush simulations, including the original baseline semi-

circular sinusoid crush model which was retroactively updated to have the new LP curve. In this way, only two parameters, SOFT and trigger thickness, were necessary to calibrate when changing the geometry of the crush specimen.

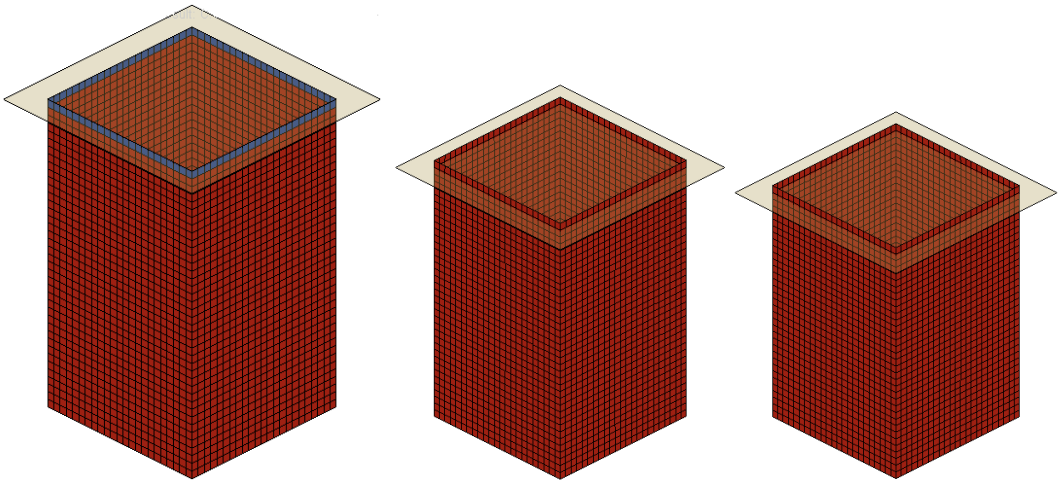

[d = 0.00 in] [d = 0.30 in] [d = 0.60 in]

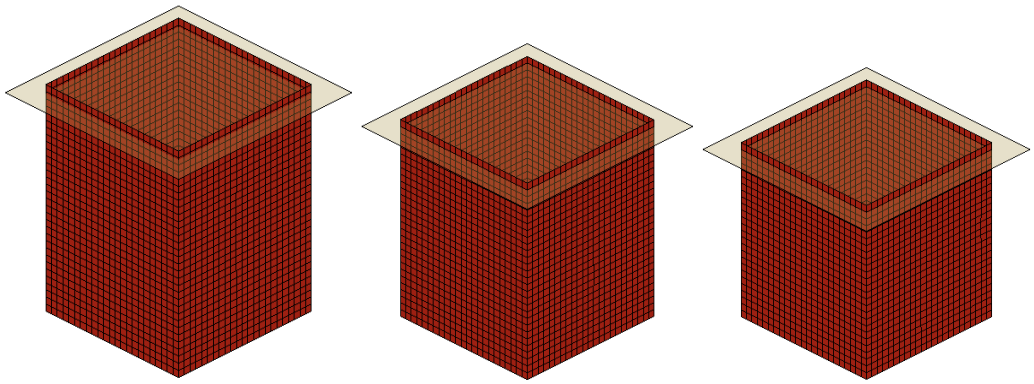

[d = 0.90 in] [d = 1.20 in] [d = 1.50 in]

Figure 129. Time progression of the crushing simulation of the square tube baseline (d: displacement).

The successful tube crush simulation was modified to simulate each of the remaining seven geometries. After inserting these specimens into the crush simulation, the SOFT parameter and trigger thickness were each calibrated in order to match the experimental crush curve. By making only these two changes, all geometries were successfully simulated in crush. Crush

curves of the LS-DYNA simulations calibrated to match the experimental load-displacement curves of the seven new geometries (excluding the square tube) are shown in Figure 130a-g. The calibrated SOFT and trigger thickness parameters used in all eight cases are given in Table 20, along with the simulated SEA results.

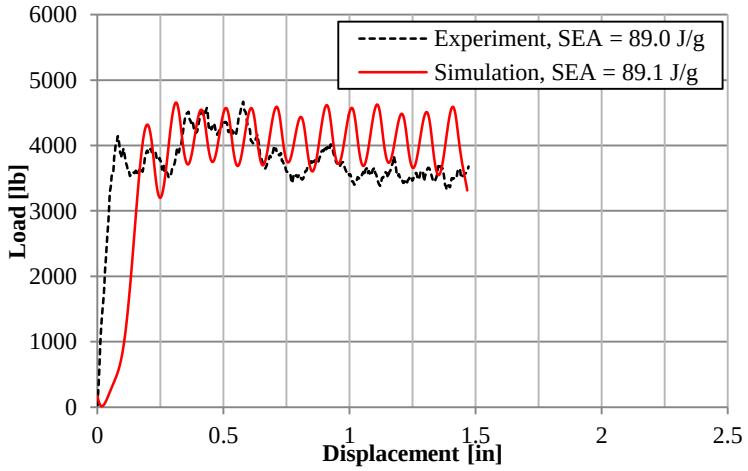

(a)

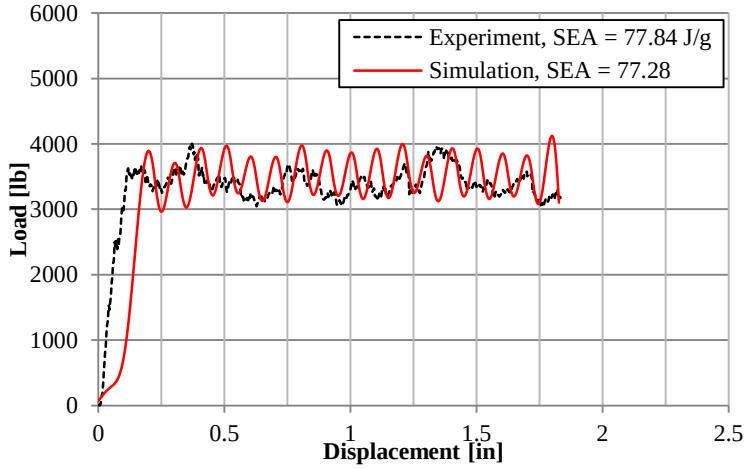

(b)

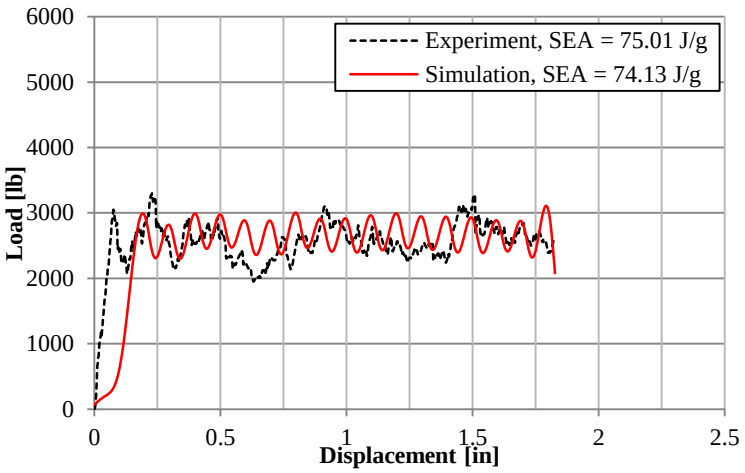
Experiment, SEA = 75.01 J/g
Simulation, SEA = 74.13 J/g
Load [lb]
Displacement [in]
0
1000
2000
3000
4000
5000
6000
0
0.5
1
1.5
2
2.5

(c)

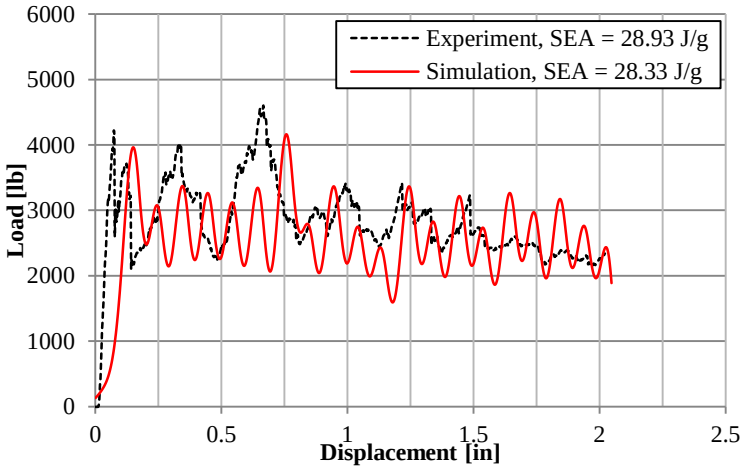
Experiment, SEA = 28.93 J/g
Simulation, SEA = 28.33 J/g
Load [lb]
Displacement [in]
0
1000
2000
3000
4000
5000
6000
0
0.5
1
1.5
2
2.5

(d)

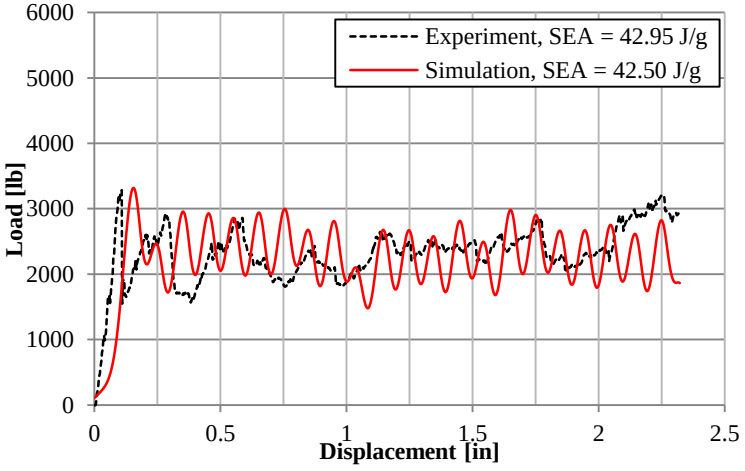
Experiment, SEA = 42.95 J/g
Simulation, SEA = 42.50 J/g
Load [lb]
Displacement [in]
0
1000
2000
3000
4000
5000
6000
0
0.5
1
1.5
2
2.5

(e)

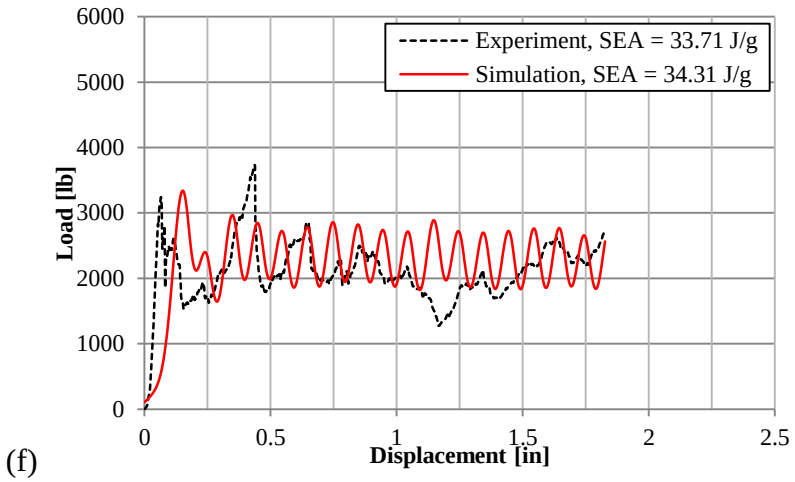

(f)

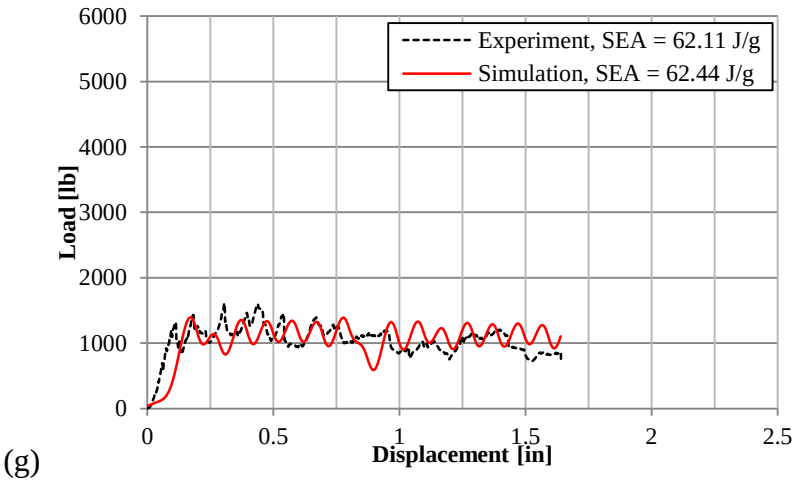

(g)

Figure 130. Load-displacement crush curve results comparing simulation with experiment for seven crush specimen geometries: (a) semi-circular sinusoid, (b) high sinusoid, (c) low sinusoid, (d) large c-channel, (e) small c-channel, (f) large corner, and (g) small corner

Table 20. Summary of the modeling parameters necessary to change for each crush element geometry in order to match the experimental results, and the resulting error between simulation and experiment.

Geometry	*Trigger Thickness [in]*	*SOFT*	*Single Test SEA [J/g]*	*Numeric SEA [J/g]*	*Error*
SC Sinusoid	0.044	0.580	88.98	89.08	0.1%
High Sinusoid	0.045	0.540	77.84	77.28	-0.7%
Low Sinusoid	0.040	0.450	75.01	74.13	-1.2%
Tube	0.015	0.145	34.55	34.99	1.3%
Large Channel	0.021	0.215	28.93	28.33	-2.1%
Small Channel	0.023	0.220	42.49	42.49	0.0%
Large Corner	0.022	0.205	33.71	33.43	-0.8%
Small Corner	0.030	0.310	62.11	62.44	0.5%

As a result of this investigation, it is possible to generate relations between experimental data and modeling parameters which would allow crush modeling of various geometries from an initial calibrated crush model. First, the linear relation between the calibrated SOFT parameter and the experimentally measured SEA is revealed in their plot, Figure 131. The SOFT parameter can be interpreted as a utility to account for the virtual damage that has propagated beyond the crush front. Figure 131 shows that greater values of SOFT yield higher SEA in the simulation. The micrographic analysis of crushed specimens from sections with varying SEA capability, Figure 36, indicates that the greater the damaged area, the smaller the SEA. This provides a new interpretation of the SOFT parameter as the degree of damage suppression provided by the geometry, thickness, lay-up, and material system. Since the thickness, lay-up, and material system remained constant, in this study we perceive the SOFT parameter as the degree of damage suppression provided by the geometry of the crush specimen. The higher the SOFT value is, the higher the crush damage suppression and SEA will be. This relationship provides a

link between an experimental measurement, SEA, and one of the modeling parameters which requires calibration when the SEA changes, SOFT.

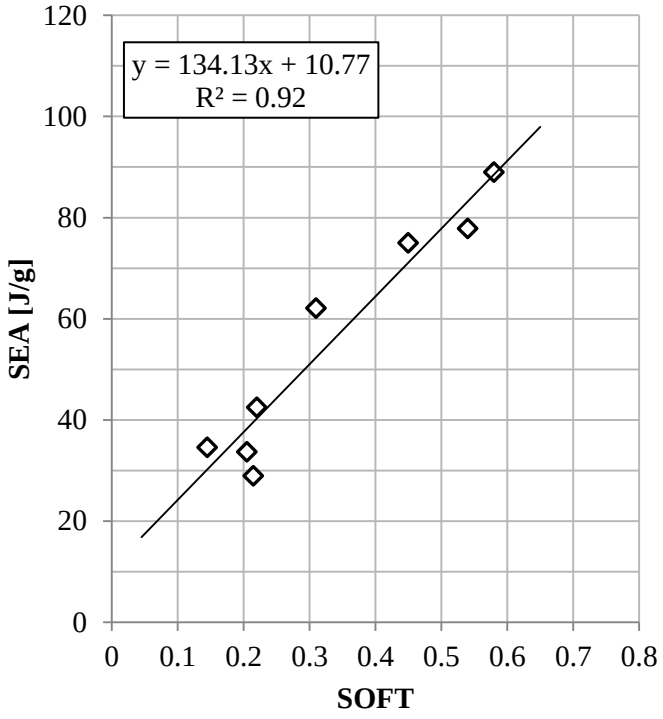

Figure 131. Linear trend between calibrated MAT54 SOFT parameter and the experimental SEA.

The only other modeling parameter which requires calibration when the geometry (and SEA) of the crush element changes is the trigger thickness. The thickness of the trigger elements is reduced to facilitate crush initiation, and the reduced cross-section of the trigger elements ensures these elements fail at a lower applied force than the full thickness elements. In this way, the trigger thickness is a strength knockdown factor for the initial row of elements, which are not subject to the SOFT knock-down since the crush front is established only after failure of the initial element row. Plotting the calibrated SOFT against the ratio of the reduced trigger thickness to the total element thickness generates another linear relationship, Figure 132. The fact that this linear relationship is nearly 1:1 suggests that the trigger row of elements has nearly

the same strength knockdown, by virtue of reducing the cross-sectional area, as that which was applied by SOFT to the rest of the elements. This implies that the correct trigger thickness value can be determined from the calibrated SOFT, and that changing the geometry of the crush element only is dependent on only a single variable.

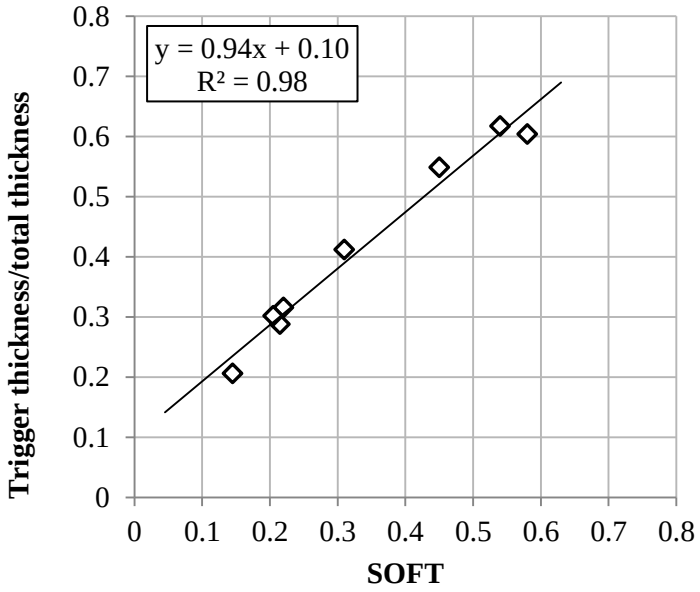

Figure 132. Linear trend between the calibrated SOFT parameter and the ratio of trigger thickness to original thickness.

For this fabric material system, if the average experimental SEA for a given crush geometry is known, the calibrated values of SOFT and trigger thickness can be estimated which will produce a fair simulated crush curve and SEA. This approach is not predictive, but can provide a good starting point for trial-and-error model calibration that is near the solution which best matches the experimental results.

Since these simulations are not predictive, a structural crush specimen at this level of complexity should be interpreted as an element-level test, from which the analysis model can be successfully calibrated for each material system. It is expected that the material model is fully calibrated

following the calibration at the element level of structural complexity, and is suitable to use in models of higher levels of complexity. For every crash element with a different thickness, geometry, or lay-up, however, additional element-level testing and model calibration is required.

Conclusions

Using the existing MAT54 material model, several simulations of crush elements with various cross-sectional geometries have been successfully calibrated to match the experimental results well. In this MAT54 crush modeling approach it is not possible to simulate different specimen geometries without making changes to the material model since specific damage and failure mechanisms (such as delamination) cannot be modeled individually. From this investigation, sensitivity studies have established important MAT54 and other modeling parameters which influence these crush simulations the most. Finally, some relationships have been established which link experimental parameters (SEA) to important modeling parameters (SOFT, trigger thickness), making the calibration of the crush simulation more focused by reducing scope the trial and error calibration process. Ultimately, this modeling approach requires a comprehensive set of experimental element-level crush data which fully characterizes the energy absorbing capability of the composite material system such that trial-and-error calibration of the SOFT parameter can be executed to develop a good crush model. The next goal in this body of work is to modify the MAT54 material model in order to investigate if a better composite material model for crush simulation can be developed and successfully implemented for these element-level crush specimens.

Modifying MAT54

A modified version of the MAT54 material model has been developed by changing an isolated portion of the source code of the LS-DYNA program. Specific details of the MAT54 source code and modifications made to the code are outlined in Appendix E.. An updated LS-DYNA User's Manual entry for the modified material model was written, and is presented in Appendix F. This section will present the results of the modified model as it was used in the single element and crush simulations.

The modification efforts of MAT54 are best understood when the composite failure model is generalized as the simulation of three phases: 1. the elastic response, 2. failure determination, and 3. post-failure degradation. These three phases are summarized in the basic stress-strain curve generated by MAT54 shown in Figure 133. In each of these three phases, modifications were made to attempt to improve the original material model.

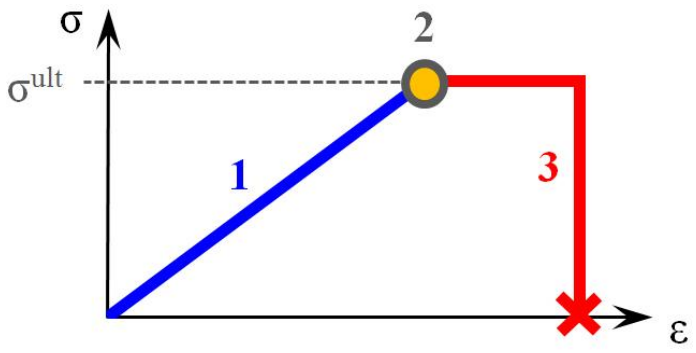

Figure 133. Material stress-strain curve outlining three the basic MAT54 composite failure regions: 1. elastic 2. failure and 3. post-failure degradation.

Elastic response

During the MAT54 single element investigation, it was determined that the elastic response of the UD material could not be modeled as it behaves physically due to the limited constitutive property input parameters of MAT54. Missing constitutive parameters included the compressive

modulus in both the axial and transverse directions, and a strain-to-failure value for compression in the transverse direction. These three missing constants were added as new user input parameters, and the single element and crush simulations which model both the unidirectional and fabric composite material systems reveal the effect of these added parameters. The compressive properties input into the modified model are taken from coupon-level material testing, as summarized in Table 2.

The improvement in the elastic definition of the UD material is immediately apparent, as the modified MAT54 is capable of exactly modeling the material as it is defined by its material properties, as shown by the stress-strain curves in Figure 134. There is noticeable improvement in the simulation of the compressive stiffness and, for the transverse case, the failure strain. The characteristic perfectly plastic region of MAT54 is no longer present in the modified model. The modified single element model of the UD cross-ply laminate also produces improved results, shown in Figure 135. For this case the simulations are compared against experimental data, resulting in a larger error mainly due to the error of the CLT calculations, used to predict the laminate behavior from the lamina properties, against the experimental laminate data. For this case, it is more useful to compare the improvement of the modified model over the original MAT54.

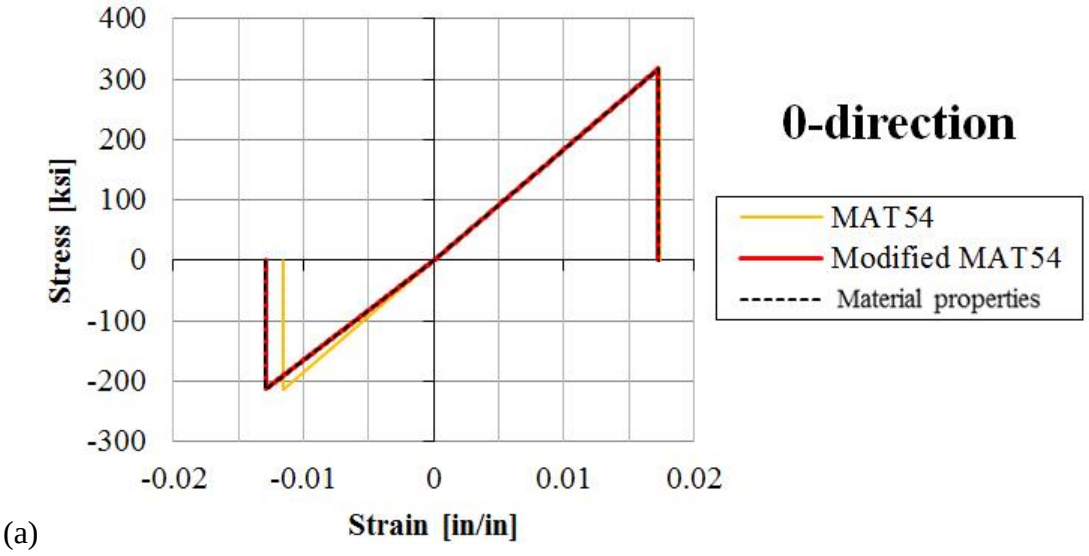

(a)

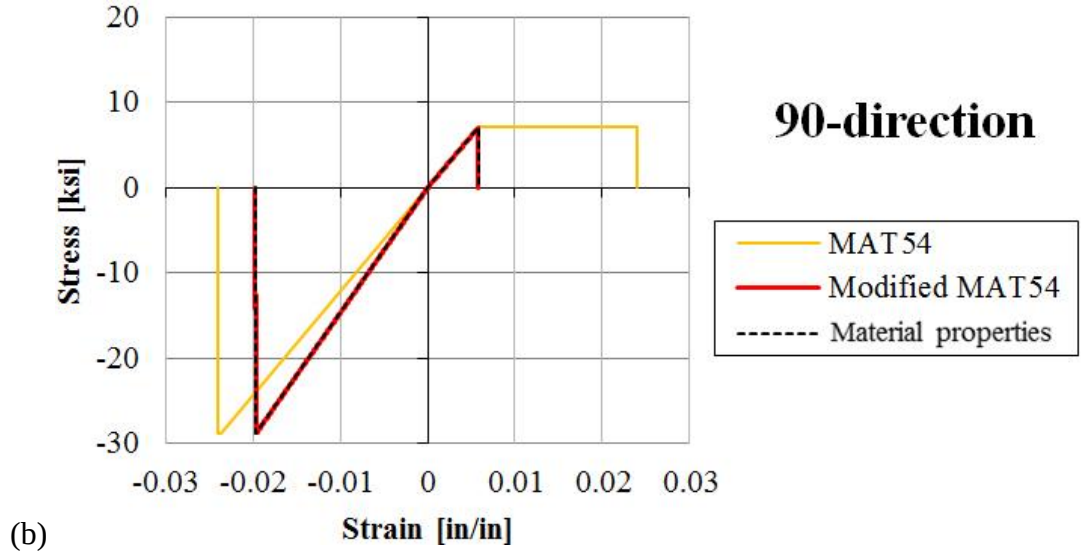

(b)

Figure 134. Results of modified elastic response on the UD single element model in the (a) axial, 0-direction and (b) transverse, 90-direction

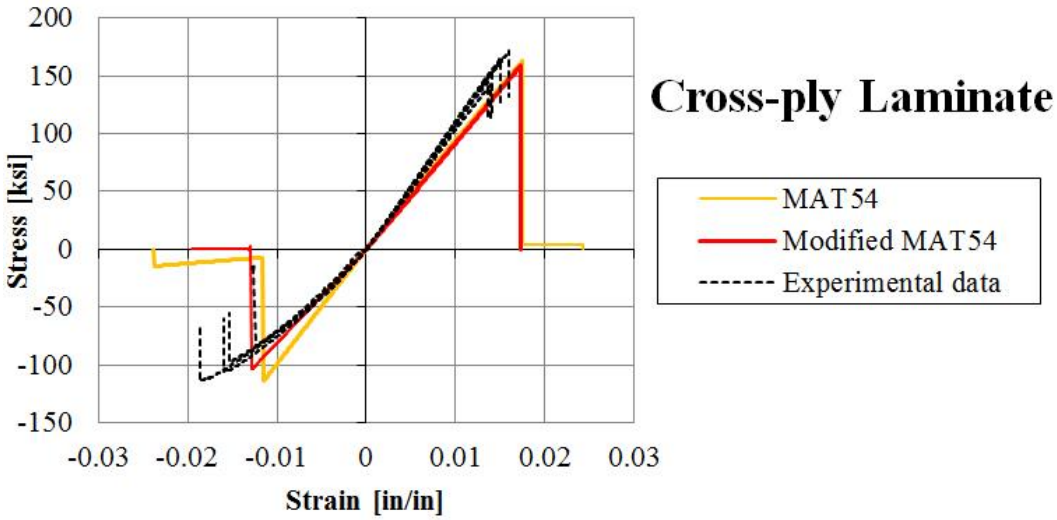

Figure 135. Results of modified elastic response on the UD cross-ply laminate single element model as compared against experimental coupon data.

The semi-circular sinusoid crush simulation is run using the modified UD material model, and the resulting crush curve is just as stable as the original model. It should be noted that since the compressive modulus was updated to reflect the true compressive modulus of the material, the DFAILC strain-to-failure value was also changed in order to maintain a material behavior that is perfectly linear elastic until failure. Recall that changes in DFAILC result in changes in the average crush load of the load-displacement curve in MAT54 crush simulations. As expected, raising DFAILC did raise the average crush load of the simulation, so a slight decrease of SOFT was necessary to match the experiment for the modified model. All of these MAT54 parameter changes that were made for the sinusoid crush simulation of the UD material are listed in Table 21.

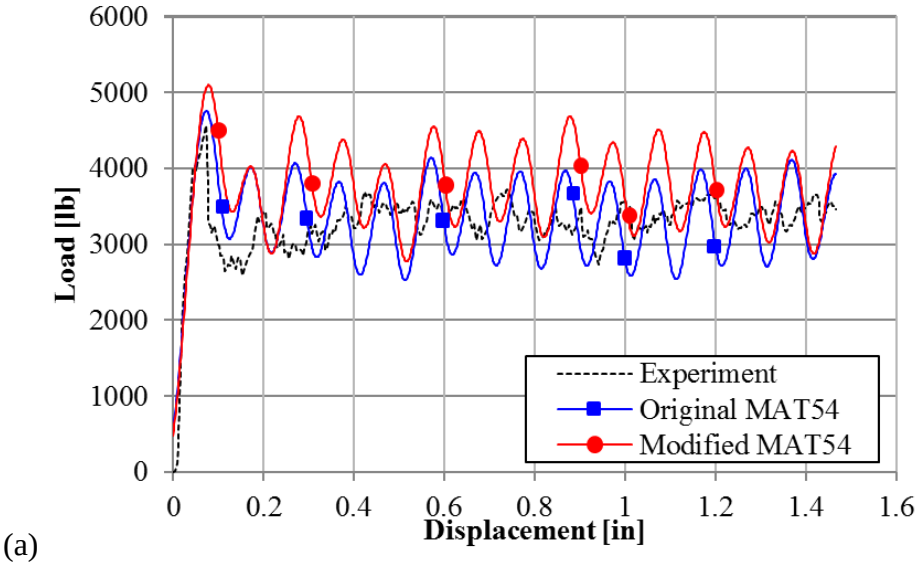

(a)

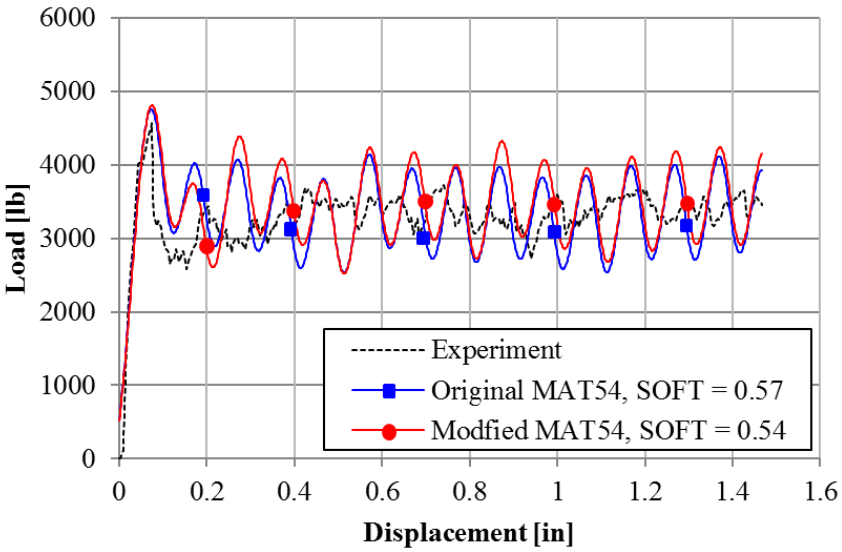

(b)

Figure 136. Crush curve results of modified elastic response on the UD sinusoid crush simulation as compared against the original MAT54 and the experimental data (a) before SOFT adjustment and (b) after.

Table 21. Original and modified material input parameters used for the UD material definition.

	MAT54	Modified MAT54
EA	18.4 Msi	18.4 Msi
EAC	18.4 Msi	16.5 Msi
EB	1.22 Msi	1.22 Msi
EBC	1.22 Msi	1.47 Msi
DFAILM	0.024	0.0058
DFAIL2M	0.024	0.0196
DFAILC	-0.0116	-0.0129
SOFT	0.57	0.54

For the model of the fabric material, there is no improvement gained by utilizing the modified model, as shown in the single element results in Figure 137. This is largely due to the fact that there is a smaller difference in compressive and tensile properties of the fabric material system, and for this reason there was little error in the original MAT54 material model of the fabric. Also, for the fabric material only the axial data is of interest since all of the elements are given a 0-degree orientation in the composite part definition of the fabric material, so the addition of the DFAIL2M parameter is not evident in this single element simulation. For these reasons, no improvement is apparent using the modified material model for the fabric material system.

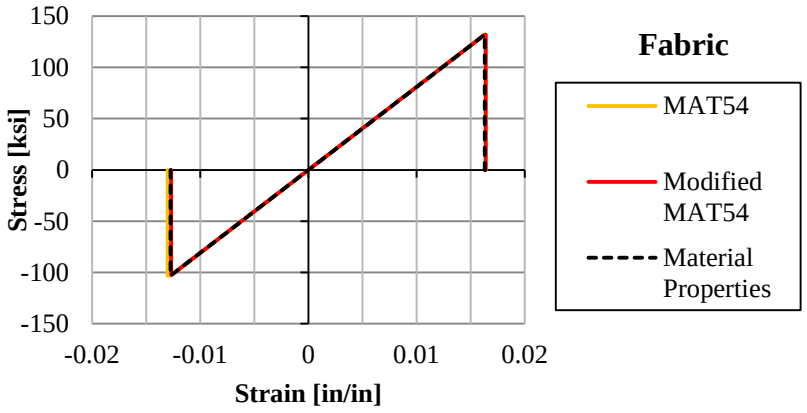

Figure 137. Results of modified elastic response on the fabric single element model.

Implementing the modified material model to simulate the fabric material for use in the crush element simulations also does not provide improvement, and in fact destabilizes some crush elements. First, the effect of using the additional compressive moduli, EAC and EBC, is investigated. When comparing the crush simulation results using the original MAT54 against those using the modified MAT54 with compressive moduli, some simulations are undisturbed, such as the simulation of the small c-channel crush element, Figure 138a, while others are slightly disrupted by the modified model, such as the small corner crush element, Figure 138b. In general, the disruptions caused by the added compressive moduli are relatively minor and tend to only slightly change the resulting crush curve while crushing remains stable and progressive.

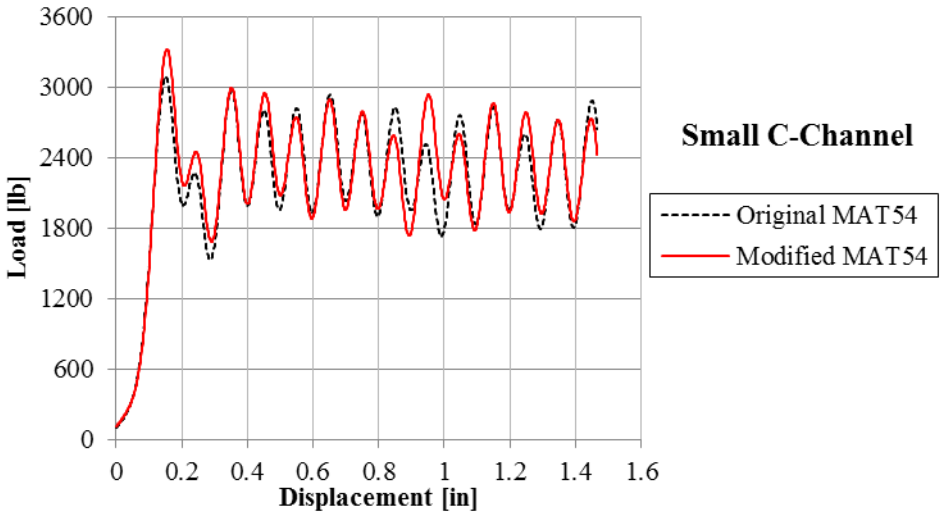

(a)

(b)

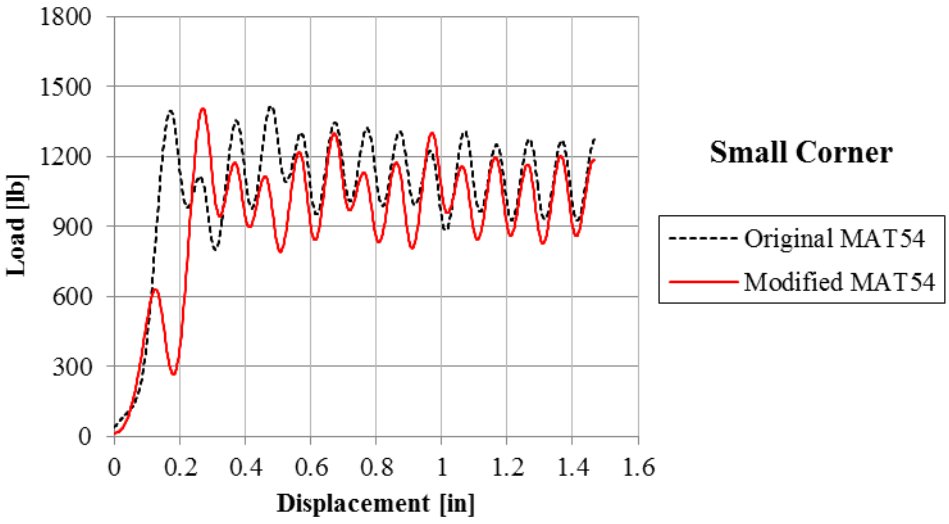

Figure 138. Crush simulation results, the original MAT54 compared against a modified version that has compressive moduli, on the (a) small c-channel and (b) small corner crush elements.

The addition of the DFAIL2M parameter in the modified MAT54 model allows for an investigation of the transverse plasticity required by the original MAT54 crush element models. Recall that when using the original MAT54, the transverse strain-to-failure parameter, DFAILM, had to be greatly increased from its measured experimental value in order to stabilize the fabric material model crush element simulations, effectively inducing artificial plasticity in the transverse direction in both tension and compression. While not all of the fabric crush elements required the increased DFAILM for stability, each of the simulations featured transverse plasticity in order to maintain a consistent material input deck.

With the modified model, it is possible to consider the transverse load cases separately and determine if plasticity is necessary in tension, compression, or both for the fabric crush element models. Each crush element was investigated using various DFAILM and DFAIL2M to do so, and it was determined that only two of the crush elements required plasticity for stability, while the rest could use the experimental strain-to-failure values for both DFAILM and DFAIL2M.

One such example is given in Figure 139, where results of the small c-channel element are shown to be stable and mostly unchanged with and without transverse plasticity.

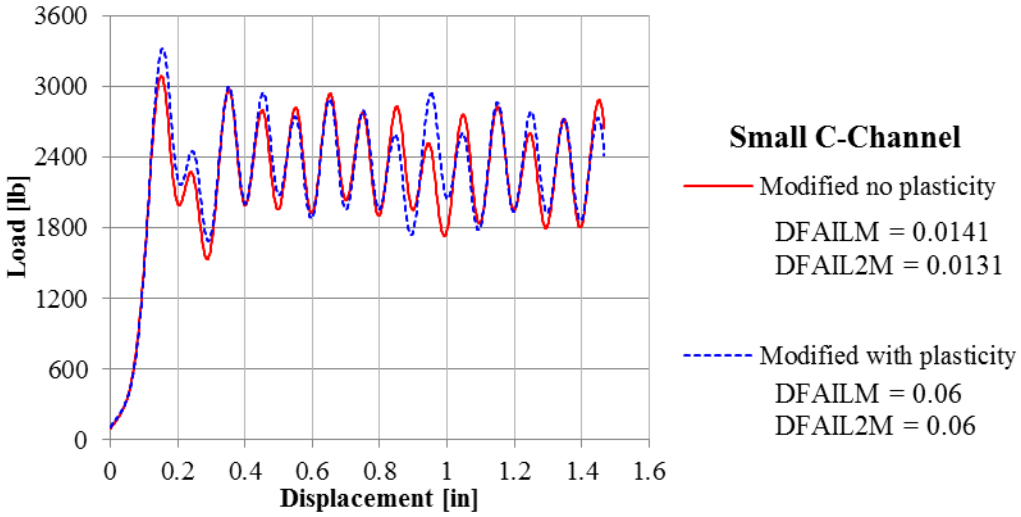

Figure 139. Stable crush simulation results of the small c-channel element using the modified material model with and without transverse plasticity.

The two crush elements which required transverse plasticity were the small corner and large c-channel elements. For both cases, plasticity was required in both the tension and compression transverse load cases in order to achieve stable and progressive crushing throughout the simulation. Results from using the modified model on the large c-channel element, Figure 140, show that without the plasticity in both DFAILM and DFAIL2M, the crush element is completely destabilized, and in fact experiences global buckling. In the case where only the tensile load case is given plasticity (DFAILM = 0.06; DFAIL2M = 0.0131), buckling occurs near the end of the simulation. This result indicates that the addition of the DFAIL2M parameter provides no real benefit for the simulation of the fabric material.

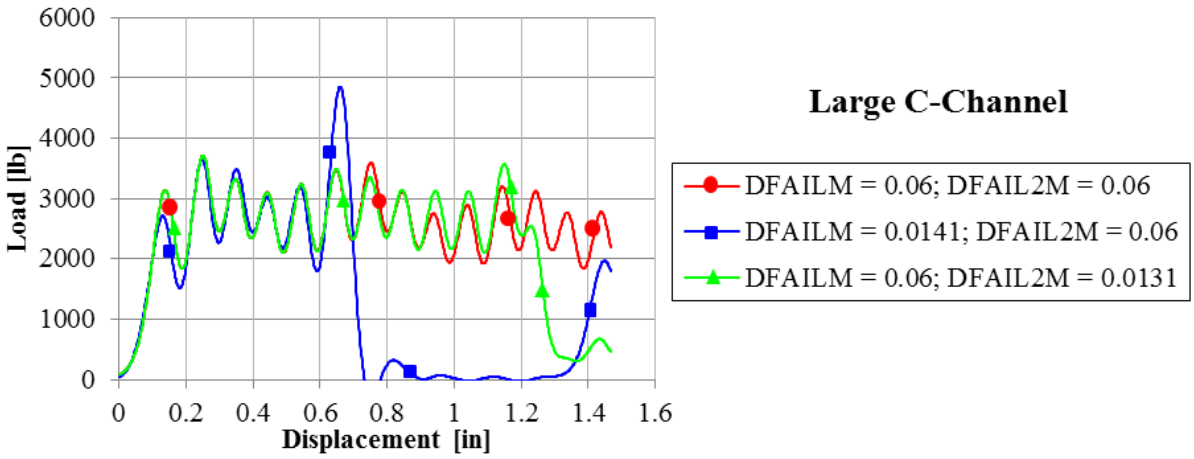

Figure 140. Crush curve results showing the destabilizing effect of changing the two transverse strain-to-failure parameters, DFAILM and DFAIL2M, in the modified model of the large c-channel crush element.

The modifications made to the MAT54 source code to improve the elastic response of the composite material model only provided benefits for the model of the UD material. These benefits were clearly evident in the single element simulations, where the true material behavior was exactly modeled; an accomplishment not possible without the modifications. The model of the fabric material was not improved using the modified model for elastic behavior, and in fact these modifications provided disruptions to the stability of the fabric crush element simulations. Overall, the modifications made for the elastic response are recommended only for the model of the UD material, and will not be used in any further models of the fabric material presented here.

Failure determination

Different failure criteria are implemented to investigate the effectiveness of the Hashin failure criteria used in MAT54, and to determine if other failure criteria can provide better results for crush simulation. Three new sets of failure criteria are investigated: a set of criteria meant for fabric materials, a maximum crush stress criterion for crush front elements, and a strain-energy based criterion. It should also be noted that LS-DYNA allows for the Tsai-Wu failure criterion

to be implemented in place of the Hashin criteria by selecting a value of 55 for the CRIT input parameter in MAT54, effectively making it the material model MAT55. This model is not appropriate for simulations which require modeling beyond failure, such as crash, since there is not a post-failure model included with MAT55. For this reason, the Tsai-Wu option of MAT54/55 is not explored in this research as a viable alternative for crash modeling.

Fabric failure criteria

The Hashin failure criteria used by MAT54 are meant to simulate the failure of a UD material, for which failure is driven by fiber breakage in the axial direction and matrix cracking in the transverse direction. For this reason, the axial and transverse failure modes are referred to as fiber and matrix modes, respectively. The matrix modes are specifically prescribed to predict matrix cracking, and in particular the compressive matrix failure mode is unique to the compressive fiber mode as evidenced by comparing the compressive criteria in Equation 26 and Equation 28. For the model of the fabric material system, it would seem that it would be more appropriate to apply the fiber failure criteria in both axial and transverse directions. It is proposed that the following failure criteria are used for the fabric material model,

Tensile Fiber Mode

$$\left(\frac{\sigma_{11}}{{F_1}^{tu}}\right)^2 + \beta\left(\frac{\sigma_{12}}{{F_{12}}^{u}}\right)^2 = 1 \qquad for\ \sigma_{11} > 0 \qquad \text{Eq. (16)}$$

Compressive Fiber Mode

$$\left(\frac{\sigma_{11}}{{F_1}^{cu}}\right)^2 = 1 \qquad for\ \sigma_{11} < 0 \qquad \text{Eq. (17)}$$

Tensile Matrix Mode

$$\left(\frac{\sigma_{22}}{{F_2}^{tu}}\right)^2 + \beta\left(\frac{\sigma_{12}}{{F_{12}}^{u}}\right)^2 = 1 \qquad for\ \sigma_{22} > 0 \qquad \text{Eq. (18)}$$

Compressive Matrix Mode

$$\left(\frac{\sigma_{22}}{F_2{}^{cu}}\right)^2 = 1 \qquad for\ \sigma_{22} < 0 \qquad \text{Eq. (19)}$$

The MAT54 code is modified to implement these fabric failure criteria, and the effect of the fabric failure criteria upon the single element and crush element simulations is investigated. For the fabric single element, no changes are observed and the result is identical to those using the Hashin failure criteria. This is expected since the single element is given basic tensile and compressive loading conditions that are shear-free. Without shear terms, the original Hashin failure criteria reduce to the fabric criteria, so the two single element simulations are expected to be identical.

The use of the fabric failure criteria has very little influence on the results of the crush element simulations as well. For most of the crush elements, the resulting crush curve is indistinguishable from the original MAT54 results, such as for the large corner element, Figure 141a. Only the large c-channel and small corner elements experience some instability, as shown in Figure 141b. It is worthwhile to note that these are also the only two elements which experienced instabilities due to the modified transverse strain-to-failure values, and in general seem to be more easily destabilized by changes in the model than any of the other elements. In general, it can be concluded that these fabric failure criteria provide no real benefit for crush modeling.

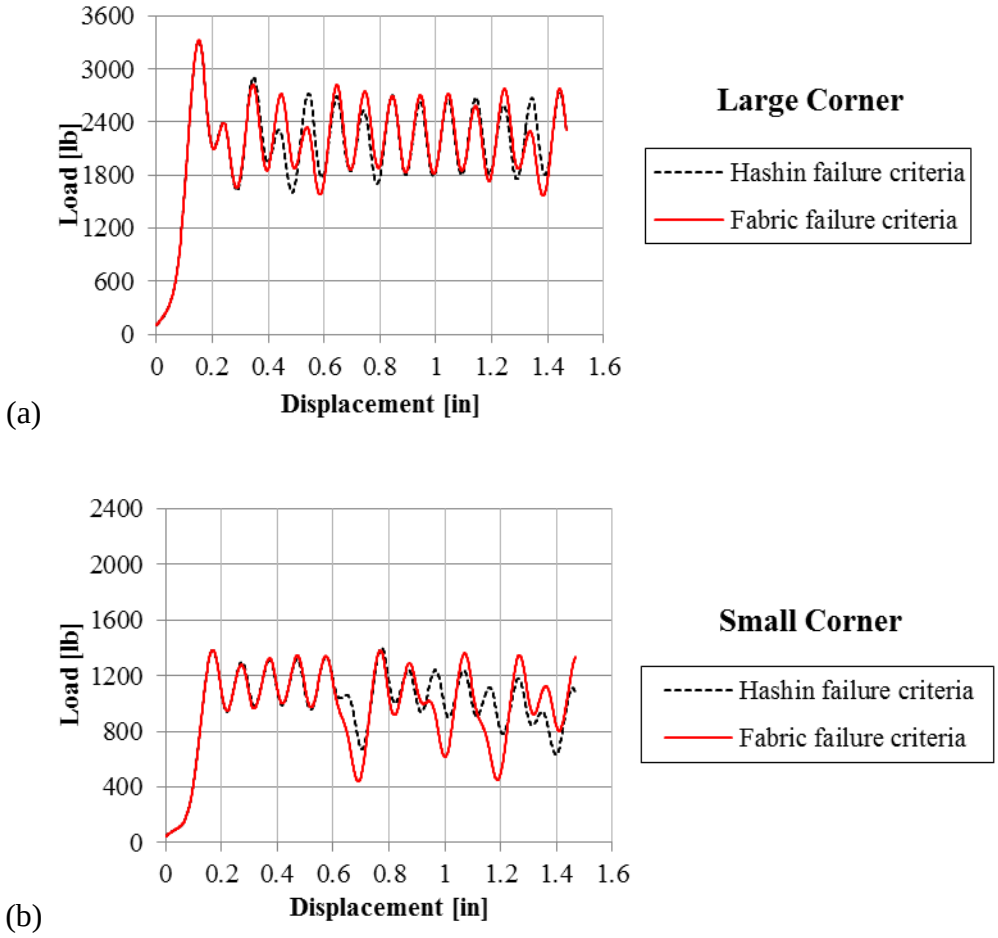

Figure 141. Effect upon the crush simulation results of changing the failure criteria from Hashin to the fabric criteria for the (a) large corner element and (b) small corner.

Crush stress criterion

It is desired to use an experimentally derived parameter as a simulation input in order to make material failure for crush simulation predictive for different crush element geometries, and not dependent on the trial and error calibration of the SOFT parameter. The crush stress criterion uses the average crush stress as measured from crush experiment as an input parameter to the simulation in place of the arbitrary material softening due to SOFT. A new maximum stress criterion is applied to crush front elements only, using the crush stress as the limiting parameter

rather than reducing the crush front element strengths by the SOFT parameter. The crush stress criterion is therefore,

$$\frac{\sigma_1}{\sigma_{crush}} = 1 \qquad \text{Eq. (20)}$$

Note that for this investigation, the crush stress criterion is only in effect in the axial direction of the element, thus the criterion utilizes the 1-direction stress component. This criterion is effective along with the existing Hashin criteria, which remain to account for any other failure modes the material may experience.

The new crush stress criterion is used in simulations of the semi-circular sinusoid crush element using both the UD and fabric material models. The average crush loads measured from the experiment of the UD and fabric sinusoid crush elements are 3,360 lb and 3,800 lb, respectively (as shown in Figure 72 and Figure 21c). Given the cross-sectional area of the semi-circular sinusoid element, the average crush stresses measured from experiment are 15 ksi for the UD element and 20 ksi for the fabric element. These values are used for the new SIGCR user input parameter, and SOFT is set to 1.0 in order to prevent material softening and instead allow for the crush stress criterion to remove elements at the crush-front. Note that the SIGCR parameter is input as a negative value since it is a compressive stress.

The resulting sinusoid crush simulation using the UD material model with the experimentally measured crush stress input, SIGCR = -15 ksi, yields a simulated crush curve with a crush load much lower than expected, as is shown in Figure 142. Increasing the maximum crush stress parameter value delays crush front element deletion and increases the crush load much in the same way that SOFT affects crush front element deletion and the resulting average crush load. It

is found that a SIGCR value of 130 ksi yields results which match the experiment well, which is nearly nine times the experimentally measured value of crush stress.

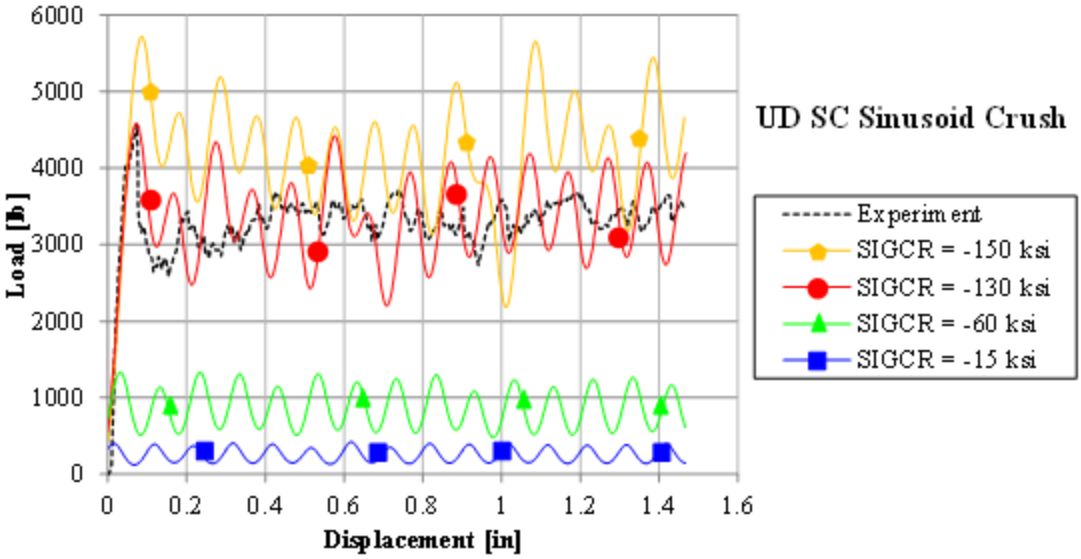

Figure 142. Effect of changing the SIGCR maximum crush stress parameter on the crush results of the semi-circular sinusoid using the UD modified material model.

The same trend is observed for the sinusoid crush simulation using the fabric material model, where a SIGCR value of 60 ksi, nearly three times the experimentally measured value of crush stress, simulates the crush experiment well, Figure 143. For the fabric material simulation, the initial load peak is not affected by the crush stress criterion since the crush front is not established until after the initial row of elements is deleted. The initial load peak is instead determined by the trigger thickness, which has not changed and remains matching the experiment well. This is different from the UD model since it uses a different contact definition for which the initial load peak represents the deletion of the first crush front row of elements, not the trigger. These contact definitions are discussed earlier during the development of the two baseline sinusoid crush models.

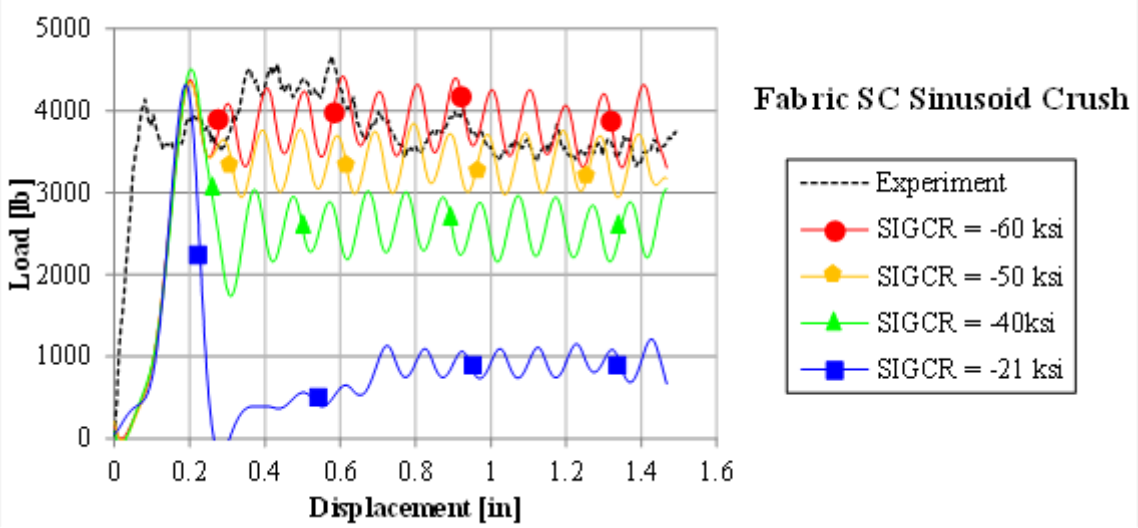

Figure 143. Effect of changing the SIGCR maximum crush stress parameter on the crush results of the semi-circular sinusoid using the fabric modified material model.

While it was expected that the experimentally measured crush stress value would be an appropriate limiting stress value for the crush front elements, these values have been shown to be too low. This is suspected to be due to the contact definition, and in particular the load-penetration curve which prescribes the load applied to the elements at the contact surface. This curve effectively alters the loads at the contact surface, causing elements to experience different stresses than they would at a purely rigid contact. Unfortunately, such a contact is required by MAT54, and contact definitions without LP curves have been shown to be ineffective with MAT54 elements (see Figure 86). For this reason, the SIGCR value which best matches the crush experiment is not the average crush stress as measured by the experiment, and its appropriate input value can only be determined by trial and error. In this way, the SIGCR parameter and the crush stress criterion have the same benefit to the MAT54 crush model as the SOFT parameter and the crush front material softening. Either parameter and crush front element deletion method can yield successful simulation results, but only after being calibrated against the crush element experiment.

Wolfe strain energy criterion

Another experimentally derived input parameter which could potentially replace the need for the empirically derived SOFT is strain energy. Wolfe's failure criterion utilizes axial, transverse, and shear strain energy components measured from coupon-level material testing to determine material failure in Equation 11, reproduced below.

$$\left(\frac{\int_{\varepsilon_1} \sigma_1 d\varepsilon_1}{\int_{\varepsilon_1^u} \sigma_1 d\varepsilon_1}\right)^{m_1} + \left(\frac{\int_{\varepsilon_2} \sigma_2 d\varepsilon_2}{\int_{\varepsilon_2^u} \sigma_2 d\varepsilon_2}\right)^{m_2} + \left(\frac{\int_{\varepsilon_6} \sigma_6 d\varepsilon_6}{\int_{\varepsilon_6^u} \sigma_6 d\varepsilon_6}\right)^{m_6} = 1 \qquad \text{Eq. (11)}$$

In order to implement this failure criterion into the modified MAT54 material model, several new user input parameters are required to define the ultimate strain energy values of the material, as listed in Table 23, as well as the three shape functions, m_1, m_2, and m_6. Altogether, eight new user inputs are implemented, as listed in Table 22.

Table 22. New modified MAT54 user input parameters added for Wolfe's strain energy failure criterion.

SEFT	Ultimate axial (fiber) tensile strain energy component
SEFC	Ultimate axial (fiber) compressive strain energy component
SEMT	Ultimate transverse (matrix) tensile strain energy component
SEMC	Ultimate transverse (matrix) compressive strain energy component
SES	Ultimate shear strain energy component
M1	Shape function value for the axial strain energy component
M2	Shape function value for the transverse strain energy component
M6	Shape function value for the shear strain energy component

The Wolfe failure criterion is first enacted along with the existing Hashin failure criteria such that either may cause element failure. Single element simulations were run using the modified material model for both the UD and fabric material models. The ultimate strain energy values input into the modified model were measured from experiment and are given in Table 23. The shape function parameters, M1, M2, and M6, were initially given default values of 1.0, as

suggested by Wolfe [61]. Results from both the UD and fabric material models indicate that the Wolfe failure criterion prematurely predicts element failure, as shown in the stress-strain curves of Figure 144. This result is not unexpected, as the results published by Wolfe when implementing this strain energy failure criterion also under-predicted failure for several different composite material systems undergoing biaxial loading conditions.

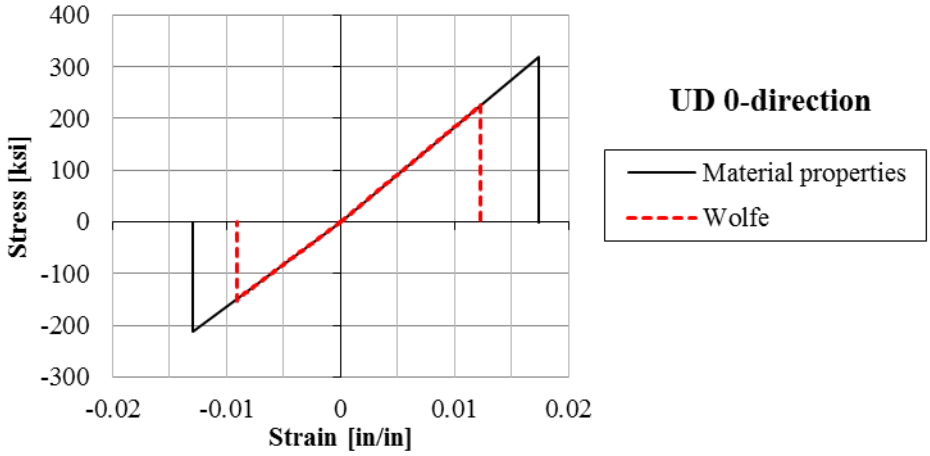

(a)

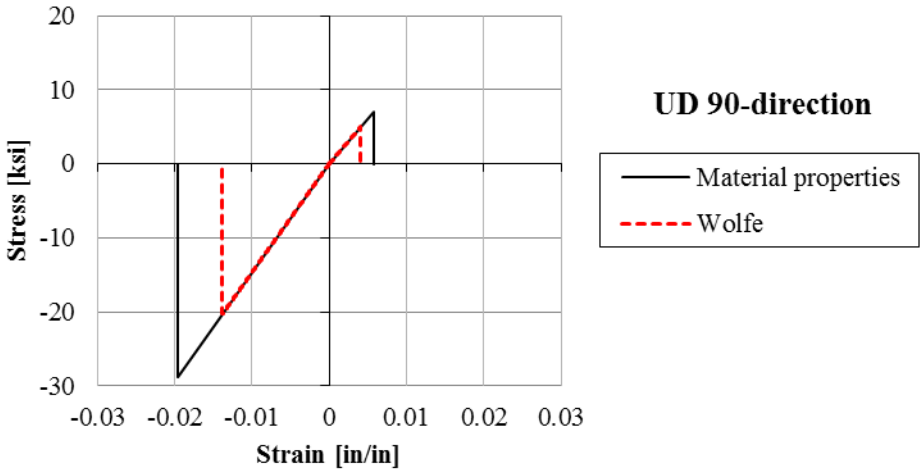

(b)

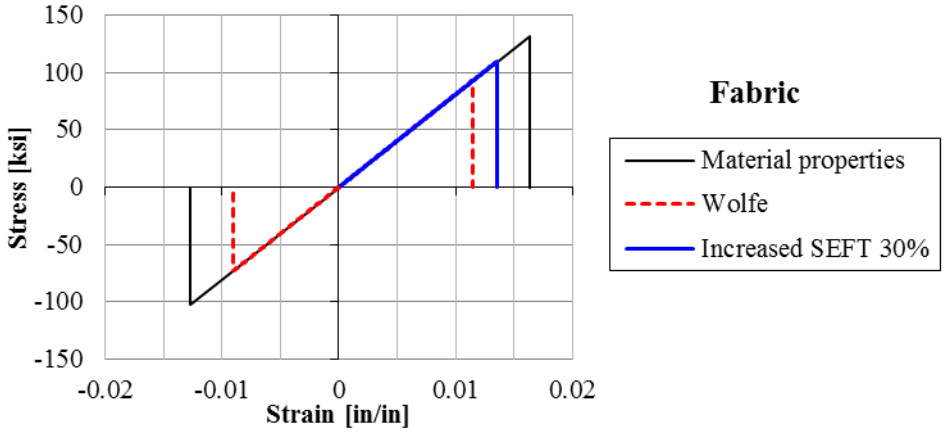

(c)

Figure 144. Single element stress-strain curves which show the result of using the Wolfe failure criterion against the material properties for the UD material in the (a) axial and (b) transverse, as well as for the (c) fabric material system.

Adjustments can be made to the new strain energy and shape function input parameters in order to reduce the error between simulation and experiment, as shown in Figure 144c, however doing so makes the implementation of the Wolfe criterion an exercise of trial and error for several new parameters. Experimentally derived values are preferred and used in the crush simulation of the semi-circular sinusoid element. The result is that several elements are deleted prematurely away from the crush front, and stable crushing is not achieved for either material system, Figure 145.

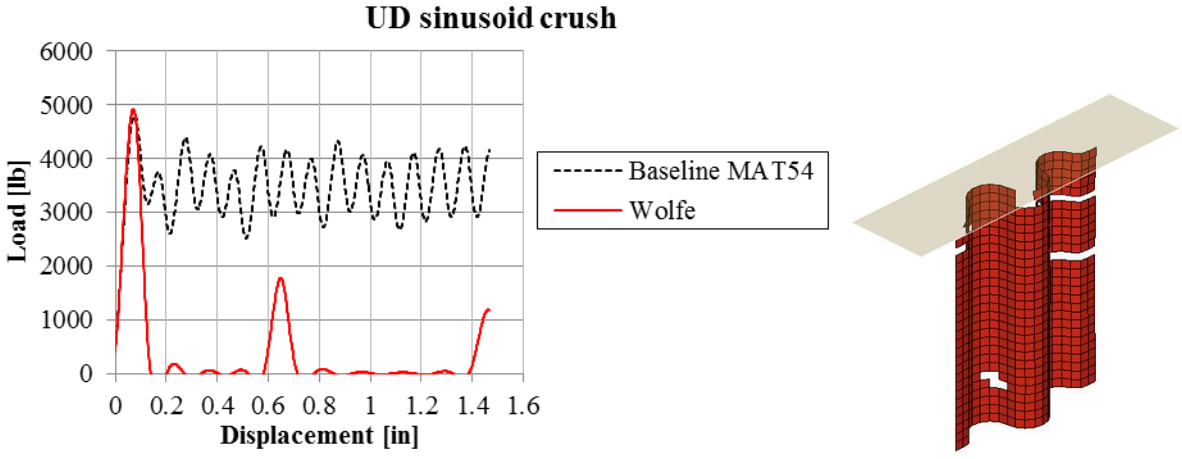

(a)

(b)

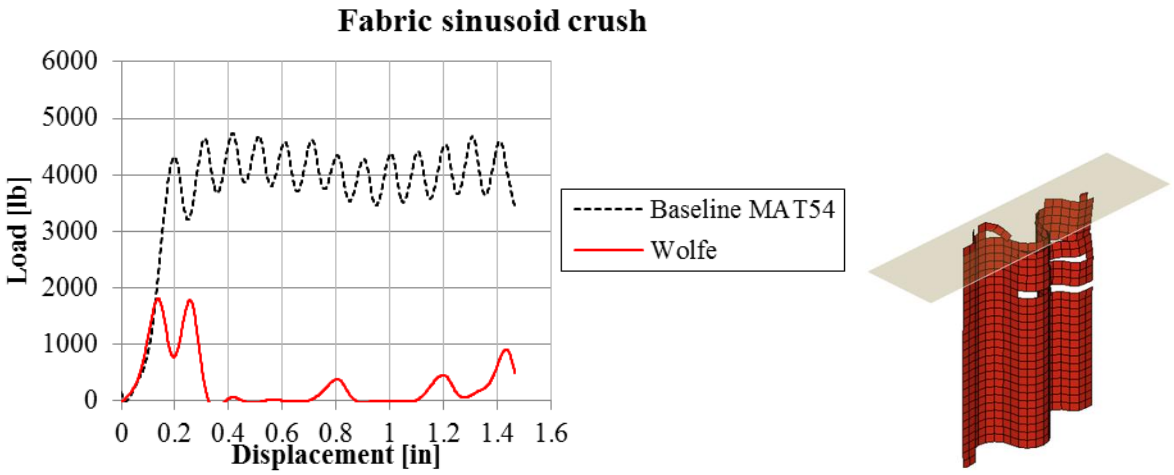

Figure 145. Unstable crush simulation results from using the Wolfe failure criterion in addition to the Hashin failure criteria on the sinusoidal crush element for the (a) UD and (b) fabric material models as compared against results from the baseline MAT54 models.

Implementing the stain energy based Wolfe failure criterion in addition to the existing Hashin criteria causes element failure predictions to be worse in situations where the Hashin criteria had successfully predicted failure (i.e. in simple loading conditions and away from the crush front). In these situations no improvement of failure prediction is necessary, and instead it is the goal to improve failure prediction at the crush front without having to rely on an empirical parameter such as SOFT. In light of this, the Wolfe failure criterion is changed such that it is only active at the crush front where premature failure predictions may be beneficial to the material model.

Simulations of the sinusoid crush element are rerun employing the Wolfe criterion only at the crush front, while setting SOFT to a value of 0.999 to prevent material softening at the crush front. The simulation results of the sinusoid crush element are greatly improved from using Wolfe on all elements, Figure 146, and the crush front Wolfe failure criterion produces a similar but less stable result than the baseline MAT54 simulations which use the calibrated SOFT parameter for the crush front elements.

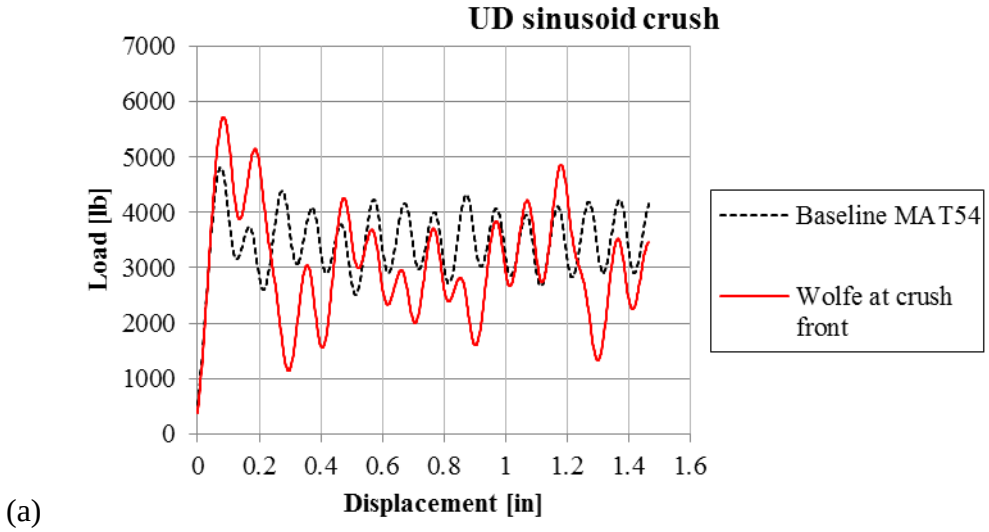

(a)

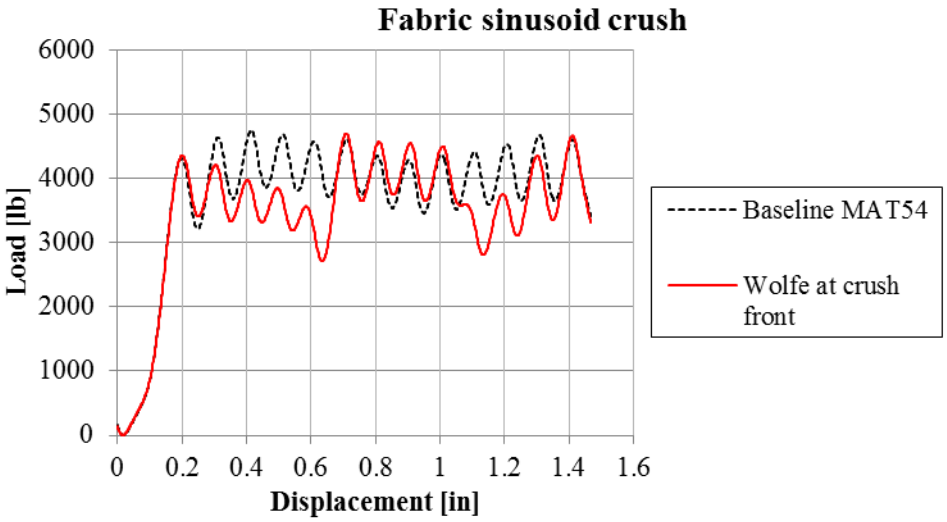

(b)

Figure 146. Crush simulation results from using the Wolfe failure criterion for the crush front elements in place of the SOFT parameter for the sinusoidal crush element using the (a) UD and (b) fabric material models as compared against results from the baseline MAT54 models.

While the simulation result of the sinusoid elements shows promise, simulations of the other crush elements reveal that the Wolfe criterion cannot predict the crushing response well. For example, Figure 147 shows that the crush simulation of the small c-channel element using the crush front Wolfe criterion produces a result where the load peak is more than double that of the

baseline simulation which causes failures beyond the crush front and ultimately global buckling of the crush element. By reducing all of the strain energy input parameters artificially by 80%, a good match to the baseline MAT54 crush simulation can be achieved, however this property reduction is entirely arbitrary and, like the SOFT parameter, cannot be determined without having the experimental results against which to calibrate the simulation. Trials in which only the shape function input parameters were adjusted did not produce improved crush simulation results.

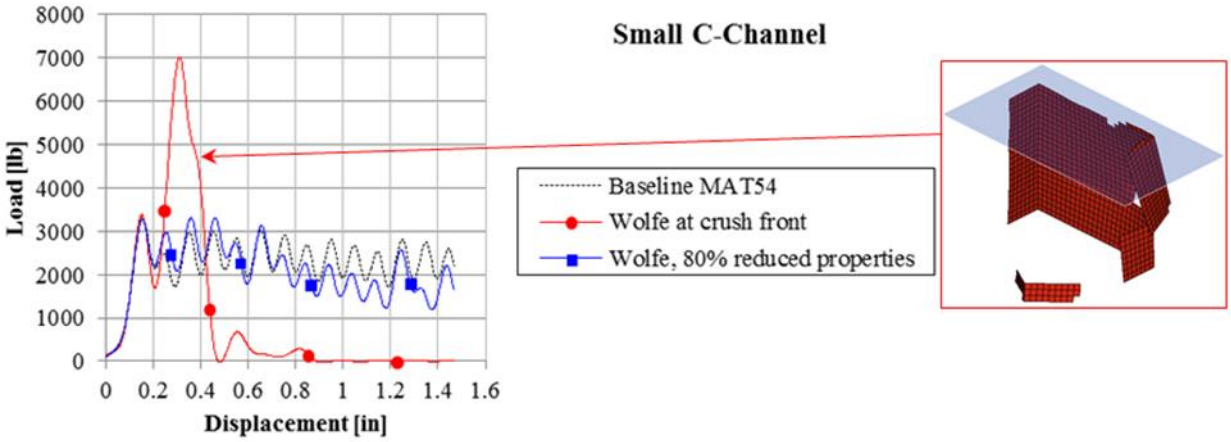

Figure 147. Crush simulation of the small c-channel element using the Wolfe criterion on the crush front elements with measured material properties, and artificially reduced properties, compared against the baseline MAT54 crush simulation.

While all of the Wolfe criterion strain energy input parameters are derived from coupon-level experiments, these baseline values do not produce good crush simulation results and ultimately, arbitrary calibration is necessary when using the crush front Wolfe criterion. For this reason, the Wolfe failure criterion does not provide improvement in failure predictions against the baseline MAT54 method of using the SOFT crush front reduction parameter with the Hashin criteria for failure prediction. At best, the crush front Wolfe criterion can be made to produce similar results to the baseline MAT54 simulations by calibrating several of its strain energy input

parameters. This approach is not preferable to the baseline MAT54 strategy in which only a single input parameter requires calibration.

Post-failure degradation

The post-failure property degradation scheme in MAT54 produces an elastic-perfectly plastic stress-strain response of the material. While this can be avoided by defining the strain-to-failure parameters to be coincident with failure, thereby creating a perfectly elastic until brittle failure behavior, it has been shown that some strain-to-failure parameters in MAT54 must be artificially increased in order to produce stable crush simulation results for some material systems. For this reason, the perfectly plastic curve following failure cannot be ignored, and several alternative post-failure property degradation schemes are investigated to determine if improvements can be made for crush simulations.

Four new approaches to model material behavior following failure are investigated: 1) reduce stress immediately to zero as a brittle material coupon behaves, 2) linearly reduce stress to zero in similar appears to a continuum damage mechanics model, 3) linearly reduce stress to a specified constant value until the strain-to-failure is achieved, and 4) reduce stress by 1% each time-step until the strain-to-failure is achieved. These approaches investigated are summarized in an idealized stress-strain curve in Figure 148.

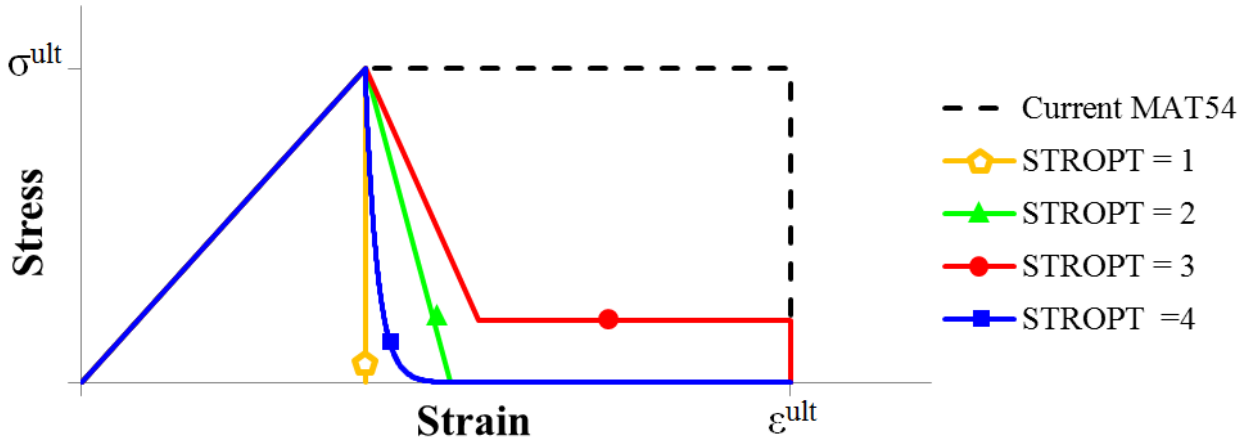

Figure 148. Idealized material stress-strain curves demonstrating four alternative post-failure property degradation schemes investigated.

Alternative versions of the modified post-failure model are also developed specifically to address crush simulation. Recall that for crash and impact simulations, the MAT54 transverse strain-to-failure parameter DFAILM must be increased to provide stability. If DFAILM is not increased, then the material behavior is linear elastic until a perfectly brittle failure upon which the stress goes to zero. In this scenario the post-failure behavior cannot be employed and is therefore not relevant, but because DFAILM is increased the post-failure behavior in the transverse direction of the element becomes important to consider. It is unknown if the artificial increase in DFAILM serves to stabilize the elements at the crush-front as they experience failure or those beyond the crush-front to prevent premature deletion. By isolating the degradation scheme to be applicable only for the crush-front elements or the rest of the elements, it can be determined for which elements the artificial plasticity is effective and necessary for providing stability. The alternative versions of the modified post-failure model isolate the application of the stress degradation schemes to the crush-front elements or the rest of the elements, as shown in Figure 149. In addition to separating the behaviors of the crush-front and all other elements, the degradation schemes have the option to be applied in only the transverse direction, which is the

direction in which the artificially increased DFAILM allows for the degradation scheme to be applicable. These alternative versions of the modified post-failure stress degradation code are only used in crush element simulations in which crush-front elements are active.

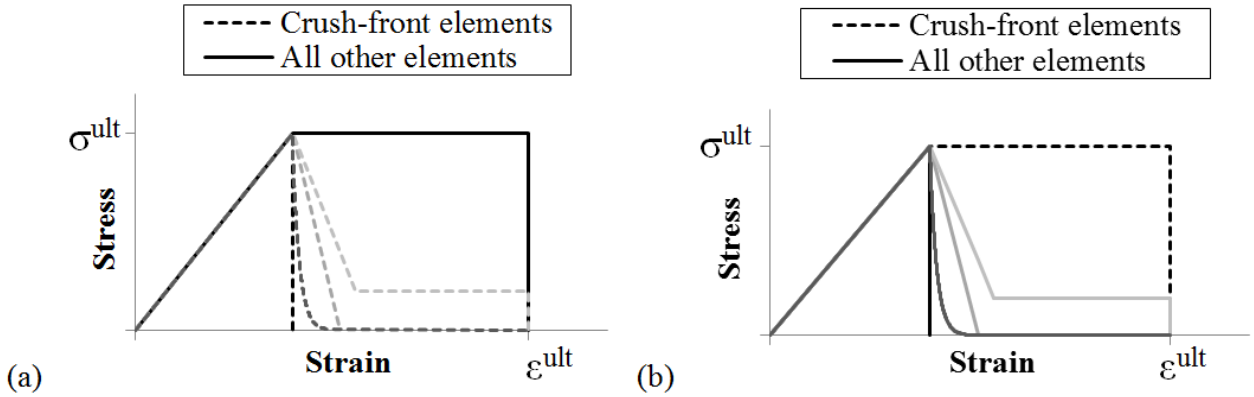

Figure 149. Idealized material stress-strain curves demonstrating the two alternate versions of the modified code in which stress degradation options presented in Figure 148 are applied to (a) crush-front elements only and (b) to all other elements only.

Single element results

The new post-failure stress degradation options are first tested using a single element under simple loading conditions in order to confirm that these new post-failure behavior schemes work as intended. The UD material model is used for this exercise, but in order to demonstrate the new behaviors after failure, the strain-to-failure parameters are modified such that the element is not deleted prior to the observation of the new post-failure behaviors. All of the failure strain parameters are extended to the arbitrary value of ±0.024 in/in. When the baseline failure strain values are used, the single elements behave exactly the same as the unmodified MAT54 material model. Each of the four post-failure stress degradation options are used with both the 0° and 90° UD single elements in tension and compression, using arbitrary baseline values of NDGRAD = 1,000 and SIGLIM = 0.2. The stress-strain results of the 0° element are given in Figure 150 while the stress-strain results from the 90° element are given in Figure 151.

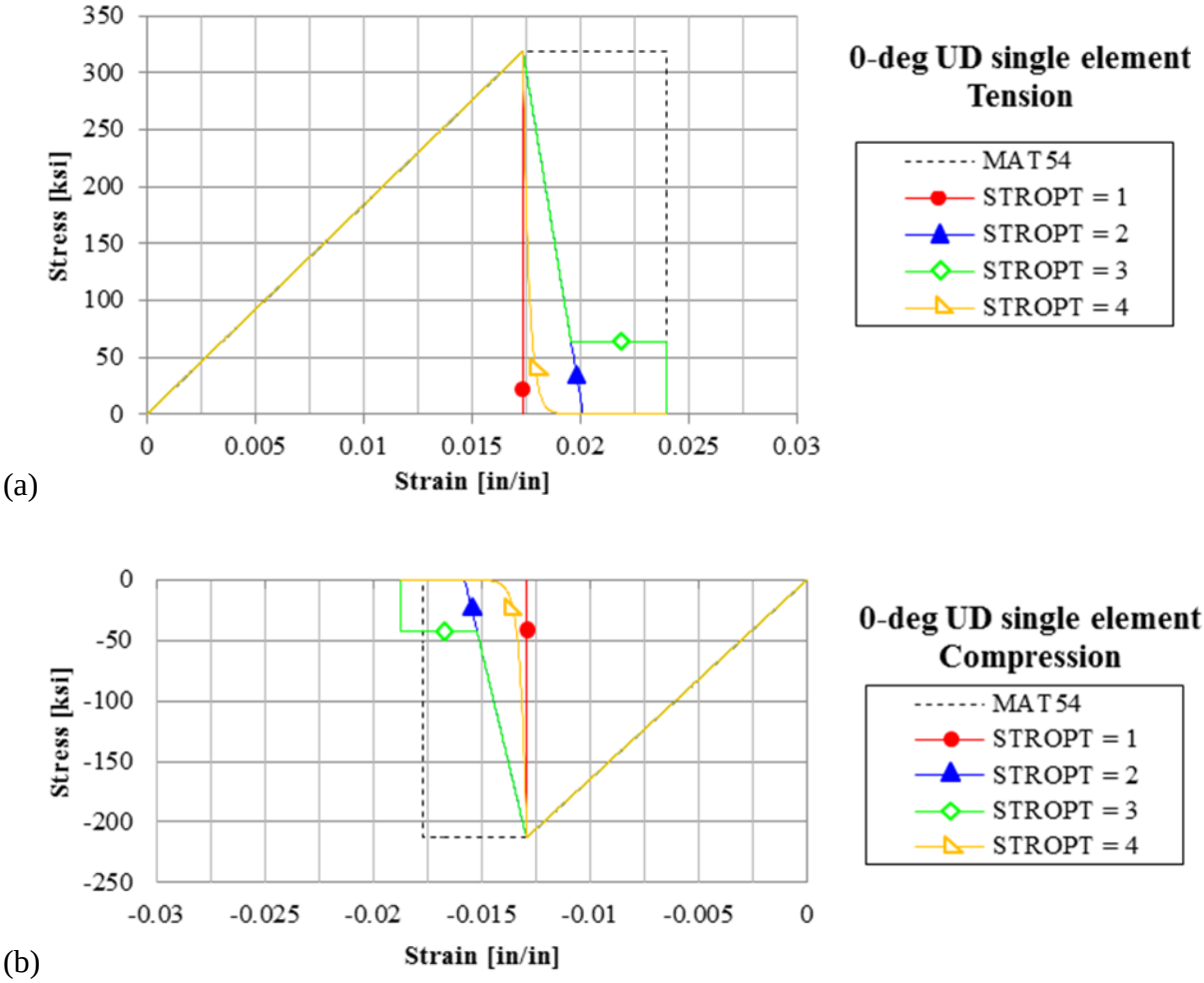

Figure 150. Stress-strain results of the 0° UD single element implementing four new post-failure stress degradation options under (a) tensile and (b) compressive loading conditions.

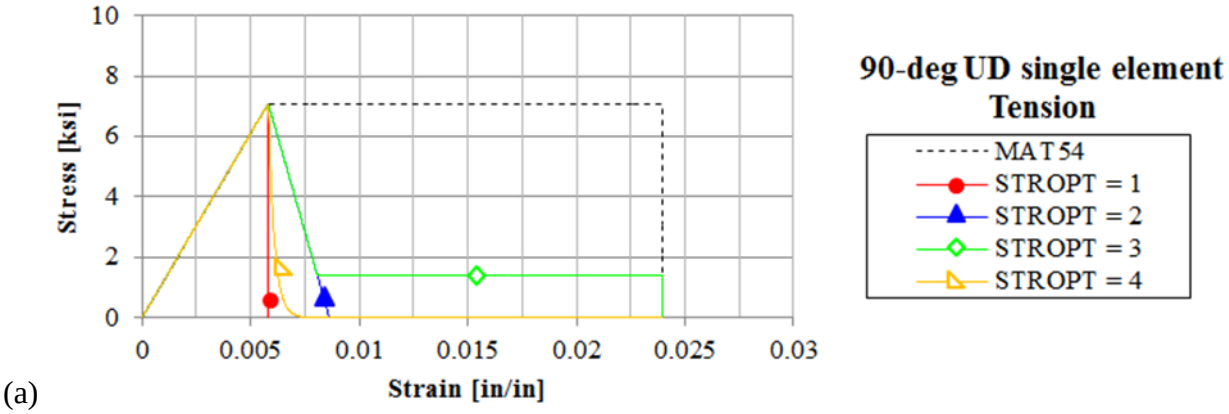

(a)

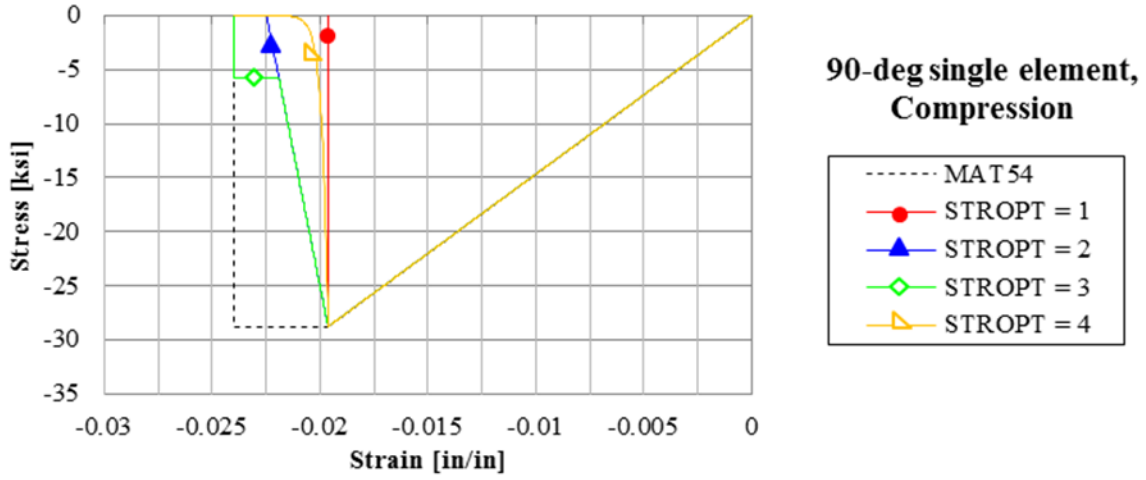

(b)

Figure 151. Stress-strain results of the 90° UD single element implementing four new post-failure stress degradation options under (a) tensile and (b) compressive loading conditions.

It is important to test all four load cases in order to make sure that all four failure modes are followed by the correct stress degradation option. From the results of the single element simulations, it is clear that the post-failure degradation schemes are working as intended and the implementation of the modified code is a success. For STROPT = 1, the element is deleted as soon as failure occurs for all load cases. The slope of the linear degradation in all four load cases, and for both STROPT = 2 and 3, is the same as NDGRAD remains constant. The plastic stress level for STROPT = 3 is 20% of the failure stress in all four load cases, and a logarithmic-like decay is observed in all load cases when STROPT = 4.

A parametric study is conducted on the two new user input parameters, NDGRAD and SIGLIM, to observe their influence on the 0° UD single element simulation under tensile loading. The NDGRAD parameter is varied using values of 100, 500, 1,000, and 2,000 iterations, while the SIGLIM parameter is varied using values of 5%, 20% and 40%. Figure 152 demonstrates that the modified model works as intended, and the NDGRAD parameter directly influences the degradation slope while the SIGLIM parameter directly influences the plastic stress level. These single element simulations and short parametric study have confirmed that the new modified post-failure degradation schemes are all working as intended.

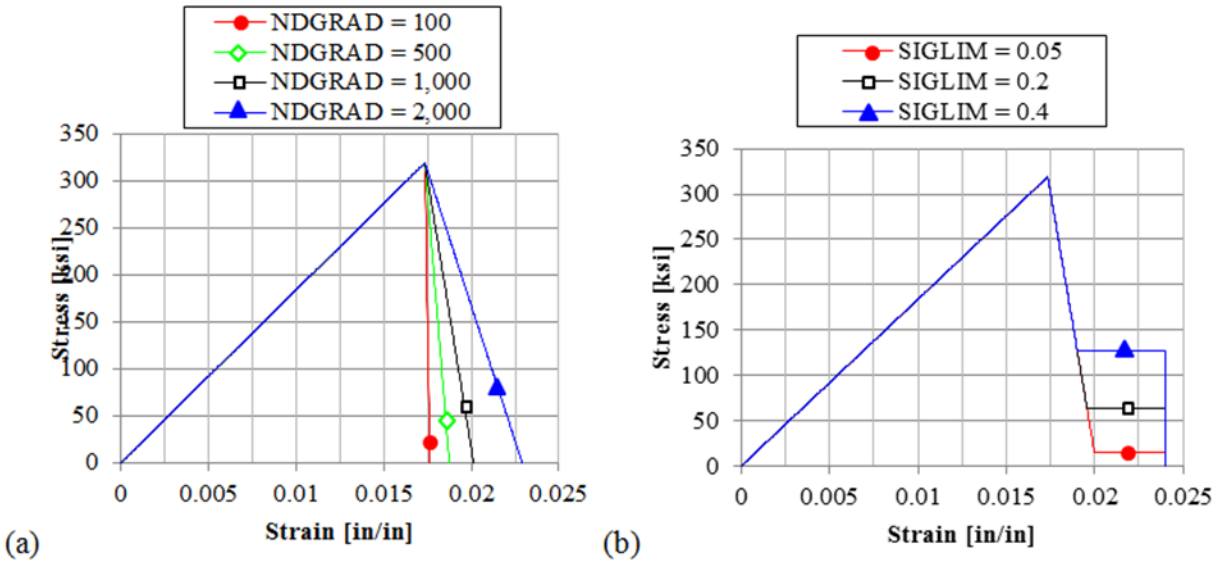

Figure 152. Influence of the new (a) NDGRAD (STROPT = 2) and (b) SIGLIM (STROPT = 3) parameters on the post-failure stress degradation schemes in 0° single element simulation under tensile loading.

Crush simulation results

The new post-degradation options are implemented with the fabric sinusoid crush element model. For the crush simulations, there are two additional variables to consider for stress degradation in the simulation test matrix. First, there are three options regarding which elements experience degradation following failure: all elements, only crush-front elements, or all except crush-front elements. Second, there are also three options regarding which stress components experience degradation: axial stresses, transverse and shear stresses, or all stresses. For each combination of these two variables, the four new post-failure stress degradation schemes are investigated and the resulting idealized material stress-strain curves are different for each case depending on the given variables. Figure 153 presents a table of the idealized material stress-strain curves in terms of the two variables: elements degraded and stresses degraded. In this visualization of the test matrix, the default MAT54 plastic behavior following failure is represented as STROPT = 0. The test matrix presented in this way identifies nine general cases for which all STROPT options are investigated in the crush simulations. The simulated load-displacement curves from this investigation, using baseline values for NDGRAD and SIGLIM, are presented in the same format as the test matrix for ease of interpretation, Figure 154. In general, the result for most cases is highly unstable. In all cases in which the crush-front elements are subjected to stress degradation following failure, presented in the first two columns of Figure 154, every simulation is destabilized and in several cases severely so. The crush-front elements in particular require plasticity within their material stress-strain definition for stability.

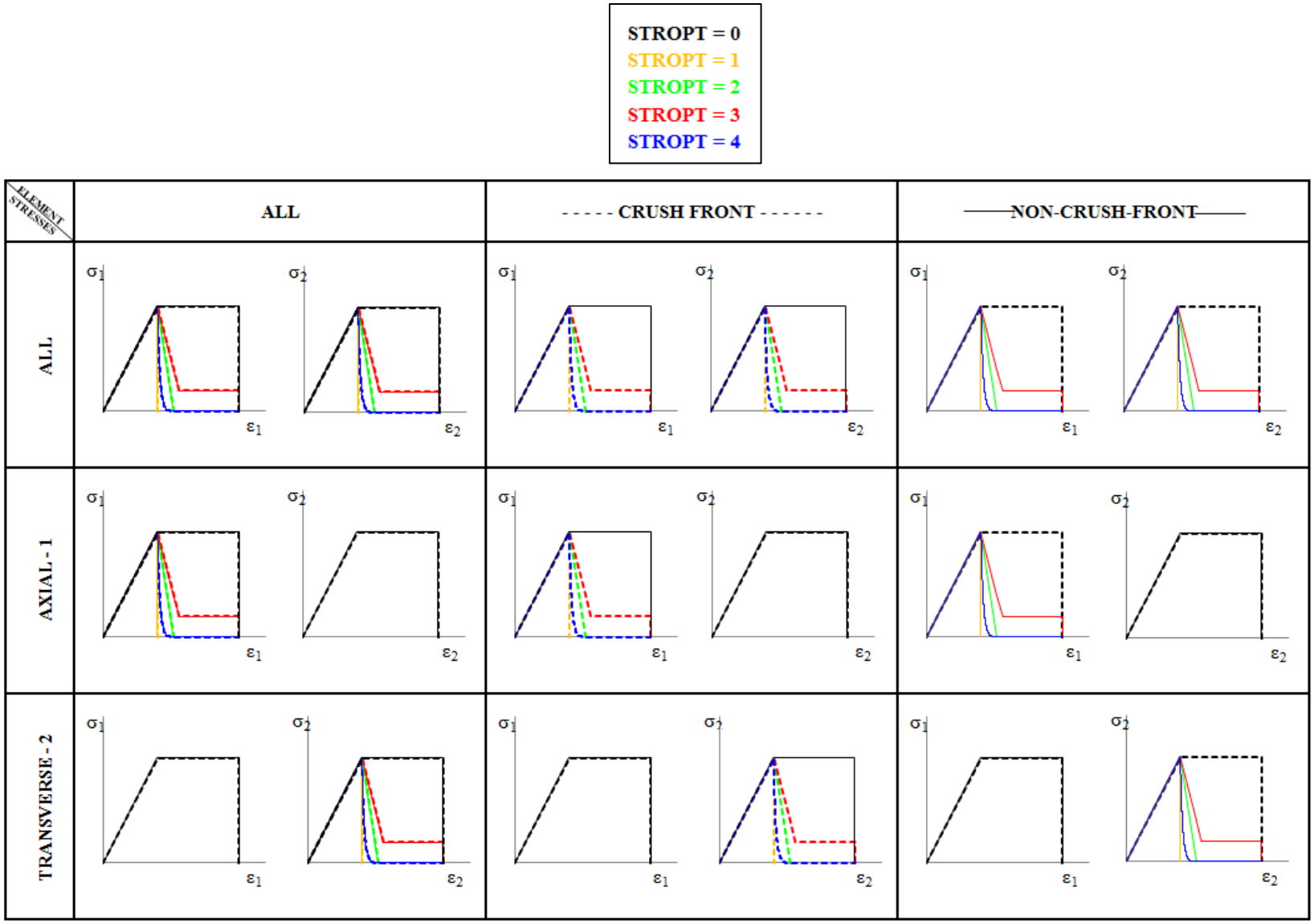

Figure 153. Idealized material stress-strain curves implemented in the test matrix of the five different post-failure degradation schemes applied to different elements: crush front (dashed) and non-crush-front (solid); and applied to different stress components: axial (1) and transverse (2). Note that the axial curves are greatly exaggerated in the amount of plasticity in order to showcase the degradation options, where in the baseline fabric material deck there is no significant amount of plasticity.

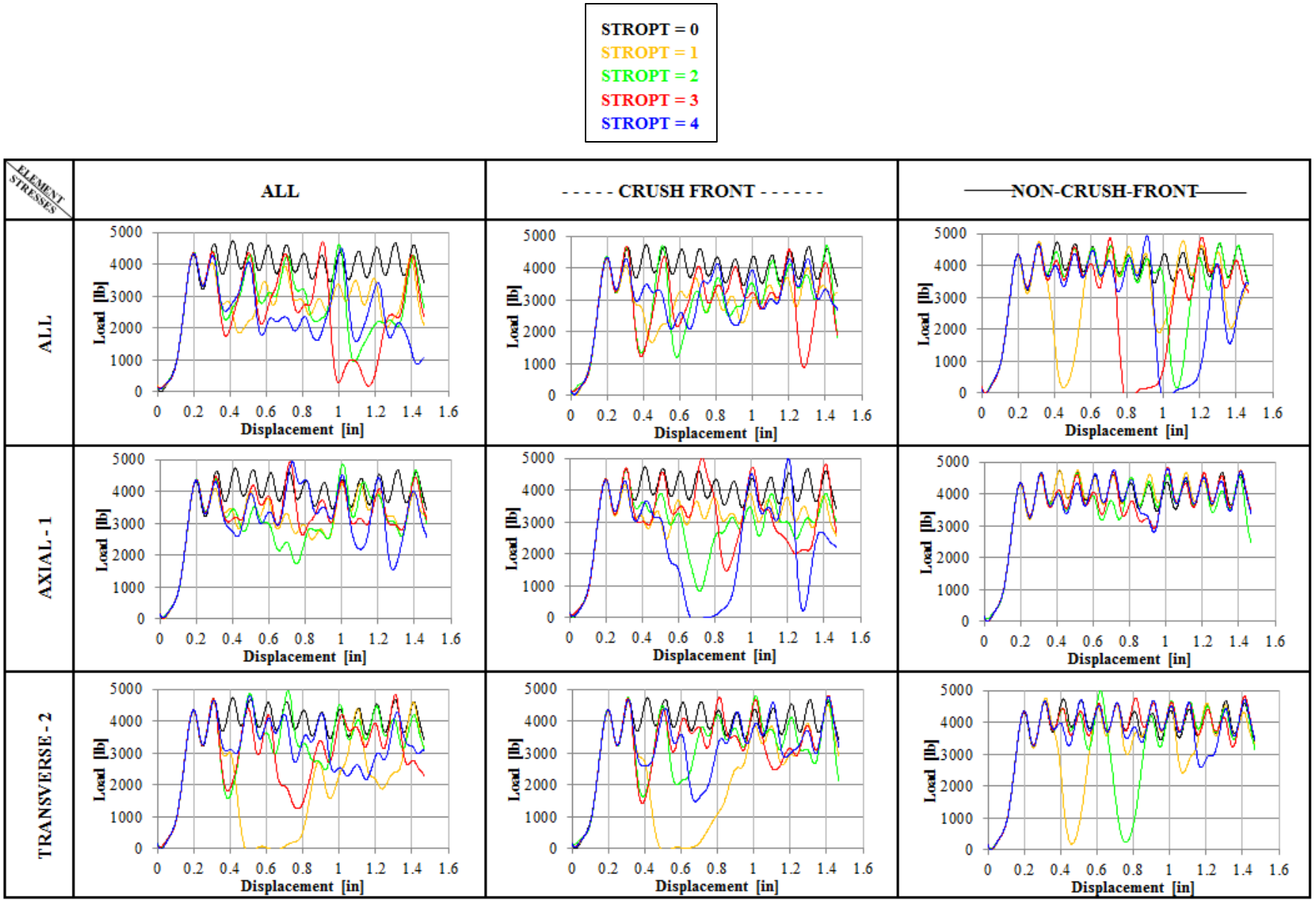

Figure 154. Simulated load-displacement crush curve results of the fabric sinusoid element subjected to the test matrix of different post-failure degradation options outlined in Figure 153.

In the cases where only the non-crush-front elements are subjected to the stress degradation schemes, presented in the third column of Figure 154, it is possible to achieve stability. In particular, when only the axial stresses are degraded and the transverse stresses are allowed to plastically deform after failure, all of the stress degradation options produce stable crush results. When the transverse stresses are not allowed to plastically deform, however, two of the degradation schemes are destabilized in the middle of seemingly stable crushing.

From these initial results, it seems as though crush-front elements must always be allowed the plastically deform, and perhaps transverse stresses must also be allowed plastic deformation following failure. A parametric study of the NDGRAD and SIGLIM parameters is performed to study their effect on the crush simulation results, both to determine if variations of these parameters can stabilize the unstable simulations and to determine the effect upon an already stable crush simulation. Changes of these two parameters are only effective for STROPT = 2 and 3. For cases where crush-front elements are degraded, columns one and two from the test matrix in Figure 153, several parametric trials using a variety of NDGRAD and SIGLIM values were consistently unable to stabilize the crush simulation. Parametric results of NDGRAD and SIGLIM are shown for the case where all stresses are degraded in all elements following failure in Figure 155. This result confirms that these parameters alone are not influential enough to stabilize an unsuccessful simulation, and that implementing new post-failure degradation schemes for crush-front elements worsens the crush simulation performance of MAT54. Crush-front elements must always be allowed to plastically deform for crash simulation.

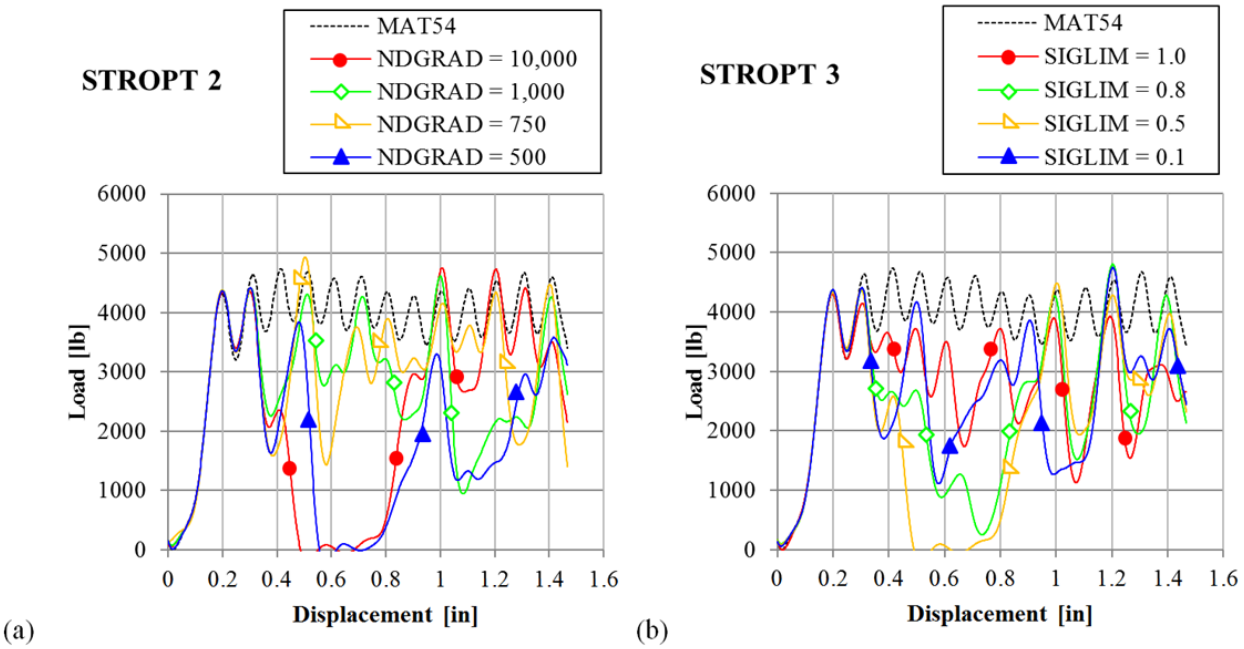

Figure 155. Changing the (a) NDGRAD and (b) SIGLIM modified MAT54 parameters when degradation is applied to all stresses in all elements does not stabilize the simulation of the sinusoid crush element.

The NDGRAD and SIGLIM parameters are varied for crush simulations for cases where only the non-crush-front elements are degraded, column three from the test matrix in Figure 153. For the case where only axial stresses are degraded (second row in Figure 153), there is little room for improvement of the already stable results, and these new parameters are investigated to see if they have a negative impact on the simulation results. Low values of NDGRAD and SIGLIM cause small destabilizations in the simulation, while values near the baseline and higher remain stable, Figure 156. Considering the shape of the material stress-strain curve, higher values of NDGRAD cause a lower degradation slope that is closer in shape to the perfectly plastic default MAT54 behavior. The same is true with higher values of SIGLIM, which is perhaps why higher values of both parameters promote stability.

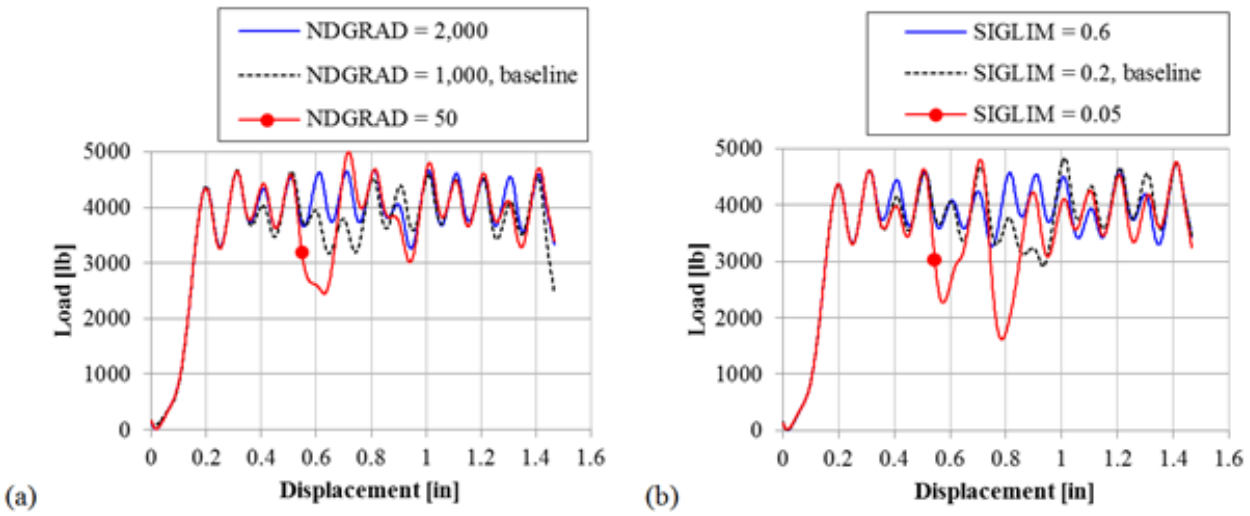

Figure 156. Effect of changing the (a) NDGRAD and (b) SIGLIM modified MAT54 parameters when degradation is applied to axial stresses only in non-crush-front elements.

The new post-failure material behavior models do not provide improvement over the default MAT54 perfectly plastic behavior. Furthermore, the new user input parameters which control the shape of the material stress-strain curve following failure do not significantly influence the result of the simulation enough to warrant further investigation. While a stable result can be obtained, it requires application of the degradation scheme to specific elements and specific stresses, and this strategy does not offer improvement over the default MAT54 model. In addition to the sinusoid crush element, other crush element geometries were investigated using the modified post-failure model with similar unsatisfactory results. For example, select results from the small c-channel crush element implementing the modified post-failure model are shown in Figure 157.

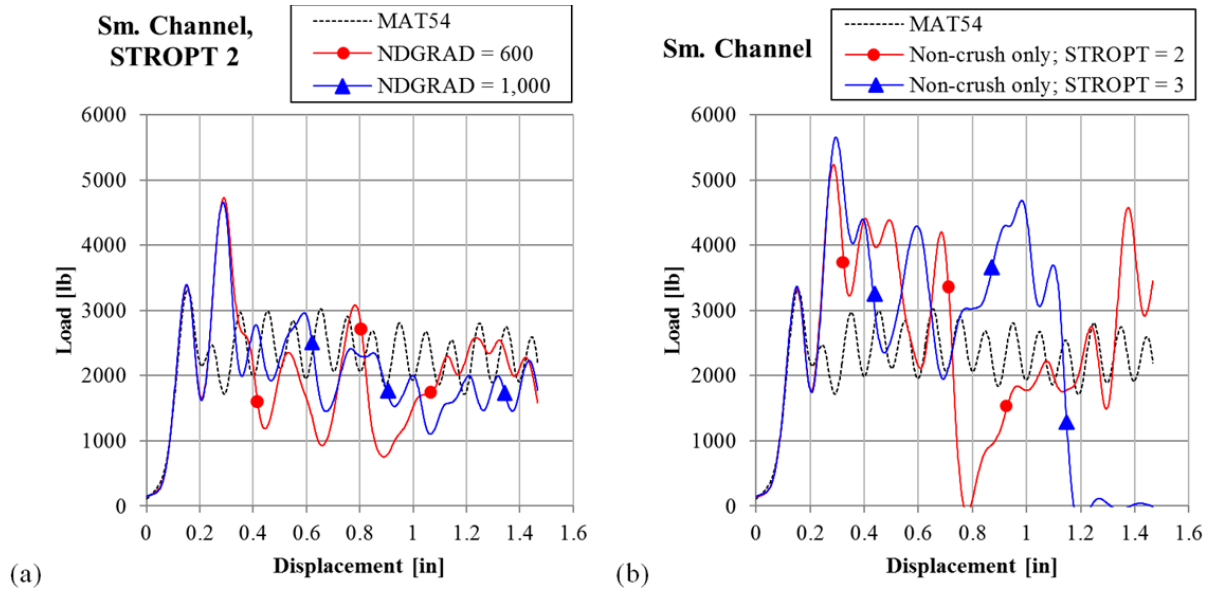

Figure 157. Simulation results from using modified post-failure stress degradation model on the small c-channel crush element (a) applied to all elements using STROPT = 2 and varying NDGRAD values and (b) applied to non-crush-elements only, using different STROPT options.

Conclusions

Access to the Fortran source code for MAT54 allowed for both a better understanding of this material model as well as the capability to modify and implement a modified composite damage material model in LS-DYNA simulations. The modification strategy of this research for MAT54 has resulted in a composite material model with a better capability to simulate the elastic behavior of an anisotropic UD composite material, has validated the selection of the built-in Hashin failure criteria to determine lamina failure, and has presented several alternatives to the post-failure model of the material. The modified model features the addition of compressive constitutive material properties which has expanded the capability of MAT54 such that it may more accurately model the composite material response to complex multi-axial loading conditions. This is an important addition since composite material systems often have significantly different moduli in tension and compression. This particular modification improved

MAT54 such that it simulated the elastic behavior exactly as the experimental material coupon tests for the UD material system.

Three other sets of failure criteria options were added in place of (or in some trials, in addition to) the default Hashin criteria. These other criteria each demonstrated an equal or worse capability to predict initial material failure, and this study has strongly validated the use of Hashin to predict the onset of initial material failure. The default approach for modeling the crush-front elements by reducing their strength using the SOFT parameter proved to be most effective for crush modeling, although an alternative method developed as a part of the modification strategy was shown to work just as well. An equivalent simulation result can be obtained by using a crush stress criterion which evaluates crush-front elements using a user-defined lower material ultimate strength. The input maximum crush stress parameter must be calibrated using experimental crush curves in the same way SOFT is calibrated.

Finally, modifications made to implement a variety of different post-failure material behaviors proved to demonstrate the particular sensitivity of crush simulations to the post-failure stress profile of the material. Four different post-failure material behaviors were implemented, each with user controlled variable stress profiles. These post-failure stress profiles varied from dropping the stress to zero as would happen in a material coupon test, to a linear stress degradation down to a constant stress level similar to that found in continuum damage mechanics composite models. Of the many different degradation methods applied to different elements and stress components produced, the resulting crush simulations did not outperform the strategy to use pure material plasticity following failure. The requirement for a high degree of material plasticity following the onset of failure in crush simulation was clearly demonstrated in the modification strategy.

Guideline for using MAT54 in crush analysis

This section sets out to provide guidelines for using the LS-DYNA built-in composite damage material model MAT54 in simulations of composite structures subjected to crush loading. Much of the information provided here comes from performing a thorough investigation on MAT54 for use in crush and impact simulations, as presented earlier, as well as some information collected from materials distributed by LSTC to its customers [11] [104] [105] [106] [107], and specified journal articles. This document focuses particularly on MAT54 and other portions of the FEA model development which affect or are affected by MAT54. For a more comprehensive review of other aspects of composite crash modeling, a NASA Technical Report from Fasanella and Jackson [50] entitled, "Best Practices for Crash Modeling and Simulation" is highly recommended. The Fasanella and Jackson report contains detailed information pertaining to many aspects of crash modeling which will not be discussed here such as the development of the geometry CAD model, dummy models, lumped mass approximations, complex initial conditions, etc. The purpose of this section is to outline the modeling strategy developed for using MAT54 for crush analysis, and most of the discussion will be relevant to the material model and aspects of the simulation which influence the material model.

The use of MAT54 for crush simulation relies on the Building Block Approach, reviewed earlier in Figure 11. A method has been developed by the author for the calibration of the MAT54 material model using a specified set of experimental crush data at the element level of the BBA which allows for the material model to be used in higher levels of the BBA without further adjustment. These guidelines will first describe the necessary set of experimental crush data necessary for the analysis calibration. Following this, recommendations are made for the initial development of the element level crush models, including the full definition of the MAT54

material input deck, as well as other model features such as control decks, damping, element type, contact definition, etc. Finally, an example exercise of the MAT54 calibration for crush simulation will be summarized, which refers to the extensive work done during the in depth investigation of MAT54 and development of various MAT54 crush models.

Required experimental data for material model

The material deck MAT_ENHANCED_COMPOSITE_DAMAGE (MAT54) found in the LS-DYNA keyword input file contains the entire material definition for the composite model. A detailed discussion of the governing equations and fundamental behaviors of the MAT54 material model is found in Appendix C: LS-DYNA material model MAT54. The categorized MAT54 input deck from Figure 168 is reproduced below, followed by the definitions of all 43 user input parameters and what experimental data is required to define each from Table 24.

*MAT_054 (ENHANCED_COMPOSITE_DAMAGE)							
mid	**ro**	**ea**	**eb**	**ec**	**prba**	~~**prca**~~	~~**prcb**~~
1	1.50E-4	1.84E+7	1.22E+6	0.0	0.02049	0.0	0.0
gab	~~**gbc**~~	~~**gca**~~	~~**kf**~~	**aopt**			
6.10E+5	6.10E+5	6.10E+5	0.0	0.0			
xp	**yp**	**zp**	**a1**	**a2**	**a3**	**mangle**	
0.0	0.0	0.0	0.0	0.0	0.0	0.0	
v1	**v2**	**v3**	**d1**	**d2**	**d3**	**dfailm**	**dfails**
0.0	0.0	0.0	0.0	0.0	0.0	0.024	0.03
tfail	**alph**	**soft**	**fbrt**	**ycfac**	**dfailt**	**dfailc**	**efs**
1.1530E-9	0.1	0.0	0.5	1.2	0.0174	-0.0116	0.0
xc	**xt**	**yc**	**yt**	**sc**	**crit**	**beta**	
213000	319000	28800	7090	22400	54	0.5	

1. Constitutive properties: RO, EA, EB, EC, PRBA, PRCA, PRCB, GAB, GBC, GCA, KF

2. Local material axes: AOPT, XP, YP, ZP, A1-A3, MANGLE, V1-V3, D1-D3

3. Shear weighing factors: ALPH, BETA

4. Deletion parameters: DFAILM, DFAILS, TFAIL, DFAILT, DFAILC, EFS

5. Damage factors: SOFT, FBRT, YCFAC

6. Material strengths: XC, XT, YC, YT, SC

7. Failure criterion selection: CRIT

Figure 168. Material deck for MAT54 and the 43 parameters shown in seven categories. Strikethrough parameters are inactive.

Table 24. MAT54 user-defined input definitions and required experimental data.

Name	Definition	Type	Experimental data
MID	Material identification number	Computational	N/A
RO	Mass per unit volume	Experimental	Density test
EA	Axial Young's modulus	Experimental	0-deg tension test
EB	Transverse Young's modulus	Experimental	90-deg tension test
EC	Through-thickness Young's modulus	(Inactive)	
PRBA	Minor Poisson's ratio v_{21}	Experimental	0-deg tension test with biaxial strain measurement
PRCA	Minor Poisson's ratio v_{31}	(Inactive)	
PRCB	Major Poisson's ratio v_{12}	(Inactive)	
GAB	Shear modulus G_{12}	Experimental	Shear test
GBC	Shear modulus G_{23}	(Inactive)	
GCA	Shear modulus G_{31}	(Inactive)	
KF	Bulk modulus	(Inactive)	
AOPT	Local material axes option	Computational	N/A
XP,YP,ZP	Used for AOPT = 1	(Inactive)	
A1,A2,A3	Vector 'a' used for AOPT = 2	Computational	N/A
MANGLE	Angle used for AOPT = 3	Computational	N/A
V1,V2,V3	Vector used for AOPT = 3	Computational	N/A
D1,D2,D3	Used for AOPT = 2, solid elements	(Inactive)	
ALPH	Elastic shear stress non-linear factor	Shear factor	**None; Default 0.1 recommended**
BETA	Shear factor in tensile axial failure criterion	Shear factor	**None; Default 0.5 recommended**
DFAILT	Axial tensile failure strain	Experimental	0-deg tension test
DFAILC	Axial compressive failure strain	Experimental	0-deg compression test
DFAILM	Transverse failure strain	Experimental	90-degree tension and compression tests; **May require calibration for stability**
DFAILS	Shear failure strain	Experimental	Shear test
EFS	Effective failure strain	Optional	Combination of standard tests
TFAIL	Time step failure value	Computational	Derived from numeric time-step
FBRT	Axial tensile strength factor after 2-dir failure	Damage factor	**None; Default 0.5 recommended**
SOFT	Material strength factor after crushing failure	Damage factor	**Calibrate using set of element-level crush data**
YCFAC	Axial compressive strength factor after 2-dir failure	Damage factor	**None; Default 1.2 recommended**
XT	Axial tensile strength	Experimental	0-deg tension test
XC	Axial compressive strength	Experimental	0-deg compression test
YT	Transverse tensile strength	Experimental	90-degree tension test
YC	Transverse compressive strength	Experimental	90-degree compression test
SC	Shear strength	Experimental	Shear test
CRIT	Specification of failure criterion	Computational	N/A; Requires value of 54 for MAT54

As outlined in Table 24, the constitutive properties, material strengths, and most deletion parameters are measured from standardized tension, compression, and shear material property experiments performed using material coupons (i.e. data from the coupon level of the BBA). The material model uses the material properties of the lamina, and the lay-up of the composite laminate is defined by the element. To ensure stability in impact and crush simulations, the DFAILM parameter requires increase from its experimentally measured value which can be done during calibration.

To use MAT54 for crush simulation, a set of element-level crush experiments must be performed which characterize the energy absorption capability of the material system such that the MAT54 SOFT parameter can be calibrated. The energy absorption of a composite material system is dependent on both the lay-up and the specimen geometry. The method developed by the author and proposed here relates the energy absorption of a composite laminate directly to the geometric feature of the crush specimen called degree of curvature. This means that while the other MAT54 input parameters can be defined by lamina properties, the SOFT parameter is a laminate property that is adjusted depending on the degree of curvature of the geometric feature it is modeling. In the simplest terms, the degree of curvature is defined to the length of curved segments over the total length of the geometry, or a percentage of the geometry that is curved.

The SEA of a composite material system increases with increased degree of curvature, to the limit that a flat crush coupon will exhibit the minimum SEA and a corrugated crush element will exhibit the maximum SEA of the material system. It is recommended that three crush element tests which represent low, medium, and high curvature specimens be tested, for example a flat coupon, a square tube or c-channel, and a corrugated specimen. Three elements-level crush tests

with significantly different degrees of curvature are sufficient to define the range of the energy absorption capability of the laminate needed for MAT54 calibration.

If the same geometric features crush tested are those used in the simulation, then the experimental load-displacement curve is itself used as the metric against which the simulation results are directly compared in order to calibrate the material model. Otherwise, an empirical relationship between the measured SEA and the degree of curvature of the crush specimen must be developed for the laminate from the element-level experiments. In this case, the SEA becomes the evaluation metric for the simulation, and the simulation is calibrated such that simulated SEA matches that expected from the laminate.

Recommended FEA model development

MAT54 material input parameter definitions

There are a number of other MAT54 input parameters aside from those which are experimentally derived. The local material axes parameters (group 2 in Figure 168) are defined using the AOPT parameter, Equation 21, and the illustration provided in Figure 158.

$$AOPT \begin{cases} = 0.0, & \textit{Locally orthotropic with material axes determined by element nodes } 1, 2, \textit{and } 4 \\ = 2.0, & \textit{Globally orthotropic with material axes determined by vector } \boldsymbol{a} \\ = 3.0, & \textit{Locally orthotropic material axes determined by rotating the cross product of the vector } \boldsymbol{V} \textit{ with the element normal } \boldsymbol{n} \textit{ by the angle MANGLE} \\ < 0.0, & \textit{The absolute value of AOPT is a coordinate system ID} \end{cases} \quad \text{Eq. (21)}$$

The material density, RO, requires special attention when using English units. Densities are often reported in terms of lbf/in^3 which is a measure of weight per unit volume. In order to maintain a consistent set of units, FE codes require density to be in terms of lbm/in^3 that is a

measure of mass per unit volume. The difference between weight and mass is the gravitational constant, g = 386.4 in/s^2, which must be divided from the weight in order to get the mass, and density with the unit lbf-s^2/in^4, which is the correct unit.

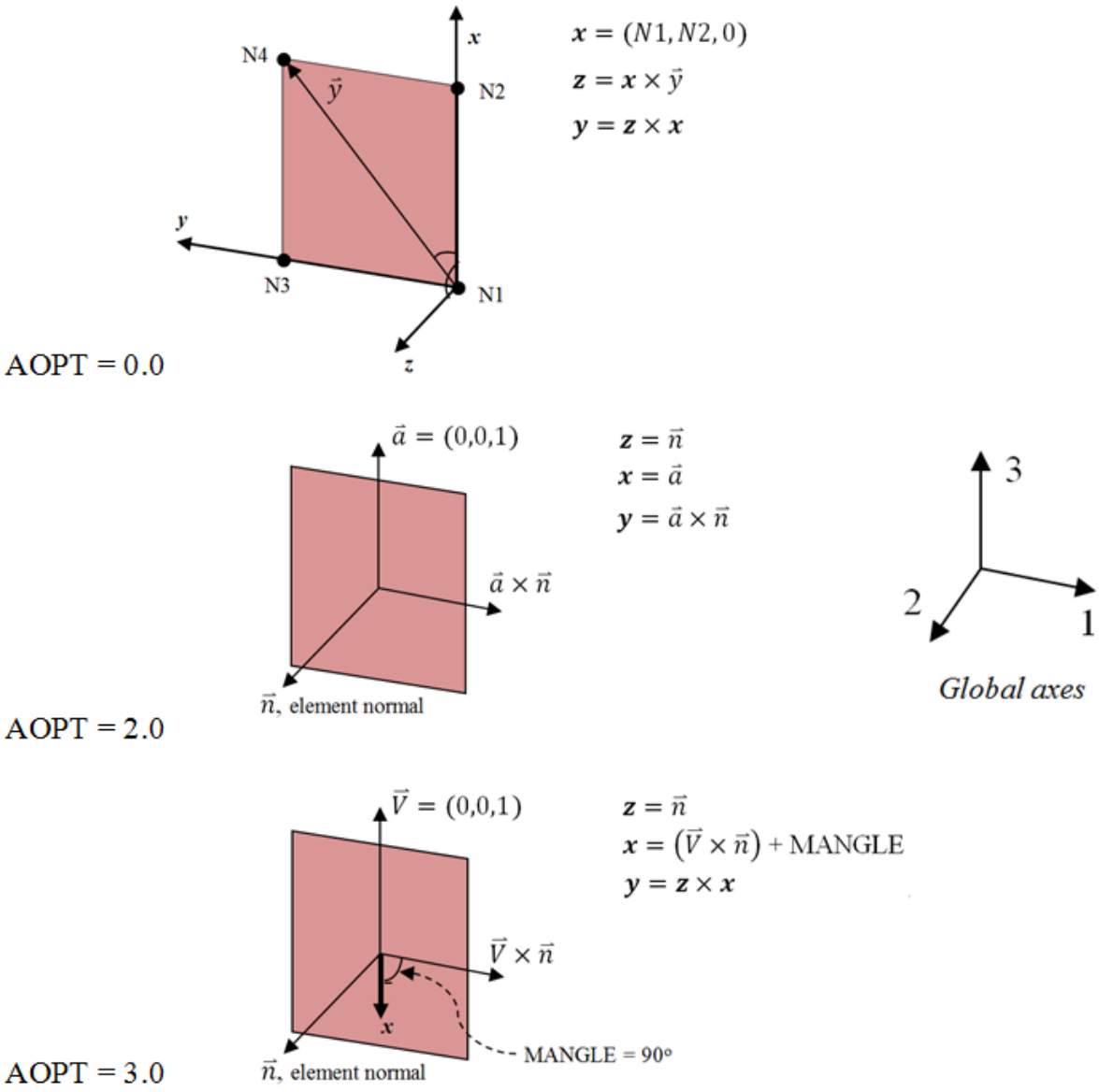

Figure 158. Illustration of three local material axes definition options for MAT54 as determined by the AOPT parameter.

Among the deletion parameters, TFAIL is the only one not directly measured from experiment and is given a value at least half of the critical time-step, as determined by the Courant condition,

Equation 34. The EFS input value can be determined from critical values of experimental failure strains, as given by Equation 33, or not be used at all by assigned a values of 0 (recommended).

Of the shear and damage factors, the default values given in Table 24 are recommended to avoid possible instabilities, with the exception of the SOFT parameter. This parameter requires calibration against the element-level crush experiments, a process which will be discussed at length later in these guidelines.

The computational parameter CRIT simply specifies whether to use MAT54 or MAT55 by assigning a value of 54 or 55, respectively. MAT55 should not be used for crash simulation since this material model does not contain element erosion/deletion criteria nor a post-failure damage model, making it unusable for crash simulation. While this is not mentioned in the LS-DYNA User's or Theory Manuals, this trait of MAT55 was discovered while investigating the modified material model presented in this paper.

Other LS-DYNA keyword input file definitions

In addition to the MAT54 material input deck, there are a number of other LS-DYNA keyword input parameters are important to discuss when using MAT54 for crush simulation. For reference, the baseline fabric sinusoid LS-DYNA keyword input file, with the element and nodal coordinate and set definition decks removed for the sake of brevity, is given in Appendix G: Keyword input file for fabric sinusoid crush.

In the CONTROL_SHELL deck, the parameter ISTUPD controls thickness changes for highly distorted and deformed shells elements. Although no significant influence was noted in this investigation, LSTC [105] strongly recommends that this parameter be turned off for composite materials for numeric stability. Also in the CONTROL_SHELL deck is the parameter LAMSHT

variable controls the use of Laminated Shell Theory in the calculation of the laminate stiffness through the thickness, which is otherwise assumed to be constant. This is especially important for sandwich composites which have great stiffness variation through the thickness, but it is not required that LAMSHT be active for a thin composite laminate undergoing crushing.

The CONTROL_TIMESTEP deck is used to manually adjust the time-step of the simulation. The variable TSSFAC is the time-step scale factor, which scales down the time-step from its critical value as determined by the Courant condition [108]. The default value of TSSFAC is 0.9, which makes the time-step 90% of the critical time-step value. It was found in several of the single element simulations where elements became highly distorted that the time-step needed to be reduced to 50% of the critical value. Reducing the time-step greatly increases the computational cost of the simulation, however it was necessary for stability when significant element distortion was simulated, an example of which is shown in Figure 159. The sensitivity of MAT54 to the time-step is a feature which may require revisiting during the calibration stage of the material model.

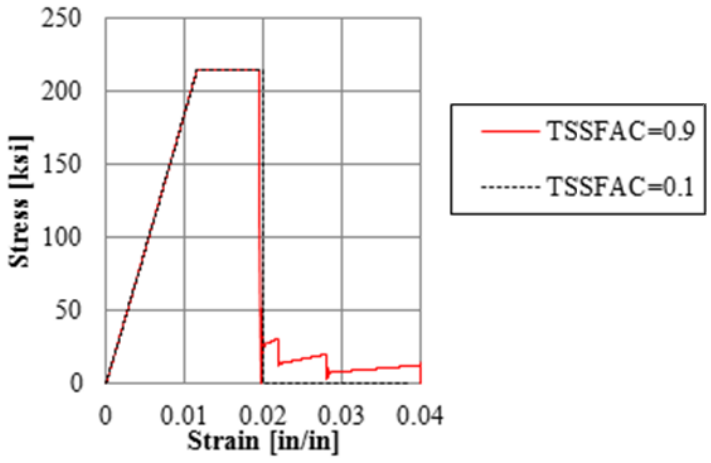

Figure 159. The reduction of the time-step factor TSSFAC improves stability in a single element simulation where the element is highly distorted at the point of deletion.

One other control deck that can be of use for crush simulations in particular is the CONTROL_ACCURACY deck, in which invariant node numbering (INN) can be turned on for shell elements. Invariant node numbering prevents the local coordinate system definition to be erroneously assigned in highly distorted elements, and makes element forces independent of node sequencing. An example of invariant node numbering comes from LSTC, shown in Figure 160 [104].

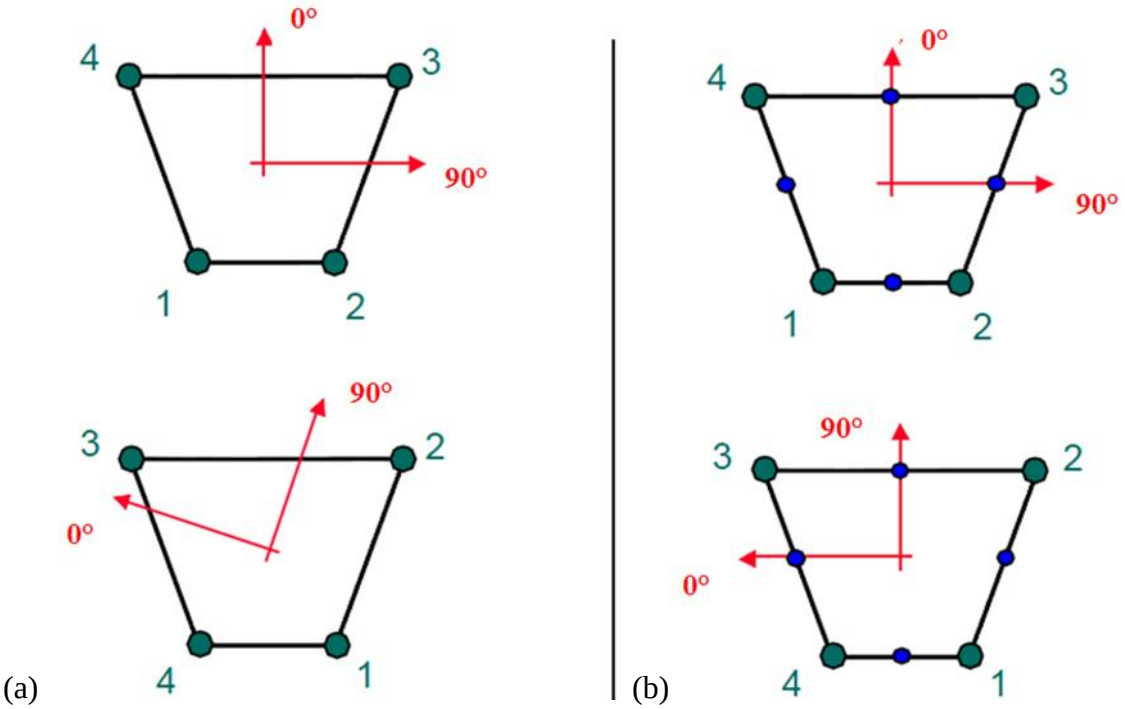

Figure 160. Example given by LSTC on the effect of invariant node numbering (INN) on the definition of local material coordinate system on a deformed element showing (a) incorrect local definition when INN is turned off and (b) correct local definition when INN is turned on [104].

The DATABASE decks define the output data that is saved, and the output files generated. The DATABASE_EXTENT_BINARY deck has two important variables relevant to MAT54 models: the number of extra history variables, NEIPS, and the number of integration points through the thickness, MAXINT. In order to record the failure mode history variables for MAT54, as

defined by Equation 25-28, NEIPS must be set to at least 6. In these studies it was set to 12 to record additional MAT54 history variables which proved to be unnecessary for this particular exercise. Also, in order to record all of the ply data generated at each integration point, the MAXINT must be set equal to the number of plies.

Part damping is recommended to represent the inherent damping that exists within real structures. Without part damping an FE code will vibrate continuously, and especially in nonlinear dynamic models these oscillations can have high amplitudes and distort data [50]. This is primarily an issue with larger models, and while damping was not observed to have a significant effect in the crush element models it is still recommended to have included. In LS-DYNA, generic part damping is achieved by using the DAMPING_PART_STIFFNESS cards, and a damping coefficient equal to 0.05 was used in this study.

Element selection

MAT54 requires shell elements, and the type used in this study is the four-node Type 16 fully integrated quadrilateral element. This type allows for a local coordinate system to be defined and has been specially formulated to be computationally inexpensive fully integrated element. It has two integration points through the thickness by default, one at the top of the shell thickness and one at the bottom, however additional integration points are added which each simulate a ply of a laminated composite material. The number of integration points, which should equal the number of plies, must be defined in the SECTION_SHELL deck variable NIP. If the PART_COMPOSITE deck is used in place of SECTION_SHELL, this variable does not require definition.

Precision solver

Although most finite element codes offer both a single and a double precision solver, it is becoming standard that the double precision solver is used by default for codes such as ABAQUS and RADIOSS. LS-DYNA still gives the user the equal option to use either single or double precision. Since explicit formulations are very computationally expensive, it may be desirable to use a single precision solver for improved utilization of memory and disk space, however, problems have been identified in this study when using the single precision solver with MAT54. Specifically, in the single element study when large deformations were imposed on the MAT54 element, the single precision solver often produced inexplicably unstable results, Figure 161. By simply changing the solver to the double precision version, these instabilities went away and the single element deformed as expected. For this reason, it is always recommended to use the double precision solver when using MAT54.

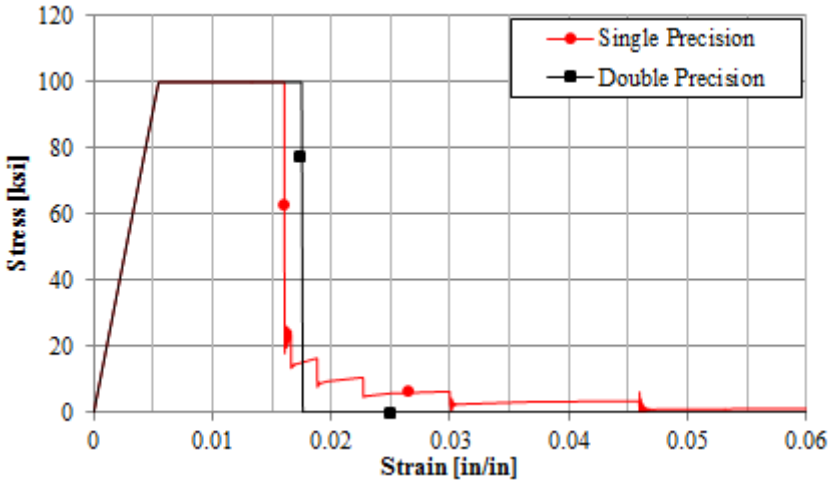

Figure 161. Example from the single element investigation of the MAT54: basic stress-strain material response is unstable using a single precision solver versus stable using a double precision solver.

Contact definition

The contact between the loading plate and the crush element is defined by the CONTACT_RIGID_NODES_TO_RIGID_BODY contact deck. MAT54 requires a contact type which employs a load-penetration curve, and automatic or eroding contact types do not work (see Figure 86). The definition of the LP curve will severely impact the stability of the crush simulation using MAT54, and is certainly the most important variable in the contact deck (the load curve identification parameter LCID in CONTACT_RIGID_NODES_TO_RIGID_BODY). A piecewise-linear curve which increases in stiffness at greater penetration values is the recommended shape of the LP curve. It was found that for stable crush geometries with high curvature, such as the sinusoid, an aggressive and stiff LP curve best modeled the experimental crush results (see Figure 119), however was not capable of modeling other geometries. Applying the aggressive LP curve to the tubular geometries did not facilitate stable crushing and a softer LP curve was required. Since it is undesirable to tailor different LP curves to different composite parts, a conservatively soft piecewise-linear LP curve is recommended for best universal results in a crush simulation using MAT54. This compromises the accuracy of the initial stiffness of the crush curve for most crush geometries (see Figure 130), but without this concession the stability of the crash model is jeopardized. The LP curve is an important parameter which may require revisiting if the MAT54 crush model is found to be unstable during initial development.

Experiment-analysis correlation

The simulation load-displacement results should be recorded at a location in the model that is representative of the experimental load data collection location. In the example exercise, data collection occurs across all of the nodes along the fixed boundary condition at the opposite end

as the loading plate as this is similar to the location of the load cell used in the crush experiments. The load data is filtered using a low-pass CFC 600 Hz filter, as is recommended practice for crash simulations [50].

Mesh size

CAD models for each crush geometry must be developed and meshed at a mesh size appropriate for scaling up to higher levels of the BBA which require up to full scale structural models. The mesh size must also be small enough to capture important geometric features such as the curvature of the structural crush elements. A mesh size was chosen for this exercise to be 0.01 in. (2.54 mm) since this was small enough to capture the curvature of the sinusoid crush element, but large enough to allow for scaling up to larger structures. The MAT54 material model alone is not mesh sensitive, since it does not include any strain-rate dependent parameters nor model any strain-rate dependent behaviors in its governing equations. The mesh insensitivity of MAT54 has been demonstrated at the element-level in the simulation of the sinusoid crush element (see Figure 91-Figure 92).

MAT54 model calibration

The element-level crush experimental data used in this exercise included a flat crush coupon and eight different crush elements of tubular (Figure 20) and corrugated (Figure 29) variants. From these crush tests, the energy absorption capability of the T700/2510 carbon fiber/epoxy plain-weave fabric $[(0/90)]_{8f}$ laminate was characterized. After performing all of the crush tests, a relationship between SEA and the geometric degree of curvature was empirically derived, reproduced below in Figure 35. From this relationship, the expected SEA of any crush element for this laminate can be determined and used to calibrate the simulation.

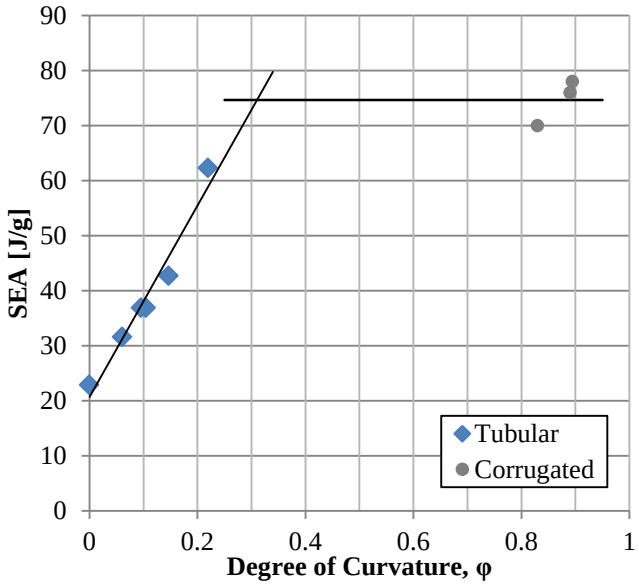

Figure 35. SEA vs. φ for nine different crush geometries of the same laminate.

The simulation of the semi-circular sinusoid element is chosen for the initial model development. Recommendations from the first part of the guidelines are followed to create the baseline input file given in Appendix G. This model uses a mesh size of 0.1 in (2.54 mm), and the RIGID_NODES_TO_RIGID_BODY contact type with a shallow and conservative LP curve (see *DEFINE_CURVE "For Contact," LCID = 82 in Appendix G). While more accurate results can be obtained from using a more aggressive LP curve, the stability of the analysis is compromised by doing so. It is recommended that the initial trigger thickness value be set to a very low value, such as 10% of the total thickness, for ease of initial calibration.

The trigger thickness is defined in the section definition for the trigger elements, *SECTION_SHELL "Trigger" using the parameters T1, T2, T3, and T4 to define the thicknesses at each node (see Appendix G). The initial MAT54 SOFT value should be an intermediate value, such as 0.5. Both this value and the trigger thickness values will change during calibration. The DFAILM parameter is preemptively increased from its experimentally

measured value of 0.012 in/in to 0.06 in/in to ensure stability of the crush simulations. It has been shown earlier that low values of DFAILM can severely inhibit stability of the crush simulation, whereas increasing DFAILM well beyond a value which results in a stable model has no adverse effect on the crush simulation (see Figure 112). The large increase of DFAILM ensures that the transverse strain limitation will not cause premature element erosion, and instead other failure strains (such as the compressive fiber strain, DFAILC) will cause element erosion prior to DFAILM, as desired.

The experimental load-displacement crush curve is compared against the load-displacement curve of the simulation generated from the sum of the forces across the bottom row of nodes. Initial results prior to calibration are expected to be either entirely unstable (i.e. erratic and uneven element erosion) or stable (i.e. even row-by-row element erosion) but with incorrect simulated load values. In the case of complete instability, the SOFT parameter should be lowered. For geometric features with low degrees of curvature, the SOFT may need to be reduced below 0.1 for stability. If stable crushing cannot be obtained from simply lowering SOFT, then the MAT54 parameter DFAILM should be further increased. Changing DFAILM is a calibration that only needs to be made once for the material model of the entire laminate.

Once simulated crush stability is obtained, the SOFT parameter should be finely adjusted to directly calibrate the average crushing load value (and subsequently, the SEA) until it matches the experiment. An example of the effect that SOFT has on the average crush load and stability of the square tube crush simulation is reproduced in Figure 126. In this case, high values of SOFT such as 0.58 destabilized the model completely and caused global buckling. SOFT was then lowered to a value of 0.2, which only semi-stabilized the model. Fine adjustments of SOFT were made around the value of 0.15 to calibrate the simulation to the experiment.

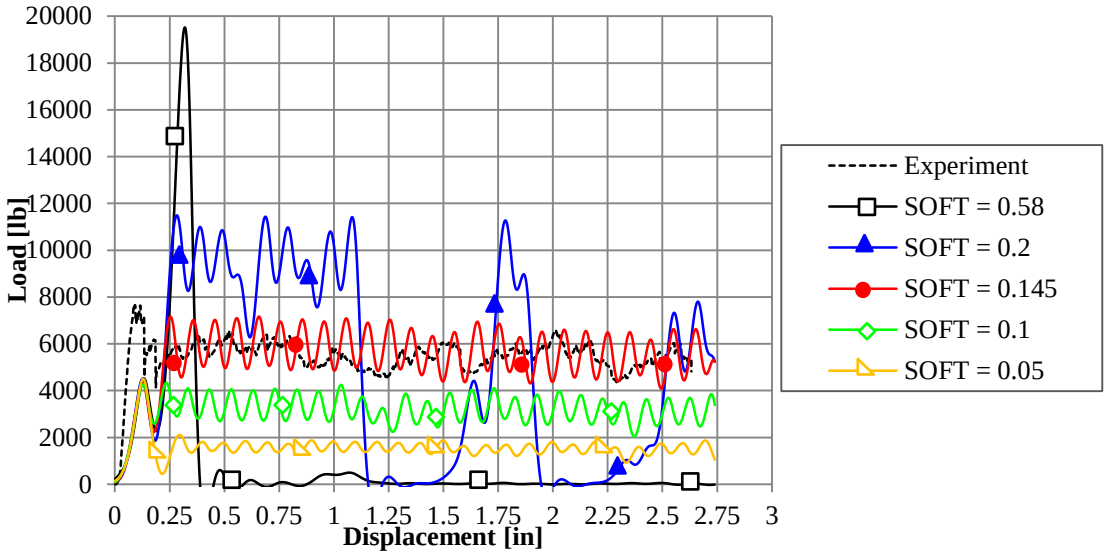

Figure 126. SOFT parameter calibration of the tube simulation using new contact LP curve.

After calibrating the SOFT, the initial peak load can be calibrated such that it also matches the experiment by adjusting the trigger thickness. An example of the effect of the trigger thickness on the square tube crush simulation is reproduced in Figure 127.

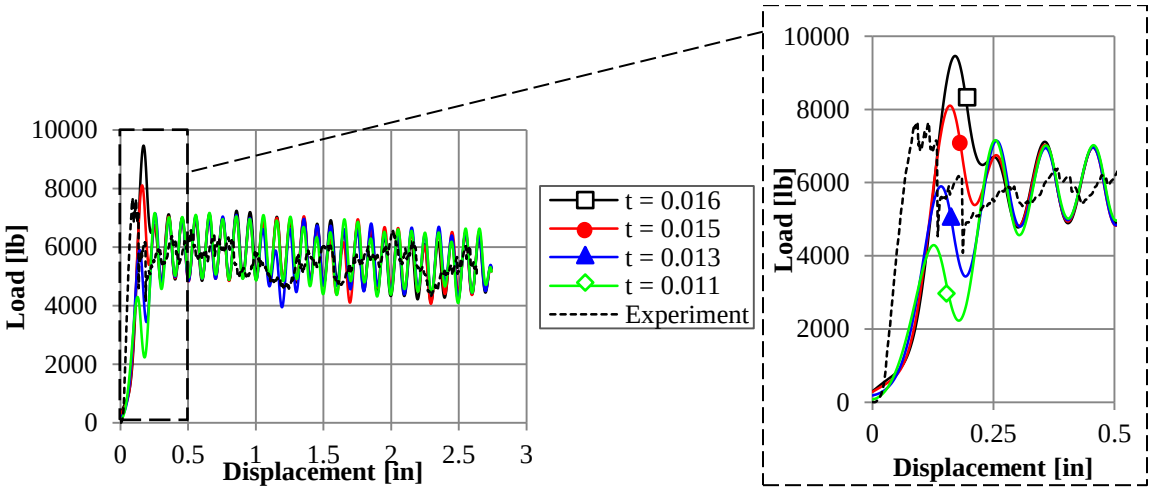

Figure 127. Trigger thickness calibration of the tube simulation using new contact LP curve.

Following the development of the baseline crush model, more crush element geometries can be simulated using the same basic model definition. The change in geometry will destabilize the model, and the modeler must determine the reason for the destabilization and evaluate if it is to be expected or if it is a greater problem. If the initial development of the model has produced a stable and robust model, then only the SOFT and trigger thickness parameters require calibration to produce successful element-level crush simulations of different geometries. If changing only the SOFT parameter does not work, then changes in other parameters such as DFAILM must be explored. Other parameters known to affect stability include the failure strains DFAILS and DFAILT. In some cases the transverse and shear material strength parameters, YT and SC, have been shown to cause instability, however this is often when given unrealistic values. If none of the parameters known to affect stability fix the problem, then changes in larger modeling definitions must be explored, such as the time-step or LP curve in the contact definition. Such an exercise was completed in the in depth investigation presented in earlier sections.

Given a stable baseline model, only two changes necessary in the model definition for each simulated geometry: SOFT to capture the average crush load and trigger thickness to capture the initial load peak. It is expected that these two parameters must be calibrated for all MAT54 crush simulations. The DFAILM parameter remained at the increased value determined during the baseline sinusoid model development for all of the element-level simulations of this particular composite material system. From the element-level material model calibration, two important empirical relationships were developed for the composite material system modeled in this example: one which relates the experimentally measured SEA to the numerically calibrated SOFT parameter (Figure 131) and one which relates the calibrated SEA and trigger thickness values (Figure 132). Both of these empirical trends are reproduced below. The first linear trend

relates SOFT to SEA and allows for the calibration of the numeric SOFT parameter using the experimentally measured SEA. Similarly, the second linear trend relates SOFT to the trigger thickness, allowing for the calibration of the trigger thickness following the calibration of SOFT without the need for an experimental load-displacement curve for calibration. These two relations are very important in the scenario where only three element geometries are crush tested to generate the relationship between SEA and degree of curvature. In this case, the MAT54 model must be calibrated using inferred SEA values without the experimental load-displacement curve. These two trends effectively prevent a blind trial-and-error process of defining the material model, and instead provide a guided calibration process which effectively generates a material model capable of simulating composites in crush failure.

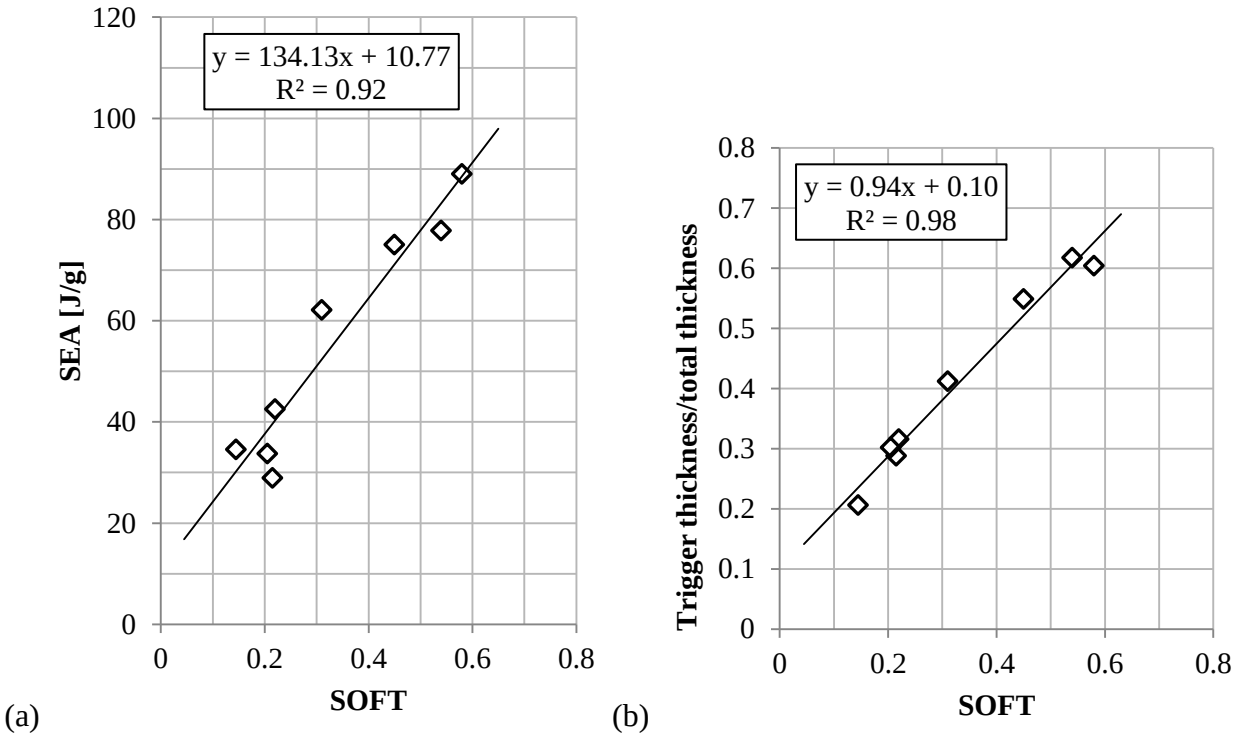

Figure 131-Figure 132: (a) Linear trend between calibrated MAT54 SOFT parameter and the experimental SEA and (b) Linear trend between the calibrated SOFT parameter and the ratio of trigger thickness to original thickness.

For the composite material system used in this study, an experimental relationship between SEA and degree of curvature was generated such that, given a new geometry for a crush element the SEA can be estimated based on the calculation of the crush element's degree of curvature. This means that if a new crush element were to be introduced at the sub-component level it would be possible to estimate the appropriate SOFT value without conducting further crush element tests. The best approach, however, is to identify in advance all of the geometric crush elements in the structure and treat each geometry as a necessary element to crush test during the BBA in order to calibrate the numeric model such that approximations are minimized. Following the successful calibration of the MAT54 material model for simulating crush at the element level, the material model can be validated at the next level of the BBA, the sub-component level.

Major Contributions of Research

The body of research presented in this dissertation has resulted in the following major contributions to the study of composites crashworthiness.

In the experimental investigation, energy absorption has been shown to be not a material property, but a function of the geometric features of the material test specimen. Specifically, the degree of curvature provided by the geometry directly influences the type of crushing failure exhibited by the specimen: more curvature means more fragmentation and more energy absorption, while more flat segments mean more delamination and less energy absorption. The linkage of failure modes directly with geometry and SEA has not been previously shown. The experimental protocol to characterize the energy absorbing capability of a composite material system must therefore include crush specimens of various geometries such that the full spectrum of failure modes and energy absorption capability can be tested and measured. Such a protocol has been demonstrated in this research using a single material system and lay-up, where a linear relationship between the degree of curvature and measured SEA has been developed. This relationship reduces the amount of element-level crush testing necessary to characterize the energy absorbing capability of the material system. It is suggested that such a relationship can be developed from crush testing a flat coupon, an intermediate curvature specimen (such as a c-channel), and a fully curved specimen (such as a corrugated specimen). The energy absorbing capability of other geometries for the composite material system can then be extrapolated from the experimental results of these three crush tests.

In the analytical investigation, extensive documentation of the LS-DYNA composite material model MAT54 has been presented which did not previously exist. This documentation includes

a thorough explanation of the model, its parameters, governing equations, source code, and parametric sensitivities to crush modeling in particular. A process to calibrate this material model for crush modeling at the element-level using the experimentally measured values of SEA has been developed and demonstrated. This material model was then modified such that compressive values of modulus can be specified by the user, expanding its capability to model complex multi-axial loading conditions of composite materials which often have significantly different moduli in tension and compression, in both the axial and transverse directions. Such a capability is not available in other material models. The compressive strain-to-failure parameter in the transverse direction was also added to the modified model, as this parameter was missing from the original model. In the process of modifying the material model, the significance of the post-failure model rather than the failure criterion was demonstrated for the first time for crush modeling. The failure criteria and post-failure model of MAT54 were also validated in the process of modification where several alternative criteria and post-failure stress profiles were studied. Finally, guidelines for using MAT54 for crush simulation were composed, which are a sought-after and valuable tool for a growing population of new modelers faced with the new requirement to develop crash models for composite vehicle design and certification.

General Conclusions

In the first portion of this work, the complex energy absorbing mechanisms of a composite material system subjected to crush loading have been investigated, and some key findings were made. First, SEA is not a material property of a composite material system and SEA measurements vary significantly according to the geometry of the crush test element as different geometries favor different failure mechanisms which in turn provide varying levels of energy absorption. This means that no single crush test can fully characterize the SEA of a composite. Instead, the characterization of the energy absorption capability of a composite material system requires a set of crush element experiments that are each representative of geometric features of the structure in consideration. In doing so, a curve can be developed that describes the SEA in terms of structural geometry. For the composite material system investigated, an empirical relationship between the SEA and the degree of curvature of the crush element was developed. This relationship can be extrapolated and applied to additional crush geometries that were not tested to provide approximate predictions for SEA.

The relationship between SEA and the degree of curvature is explained by the failure modes observed during crush testing. These failure modes are divided into two extremes, delamination/splaying and fragmentation, for which crush failure is a combination of varying degrees of both. During delamination, little energy is absorbed in splitting the material along an interlaminar crack front and the resulting SEA measurement is low. Flat segments of crush elements do not provide delamination suppression and are prone to this low-SEA failure mode. Fragmentation failure is a destructive mode which leaves little material intact and expends a lot of energy to completely break up the material, resulting in high SEA. Curved geometries suppress delamination fronts, and fragmentation occurs causing great energy absorption.

In the second portion of this work, an advanced simulation method using the LS-DYNA material model MAT54 to simulate crush failure has been investigated, and a modified version of the composite material model which simulates failure and post-failure behaviors has been developed. This composite damage material model was thoroughly investigated using single element models and several crush models in order to provide a comprehensive overview of its theory, parameters, and parametric sensitivities with regards to crush modeling, details of which were all previously unavailable. MAT54 has been successfully used to capture the behavior of unidirectional and fabric material systems for the simulation of specimens undergoing axial crushing. It was found that the SOFT crush front parameter is the single most influential parameter for determining the success of the crush simulation. Through a careful calibration by trial-and-error, the right value for the SOFT parameter can be identified, but there is no way of determining it *a priori* or measuring it experimentally.

Following the development of the stable crush simulation of a sinusoid crush element using MAT54, several simulations of crush elements with various cross-sectional geometries were calibrated using SOFT to match the experimental results well. It is not possible to simulate different specimen geometries without making changes to the material model since specific and individual damage and failure mechanisms (such as delamination versus fragmentation) cannot be modeled using MAT54. Empirical curves have been established which relate experimental parameters (SEA) to important modeling parameters (SOFT, trigger thickness), making the calibration of the crush simulation more focused by reducing scope the trial and error calibration process. Ultimately, this modeling approach requires experimental element-level crush data such that trial-and-error calibration of the SOFT parameter can be executed to develop a good crush model. Therefore, consistent with other findings of the CMH-17 Crashworthiness

Working Group Numerical Round Robin, it cannot be said that LS-DYNA MAT54 can be a predictive tool for simulating simple shapes such as tubes or stiffeners.

Finally, the MAT54 source code was edited such that a modified composite damage material model composite was implemented in single element and crush simulations. The modified model has an improved capability to simulate the elastic behavior. Several alternative failure criteria were investigated in the modified model which each demonstrated an equal or worse capability to predict initial failure than MAT54, thus validating its use of the Hashin criteria to determine lamina failure. The default approach for modeling the crush elements by reducing their strength using the SOFT parameter proved to be most effective for crush modeling as well. While several modifications were made in the post-failure material behavior, none produced favorable crush results thereby reinforcing the importance of the plasticity used by MAT54 for crush stability. Overall, while the modified model improved some aspects of MAT54, it primarily served to confirm that regardless of the scientific details of the approach chosen to approximate the post-failure behavior, it is more important to capture the macroscopic engineering behavior.

References

[1] Composite Materials Handbook (CMH-17), Rev. G., Vol. 3, Chapter 16.

[2] C. Nailadi, "A summary of the ACC tube testing program," in *Proceedings of the 49th MIL-HDBK-17 Coordination Meeting*, Santa Monica, CA, December 2005.

[3] A. Browne, N. Johnson and M. Botkin, "Dynamic crush response of composite crash boxes: effects of impact angle and bumper attachment," in *Proceedings of the ASC 27th Technical Conference*, Dayton, OH, September 2010.

[4] C. Bisagni, "Experimental investigation of the collapse modes and energy absorption characteristics of composite tubes," *International Journal of Crashworthiness*, vol. 14, no. 4, pp. 365-378, 2009.

[5] R. Jeryan, "Energy management working group activities," in *Proceedings of the 48th MIL-HDBK-17 Coordination Meeting - Crashworthiness Working Group*, Charlotte, NC, March 2005.

[6] K. Jackson and E. Fasanella, "Development of an LS-DYNA model of an ATR42-300 aircraft for crash simulation," in *Proceedings of the 8th International LS-DYNA User's Conference*, Detroit, MI, May 2004.

[7] J. Wiggenraad, "Crashworthiness research at NLR: 1990-2003.," NLR TP-2003-217, June 2003.

[8] M. McCarthy, G. Harte, J. Wiggenraad, A. Michielsen, D. Kohlgrüber and A. Kamoulakos, "Finite element modeling of crash response of composite aerospace sub-floor structures," *Computational Mechanics,* vol. 26, pp. 250-258, 2000.

[9] D. Hull, "A unified approach to progressive crushing of fibre-reinforced compsite tubes.," *Composite Science & Technology,* no. 40, pp. 377-421, 1991.

[10] A. Pickett, T. Pyttel, F. Payen, F. Lauro, N. Petrinic, H. Werner and J. Christlein, "Failure prediction for advanced crashworthiness of transportation vehicles.," *International Journal of Impact Engineering,* vol. 30, pp. 853-872, 2004.

[11] P. Du Bois, "Crashworthiness engineering with LS-DYNA," in *FEA Information International News for the World-Wide Engineering Community,* December 2001.

[12] P. Feraboli, "Development of a modified flat plate test and fixture specimen for composite materials crush energy absorption," *Journal of Composite Materials,* vol. 43, no. 19, pp. 1967-1990, 2009.

[13] W. Lestari, H. Thuis and J. Wiggenraad, "Development of a trigger mechanism to reduce peak forces in crash loaded composite sine-wave spars," in *20th European Rotorcraft Forum,* Amsterdam, October 1994.

[14] G. Farley and R. Jones, "Energy-absorption capability of composite tubes and beams," NASA TM 101634, Hampton, VA, 1989.

[15] G. Farley and R. Jones, "Crushing characteristics of continuous fiber-reinforced composite

tubes," *Journal of Composite Materials,* vol. 26, no. 1, pp. 37-50, 1992.

[16] J. Carruthers, A. Kettle and A. Robinson, "Energy absorption capability and crashworthiness of composite material structures: A review.," *Applied Mechanics Reviews,* no. 51, pp. 635-649, 1998.

[17] H. Hamada, J. Coppola, D. Hull, Z. Maekawa and H. Sato, "Comparison of energy absorption of carbon/epoxy and carbon/PEEK composite tubes," *Composites,* vol. 23, pp. 245-252, 1992.

[18] D. Adams, "Crashworthiness test methods," in *Proceedings of the 57th CMH-17 Coordination Meeting - Crashworthiness Working Group*, Atlanta, GA, November 2009.

[19] J. Lavoie and J. Morton, "Design and applicaiton of a quasi-static crush test fixture for investigating scale effects in energy absorbing composite plates.," NASA CR 4526, July 1993.

[20] A. Johnson and D. Kohlgruber, "Design and performance of energy absorbing subfloor structures in aerospace applications.," in *IMechE Seminar S672*, London, England, May 2000.

[21] G. Jacob, J. Fellers, J. Starbuck and S. Simunovic, "Crashworthiness of automotive composite material systems," *Journal of Applied Polymer Science,* vol. 92, pp. 3218-3225, 2004.

[22] N. Feindler, J. Döll and K. Drechsler, "Test method to analyse the energy absorption of composite material using flat coupon testing," in *5th International Conference on*

Composites Testing and Model Simulation, Lausanne, Switzerland, February 2011.

[23] P. Thornton, "Energy absorption in composite structures," *Journal of Composite Materials*, pp. 248-262, July 1979.

[24] A. Mamalis, M. Robinson, D. Manolakos, G. Demosthenous, M. Ioannidis and J. Carruthers, "Review: Crashworthy capability of composite material structures," *Composite Structures*, vol. 37, pp. 109-134, 1997.

[25] G. Jacob, J. Fellers, S. Simunovic and J. Starbuck, "Energy absorption in polymer composites for automotive crashworthiness," *Journal of Composite Materials*, vol. 36, pp. 813-850, 2002.

[26] G. Farley, "Energy absorption of composite materials," *Journal of Composite Materials*, vol. 17, pp. 267-279, 1983.

[27] D. Schmueser and L. Wickcliffe, "Impact energy absorption of constinuous fiber composite tubes," *Journal of Engineering Material and Technology*, vol. 109, pp. 72-77, 1987.

[28] H. Hamada, S. Ramakrishna and H. Satoh, "Crushing mechanism of carbon fibre/PEEK composite tubes," *Composites: Part A*, vol. 26, pp. 749-755, 1995.

[29] W. Tao, R. Robertson and P. Thornton, "Effects of material properties and crush conditions on the crush energy absorption of fiber compsoite rods," *Composites Science and Technology*, vol. 47, pp. 405-418, 1993.

[30] C. Kindervater, "Energy absorption of composites as an asepct of aircraft structural crash-resistance," in *Developments in the Science and Technology of Composite Materials*, Stuttgart, Germany, Elsevier Applied Science Publishers, 1990, pp. 643-651.

[31] G. Farley, "Effect of specimen geometry on the energy absorption capability of composite materials," *Journal of Composite Materials,* vol. 20, pp. 390-400, 1986.

[32] A. Mamalis, D. Manolakos, G. Viegelahn, Sin Min Yap and G. Demosthenous, "On the axial crumpluing of fiber-reinforced composite thin-walled conical shells," *International Journal of Vehicle Design,* vol. 12, pp. 450-467, 1991.

[33] G. Farley and R. Jones, "Crushing characteristics of composite tubes with 'near elliptical' cross sections," *Journal of Composite Materials,* vol. 26, pp. 1741-1751, 1992.

[34] S. Hanagud, I. Craig, P. Sriram and W. Zhou, "Energy absorption behavior of graphite epoxy composite sine webs," *Journal of Composite Materials,* vol. 23, no. 5, pp. 448-459, 1989.

[35] M. McCarthy and J. Wiggenraad, "Numerical investigation of a crash test of a composite helicopter subfloor structure," *Composite Structures,* vol. 51, pp. 345-359, 2001.

[36] J. San Vicente, F. Beltran and F. Martinez, "Simulation of impact on composite fuselage structures," in *European Conference on Computational Methods in Applied Sciences and Engineering, ECCOMAS,* Barcelona, Spain, September 2000.

[37] A. Jackson, S. Dutton, A. Gunnion and D. Kelly, "Investigation into laminate designe of open carbon-fibre/epoxy sections by quasi-static and dynamic crushing," *Composite*

Structures, vol. 93, pp. 2646-2654, 2011.

[38] T. Hurley and J. Vandenburg, "Small Airplane Crashworthiness Design Guide," Simulia Technologies TR-98099; AGATE Integrated Design and Manufacturing AGATE-WP3.4-034043-036, Phoenix, AZ, 2002.

[39] G. Farley and R. Jones, "Prediction of the energy-absorption capability of composite tubes," *Journal of Composite Materials,* vol. 26, no. 3, pp. 388-404, 1992.

[40] H. Hamada and S. Ramakrishna, "A FEM method for prediction of energy absorption capability of crashworthy polymer composite materials," *Journal of Reinforced Plastics and Composites,* vol. 16, pp. 226-242, 1997.

[41] A. Tabiei and Q. Chen, "Micromechanics based composite material model for impact and crashworthiness explicit finite element simulation," in *6th International LS-DYNA Conference*, Detroit, MI, April 2000.

[42] M. Morthorst and P. Horst, "Failure model for composite materials under quasi-static crushing conditions," *Journal of Strain Analysis for Engineering Design,* vol. 39, pp. 411-421, 2004.

[43] C. McGregor, R. Vaziri, A. Poursartip, X. Xiao and N. Johnson, "Simulation of progressive damage developement in braided composite tubes undergoing dynamic axial crushing," in *9th International LS-DYNA Conference*, Detroit, MI, June 2006.

[44] M. Fouinneteau and A. Pickett, "Shear mechanism modelling of heavy tow braided composites using a meso-mechanical damage model," *Composites: Part A,* vol. 38, pp.

2294-2306, 2007.

[45] L. Greve, A. Pickett and F. Payen, "Experimental testing and phenomenological modelling of the fragmentation process of braided carbon/epoxy composite tubes under axial and oblique impact," *Composites: Part B,* vol. 39, pp. 1221-1232, 2008.

[46] A. Najafi, D. Huang, M. Rais-Rohani, F. Abdi and C. Heydari, "Simulation of crushing process in composite tubes," in *51st AIAA/ASME/ASCE/AHA/ASC Structures, Structural Dynamics, and Materials Conference,* Orlando, FL, April 2010.

[47] E. Fasanella, K. Jackson and K. Lyle, "Finite element simulation of a full-scale crash test of a composite helicopter," in *American Helicopter Society 56th Annual Forum*, Virginia Beach, VA, May 2000.

[48] A. Johnson and A. Pickett, "Impact and crash modeling of composite structures: A challenge for damage mechanics," in *Proceedings of ECCM'99 Conference*, Munich, Germany, September 1999.

[49] X. Li, C. Ferrie, E. Nottorf, B. Mullins and M. Portanova, "A building block method for damage tolerance evaluation of impacted composite stringer panel," in *American Helicopter Society 61st Annual Forum,* Grapevine, TX, June 2005.

[50] E. Fasanella and K. Jackson, "Best practices for crash modeling simulation," National Aeronautics and Space Administration and Langley Research Center (U.S.), Hampton, VA, October 2002.

[51] R. Sandhu, "A survey of failure theories of isotropic and anisotropic materials," No. AFFDL-TR-72-71. Air Force Flight Dynamics Laboratory, Wright-Patternson Air Force Base, OH, 1972.

[52] S. Soni, "A comparative study of failure envelopes in composite laminates," *Journal of Reinforced Plastic Composites,* vol. 2, pp. 34-42, 1983.

[53] S. Tsai, "A survey of macroscopic failure criteria for composite materials," *Journal of Reinforced Plastic Composites,* vol. 3, pp. 40-62, 1984.

[54] M. Nahas, "Survey of failure and post-failure theories of laminated fibre reinforced composites," *Journal of Composites, Technology, & Research,* vol. 8, pp. 138-153, 1986.

[55] P. Soden, A. Kaddour and M. Hinton, "Recommendations for designers an researchers resulting from the world-wide failure exercise," *Composite Science & Technology,* no. 64, pp. 589-604, 2004.

[56] A. Orifici, I. Herszberg and R. Thomson, "Review of methodologies for composite material modelling incorporating failure," *Compsite Structures,* vol. 86, pp. 194-210, 2008.

[57] Z. Hashin, "Failure criteria for unidirectional fiber composites," *Journal of Applied Mechanics,* vol. 47, pp. 329-334, 1980.

[58] F. Chang and K. Chang, "A progressive damage model for laminated composites containing stress concentrations," *Journal of Composite Materials,* vol. 21, pp. 834-855, 1987.

[59] A. Puck and H. Schurmann, "Failure analysis of FRP laminates by means of physically based phenomenological models," *Composites Science & Technology,* vol. 58, pp. 1045-1067, 1998.

[60] M. Hinton, A. Kaddour and P. Soden, "A comparison of the predictive capabilities of current failure theories for composite lamiates, judged against experimental evidence," *Composites Science & Technology,* vol. 62, pp. 1725-1797, 2002.

[61] W. Wolfe and T. Butalia, "A strain-energy based failure criterion for non-linear analysis of composite laminates subjected to biaxial loading," *Composites Sciences and Technology,* vol. 58, pp. 1107-1124, 1998.

[62] T. Butalia and W. Wolfe, "A strain-energy-based non-linear failure criterion: comparison of numerical predictions and experimental observations for symmetric composite laminates," *Composites Science and Technology,* vol. 62, pp. 1697-1710, 2002.

[63] R. Talreja, "Modeling of damage development in composites using internal variable concepts," in *Damage Mechanics in Composites*, A. Wang and G. Haritos, Eds., ASME AD-Vol. 12, 1987, pp. 11-16.

[64] A. Johnson, A. Pickett and P. Rozycki, "Computational methods for predicting impact damage in composite structures," *Composites Science and Technology*, vol. 61, pp. 2183-2192, 2001.

[65] V. Sokolinsky, K. Indermuehle and J. Hurtado, "Numerical simulation of the crushing process of a corrugated composite plate," *Composites: Part A*, vol. 42, pp. 1119-1126,

2011.

[66] P. Feraboli, "Composite materials strength determination within the current certification methodology for aircraft structures," *Journal of Aircraft,* vol. 46, no. 4, pp. 1365-1374, 2009.

[67] M. Rassaian and K. Davis, "Use of nonlinear analysis for crashworthiness certification," in *Aerospace Structural Impact Dynamics International Conference,* Wichita, KS, November 2012.

[68] P. Feraboli, F. Deleo, B. Wade, M. Rassaian, M. Higgins, A. Byar, M. Reggiani, A. Bonfatti, L. DeOto and A. Masini, "Predictive modeling of an energy-absorbing sandwich structural concept using the building block approach," *Composites: Part A,* vol. 41, pp. 774-786, 2010.

[69] S. Heimbs, M. Hoffman, M. Waimer, S. Schmeer and J. Blaurock, "Dynamic testing and modelling of composite fuselage frames and fasteners for aircraft crash simulations," *International Journal of Crashworthiness,* vol. 18, pp. 406-422, 2013.

[70] K. Jackson, E. Fasanella, R. Boitnott and K. Lyle, "Full-scale crash test and finite element simulation of a composite prototype helicopter," NASA TP-2003-212641, ARL-TR-2824, Hampton, VA, 2003.

[71] A. Stockwell, "Simulation of an impact test of the all-composite lear fan aircraft," NASA CR-2002-211458, Hampton, VA, 2002.

[72] J. Terry, S. Hooper and M. Nicholson, "Design and test of an improved crashworthiness small composite airframe," NASA CR-2002-211774, Hampton, VA, 2002.

[73] D. Delsart, D. Joly, M. Mahe and G. Winkelmuller, "Evaluation of finite element modelling methodologies for the design of crashworthy composite commercial aircraft fuselage," in *24th International Congress of the Aeronautical Sciences*, Yokohama, Japan, September 2004.

[74] K. Jackson, "Impact testing and simulation of a crashworthy composite fuselage concept," *International Journal of Crashworthiness*, vol. 6, pp. 107-122, 2001.

[75] L. Maia and P. de Oliveira, "A review of finite element simulation of aircraft crashworthiness," SAE Technical Paper 2005-01-4012, 2005.

[76] V. Sokolinksy, K. Indermuehle and J. Hurtado, "Numerical simulation of the crushing process of a corrugated composite plate," *Composites: Part A*, vol. 42, pp. 1119-1126, 2011.

[77] D. Fleming, "Delamination modeling of composites for improved crash analysis," *Journal of Composite Materials*, vol. 35, pp. 1777-1792, 2001.

[78] M. Rassaian and B. Wade, "Numerical Round Robin action items," in *9th CMH-17 Crashworthiness Working Group Meeting*, Costa Mesa, CA, July 2010.

[79] A. Byar, "A crashworthiness study of a Boeing 737 fuselage section," Drexel University Doctoral Dissertation, Philadelphia, PA, 2004.

[80] J. Gabrys, J. Schatz, K. Carney, M. Melis, E. Fasanella and K. Lyle, "The use of LS-DYNA in the Columbia accident investigation and Return to Flight activities," in *Proceedings of the 8th International LS-DYNA User's Conference*, Detroit, MI, May 2004.

[81] J. Tomblin, J. Sherraden, W. Seneviratne and K. Raju, "A-basis and B-basis design allowables for epoxy-based prepreg: Toray T700SC-12k-50C/#2510 Plain Weave Fabric (AGATE-WP3.3-033051-134)," National Institute for Aviation Research, Wichita, KS, October 2002.

[82] J. Tomblin, J. Sherraden, W. Seneviratne and K. Raju, "A-basis and B-basis design allowables for epoxy-based prepreg: Toray T700GC-12k-31E/#2510 Unidirectional tape. (AGATE-WP3.3-033051-135)," National Institute for Aviation Research, Wichita, KS, October 2002.

[83] J. Lavoie and S. Kellas, "Dynamic crush tests of energy-absorbing laminated composite plates," *Composites Part A*, vol. 27, no. 6, pp. 467-475, 1996.

[84] A. Bolukbasi and D. Laananen, "Energy absorption in composite stiffeners," *Composites*, vol. 26, no. 4, pp. 291-301, 1995.

[85] P. Feraboli, "Development of a corrugated test specimen for composite materials energy absorption," *Journal of Composite Materials*, vol. 42, pp. 229-256, 2008.

[86] B. Wade, P. Feraboli and M. Rassaian, "The long and winding road toward standardization," in *Proceedings of the 7th CMH-17 Crashworthiness Working Group Meeting*, Salt Lake City, UT, March 2009.

[87] P. Feraboli, B. Wade, F. Deleo and M. Rassaian, "Crush energy absorption of composite channel section specimens," *Composites: Part A*, vol. 40, no. 8, pp. 1248-1256, 2009.

[88] F. Deleo, "Crashworthiness energy absorption of carbon fiber composites: experiment and simulation," University of Washington Master's Thesis, Seattle, WA, 2011.

[89] A. Bolukbasi, T. Baxter, T. Nguyen, M. Rassaian, K. Davis, W. Koch and L. Firth, "Energy absorbing structure for aircraft". United States Patent 8376275.

[90] K. Jackson, J. Morton, J. Lavoie and R. Boitnott, "Scaling of energy absorbing composite plates," *Journal of American Helicopter Society*, vol. 39, no. 1, pp. 17-23, 1994.

[91] Livermore Software Technology Corporation, "LS-DYNA Keyword User's Manual Version 971", May 2007.

[92] M. Osborne, "Single-Element Characterization of the LS-DYNA MAT54 Material Model," University of Washington Master's Thesis, Seattle, WA, 2012.

[93] P. Feraboli, B. Wade, F. Deleo, M. Rassaian, M. Higgins, M. Higgins and A. Byar, "LS-DYNA MAT54 modeling of the axial crushing of a composite tape sinusoidal specimen," *Composites: Part A*, vol. 42, pp. 1809-1825, 2011.

[94] P. Feraboli and B. Wade, "Crushing behavior of a composite corrugated specimen representative of an aircraft subfloor: Experiment and simulation," FAA Technical Report, DOT/FAA/AR-11/21, Sept 2013.

[95] S.A.E. Recommended Practice J211b, "Instrumentation for Impact Tests," Society of

Automotive Engineers, Warrendale, PN, 1974.

[96] J. Reichert and J. Landolt, "Digital and Analog Filters for Processing Impact Test Data," SAE Technical Paper Series 810813, Dearborn, MI, 1981.

[97] P. Feraboli and M. Rassaian, "Proceedings of the CMH-17 (MIL-HDBK-17) Crashworthiness Working Group Numerical Round Robin," Costa Mesa, CA, July 2010.

[98] M. Paz, Structural Dynamics Theory and Computation, 3rd ed., New York: Van Nostrand Reinhold, 1991.

[99] C. Meyer and K. Will, Models for Dynamic Analysis in Finite Element Idealization, New York: American Society of Civil Engineers, 1987.

[100] J. Zukas, T. Nicholas, H. Swift, L. Greszczuk and D. Curran, Impact Dynamics, 1st ed., John Wiley & Sons, 1982.

[101] Livermore Software Technology Corporation, ""LS-DYNA Theory Manual"," March 2006.

[102] S. Krishnamoorthy, J. Höptner, G. Kopp and H. Friedrich, "Prediction of structural response of FRP composites for conceptual design of vehicles under impact loading," in *8th European LS-DYNA User's Conference*, Strasbourg, Germany, May 2011.

[103] G. Mabson, O. Weckner and M. Ramnath, "Finite element based decohesive failure simulation sensitivity studies," in *53rd AIAA/ASME/ASCE/AHS/ASC Structures, Structural Dynamics and Materials Conference*, Honolulu, HI, April 2012.

[104] S. Bala and J. Day, "General guidelines for crash analysis in LS-DYNA," Livermore Software Technology Corporation, [Online]. Available: http://blog2.d3view.com/general-guidelines-for-crash-analysis-in-ls-dyna. [Accessed 2010].

[105] J. Day, "Modeling of Composites in LS-DYNA," Livermore Software Technology Corporation, [Online]. Available: awg.lstc.com/tiki/tiki-download_file.php?fileId=19. [Accessed 2010].

[106] S. Bala, "Contact Modeling in LS-DYNA - Some Recommendations," *FEA Information International News*, August 2001.

[107] S. Bala, "Initial Penetrations in Contact Interfaces," Livermore Software Technology Corporation, 2006. [Online]. Available: http://blog2.d3view.com/initial-penetrations-in-contact-interfaces. [Accessed 2010].

[108] R. Courant, K. Friedrichs and H. Lewy, "Über die partiellen Differentialgleichungen der mathematischen Physik," *Mathematische Annelen*, vol. 100, pp. 32-74, 1928.

[109] *ASTM Standard D3039 "Standard Test Method for Tensile Properties of Polymer Matrix Composite Materials"*, West Conshohocken, PA: ASTM International, 2000.

[110] SACMA Recommended Method SRM 3R-94, *"Open-Hole Compression Properties of Oriented Fiber-Resin Composites"*, Arlington, VA: Suppliers of Advanced Composite Materials Association, Revised 1994.

[111] T. Erhart, "An overview of user defined interfaces in LS-DYNA," in *8th European LS-*

DYNA Conference, Strasburg, Germany, May 2011.

Appendix A: Additional experimental data

Shear stress-strain curves were generated for both UD and PW AGATE material systems from shear best-fit equations contained in the published AGATE data. These curves, along with their equations are given in Figure 162.

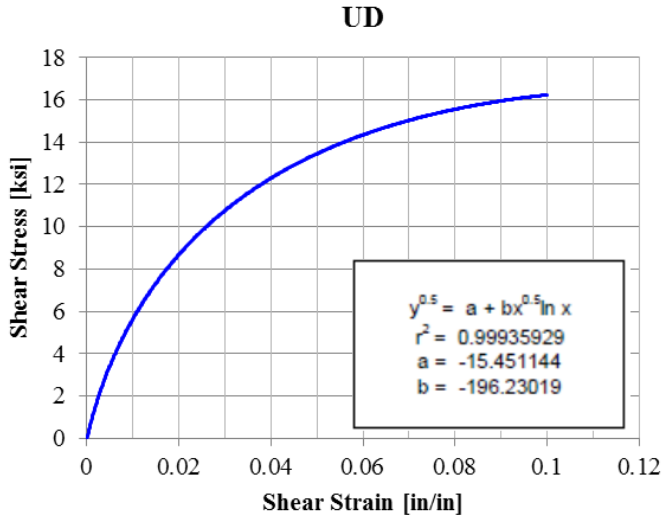

(a)

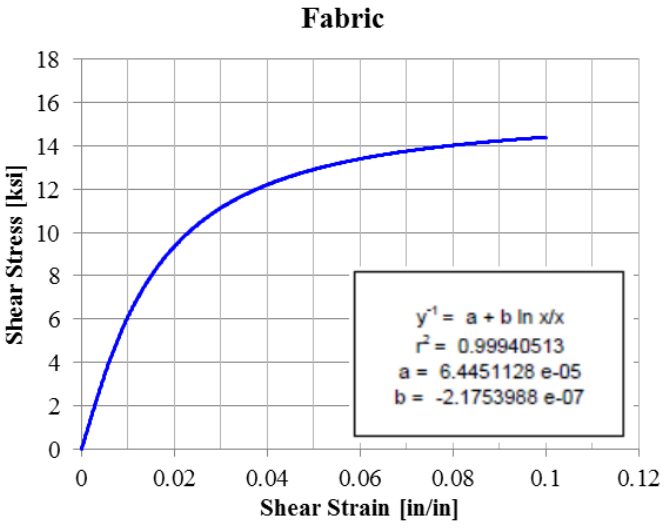

(b)

Figure 162. Shear stress-strain curves from the published AGATE data of the (a) UD [82] and (b) fabric [81] material systems.

From the material curves of Figure 15 and Figure 162, the strain-energy axial, transverse, and shear components are measured by taking the integral of the stress over the strain and calculating the area under the stress-strain curves. This is done for both material systems, in tension and in compression separately, and the strain energy per unit volume data is presented in Table 23. This data is used for the Wolfe strain energy failure criterion [61].

Table 23. Measured strain-energy component data for the UD and PW fabric material systems.

Strain energy per unit volume *[psi]*	**UD**	**PW**
$\mathbf{SE_1^{tu}}$	2765	1077
$\mathbf{SE_1^{cu}}$	1375	656
$\mathbf{SE_2^{tu}}$	21	788
$\mathbf{SE_2^{cu}}$	282	669
$\mathbf{SE_{12}^{u}}$	1205	1148

The two lay-ups considered were a UD cross-ply $[0/90]_{3s}$ and a fabric $[(0/90)]_{8f}$, which yielded average cured laminate thicknesses of 0.065 in. (1.65 mm) and 0.073 in. (1.85 mm), respectively. For the UD cross-ply lay-up, additional material testing was necessary to supplement the published AGATE material data during the validation process of the numeric material model. Material properties were measured from standardized testing performed at the University of Washington using flat coupons manufactured by the material supplier, TCA. Basic mechanical properties were tested using standard test methods for tensile strength and modulus [109], as well as compressive strength and modulus [110]. Images of the tests are shown in Figure 163. A minimum of 6 repetitions were used.

(a) 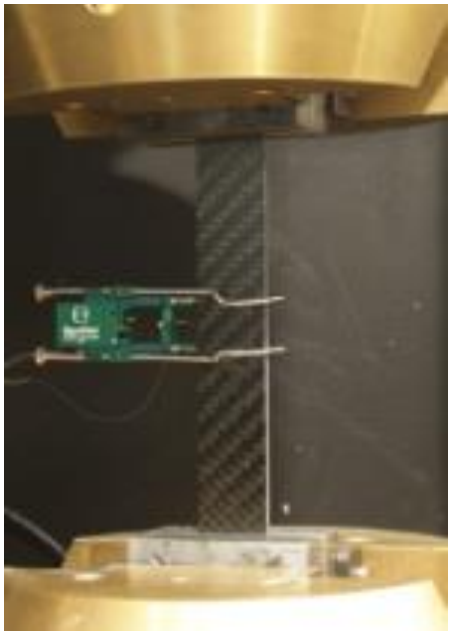 (b) 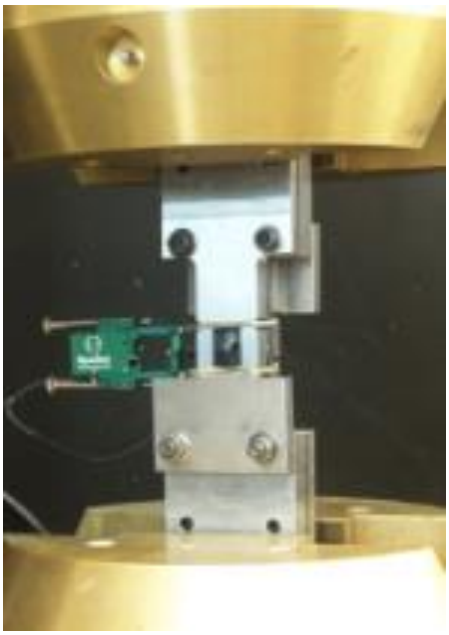

Figure 163. Mechanical material property testing in (a) tension and (b) compression

The experimental stress-strain curves of the cross-ply UD test coupons are plotted against an idealized linear curve determined based on the UD properties published in the AGATE documentation in Figure 164. The idealized curve was generated using Classical Laminate Theory (CLT) with the UD lamina properties and progressive ply failure using the maximum stress failure criterion. The cross-ply laminate test results had excellent matching prior to first ply failure, after which the experimental curve became non-linear and no longer matched the expected linear results. Otherwise, the measured strength values were very close to what would be expected from the CLT estimation.

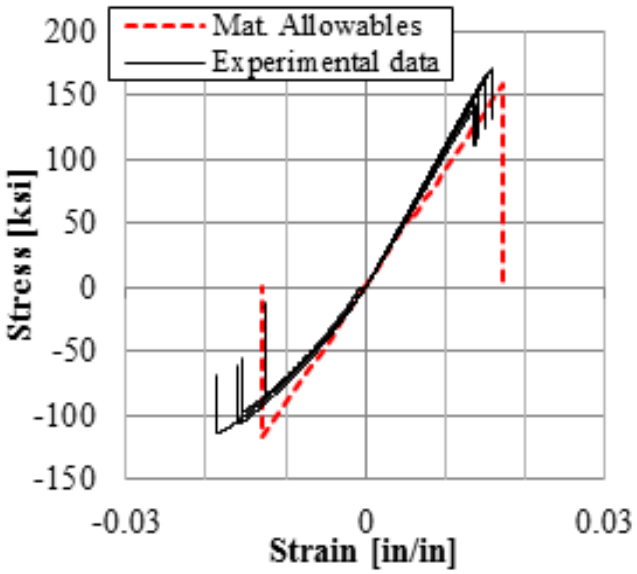

Figure 164. Experimental stress-strain curves from coupon-level tests of $[0/90]_{3s}$ cross-ply specimens compared with expected results based on material properties.

For the crush specimens of various geometries, the load, energy absorbed, and SEA vs. displacement curves from each repetition are given in the following Figure 165-Figure 167, respectively.

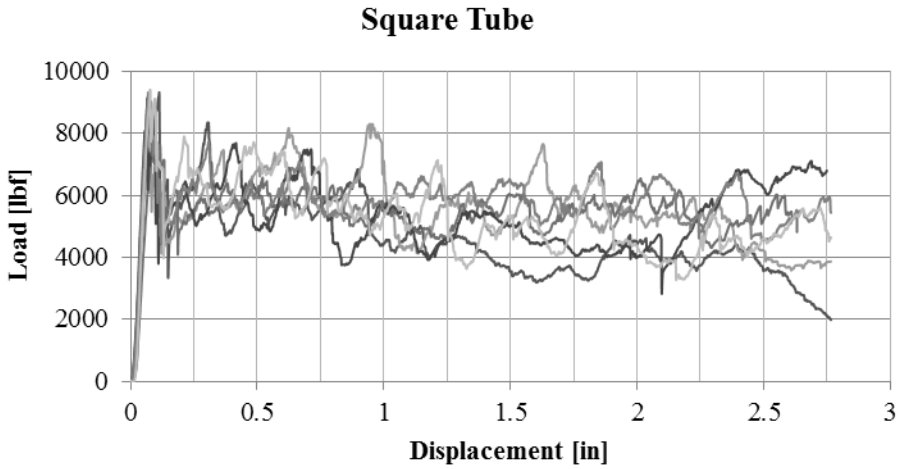

(a)

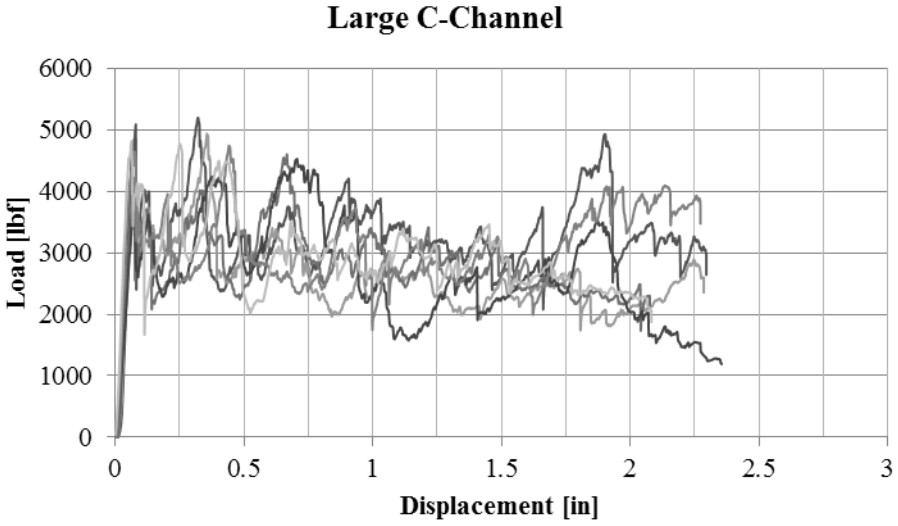
Large C-Channel
Load [lbf]
Displacement [in]
6000
5000
4000
3000
2000
1000
0
0
0.5
1
1.5
2
2.5
3

(b)

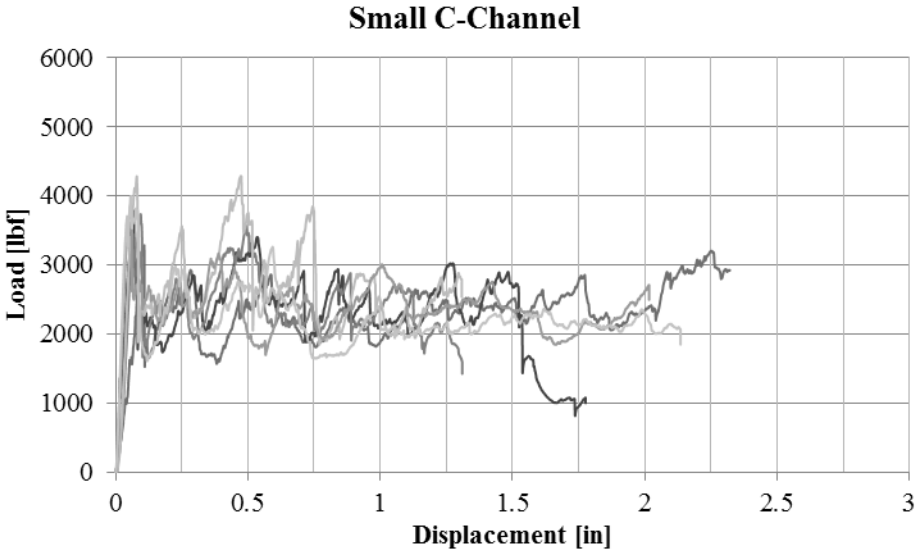
Small C-Channel
Load [lbf]
Displacement [in]
6000
5000
4000
3000
2000
1000
0
0
0.5
1
1.5
2
2.5
3

(c)

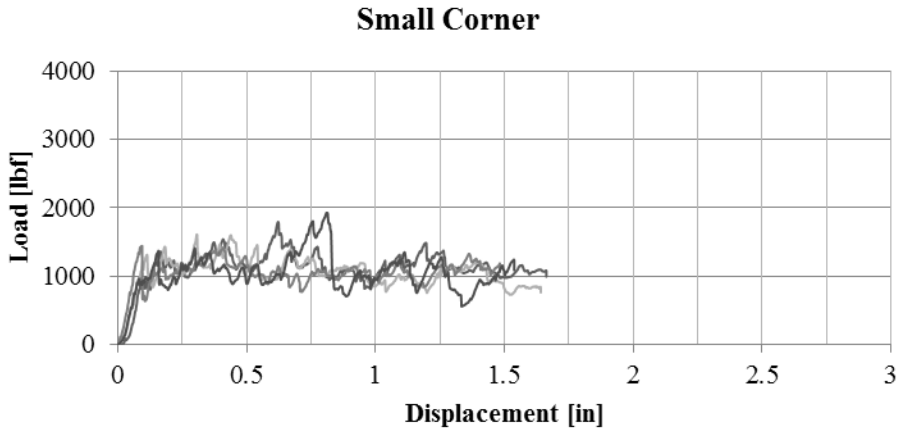

(d)

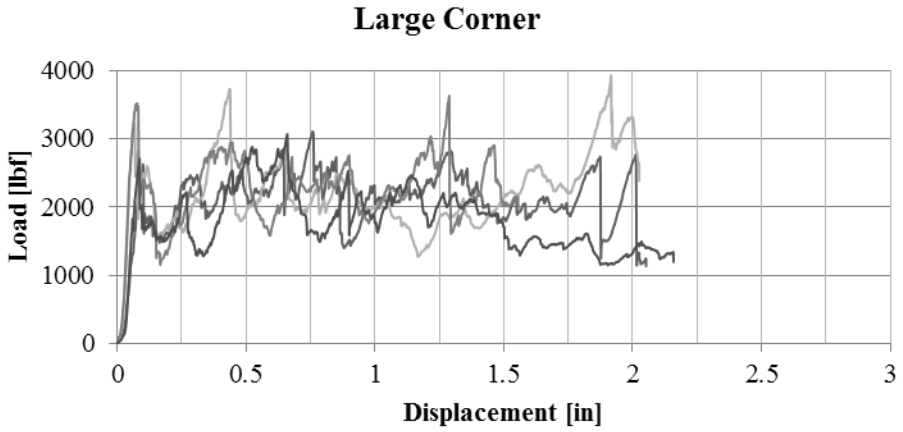

(e)

Figure 165. Load-displacement curves measured from crush experiments of (a) square tube, (b) large c-channel, (c) small c-channel, (d) small corner, and (e) large corner elements.

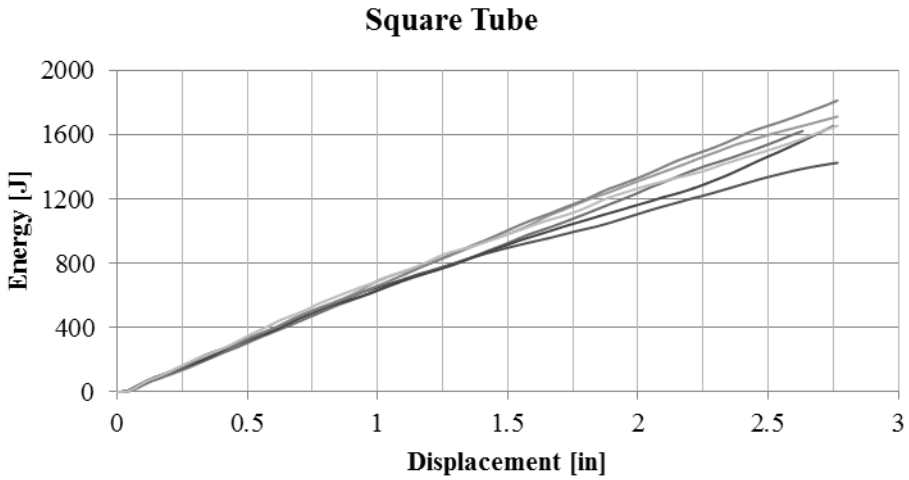

(a)

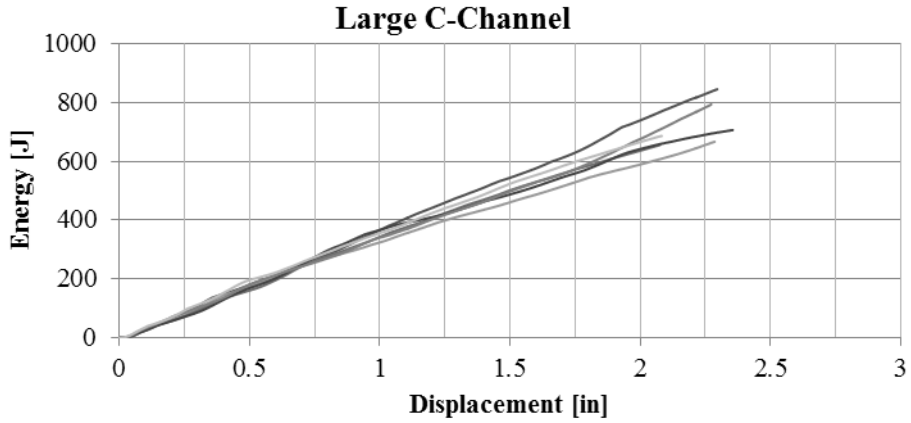
Large C-Channel
Energy [J]
1000
800
600
400
200
0
0
0.5
1
1.5
2
2.5
3
Displacement [in]

(b)

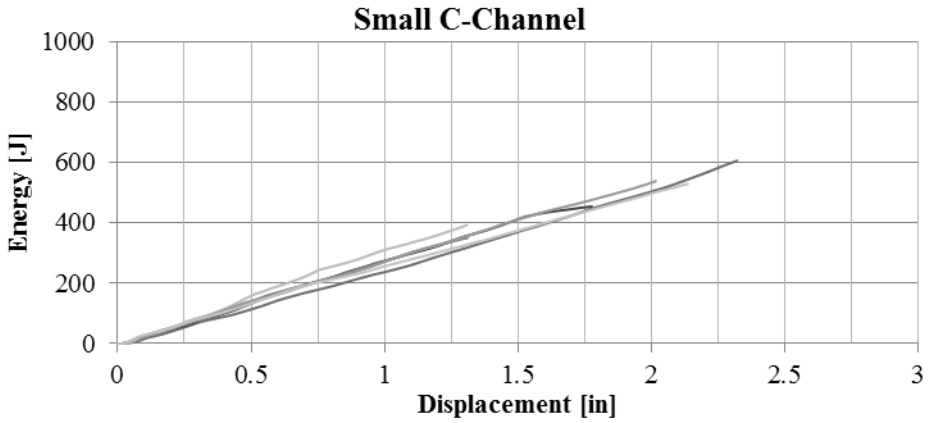
Small C-Channel
Energy [J]
1000
800
600
400
200
0
0
0.5
1
1.5
2
2.5
3
Displacement [in]

(c)

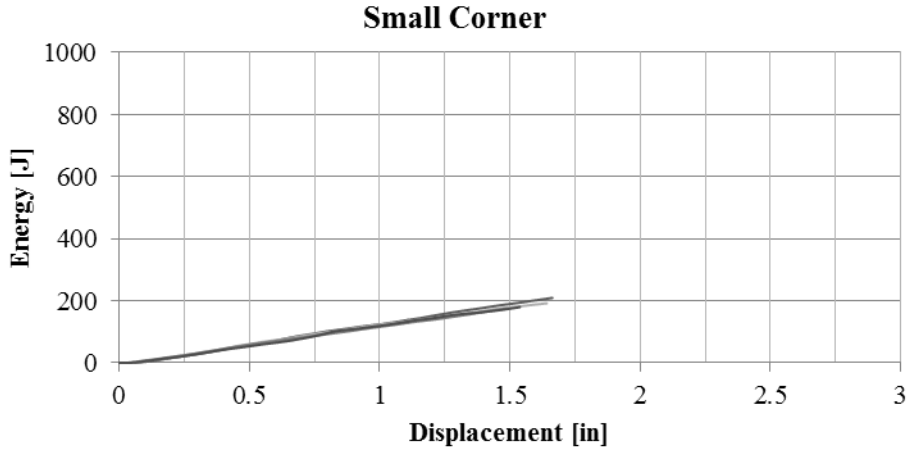
Small Corner
Energy [J]
1000
800
600
400
200
0
0
0.5
1
1.5
2
2.5
3
Displacement [in]

(d)

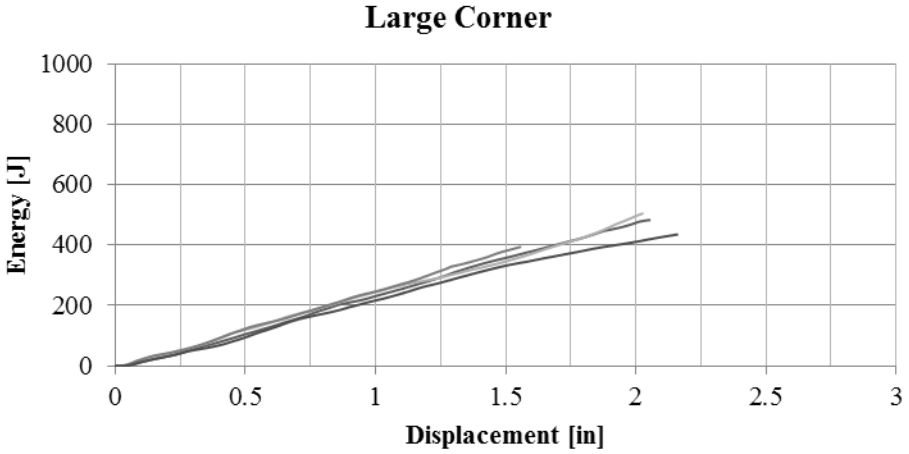

(e)

Figure 166. Energy absorption curves measured from crush experiments of (a) square tube, (b) large c-channel, (c) small c-channel, (d) small corner, and (e) large corner elements.

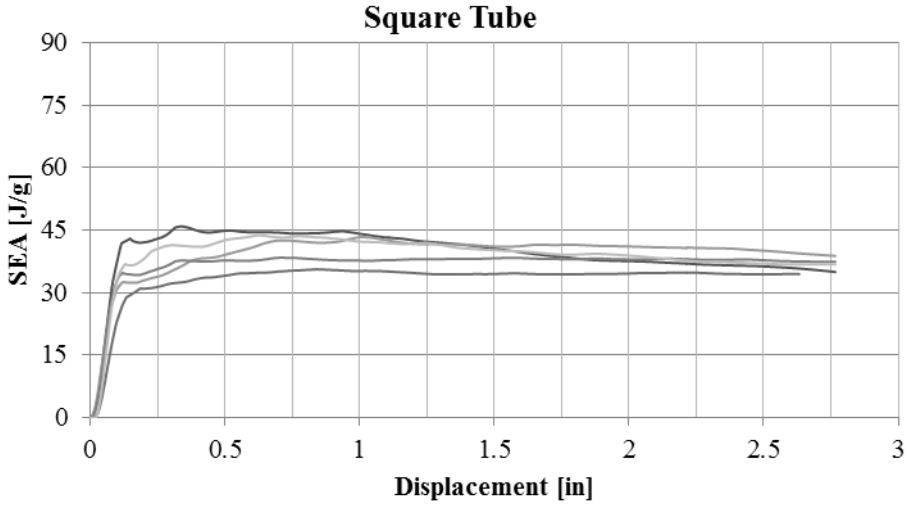

(a)

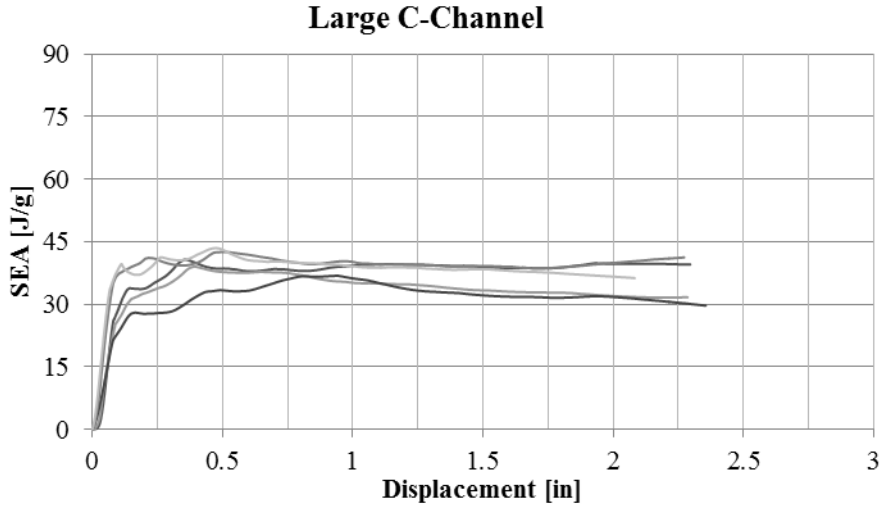
Large C-Channel
SEA [J/g]
90
75
60
45
30
15
0
0
0.5
1
1.5
2
2.5
3
Displacement [in]

(b)

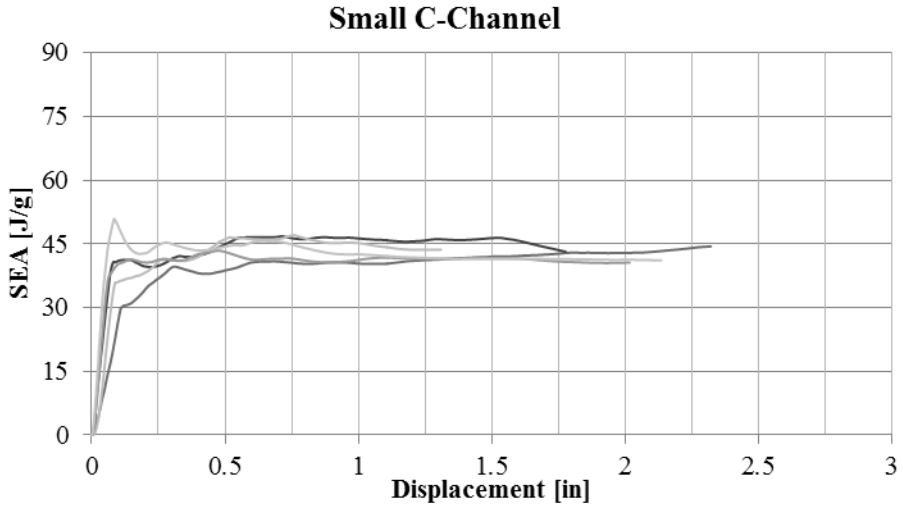
Small C-Channel
SEA [J/g]
90
75
60
45
30
15
0
0
0.5
1
1.5
2
2.5
3
Displacement [in]

(c)

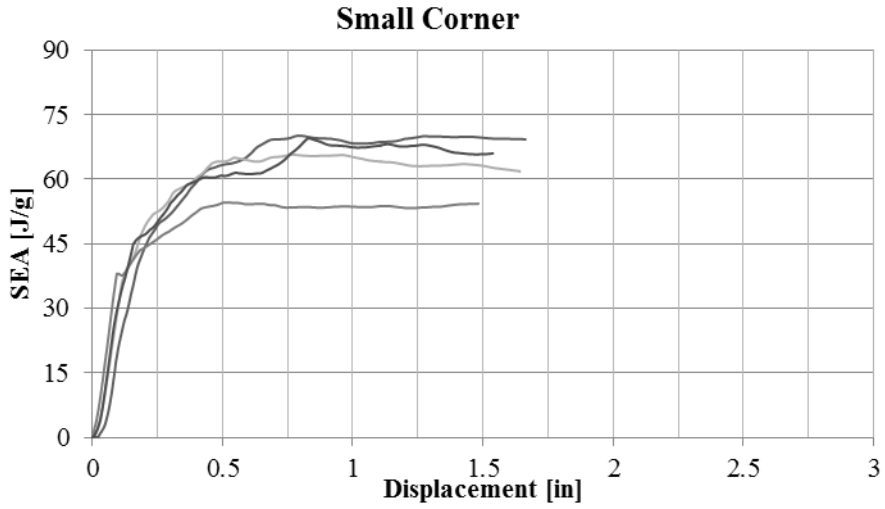
Small Corner
SEA [J/g]
90
75
60
45
30
15
0
0
0.5
1
1.5
2
2.5
3
Displacement [in]

(d)

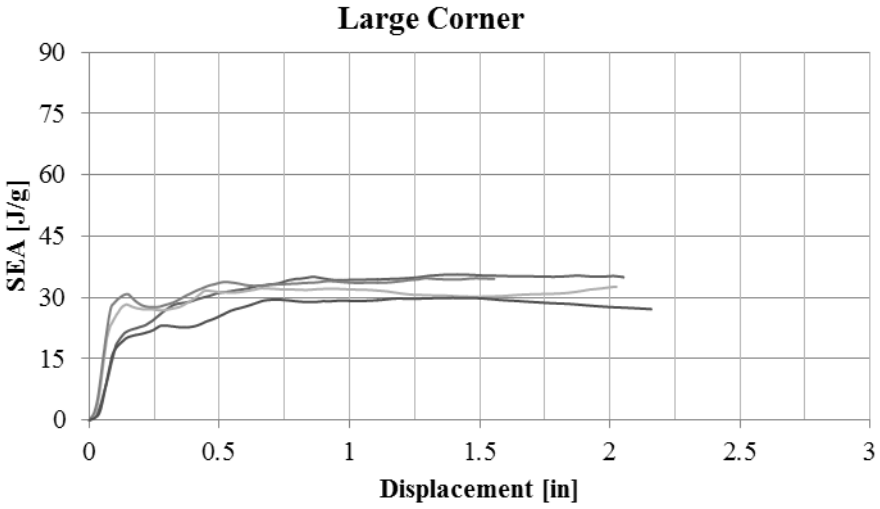

(e)

Figure 167. SEA curves measured from crush experiments of (a) square tube, (b) large c-channel, (c) small c-channel, (d) small corner, and (e) large corner elements.

Appendix B: LS-DYNA theory manual entry for MAT22 & MAT54

The MAT54 material model uses the MAT22 stress-strain equations in the elastic region, therefore the appropriate portion from the LS-DYNA Theory Manual for MAT22 is presented here in addition to the entire section of the LS-DYNA Theory Manual for the MAT54 material model.

Material Model 22: Chang-Chang Composite Failure Model

In plane stress, the strain is given in terms of the stress as

$$\varepsilon_1 = \frac{1}{E_1}(\sigma_1 - v_{12}\sigma_2) \tag{B-1}$$

$$\varepsilon_2 = \frac{1}{E_2}(\sigma_2 - v_{21}\sigma_1) \tag{B-2}$$

$$2\varepsilon_{12} = \frac{1}{G_{12}}\tau_{12} + \boldsymbol{\alpha}{\tau_{12}}^3 \tag{B-3}$$

The third equation defines the nonlinear shear stress parameter α.

Material Models 54 and 55: Enhanced Composite Damage Model

These models are very close in their formulations. Material 54 uses Chang matrix failure criterion (as Material 22), and material 55 uses the Tsai-Wu criterion for matrix failure.

Arbitrary orthotropic materials, e.g., unidirectional layers in composite shell structures can be defined. Optionally, various types of failure can be specified following either the suggestions of Chang and Chang [b1] or Tsai and Wu [b2]. In addition special measures are taken for failure

under compression. See Matzenmiller and Schweizerhof [b3]. This model is only valid for thin shell elements.

The Chang/Chang criteria is given as follows:

for the tensile fiber mode,

$$\sigma_{aa} > 0 \quad then \quad e_f^2 = \left(\frac{\sigma_{aa}}{X_t}\right)^2 + \beta\left(\frac{\sigma_{ab}}{S_c}\right) - 1 \begin{cases} \geq 0 \; failed \\ < 0 \; elastic \end{cases}, \tag{B-4}$$

Upon failure: $E_1 = E_2 = G_{12} = \nu_{12} = \nu_{21} = 0$

for the compressive fiber mode,

$$\sigma_{aa} < 0 \quad then \quad e_c^2 = \left(\frac{\sigma_{aa}}{X_c}\right)^2 - 1 \begin{cases} \geq 0 \; failed \\ < 0 \; elastic \end{cases}, \quad e_c{}^2 = \left(\frac{\sigma_{11}}{XC}\right)^2 \begin{cases} \geq 1 \text{failed} \\ < 1 \text{elastic} \end{cases} \tag{B-5}$$

Upon failure: $E_1 = \nu_{12} = \nu_{21} = 0$

for the tensile matrix mode,

$$\sigma_{bb} > 0 \quad then \quad e_m^2 = \left(\frac{\sigma_{bb}}{Y_t}\right)^2 + \left(\frac{\sigma_{ab}}{S_c}\right)^2 - 1 \begin{cases} \geq 0 \; failed \\ < 0 \; elastic \end{cases}, \quad e_m{}^2 = \left(\frac{\sigma_{22}}{YT}\right)^2 + \left(\frac{\sigma_{12}}{SC}\right)^2 \begin{cases} \geq 1 \text{failed} \\ < 1 \text{elastic} \end{cases} \tag{B-6}$$

Upon failure: $E_2 = \nu_{21} = G_{12} = 0$

and for the compressive matrix mode,

$$\sigma_{bb} < 0 \quad then \quad e_d^2 = \left(\frac{\sigma_{bb}}{2S_c}\right)^2 + \left[\left(\frac{Y_c}{2S_c}\right)^2 - 1\right]\frac{\sigma_{bb}}{Y_c} + \left(\frac{\sigma_{ab}}{S_c}\right)^2 - 1 \begin{cases} \geq 0 \; failed \\ < 0 \; elastic \end{cases} \tag{B-7}$$

Upon failure: $E_2 = \nu_{21} = \nu_{12} = 0 = G_{12} = 0$

$X_c = 2Y_c$ *for 50% fiber volume*

For β=1 we get the original Hashin [b4] in the tensile fiber mode.

For β=0, we get the maximum stress criterion which is found to compare better to experiments.

Failure can occur in any of four different ways:

1. If DFAILT is zero, failure occurs if the Chang/Chang failure criterion is satisfied in the tensile fiber mode.
2. If DFAILT is greater than zero, failure occurs if the tensile fiber strain is greater than DFAILT or less than DFAILC.
3. If EFS is greater than zero, failure occurs if the effective strain is greater than EFS.
4. If TFAIL is greater than zero, failure occurs according to the element time step as described in the definition of TFAIL.

When failure has occurred in all the composite layers (through-thickness integration points), the element is deleted. Elements which share nodes with the deleted element become "crashfront" elements and can have their strengths reduced by using the SOFT parameter with TFAIL greater than zero.

Information about the status in each layer (integration point) and element can be plotted using additional integration point variables. The number of additional integration point variables for shells written to the LS-DYNA database is input by the *DATABASE_BINARY definition as variable NEIPS. For Models 54 and 55 these additional variables are tabulated below (*i* = shell integration point):

History Variable	Description	Value	LS-PREPOST History Variable
1. *ef(i)*	*tensile fiber mode*	*1 – elastic* *0 – failed*	*1*
2. *ec(i)*	*compressive fiber mode*		*2*
3. *em(i)*	*tensile matrix mode*		*3*
4. *ed(i)*	*compressive matrix mode*		*4*
5. *efail*	*max[ef(ip)]*		*5*
6. *dam*	*damage parameter*	*-1 – element intact* *10^{-8} – element in crashfront* *+1 – element failed*	*6*

The following components, defined by the sum of failure indicators over all through-thickness integration points, are stored as element component 7 instead of the effective plastic strain:

Description	Integration point
$\frac{1}{nip}\sum_{i=1}^{nip} ef(i)$	*1*
$\frac{1}{nip}\sum_{i=1}^{nip} ec(i)$	*2*
$\frac{1}{nip}\sum_{i=1}^{nip} em(i)$	*3*

REFERENCES.

B-1. Chang, F.K., Chang, K.Y., "Post-Failure Analysis of Bolted Composite Joints in Tension or Shear-Out Mode Failure", *Journal of Composite Materials*, Vol. 21, pp. 809-833, 1987.

B-2. Tsai, S.W., Wu, E.M., "A General Theory of Strength for Anisotropic Materials", *Journal of Composite Materials*, Vol. 5, pp. 58-80, 1971.

B-3. Matzenmiller, A., Schweizerhof, K., "Crashworthiness Simulations of Composite Structures – A First Step with Explicit Time Integration", Nonlinear Computational Mechanics – A State of the Art, edited by P.W. Wriggers, et. al., Springer-Verlag, 1991.

B-4. Hashin, Z., "Failure Criteria for Unidirectional Fiber Composites", *Journal of Applied Mechanics*, Vol. 47, pp. 329-335, 1980.

Appendix C: LS-DYNA material model MAT54

Although several other codes are available, LS-DYNA has traditionally been considered the benchmark for composite crash simulations and is extensively used in the automotive and aerospace industries to perform explicit dynamic post-failure simulations [6] [79] [68] [80]. LS-DYNA has a handful of preexisting composite material models such as MAT22 and MAT54/55, which are progressive failure models that use a ply discount method to degrade elastic material properties; and MAT58, MAT158, and MAT162, which use continuum damage mechanics to degrade the elastic properties after failure. The LS-DYNA MAT54 material model is of interest for large full-scale structural damage simulations because it is a relatively simple material model which requires minimal input parameters. Not only does this reduce the computational requirement of a simulation, it also reduces the difficulty and amount of material testing necessary to generate input parameters.

MAT54 is a progressive failure model which is designed specifically to handle orthotropic materials such as unidirectional tape composite laminates. To support the following discussion, the entire MAT54 input deck is given in Figure 168, with all 43 user-defined input parameters grouped into seven categories for clarity. The definitions for all of these parameters are listed in Table 24. The LS-DYNA user's manual entry for MAT54 is reproduced in Appendix B: LS-DYNA theory manual entry for MAT22 & MAT54 [91].

*MAT_054 (ENHANCED_COMPOSITE_DAMAGE)

mid	ro	ea	eb	ec	prba	~~prca~~	~~prcb~~
1	1.50E-4	1.84E+7	1.22E+6	0.0	0.02049	0.0	0.0
gab	**~~gbc~~**	**~~gca~~**	**~~kf~~**	**aopt**			
6.10E+5	6.10E+5	6.10E+5	0.0	0.0			
xp	**yp**	**zp**	**a1**	**a2**	**a3**	**mangle**	
0.0	0.0	0.0	0.0	0.0	0.0	0.0	
v1	**v2**	**v3**	**d1**	**d2**	**d3**	**dfailm**	**dfails**
0.0	0.0	0.0	0.0	0.0	0.0	0.024	0.03
tfail	**alph**	**soft**	**fbrt**	**ycfac**	**dfailt**	**dfailc**	**efs**
1.1530E-9	0.1	0.0	0.5	1.2	0.0174	-0.0116	0.0
xc	**xt**	**yc**	**yt**	**sc**	**crit**	**beta**	
213000	319000	28800	7090	22400	54	0.5	

1. Constitutive properties: RO, EA, EB, EC, PRBA, PRCA, PRCB, GAB, GBC, GCA, KF

2. Local material axes: AOPT, XP, YP, ZP, A1-A3, MANGLE, V1-V3, D1-D3

3. Shear weighing factors: ALPH, BETA

4. Deletion parameters: DFAILM, DFAILS, TFAIL, DFAILT, DFAILC, EFS

5. Damage factors: SOFT, FBRT, YCFAC

6. Material strengths: XC, XT, YC, YT, SC

7. Failure criterion selection: CRIT

Figure 168. Material deck for MAT54 and the 43 parameters shown in seven categories. Strikethrough parameters are inactive.

In order to establish the local material coordinate system of the orthotropic composite material system, several options are available through the AOPT parameter. As given in the LS-DYNA User's Manual entry for MAT54, the AOPT options are:

$$AOPT \begin{cases} = 0.0, & \textit{Locally orthotropic with material axes determined by element nodes } 1, 2, \textit{and } 4 \\ = 2.0, & \textit{Globally orthotropic with material axes determined by vector } \boldsymbol{a} \\ = 3.0, & \textit{Locally orthotropic material axes determined by rotating the cross product of the vector } \boldsymbol{V} \textit{ with the element normal } \boldsymbol{n} \textit{ by the angle MANGLE} \\ < 0.0, & \textit{The absolute value of AOPT is a coordinate system ID} \end{cases} \quad \text{Eq. (21)}$$

An illustration for the local material axes options described in Equation 21 is given in Figure 158.

Table 24. MAT54 user-defined input definitions and required experimental data

Name	Definition	Type	Measurement
MID	Material identification number	Computational	N/A
RO	Mass per unit volume	Experimental	Density test
EA	Axial Young's modulus	Experimental	0-deg tension test
EB	Transverse Young's modulus	Experimental	90-deg tension test
EC	Through-thickness Young's modulus	(Inactive)	
PRBA	Minor Poisson's ratio v_{21}	Experimental	0-deg tension test with biaxial strain measurement
PRCA	Minor Poisson's ratio v_{31}	(Inactive)	
PRCB	Major Poisson's ratio v_{12}	(Inactive)	
GAB	Shear modulus G_{12}	Experimental	Shear test
GBC	Shear modulus G_{23}	(Inactive)	
GCA	Shear modulus G_{31}	(Inactive)	
KF	Bulk modulus	(Inactive)	
AOPT	Local material axes option	Computational	N/A
XP,YP,ZP	Used for AOPT = 1	(Inactive)	
A1,A2,A3	Vector 'a' used for AOPT = 2	Computational	N/A
MANGLE	Angle used for AOPT = 3	Computational	N/A
V1,V2,V3	Vector used for AOPT = 3	Computational	N/A
D1,D2,D3	Used for AOPT = 2, solid elements	(Inactive)	
ALPH	Elastic shear stress non-linear factor	Shear factor	**None; Default 0.1 recommended**
BETA	Shear factor in tensile axial failure criterion	Shear factor	**None; Default 0.5 recommended**
DFAILT	Axial tensile failure strain	Experimental	0-deg tension test
DFAILC	Axial compressive failure strain	Experimental	0-deg compression test
DFAILM	Transverse failure strain	Experimental	90-degree tension and compression tests; **May require adjustment for stability**
DFAILS	Shear failure strain	Experimental	Shear test
EFS	Effective failure strain	Optional	Combination of standard tests
TFAIL	Time step failure value	Computational	Derived from numeric time-step
FBRT	Axial tensile strength factor after 2-dir failure	Damage factor	**None; Default 0.5 recommended**
SOFT	Material strength factor after crushing failure	Damage factor	**Requires calibration against element-level crush data**
YCFAC	Axial compressive strength factor after 2-dir failure	Damage factor	**None; Default 1.2 recommended**
XT	Axial tensile strength	Experimental	0-deg tension test
XC	Axial compressive strength	Experimental	0-deg compression test
YT	Transverse tensile strength	Experimental	90-degree tension test
YC	Transverse compressive strength	Experimental	90-degree compression test
SC	Shear strength	Experimental	Shear test
CRIT	Specification of failure criterion	Computational	N/A; Requires value of 54 for MAT54

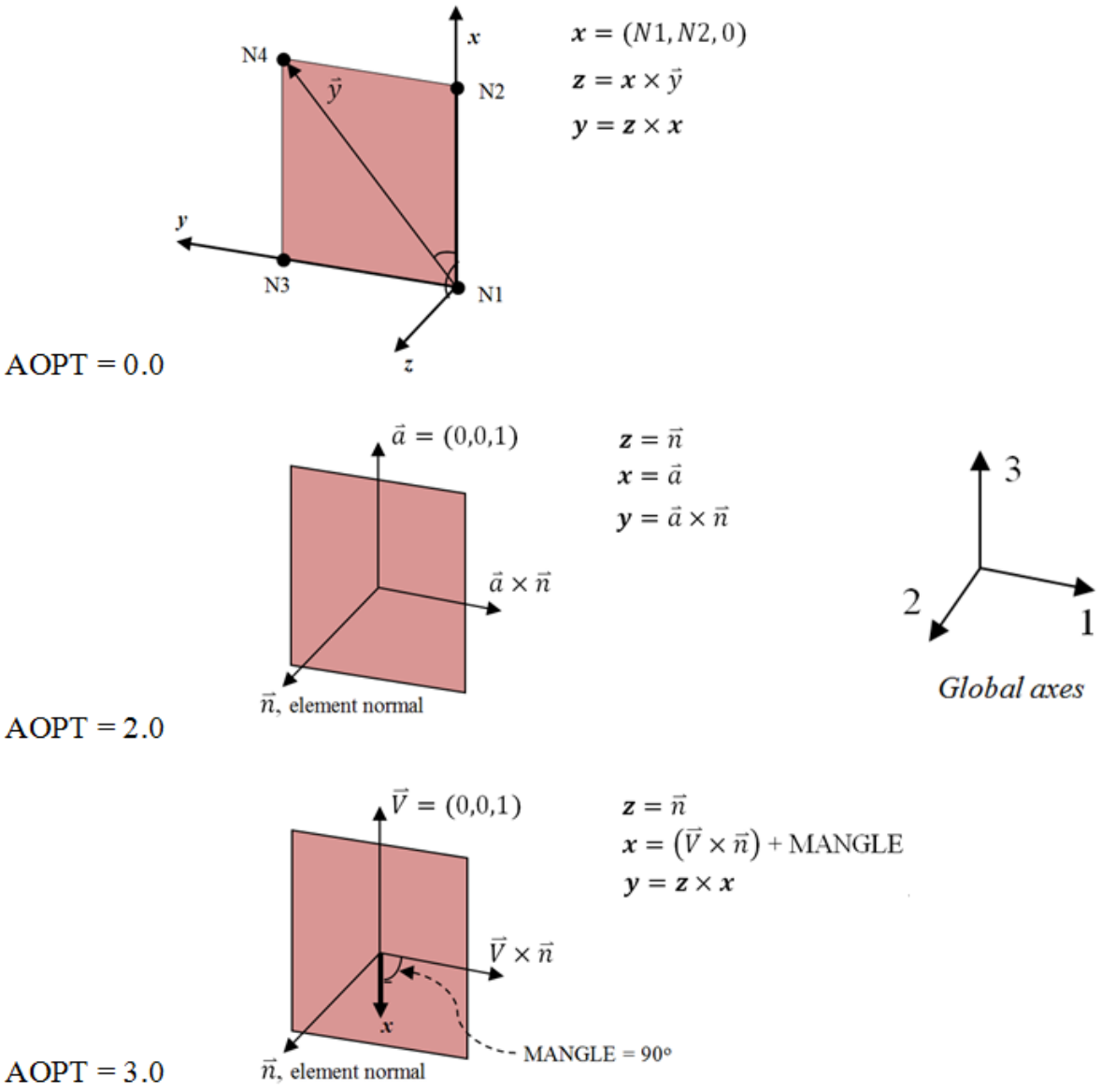

Figure 158. Illustration of three local material axes definition options for MAT54 as determined by the AOPT parameter.

In the elastic region, the material stress-strain behaviors for fiber (axial, 1-direction), matrix (transverse, 2-direction), and shear (12-direction) are given by:

$$\varepsilon_{11} = \frac{1}{E_1}(\sigma_{11} - v_{12}\sigma_{22}) \quad \text{Eq. (22)}$$

$$\varepsilon_{22} = \frac{1}{E_2}(\sigma_{22} - v_{21}\sigma_{11}) \quad \text{Eq. (23)}$$

$$2\varepsilon_{12} = \frac{1}{G_{12}}\sigma_{12} + \alpha{\sigma_{22}}^3 \quad \text{Eq. (24)}$$

In Equation 24, the α (ALPH in MAT54) input parameter is a weighing factor for the nonlinear shear stress term. ALPH cannot be experimentally determined, but needs to be calibrated by trial and error whenever shear is present.

Beyond the elastic region, MAT54 uses the Hashin [57] failure criteria to determine individual ply failure, as given by Equations 5-8. These equations are reproduced in Equations 25-28 using MAT54 notations, where *ef, ec, em* and *ed* are called history variables and they are failure flags which represent tension and compression for the fiber direction, and tension and compression for the matrix direction, respectively. XT is the fiber tensile strength, XC is the fiber compressive strength, YT is the matrix tensile strength, YC is the matrix compressive strength, and SC is the shear strength of the unidirectional ply. These input parameters can be measured through testing of the unidirectional tape lamina. It should be noted that all of these quantities assume that the 1-direction (axial) is the fiber direction, while the 2-direction (transverse) is the matrix direction.

For the tensile fiber mode where $\sigma_{11} \geq 0$:

$$ef^2 = \left(\frac{\sigma_{11}}{XT}\right)^2 + \beta\left(\frac{\sigma_{12}}{SC}\right)^2 - 1 \begin{cases} \geq 0 \; failed \\ < 0 \; elastic \end{cases} \quad \text{Eq. (25)}$$

Upon failure: $E_1 = E_2 = G_{12} = v_{12} = v_{21} = 0$.

The shear stress weighing factor β (BETA in MAT54) allows the user to explicitly define the influence of shear in the tensile fiber mode. Setting BETA = 0 reduces Eq. (4) to the Maximum Stress failure criterion. Selecting the BETA value is a matter of preference, and otherwise can be done by trial and error.

For the compressive fiber mode where $\sigma_{11} < 0$:

$$ec^2 = \left(\frac{\sigma_{11}}{XC}\right)^2 - 1 \begin{cases} \geq 0 \; failed \\ < 0 \; elastic \end{cases} \qquad \text{Eq. (26)}$$

Upon failure: $E_1 = \nu_{12} = \nu_{21} = 0$.

For the tensile matrix mode where $\sigma_{22} \geq 0$:

$$em^2 = \left(\frac{\sigma_{22}}{YT}\right)^2 + \left(\frac{\sigma_{12}}{SC}\right)^2 - 1 \begin{cases} \geq 0 \; failed \\ < 0 \; elastic \end{cases} \qquad \text{Eq. (27)}$$

Upon failure: $E_2 = \nu_{21} = G_{12} = 0$.

For the compressive matrix mode where $\sigma_{22} < 0$:

$$ed^2 = \left(\frac{\sigma_{22}}{2SC}\right)^2 + \left[\left(\frac{YC}{2SC}\right)^2 - 1\right]\frac{\sigma_{22}}{YC} + \left(\frac{\sigma_{12}}{SC}\right)^2 - 1 \begin{cases} \geq 0 \; failed \\ < 0 \; elastic \end{cases} \qquad \text{Eq. (28)}$$

Upon failure: $E_2 = \nu_{12} = \nu_{21} = G_{12} = 0$.

When one of the above conditions is exceeded in a ply within the element, the specified elastic properties for that ply are set to zero. The mechanism by which MAT54 applies this elastic property reduction, however, only prevents the failed ply from carrying increased stress rather than reducing the stress to zero or a near zero value. The equation used by MAT54 to determine 1- and 2-direction element stresses in the i^{th} time step provides insight into this mechanism:

$$\begin{bmatrix}\sigma_{11} \\ \sigma_{22}\end{bmatrix}_i = \begin{bmatrix}\sigma_{11} \\ \sigma_{22}\end{bmatrix}_{i-1} + \begin{bmatrix}C_{11} & C_{12} \\ C_{21} & C_{22}\end{bmatrix}_i \begin{bmatrix}\Delta\varepsilon_{11} \\ \Delta\varepsilon_{22}\end{bmatrix}_i \qquad \text{Eq. (29)}$$

When ply failure occurs in the i^{th} time step, constitutive properties in the stiffness matrix C go to zero, but the stresses from the *i-1* time step are non-zero. This leads the failed ply stresses to be constant and unchanged from the stress state just prior to failure. The resulting 'plastic' behavior, shown in Figure 169, occurs only when the strength is reached before the failure strain ('DFAIL' in Figure 169). Elastic property degradation following failure in MAT54 works in this way rather than degrading properties in the elastic equations, Equations 22-24, which would result in a reduced or zero stress state in a failed ply.

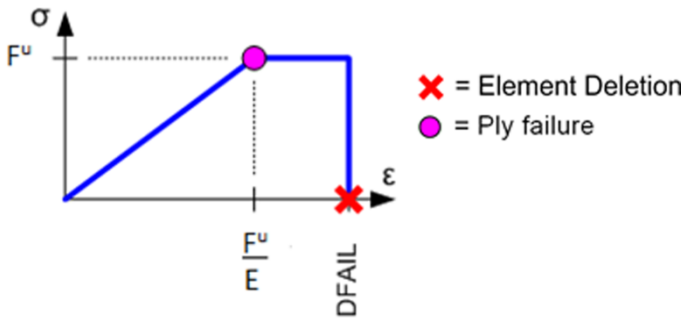

Figure 169. Elastic-plastic stress-strain behavior of MAT54.

The MAT54 FBRT and YCFAC strength reduction parameters are used to degrade the pristine fiber strengths of a ply if compressive matrix failure takes place. This strength reduction simulates damage done to the fibers from the failed matrix and it is applied using:

$$XT = XT^* * FBRT \qquad \text{Eq. (30)}$$

$$XC = YC^* * YCFAC \qquad \text{Eq. (31)}$$

The FBRT parameter defines the percentage of the pristine fiber strength that is left following failure, therefore its value should be in the range [0,1]. The YCFAC parameter uses the pristine matrix strength YC to determine the damaged compressive fiber strength, which means that the upper limit of YCFAC is XC/YC. The input value for the two parameters FBRT and YCFAC cannot be measured experimentally and must be determined by trial and error.

The SOFT parameter is a strength reduction factor for crush simulations. This parameter reduces the strength of the elements immediately ahead of the crush front in order to simulate damage propagating from the crush front. The strength degradation is applied to four of the material strengths as follows:

$$\{XT, XC, YT, YC\} = \{XT, XC, YT, YC\}^* * SOFT \quad \text{Eq. (32)}$$

where the asterisk indicates the pristine strength value. Reducing material strengths using SOFT allows for greater stability to achieve stable crushing by softening the load transition from the active row of elements to the next. The SOFT parameter is active within the range [0,1], where SOFT = 1 indicates that the elements at the crush front retain their pristine strength and no softening occurs. Since this parameter cannot be measured experimentally, it must be calibrated by trial and error for crush simulations.

The failure equations described in Equations 25-28 provide the maximum stress limit of a ply, and the damage mechanisms described in Equations 30-32 reduce the stress limit by a specified value given specific loading conditions. None of these mechanisms, however, cause the ply stress to go to zero. Instead, there are five critical strain values which reduce the ply stresses to zero. These are the strain to failure values in the positive fiber direction (tension) DFAILT, in the negative fiber direction (compression) DFAILC, in the matrix direction DFAILM, in shear DFAILS, and a non-physical failure strain parameter called EFS. It is important to note that in the matrix direction there is only one failure strain value which is used for both tension and compression.

Four of the failure strains can be measured through coupon-level tests, but if they are not known, LS-DYNA gives the user the option to employ a generic failure strain parameter, EFS (effective

failure strain). The EFS immediately reduces the ply stresses to zero when the strain in any direction exceeds EFS, which is given by:

$$EFS = \sqrt{\frac{4}{3}({\varepsilon_{11}}^2 + \varepsilon_{11}\varepsilon_{22} + {\varepsilon_{22}}^2 + {\varepsilon_{12}}^2)} \qquad \text{Eq. (33)}$$

A critical EFS value can be calculated for any simulation by determining 1-, 2-, and 12-strains at element failure and using them in Equation 33. EFS values below the critical EFS will cause premature element deletion. The default value for EFS is zero, which is interpreted by MAT54 to be numerically infinite.

An element is deleted once the stress in all of the plies has been reduced to zero. Element deletion can also occur when the element becomes highly distorted and requires a very small time step. A minimum time step parameter, TFAIL, removes distorted elements as follows:

TFAIL ≤ 0: No element deletion by time step

$0 <$ TFAIL ≤ 0.1: Element is deleted when its time step is smaller than TFAIL

TFAIL > 0.1: Element is deleted when $\frac{\text{current time-step}}{\text{original time-step}} <$ TFAIL

Defining TFAIL to be very near or greater than the element time step will cause premature element deletion since the element will violate the TFAIL condition in its initial state. If significant element distortion is not a concern, it is recommended to choose a value that is an order of magnitude smaller than the element time step for TFAIL. LS-DYNA assigns the element time-step automatically to ensure that the Courant condition is satisfied,

$$\Delta t = \frac{k\Delta h}{c} \qquad \text{Eq. (34)}$$

Where Δt is the time step of integration, Δh is the characteristic mesh dimension, k is a stability factor (0.6-0.8), and c is the speed of the sound wave through the material. For a one-dimensional longitudinal wave, the speed of the sound wave is $c = \sqrt{E/\rho}$, where E is the modulus of elasticity and ρ is the density [98] [100].

Unlike the strength-based ply failure criteria in Equations 25-28, there are no history variables for ply failure due to maximum strains or element deletion due to TFAIL. For this reason, it is not possible to distinguish the failure mode which causes element deletion from the simulation results.

Appendix D: Additional crush element simulation results

The following are the simulation results obtained from using the semi-circular sinusoid simulation and replacing the geometry to those of the seven other geometries investigated: two additional sinusoids and five tubular/channel-based geometries. For each geometry, the load-displacement crush curve (simulation vs. experiment) and a time-progression of the destabilized region of the simulation are shown. For optimal clarity, the loading plate is not shown in the time progression of these simulations. Each crush specimen is shown in an orientation with the trigger, thus loading plate, on the top. Without changing any parameters from the semi-circular sinusoid baseline simulation, all of the additional geometry crush simulations were too unstable and were unable to simulate the energy absorption of the crush element experiments.

D1. Square tube simulation

The square tube experienced multiple element erosions away from the crush-front at the onset of loading, which simulated a load peak over four times what was recorded from the crush experiment.. The first three rows of elements beyond the trigger broke away from the tube due to the failure of the fourth row of elements, while simultaneously several neighboring elements in the sixth to last row eroded. Shortly after, the rest of this element row near the bottom of the tube eroded, causing the entire tube to split into two portions, the largest of which was no longer held in place by the boundary conditions on the bottom row of nodes. This ended the simulation as load was no longer transmitted from the loading plate into the tube.

(a)

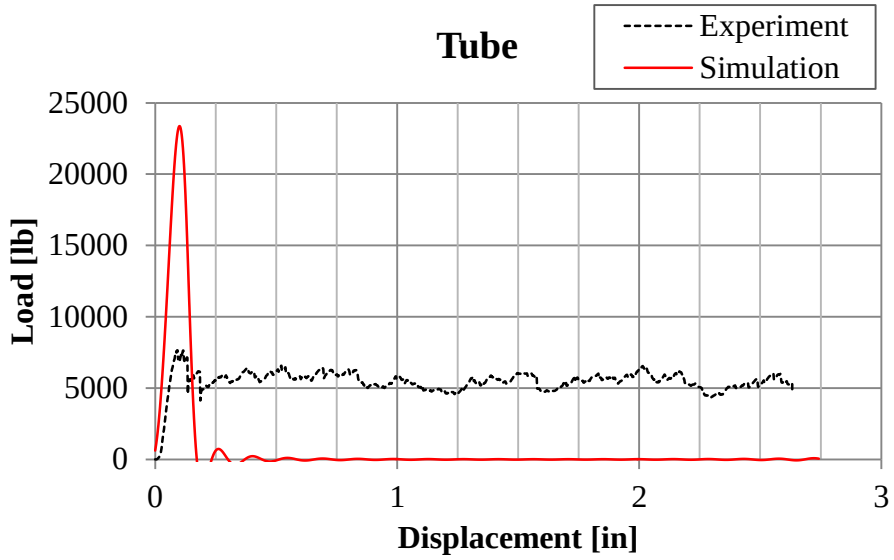

(b)

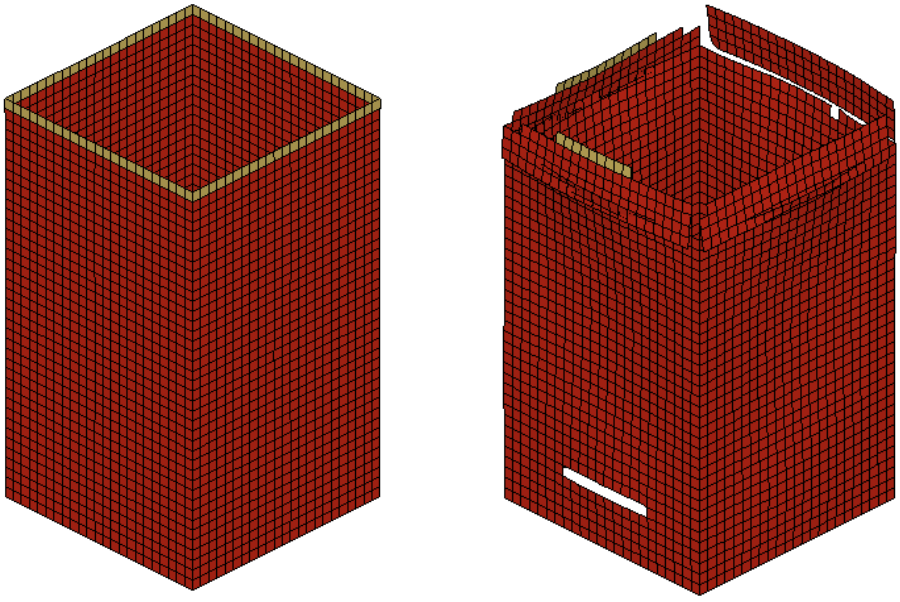

[d = 0.12 in] [d = 0.14 in]

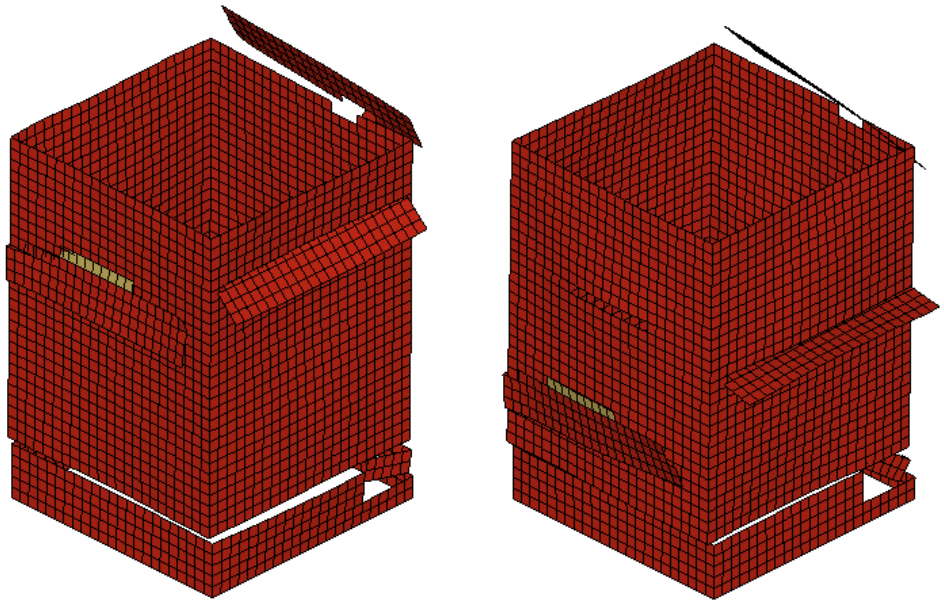

[d = 0.15 in] [d = 0.18 in]

Figure 170. No changed parameters from sinusoid model baseline: poor results of (a) simulated load-displacement crush curve and (b) unstable time-progression for the square tube geometry.

D2. Large c-channel simulation

The trigger row and first row of elements beyond the trigger failed progressively, however the initial load peak was more than double that recorded by the experiment, indicating larger forces being transmitted into the specimen than desired. Following this, several elements eroded beyond the crush front, causing a large portion of the channel to break away from the main specimen. This prevented load transmission into the channel until the loading plate came into contact with the specimen again (around d = 0.75 in displacement), at which point several more elements beyond the crush front eroded and the specimen broke apart.

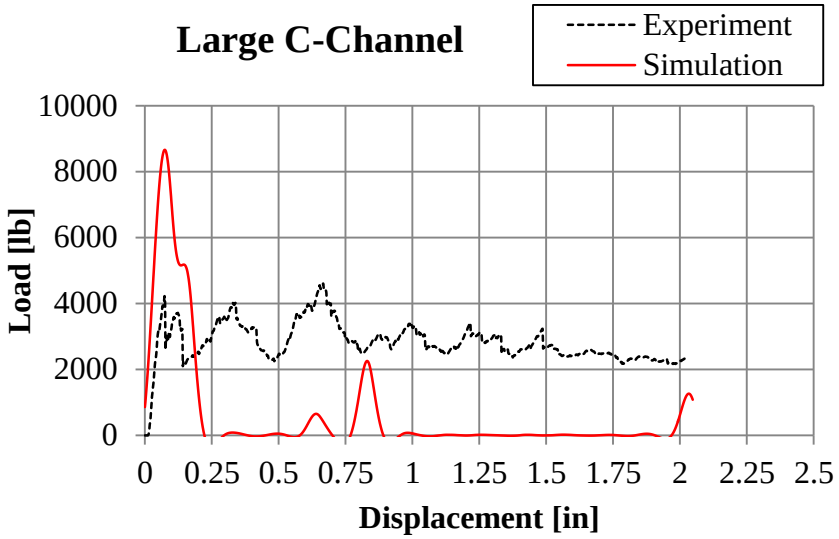

(a)

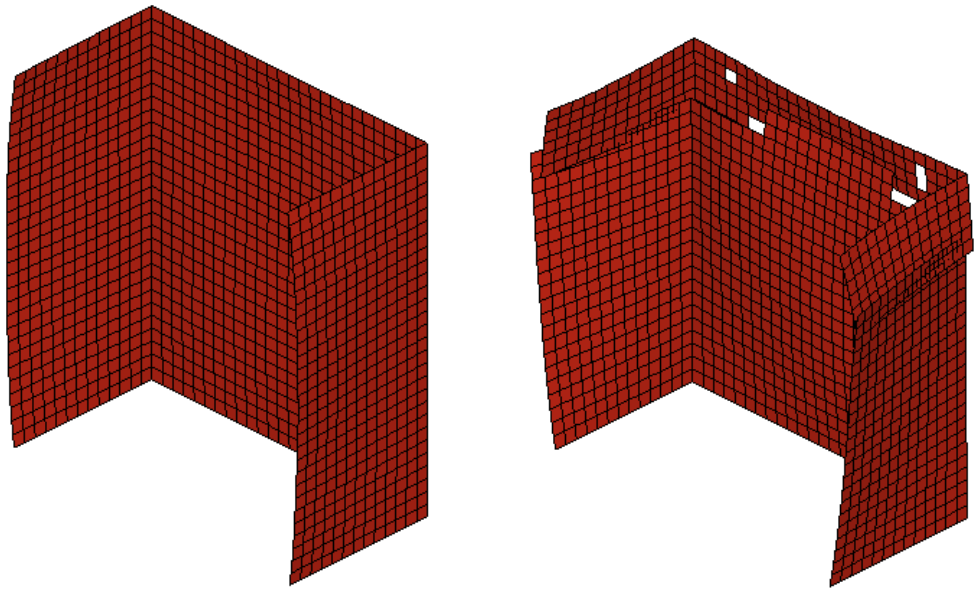

(b)

[d = 0.0150 in] [d = 0.0165 in]

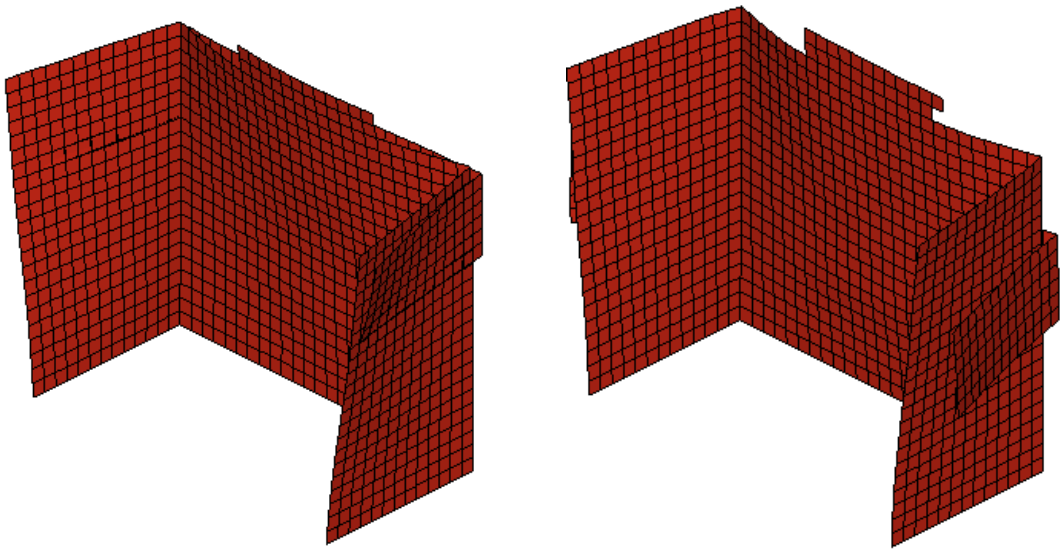

[d = 0.0180 in] [d = 0.0195 in]

Figure 171. No changed parameters from sinusoid model baseline: poor results of (a) simulated load-displacement crush curve and (b) unstable time-progression for the large c-channel geometry.

D3. Small c-channel simulation

Similarly to the large c-channel, the first couple rows of elements failed progressively, however at load values much higher than the crush experiment. Subsequently, several elements failed away from the crush front, breaking the small channel into several portions which fell away from the loading plate. A final peak at the end of the simulation represents when the loading plate came into contact with the last remaining elements at the end of the simulation.

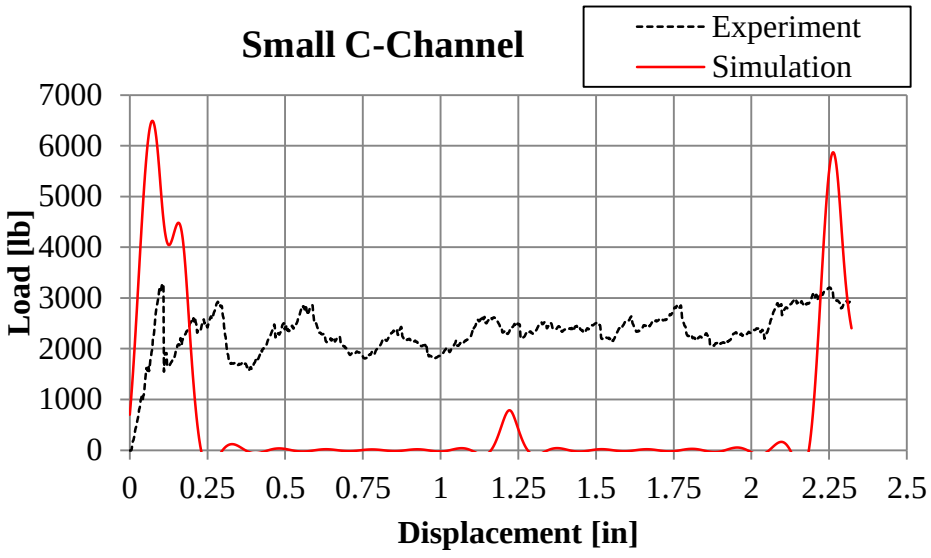

(a)

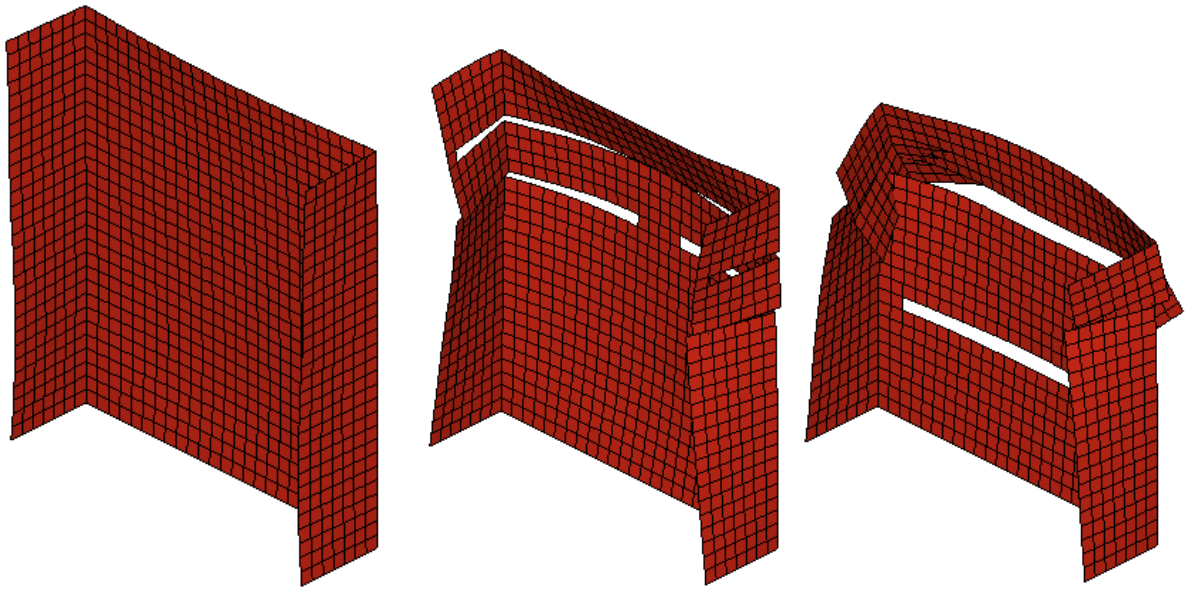

(b)

[d = 0.15 in] [d = 0.18 in] [d = 0.21 in]

Figure 172. No changed parameters from sinusoid model baseline: poor results of (a) simulated load-displacement crush curve and (b) unstable time-progression for the small c-channel geometry.

D4. Large corner simulation

Upon initial loading, the large corner simulation experienced element erosion at final row of elements, where the fixed boundary condition is imposed. This can be seen in the corner and along the flange of this crush geometry. The intiail load peak, like the other geometries, is much too high when compared with the experiment.

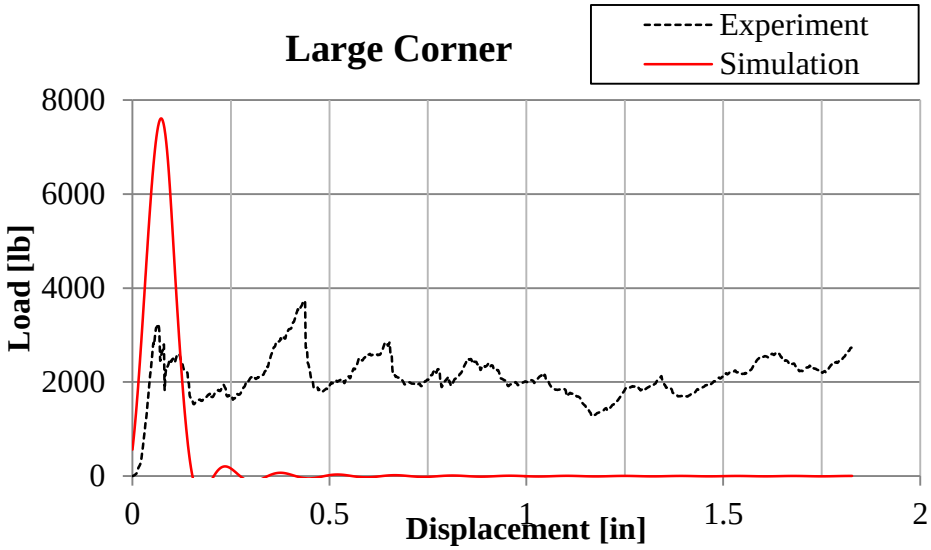

(a)

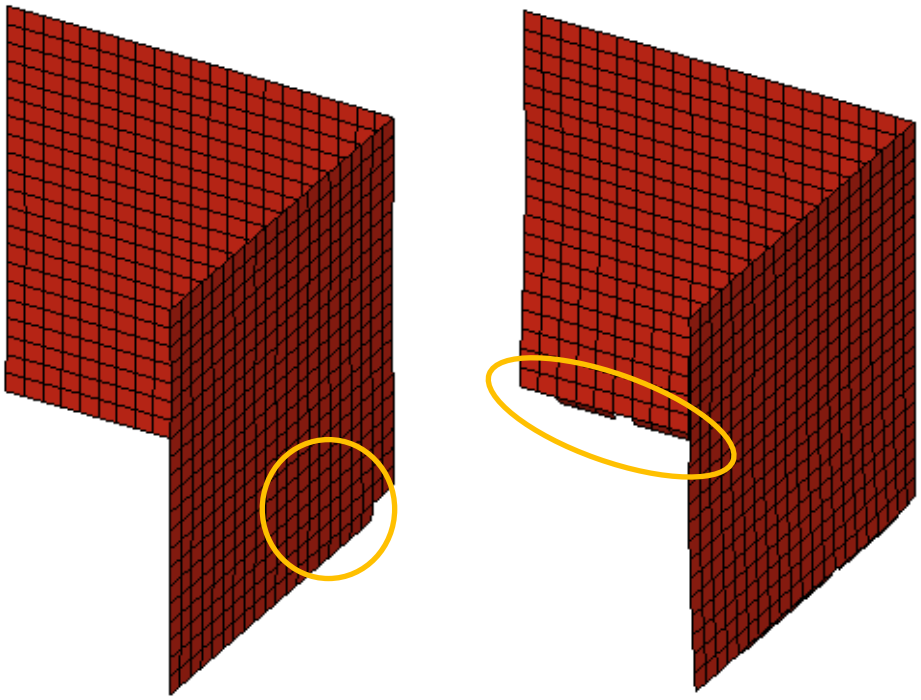

(b)

[d = 0.11 in] [d = 0.13 in]

Figure 173. No changed parameters from sinusoid model baseline: poor results of (a) simulated load-displacement crush curve and (b) element erosion at the boundary condition for the large corner geometry.

D5. Small corner simulation

The first two rows of elements in the small corner simulation eroded progressively, and the resulting crush loads are only about 50% higher than what was recorded from the experiment. Following this, however, an entire row of elements away from the crush front eroded, thus ending the simulation as the loading plate no longer transmitted forces into the small corner specimen.

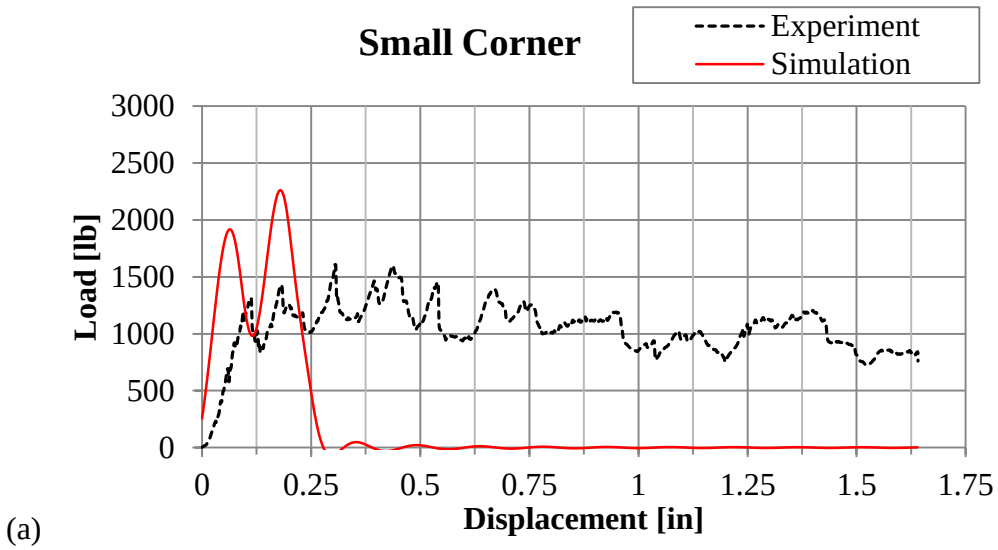

(a)

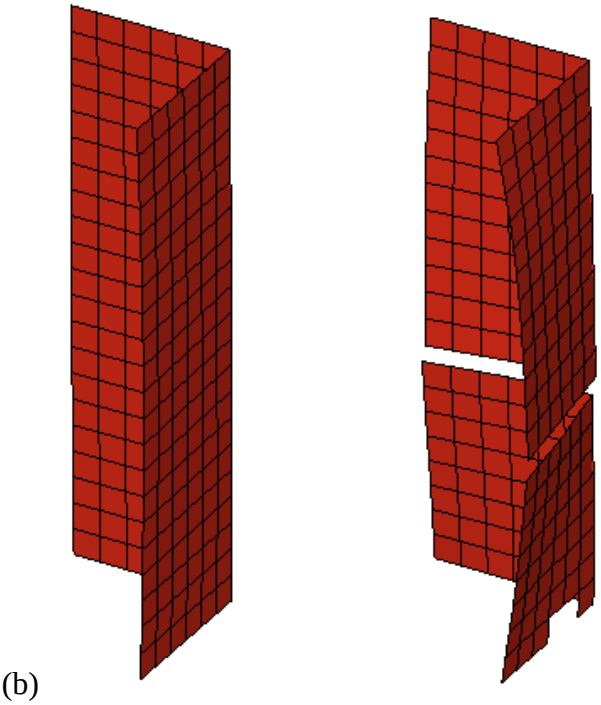

(b)

[d = 0.30 in] [d = 0.32 in]

Figure 174. No changed parameters from sinusoid model baseline: poor results of (a) simulated load-displacement crush curve and (b) unstable time-progression for the small corner geometry.

D6. Low sinusoid simulation

Being more similar in geometry to the baseline semi-circular sinusoid model from which tehse simulations were based from, the low and high sinusoids had more success than the tubular, channel, and corner sections. The low sinuoid experienced progressive crushing through the first several rows of elements, and the average crush load was the same as that of the experiment. Elements began eroding a few rows away from the crush-front in the middle of the simultaion, breaking progressive crushing, and in total three rows fell away from the top edge of the specimen. After the loading plate resumed contact with the specimen, progressive crushing resumed until near the end of the simulation, where elements eroded away from the crush front and broke the specimen in two parts for a second time, ending the load transfer to the specimen.

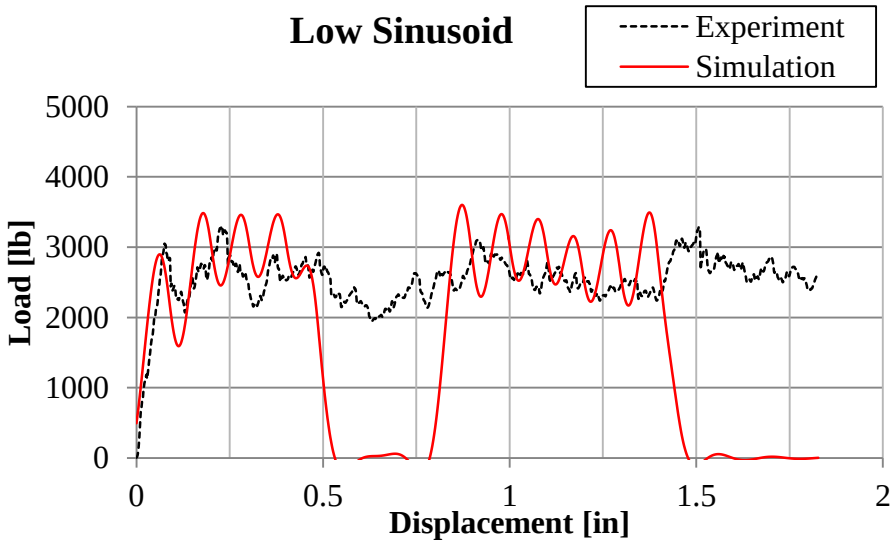

(a)

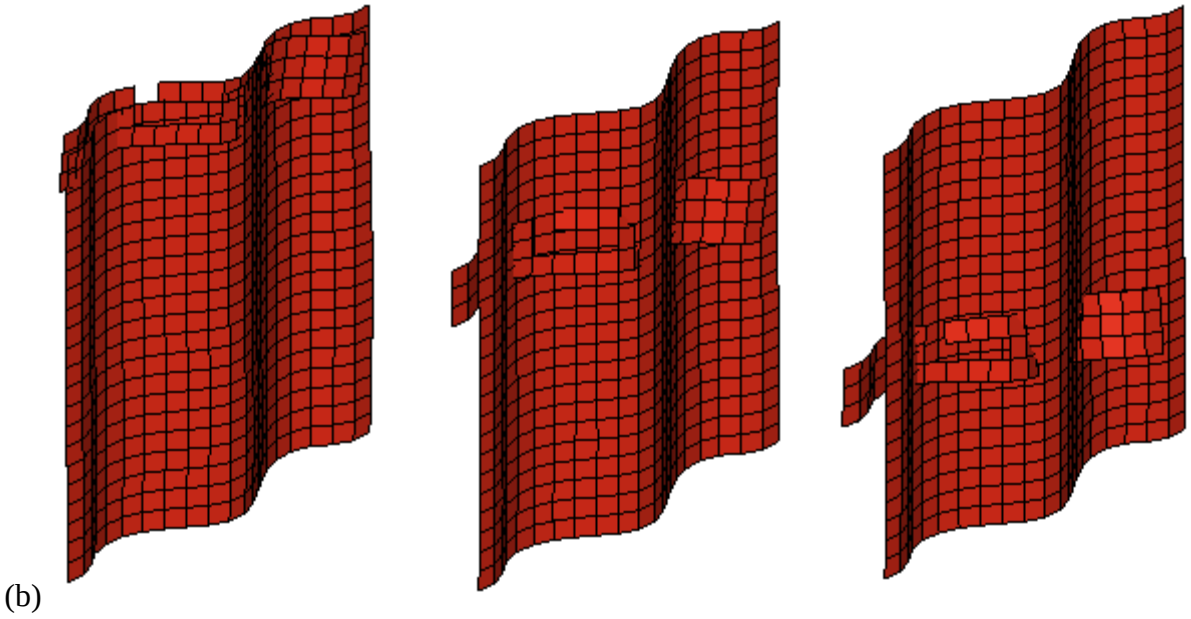

(b)

[d = 0.50 in] [d = 0.51 in] [d = 0.52 in]

Figure 175. No changed parameters from semi-circular sinusoid model baseline: unsatisfactory results of (a) simulated load-displacement crush curve and (b) unstable time-progression for the low sinusoid geometry.

D7. High sinusoid simulation

Like the low sinuoid, the high sinusoid experienced progressive crushing through the first several rows of elements, and the average crush load was the same as that of the experiment. Elements eroded away from the crush-front in the middle of the simultaion in two instances, causing large portions of the specimen to fall away and pausing the load transfer from the loading plate.. Progressive crushing resumed in between these large failures.

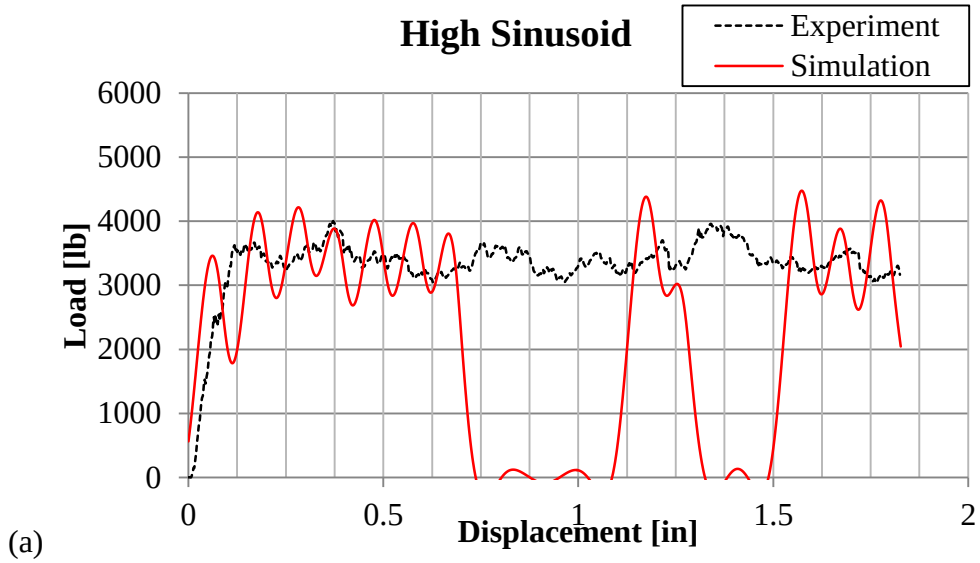

(a)

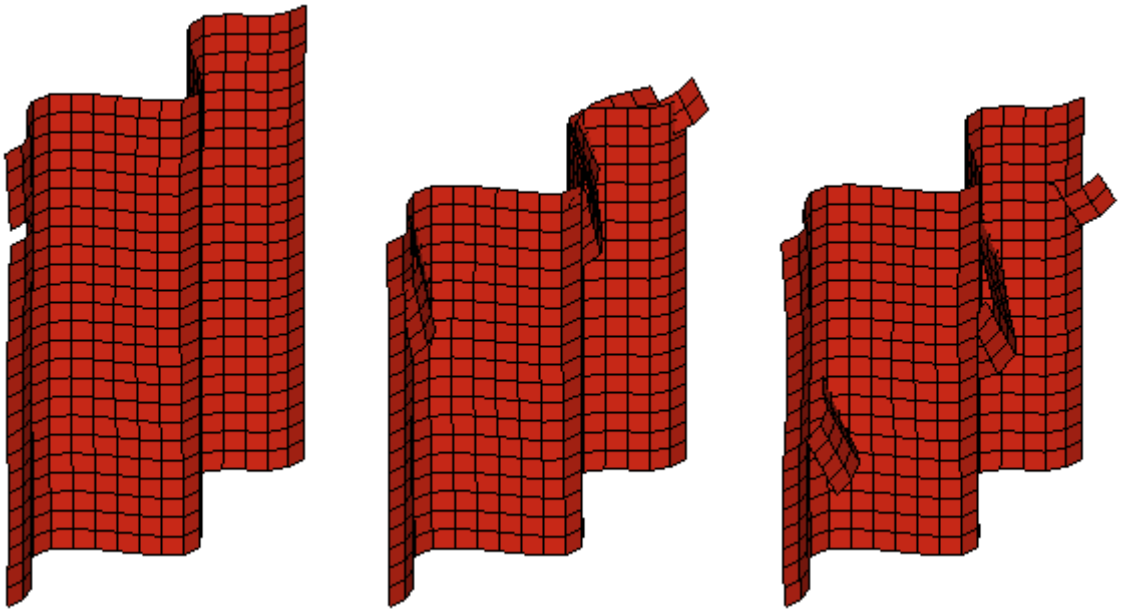

(b)

[d = 0.69 in] [d = 0.70 in] [d = 0.71 in]

Figure 176. No changed parameters from semi-circular sinusoid model baseline: unsatisfactory results of (a) simulated load-displacement crush curve and (b) unstable time-progression for the high sinusoid geometry.

Appendix E: MAT54 source code & modifications

The Fortran source code of MAT54 was provided by Livermore Software Technology Corporation (LSTC). LSTC also provides resources for its licensed users to implement user defined material models [111], however these models follow an incompatible format against the built-in models such as MAT54, so a different approach for compiling the existing code and implementing the modified model in an LS-DYNA executable was necessary. This section will discuss the method in which code compilation was achieved, an interpretation of the MAT54 source code, and the modifications made to the code in order to alter its material modeling capability.

E1. Compilation of the Fortran code

LSTC provides a so-called usermat package for its users to implement user defined interfaces, such as material models (UMATs), contact definitions, friction formulations, etc. Most of the files contained in this package are library files which cannot be read or edited as they are the make-up of the 99.5% of the LS-DYNA source code which is not necessary to implement user defined interfaces. The other files in this package are the dyn21.F, dyn21b.F Fortran files, and a makefile command for compilation. The two Fortran files contain all of the necessary code to define user interfaces, and the makefile file contains the commands which direct the compilation of the two Fortran files into the rest of the code to create an LS-DYNA executable with user defined content. Each usermat package is unique to the LS-DYNA version, operating system, precision (single or double), and processor (multi- or single), and the compiler necessary to create new LS-DYNA executable files must be the exact same compiler as used by LSTC when creating the original executable for that version, operating system, precision, and processor type.

For the usermat package used in this research, the LS-DYNA version 971 R5.1.1 on 64-bit Windows was used, with double precision and a single processor (rendering the file name ls971_d_R5.1.1_winx64_p_lib). For this particular set-up, LSTC prescribes to use the "Intel Visual Fortran Compiler for applications running on Intel 64, Version 10.1.034" and it must be noted that using any version other than this exact one does not work.

With the usermat package users can only modify and implement user defined interfaces as allowed by LSTC in the dyn21.F and dyn21b.F files, and existing models such as MAT54 are not visible and cannot be modified. The MAT54 subroutine made available by LSTC for this research was contained in its own external Fortran file. Initial trials to compile the MAT54 subroutine Fortran file into the usermat package did not work since the original code for MAT54 subroutine contained in the unavailable library files overwrites any external definition thereby overwriting any modifications made in the separate Fortran file. Given this, attempts were made to create a UMAT which replicated MAT54, then modify this UMAT.

It was quickly determined that making MAT54 into a UMAT was not feasible since the fundamental structure of the MAT54 subroutine code varied significantly from that of the UMAT models. For instance, the manner in which common variables are passed in blocks between the material subroutine and the main routine is different in the UMAT, where it appeared that many of the common blocks referenced by the UMAT were organized and named differently than those used by MAT54. MAT54 declares 16 common blocks which contain 166 common Fortran variables necessary for the code, and simply declaring these 16 blocks in the UMAT caused grave errors due to naming mismatches and other unknown problems. These errors could not be explored further without greater access to the LS-DYNA source code. Similarly, the Fortran variables passed directly from the main routine to the material subroutine

during the subroutine call were inconsistent between the UMAT and MAT54. This meant that the UMAT could not be called in the same fashion as MAT54 is, and the appropriate variables necessary for MAT54 could not be passed correctly. Furthermore, the input parameters specified by the user in the keyword file are organized in a particular way in the UMAT which differs from MAT54, and could not be easily remedied. Without having access to the main LS-DYNA source code to decipher these discrepancies made it virtually impossible to define MAT54 as a UMAT.

With the further cooperation of LSTC, the development team provided a slightly modified usermat package which had the original MAT54 subroutine removed from the main code such that an external subroutine would not be overwritten and could be compiled in with the rest of the code. This allowed for the MAT54 source code originally provided by LSTC to be externally modified and compiled into a new LS-DYNA executable which used the modified material model. For the compilation, the makefile file was modified to include commands to compile the MAT54 Fortran file (shl54s.F) by adding similar lines of code that already existed for the dyn21.F and dyn21b.F as shown in the highlighted portions of Figure 177.

```
12  FFLAGS = $(FLAGS) $(SMPD)
13  LFLAGS = -link -force -nodefaultlib:msvcrt.lib
14  OBJS= dyn21.obj dyn21b.obj shl54s.obj
15  LIBS= libdyna.lib libansys.lib shell32.lib libguide.lib user32.lib comctl32.lib comdlg32.
16
17  ls971.exe: $(OBJS)
18      $(FC) -w -q -o ls971.exe $(OBJS) $(LIBS) $(LFLAGS)
19
20  dyn21.obj: dyn21.F
21      $(FC) $(FFLAGS) dyn21.F
22  dyn21b.obj: dyn21b.F
23      $(FC) $(FFLAGS) dyn21b.F
24  shl54s.obj: shl54s.F
25      $(FC) $(FFLAGS) shl54s.F
```

Figure 177. Additional makefile commands to include the modified MAT54 Fortran file in the compilation of the LS-DYNA executable.

Given the unique usermat package from LSTC, the correct compiler for that package, and the changes made to the makefile routine, the MAT54 Fortran source code was a standalone file which could be independently edited to implement the desired modifications of the material model calculations and behaviors. In order to verify that this compilation process was working, the MAT54 subroutine was compiled without any modifications and the baseline semi-circular sinusoid crush simulation was run. The results from this simulation were compared against those obtained using the same keyword input file in the standard LS-DYNA executable, and their crush curves are shown in Figure 178. The very slight differences between the two results are similar to those that have been shown to occur when using different computers, operating systems, versions of LS-DYNA, 32- versus 64-bit, etc.

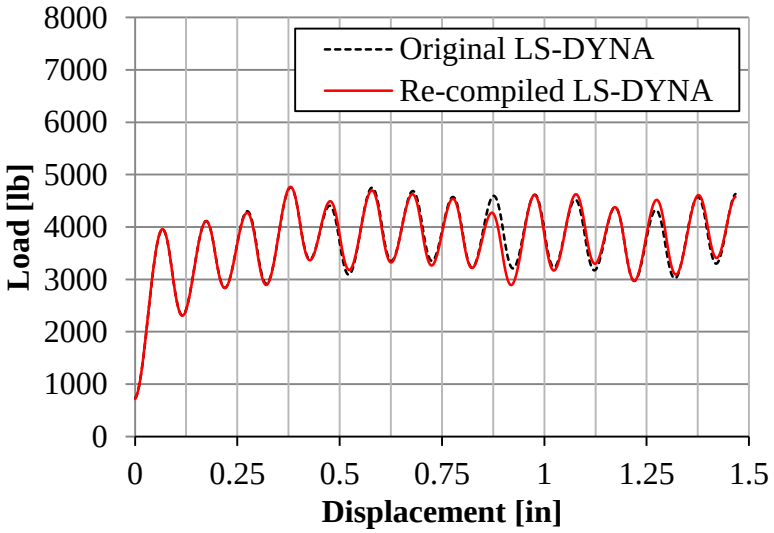

Figure 178. Filtered crush simulation results of the original and recompiled LS-DYNA MAT54 which verifies the compilation process of the new MAT54 subroutine.

E2. Interpretation of the MAT54 source code

The entirety of the MAT54 Fortran source code was provided for the purpose of this research by LSTC. In general, this code is not made available to the public and for this reason irrelevant portions of the code are omitted in this publication. For instance, the code which calls and initializes the common and user defined variables from the main LS-DYNA code is not included since it is not relevant to the actual function of the MAT54 material model, however variables that are relevant will be defined as they appear in the code. The code replicated here represents approximately 75% of the original MAT54 source code, along with a thorough explanation of the code. The line numbering is unique to this publication of the code, and used solely for the purpose of referencing specific portions of the code in this document.

The MAT54 material model is a vectorized model, which means that it performs its operations upon groups of elements rather than one element at a time in order to achieve better efficiency. For a composite material model, operations are performed in each element upon a user specified number of integration points through the thickness which are representative of the composite material plies, and each have their own material orientation angle (also user-specified). Although these are important definitions for the material model, they are defined in the shell element model code and are therefore not present in the MAT54 source code. Instead, by the time stresses and strains are passed to the material model subroutine, the operations are performed across a vector of integration points which has a length of 'nlq'. The length 'nlq' is determined by the number of elements in a vectorized material model computation cycle and the number of integration points per element as specified by the user. A vectorized material model contains variables (such as stresses, strains, etc.) that are vectors with length 'nlq' which hold the variable value at each integration point in the cycle. Every operation of these variables occurs

within ‘do’ loops which cycle through the variable ‘i’ from the variable ‘lft’ to the variable ‘llt’, which are the first and last integration point considered in the cycle.

The MAT54 Fortran code presented here can be summarized into several sections which perform its major operations. These sections are summarized in a flow chart in Figure 179, and the corresponding code attributed to each section is listed in Table 25.

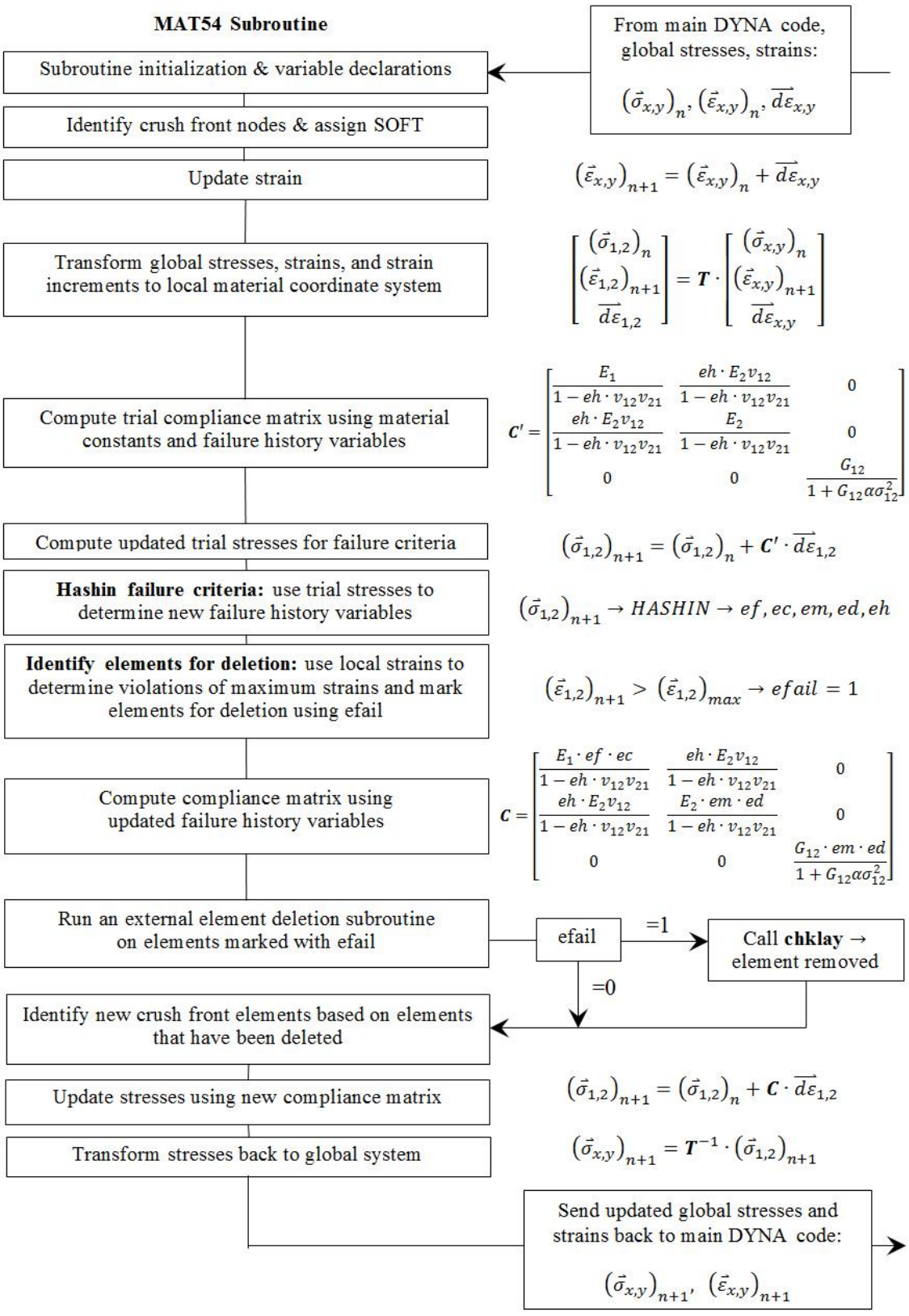

Figure 179. Simplified flow chart of MAT54 source code operations.

Table 25. Contents of major operations performed in MAT54

Lines 001-039	Initialization and variable declaration, basic constant operations
Lines 040-052	Crush front initialization and material softening definition
Lines 053-067	Global to local transformation of stresses
Lines 068-072	Update strain
Lines 073-093	Global to local transformation of strains and strain increments
Lines 094-107	Compliance matrix computation for trial stresses
Lines 108-114	Trial stress computation
Lines 115-142	Failure criteria
Lines 143-170	Elements marked for deletion
Lines 171-203	New compliance matrix computation which takes failure into account
Lines 204-248	Element deletion and new crush front elements flagged
Lines 249-255	Update stresses
Lines 256-271	Transform stresses back to global system

The line-by-line presentation and explanation of the code begins with the subroutine declaration of the MAT54 subroutine, called shl54s. This name needed to remain unchanged as it is referred to within the main LS-DYNA source code.

```
001       subroutine shl54s (cm,capa,nnm1,nshbwp,tfail,lft,llt,
002      . ncrshf,ipt,nip,ipt_thk,eosp)
003c
004c=======================================================================
005c|  Livermore Software Technology Corporation  (LSTC)                  |
006c|  ---------------------------------------------------------  |
007c|  Copyright 1987-2008 Livermore Software Tech. Corp                  |
008c|  All rights reserved                                                |
009c=======================================================================
```

Following the subroutine declaration, the common variables from the main LS-DYNA code are initialized, for example the declaration of the global stresses, sig1, sig2, sig3, sig4, sig5, sig6, and sig7 from common block aux14loc as shown below. As stated previously, most of this section of the source code has been omitted from this publication.

```
010       common/aux14loc/
011      &sig1(nlq),sig2(nlq),sig3(nlq),sig4(nlq),
012      &sig5(nlq),sig6(nlq),sig7(nlq),
```

This is followed by the declaration of the constants defined by the user in the keyword simulation input file, which are passed into the MAT54 subroutine in the vector ‘cm’. The code specifies the location within the ‘cm’ vector using a constant ‘mx’ which accounts for an offset that is necessary as a result of being a vectorized material model. An example follows:

```
013       ymx =cm(mx+1)
014       ymy =cm(mx+2)
015       nuy =cm(mx+4)
016       nux =nuy*ymx/ymy
```

The location of the user defined parameters in the ‘cm’ vector is not the same as their location in the keyword input file, and it is useful to make this distinction in order to understand how and where to add new user input parameters when modifying the code. The MAT54 keyword input deck is replicated in Figure 180 where each parameter is shown in terms of its keyword name (in bold), 'cm' vector location (in terms of mx+n) and the name of the variable as found in the MAT54 source code, which is often different than the keyword name.

*MAT_054 (ENHANCED_COMPOSITE_DAMAGE)

	RO mx+21 *N/A*	**EA** mx+1 ymx	**EB** mx+2 ymy	mx+3	**PRBA** mx+4 nuy	mx+5	mx+6
GAB mx+7 sxy	**GBC** mx+8 syz	**GCA** mx+9 szx					
Local coordinate definitions not used in material model code							
						DFAILM mx+35 dfail1m	**DFAILS** mx+36 dfail1s
TFAIL mx+31 tsize	**ALPH** mx+30 alp	**SOFT** mx+43 soft1	**FBRT** mx+42 fbrt	**YCFAC** mx+46 ycfac	**DFAILT** mx+32 dfail1t	**DFAILC** mx+33 dfail1c	**EFS** mx+34 erodefl
XC mx+44 xc	**XT** mx+27 xt	**YC** mx+29 yc	**YT** mx+28 yt	**SC** mx+26 sc		**BETA** mx+45 beta	
mx+37	mx+38	mx+39	mx+40	mx+47			
eosp+1	eosp+2	eosp+3	eosp+4	eosp+5	eosp+6		

Figure 180. User defined input parameters for MAT54 in terms of their keyword name, ‘cm’ vector location, and source code variable name.

The additional two cards which contain spaces (mx+37-mx+47) and a new user input vector (eosp+1-eosp+6) are optional cards in MAT54 within which contains variables that are not used in this study. Instead, these two cards provided user input vector locations for new user inputs to be defined during modification of the material model.

For many of the user input parameters, their introduction is immediately followed by an operation to address the case of a zero value. For many, the solution is to set the variable to a numerically infinite value (1E+16). For others the variable is given a default value, such as YCFAC = 2. These operations are:

```
017       if (ycfac.le.0.) ycfac=2.
018       if (dfail1m.eq.0.0) dfail1m=1.e+16
019       if (dfail1s.eq.0.0) dfail1s=1.e+16
020       if (erodefl.eq.0.0) erodefl=1.e+16
021       if (sc.eq.0.0) sc=1.e+08
022       if (xc.eq.0.0) xc=1.e+16
023       if (yt.eq.0.0) yt=1.e+16
024       if (yc.eq.0.0) yc=1.e+16
```

Other operations are performed to alter the user input variable values to a form that is more useful to use in later calculations. For instance, 'mlt1' is a constant multiplier used to compute nonlinear shear terms in the failure criteria, and 'mlt2' is a constant multiplier used in the compressive matrix failure criterion. These operations and their resulting new variables are:

```
025       xt2 =1./(xt*xt)
026       if(fbrt.gt.0.) then
027         xt2fbrt=xt2/(fbrt*fbrt)
028       else
029         xt2fbrt=xt2
030       endif
```

$$\text{xt2fbrt} = \begin{cases} \left(\frac{1}{XT}\right)^2 & if\ FBRT = 0 \\ \left(\frac{1}{XT*FBRT}\right)^2 & else \end{cases} \qquad \text{Eq. (35)}$$

```
031       yt2 =1./(yt*yt)
```

$$\text{yt2} = \left(\frac{1}{YT}\right)^2 \qquad \text{Eq. (36)}$$

```
032       sc2 =sc*sc
033       sd2 =.25/sc2
```

$$\text{sd2} = \left(\frac{1}{2SC}\right)^2 \qquad \text{Eq. (37)}$$

```
034       ap3 =3.0*alp
035       ap34=.75*alp
036       od2g=.5/sxy
037       mlt1=1./(sc2*(od2g+ap34*sc2))
038       mlt2=(yc*yc*sd2-1.)/yc
```

$$\text{mlt1} = \frac{1}{SC^2\left(\frac{1}{2G_{12}}+\frac{3}{4}\alpha SC^2\right)} \qquad \text{Eq. (38)}$$

$$\text{mlt2} = \left(\left(\frac{YC}{2SC}\right)^2 - 1\right)\frac{1}{YC} \qquad \text{Eq. (39)}$$

The variable icrash_loc is a logical parameter which is true when the user defines an active SOFT value less than 1. This parameter enables crash-front elements to be determined.

```
039       icrash_loc = soft1.lt.0.9999
```

Next, the crash-front nodes are identified and material softening using the SOFT parameter is prepared within the do loop numbered 5 (lines 041-047). This is preceded by an if statement which checks the value of the logical icrash_loc to determine if material softening due to the crash front is in use. Note that the crash-front elements are determined at the end of the subroutine after failure is determined, therefore no crash-front nodes are identified in the first several cycles until after initial failure occurs. Crash-front nodes are identified by flagging the variable 'ncrshf' to a value of 1. At each integration point in an element, there are four 'ncrshf' values, one for each node denoted (ix1) through (ix4). The initial value of the crash-front flag at each node is zero and none of the following softening code is executed until after one of the nodes is flagged, as indicated by the second if statement:

```
040       if(icrash_loc) then
041       do 5 i=lft,llt
042       if (max(ncrshf(ix1(i)),ncrshf(ix2(i)),
043      .         ncrshf(ix3(i)),ncrshf(ix4(i))).eq.1) then
```

If any of the nodes in the element is flagged, then two values are initialized in the crush front element, 'dam' and 'soft'. A second do loop, numbered 7 (lines 049-052) calculates the multipliers 'qq1' and 'qq2' which are directly used in the failure criteria to perform material softening. The qq1 variable acts as a flag within the Fortran code for crush-front elements.

```
044           dam(i)=1.e-08
045           soft=soft1
046           endif
047        5  continue
048         endif
049         do 7 i=lft,llt
050           qq1(i)=1.0-(1.0-soft)*(0.5+sign(0.5,dam(i)))
051           qq2(i)=1./(qq1(i)*qq1(i))
052        7 continue
```

$$qq1 = \begin{cases} SOFT, & crush\ front\ element \\ 1.0, & all\ other\ elements \end{cases} \quad \text{Eq. (40)}$$

$$qq2 = \begin{cases} \left(\frac{1}{SOFT^2}\right), & crush\ front\ element \\ 1.0, & all\ other\ elements \end{cases} \quad \text{Eq. (41)}$$

Next, the stresses are transformed from the global system to the material system in the do loop numbered 20 (lines 053-067). Before the stresses are transformed, the strain energy at the integration point, einc(i), is calculated by summing the product of the global stresses components sig1(i)-sig6(i) and the global strain components e1(i)-e6(i). The component numbering follows the common scheme adopted for composite materials,

$$\begin{bmatrix} \sigma_{11} \\ \sigma_{22} \\ \sigma_{33} \\ \sigma_{12} \\ \sigma_{23} \\ \sigma_{13} \end{bmatrix} = \begin{bmatrix} \sigma_1 \\ \sigma_2 \\ \sigma_3 \\ \sigma_4 \\ \sigma_5 \\ \sigma_6 \end{bmatrix} = \begin{bmatrix} sig1 \\ sig2 \\ sig3 \\ sig4 \\ sig5 \\ sig6 \end{bmatrix} \quad \text{Eq. (42)}$$

```
053         do 20 i=lft,llt
054         einc(i)=e1(i)*sig1(i)+e2(i)*sig2(i)+e4(i)*sig4(i)+
055        1         e5(i)*sig5(i)+e6(i)*sig6(i)
```

The transformation occurs in two steps, first defining an intermediary matrix ‘a’ in terms of the sine (q2(i)) and cosine (q1(i)) of the material multiplied against the stresses. The ‘a’ matrix is defined as follows,

$$\begin{bmatrix} a_{11} \\ a_{12} \\ a_{21} \\ a_{22} \end{bmatrix} = \begin{bmatrix} cos\theta & 0 & -sin\theta \\ sin\theta & 0 & cos\theta \\ 0 & -sin\theta & cos\theta \\ 0 & cos\theta & sin\theta \end{bmatrix} \begin{bmatrix} sig1 \\ sig2 \\ sig4 \end{bmatrix} \quad \text{Eq. (43)}$$

```
056       stg5(i)=sig5(i)
057       stg6(i)=sig6(i)
058       a11(i) =q1(i)*sig1(i)-q2(i)*sig4(i)
059       a12(i) =q2(i)*sig1(i)+q1(i)*sig4(i)
060       a21(i) =q1(i)*sig4(i)-q2(i)*sig2(i)
061       a22(i) =q2(i)*sig4(i)+q1(i)*sig2(i)
```

The ‘a’ matrix is then multiplied against more sine and cosine terms to achieve the desired transformation. For the stress variables, the transformed local stress vector takes the place of the original global stress vector sig1(i)-sig6(i):

$$\begin{bmatrix} sig1 \\ sig2 \\ sig4 \\ sig5 \\ sig6 \end{bmatrix} = \begin{bmatrix} cos^2\theta & sin^2\theta & -2cos\theta sin\theta & 0 & 0 \\ sin^2\theta & cos^2\theta & 2cos\theta sin\theta & 0 & 0 \\ cos\theta sin\theta & -cos\theta sin\theta & cos^2\theta - sin^2\theta & 0 & 0 \\ 0 & 0 & 0 & cos\theta & sin\theta \\ 0 & 0 & 0 & -sin\theta & cos\theta \end{bmatrix} \begin{bmatrix} sig1 \\ sig2 \\ sig4 \\ sig5 \\ sig6 \end{bmatrix} \quad \text{Eq. (44)}$$

```
062       sig1(i)=q1(i)*a11(i)-q2(i)*a21(i)
063       sig2(i)=q2(i)*a12(i)+q1(i)*a22(i)
064       sig4(i)=q1(i)*a12(i)-q2(i)*a22(i)
065       sig5(i)=q2(i)*stg6(i)+q1(i)*stg5(i)
066       sig6(i)=q1(i)*stg6(i)-q2(i)*stg5(i)
067    20 continue
```

Next, the global strains are updated, the strain and strain increments are transformed from the global system to the material system, and the effective plastic strain is computed in the do loop numbered 30 (lines 068-093). First the strains are updated by summing the strain plus the new strain increment. Note that the shear strain increment (e4(i)) is multiplied by 0.5 in order to resolve the difference between engineering and tensor strains:

```
068       do 30 i=lft,llt
069       d4(i)  =.5*e4(i)
070       eps1(i)=eps1(i)+e1(i)
071       eps2(i)=eps2(i)+e2(i)
072       eps4(i)=eps4(i)+d4(i)
```

Then the strain increment transformation occurs in two steps in the same fashion as the stress transformation. First the intermediary matrix 'a' is redefined for the strain increment transformation:

$$\begin{bmatrix} a_{11} \\ a_{12} \\ a_{21} \\ a_{22} \end{bmatrix} = \begin{bmatrix} cos\theta & 0 & -sin\theta \\ sin\theta & 0 & cos\theta \\ 0 & -sin\theta & cos\theta \\ 0 & cos\theta & sin\theta \end{bmatrix} \begin{bmatrix} e1 \\ e2 \\ d4 \end{bmatrix} \qquad \text{Eq. (45)}$$

```
073       a11(i) =q1(i)*e1(i)-q2(i)*d4(i)
074       a12(i) =q2(i)*e1(i)+q1(i)*d4(i)
075       a21(i) =q1(i)*d4(i)-q2(i)*e2(i)
076       a22(i) =q2(i)*d4(i)+q1(i)*e2(i)
```

The 'a' matrix is then multiplied against more sine and cosine terms to achieve the desired transformation. The transformed local strain vector d1(i)-d6(i) is given a separate vector from the original global strain increment vector e1(i)-e6(i):

$$\begin{bmatrix} d1 \\ d2 \\ d4 \\ d5 \\ d6 \end{bmatrix} = \begin{bmatrix} cos^2\theta & sin^2\theta & -2cos\theta sin\theta & 0 & 0 \\ sin^2\theta & cos^2\theta & 2cos\theta sin\theta & 0 & 0 \\ 2cos\theta sin\theta & -2cos\theta sin\theta & 2(cos^2\theta - sin^2\theta) & 0 & 0 \\ 0 & 0 & 0 & cos\theta & sin\theta \\ 0 & 0 & 0 & -sin\theta & cos\theta \end{bmatrix} \begin{bmatrix} e1 \\ e2 \\ d4 \\ e5 \\ e6 \end{bmatrix} \qquad \text{Eq. (46)}$$

```
077       d1(i)  =q1(i)*a11(i)-q2(i)*a21(i)
078       d2(i)  =q2(i)*a12(i)+q1(i)*a22(i)
079       d4(i)  =2.*(q1(i)*a12(i)-q2(i)*a22(i))
080       d5(i)  =q2(i)*e6(i)+q1(i)*e5(i)
081       d6(i)  =q1(i)*e6(i)-q2(i)*e5(i)
```

This is followed by the total strain transformation and the intermediary matrix 'a' is redefined for the total strain transformation:

$$\begin{bmatrix} a_{11} \\ a_{12} \\ a_{21} \\ a_{22} \end{bmatrix} = \begin{bmatrix} cos\theta & 0 & -sin\theta \\ sin\theta & 0 & cos\theta \\ 0 & -sin\theta & cos\theta \\ 0 & cos\theta & sin\theta \end{bmatrix} \begin{bmatrix} \text{eps1} \\ \text{eps2} \\ \text{eps4} \end{bmatrix} \quad \text{Eq. (47)}$$

```
082       a11(i)   =q1(i)*eps1(i)-q2(i)*eps4(i)
083       a21(i)   =q1(i)*eps4(i)-q2(i)*eps2(i)
084       a12(i)   =q2(i)*eps1(i)+q1(i)*eps4(i)
085       a22(i)   =q2(i)*eps4(i)+q1(i)*eps2(i)
```

The ‘a’ matrix is then multiplied against more sine and cosine terms to achieve the desired transformation. The transformed total strain vector strn1(i)-strn4(i) is given a separate vector from the original global total strain vector eps1(i)-eps4(i):

$$\begin{bmatrix} \text{strn1} \\ \text{strn2} \\ \text{strn4} \end{bmatrix} = \begin{bmatrix} cos^2\theta & sin^2\theta & -2cos\theta sin\theta \\ sin^2\theta & cos^2\theta & 2cos\theta sin\theta \\ cos\theta sin\theta & -cos\theta sin\theta & cos^2\theta - sin^2\theta \end{bmatrix} \begin{bmatrix} \text{eps1} \\ \text{eps2} \\ \text{eps4} \end{bmatrix} \quad \text{Eq. (48)}$$

```
086       strn1(i)=q1(i)*a11(i) -q2(i)*a21(i)
087       strn2(i)=q2(i)*a12(i)+q1(i)*a22(i)
088       strn4(i)=q1(i)*a12(i)-q2(i)*a22(i)
```

Finally, the effective plastic strain is calculated using the global strains, as given by:

$$effstn = \sqrt{(eps1 + eps2)^2 + \frac{1}{3}(eps1 - eps2)^2 + \frac{3}{4}eps4^2} \quad \text{Eq. (49)}$$

```
089       sa=0.5*(eps1(i)+eps2(i))
090       sb=0.5*(eps1(i)-eps2(i))
091       scc=     sb**2+eps4(i)**2
092       effstn(i)=1.1547*sqrt(3.0*sa**2+scc)
093    30 continue
```

Next, the compliance matrix is calculated such that the trial stresses for failure determination can be calculated. The compliance matrix is determined in the do loop numbered 40 (lines 094-107) and uses several of the user defined constitutive parameters. The variables em(i), ef(i), and ed(i) are failure flags which assume a value of 0 if the ply has failed in matrix tension, fiber tension, r

matrix compression modes, respectively. These get grouped into the failure flag eh(i) which is then multiplied into the compliance matrix to reduce the constitutive properties (and thereby stiffness) of failed elements to zero. The shear modulus, gxy(i) is assured a nonzero value by adding a infinitesimally small non-zero value 1E-17.

```
094       do 40 i=lft,llt
095       eg(i) =em(i)*ef(i)
096       eh(i) =eg(i)*ed(i)
097       ex(i) =ymx
098       ey(i) =ymy
099       prx(i)=eh(i)*nux
100       pry(i)=eh(i)*nuy
101       gxy(i)=1.e-17+sxy
102       pxy(i)=1.0/(1.-prx(i)*pry(i))
```

Following the initialization of all of the necessary parameters, the compliance matrix is calculated as follows:

$$\boldsymbol{C} = \begin{bmatrix} \frac{E_1}{1-eh\cdot v_{12}v_{21}} & \frac{eh\cdot E_2 v_{12}}{1-eh\cdot v_{12}v_{21}} & 0 \\ \frac{eh\cdot E_2 v_{12}}{1-eh\cdot v_{12}v_{21}} & \frac{E_2}{1-eh\cdot v_{12}v_{21}} & 0 \\ 0 & 0 & \frac{G_{12}}{1+G_{12}\alpha\sigma_{12}^2} \end{bmatrix} \qquad \text{Eq. (50)}$$

```
103       c11(i)=pxy(i)*ex(i)
104       c12(i)=pxy(i)*prx(i)*ey(i)
105       c22(i)=pxy(i)*ey(i)
106       c44(i)=gxy(i)/(1.+gxy(i)*ap3*sig4(i)*sig4(i))
107    40 continue
```

Next, the trial stresses are calculated in an unnumbered do loop (lines 108-114) such that failure determination can be made. The trial stresses are calculated by taking the sum of the stress from the previous cycle (sig1(i)-sig4(i)) and the product of the strain increment (d1(i)-d4(i)) with the compliance matrix (c11(i)-c44(i)) as follows,

$$\vec{\sigma}_n = \vec{\sigma}_{n-1} + \boldsymbol{C}\overrightarrow{d\varepsilon} \qquad \text{Eq. (51)}$$

```
108       do i=lft,llt
109       stg1(i)=sig1(i)+c11(i)*d1(i)+c12(i)*d2(i)
110       stg2(i)=sig2(i)+c12(i)*d1(i)+c22(i)*d2(i)
111       stg4(i)=sig4(i)+c44(i)*d4(i)
```

Further operations are performed on the shear stress which are of use during the failure criteria calculations. After these operations, the non-linear fiber-matrix shearing term which augments each damage mode is calculated, as defined in the LS-DYNA Theory Manual (see Material Model 22). This term, sg44(i) is simply a non-linear shear stress term divided by its equivalent nonlinear shear strength term:

$$\text{sg44} = \frac{\frac{{\tau_{12}}^2}{2G_{12}} + \frac{3}{4}\alpha {\tau_{12}}^4}{\frac{SC^2}{2G_{12}} + \frac{3}{4}\alpha SC^4} \qquad \text{Eq. (52)}$$

```
112       sg42(i)=stg4(i)*stg4(i)
113       sg44(i)=mlt1*sg42(i)*(od2g+ap34*sg42(i))*qq2(i)
114       enddo
```

Next, the four failure criteria are calculated and failure flags are defined in the do loop numbered 50 (lines 115-142). Failure modes are determined by considering the sign of the 1- and 2-direction local stresses, stg1(i) and stg2(i) respectively. For each mode, the criterion is calculated and saved to a variable which is then checked to see if its value exceeds 0, which is an indication of failure. Most of the terms used in the failure criteria calculations have already been calculated earlier in the code.

First, the tensile fiber mode uses the variable ef2(i) and calculates the criterion when the 1-direction stress is greater than zero (tension). For this case ec2(i), the compressive fiber variable, is assigned a value of -1 since the element cannot fail in this mode while undergoing tensile stresses. Some earlier calculations are useful to recall when interpreting the fiber failure criteria:

- $qq2 = \begin{cases} \left(\frac{1}{SOFT^2}\right), & crush\ front\ element \\ 1.0, & all\ other\ elements \end{cases}$
- $xt2fbrt = \frac{1}{XT^2 \cdot FBRT^2}$
- $xt2 = \frac{1}{XT^2}$
- $ed = \begin{cases} 1.0, & no\ matrix\ failure \\ 0, & matrix\ failure \end{cases}$
- $xc2 = \frac{1}{XC^2}$ where $XC = \begin{cases} XC, & no\ matrix\ failure \\ YC * YCFAC, & matrix\ failure \end{cases}$

```
115       do 50 i=lft,llt
116       if (stg1(i).gt.0.) then
117         ef2(i)=qq2(i)*(xt2fbrt+(xt2-xt2fbrt)*ed(i))*
118      .            max(0.0,stg1(i))**2+beta*sg44(i)-1.0
119         ec2(i)=-1.
```

Thus, the fiber tension failure criterion becomes,

$$ef2 = \left[\begin{matrix}\left(\frac{1}{SOFT^2}\right) \\ or \\ 1.0\end{matrix}\right] * \left[\begin{matrix}\left(\frac{1}{FBRT^2}\right) \\ or \\ 1.0\end{matrix}\right] * \left(\frac{\sigma_{11}}{XT}\right)^2 + \beta * \left(\frac{\frac{\tau_{12}^2}{2G_{12}} + \frac{3}{4}\alpha\tau_{12}^4}{\frac{SC^2}{2G_{12}} + \frac{3}{4}\alpha SC^4}\right) * \left[\begin{matrix}\left(\frac{1}{SOFT^2}\right) \\ or \\ 1.0\end{matrix}\right] - 1 \qquad \text{Eq. (53)}$$

The compressive fiber mode is calculated if the circumstance of the previous if statement for a positive 1-direction stress is false, as indicated by the else statement. This mode uses the variable ec2(i) and the tensile fiber variable ef2(i) is assigned a value of -1. The compressive fiber failure criterion becomes,

$$ec2 = \left[\begin{matrix}\left(\frac{1}{SOFT^2}\right) \\ or \\ 1.0\end{matrix}\right] * \left[\begin{matrix}\left(\frac{1}{XC^2}\right) \\ or \\ \left(\frac{1}{YC * YCFAC^2}\right)\end{matrix}\right] * \sigma_{11}^2 - 1 \qquad \text{Eq. (54)}$$

```
120       else
121         ef2(i)=-1.
122         xc2(i) = ed(i)*xc + (1.0-ed(i))*ycfac*yc
123         xc2(i)  = 1/(xc2(i)*xc2(i))
124         ec2(i)= qq2(i)*xc2(i)*  min(0.0,stg1(i))**2-1.0
125       endif
```

Next, the tensile matrix mode is calculated using the variable em2(i) for the case that the 2-direction stress is greater than zero. For this case ed2(i), the compressive matrix variable, is assigned a value of -1 since the element cannot fail in this mode while undergoing tensile stresses. Some earlier calculations are useful to recall when interpreting the matrix failure criteria:

- $\text{yt2} = \frac{1}{YT^2}$
- $\text{sd2} = \frac{1}{4SC^2}$
- $\text{mlt2} = \frac{1}{YC}\left(\frac{YC^2}{4SC^2} - 1\right)$
- $\text{qq1} = \begin{cases} SOFT, & crashfront\ element \\ 1.0, & all\ other\ elements \end{cases}$

```
126       if (stg2(i).gt.0.) then
127         em2(i)=qq2(i)*yt2*  max(0.0,stg2(i))**2+sg44(i)-1.0
128         ed2(i)=-1.
```

Thus, the matrix tension failure criterion becomes,

$$\text{em2} = \left[\begin{matrix}\left(\frac{1}{SOFT^2}\right) \\ or \\ 1.0\end{matrix}\right] * \left(\frac{\sigma_{11}}{YT}\right)^2 + \left(\frac{\frac{\tau_{12}^2}{2G_{12}} + \frac{3}{4}\alpha\tau_{12}^4}{\frac{SC^2}{2G_{12}} + \frac{3}{4}\alpha SC^4}\right) * \left[\begin{matrix}\left(\frac{1}{SOFT^2}\right) \\ or \\ 1.0\end{matrix}\right] - 1 \qquad \text{Eq. (55)}$$

The compressive matrix mode is calculated if the circumstance of the previous if statement for a positive 2-direction stress is false, as indicated by the else statement. This mode uses the variable ed2(i) and the tensile matrix variable em2(i) is assigned a value of -1. The compressive matrix failure criterion becomes,

$$\text{ed2} = \left[\begin{matrix}\left(\frac{1}{SOFT^2}\right) \\ or \\ 1.0\end{matrix}\right] * \frac{\sigma_{22}^2}{4SC^2} + \left[\begin{matrix}SOFT \\ or \\ 1.0\end{matrix}\right] * \frac{\sigma_{22}}{YC}\left(\frac{YC^2}{4SC^2} - 1\right) + \left(\frac{\frac{\tau_{12}^2}{2G_{12}} + \frac{3}{4}\alpha\tau_{12}^4}{\frac{SC^2}{2G_{12}} + \frac{3}{4}\alpha SC^4}\right) * \left[\begin{matrix}\left(\frac{1}{SOFT^2}\right) \\ or \\ 1.0\end{matrix}\right] - 1 \qquad \text{Eq. (56)}$$

```
129       else
130         em2(i)=-1.
131         ed2(i)=qq2(i)*sd2*  min(0.0,stg2(i))**2+
132      1          mlt2*stg2(i)/qq1(i)+sg44(i)-1.0
133       endif
```

Flags for each failure mode are assigned, followed by history variable assignment. The history variables, ef(i), ec(i), em(i), and ed(i) are used during the calculation of the compliance matrix in order to reduce constitutive properties to zero following failure. The Fortran **sign** command used to determine the history variable values takes the magnitude of the first argument, and the sign of the second argument to produce a number. In this way, when failure is present and the ef2(i), ec2(i), em2(i), or ed2(i) value is greater than zero, the history variables take on a value of 0. Otherwise when there is no failure, the history variables take on a value of 1.

```
134       if(ed2(i).gt.0.) iflagd=1
135       if(em2(i).gt.0.) iflagm=1
136       if(ef2(i).gt.0.) iflagf=1
137       if(ec2(i).gt.0.) iflagc=1
138       ef(i)  =ef(i)*(.5-sign(.5,ef2(i)))
139       ec(i)  =ec(i)*(.5-sign(.5,ec2(i)))
140       em(i)  =em(i)*(.5-sign(.5,em2(i)))
141       ed(i)  =ed(i)*(.5-sign(.5,ed2(i)))
142    50 continue
```

Plies are marked for deletion using the efail(i) variable which is given a value of 0 to indicate deletion. This occurs due to maximum strain violations in the do loop numbered 55 (lines 144-169). First, the code addresses the case where maximum strain parameters are not defined by setting DFAILM and DFAILS to numerically infinite values (earlier in the code), initializing the parameter efmin to a zero or near-zero value, and beginning the do loop with an if statement checking if DFAILT is nonzero and initializing efail(i) to a value of 1:

```
143       efmin=(.5+sign(.5,fbrt-1.e-15))*1.0e-05
144       do 55 i=lft,llt
145        if(dfail1t.gt.0.0) then
146         efail(i)=1.0
```

For the case where maximum strain parameters are defined, the local strain components strn(i), strn2(i) and strn4(i) are compared against the corresponding maximum strain parameter values and, if violated, efail(i) is set to zero indicating ply deletion:

```
147         if (dfail1t-strn1(i).lt.0.) then
148             efail(i)=0.0
149         endif
150         if (strn1(i)-dfail1c.lt.0.) then
151             efail(i)=0.0
152         endif
153         if (dfail1m-strn2(i).lt.0.) then
154             efail(i)=0.0
155         endif
156         if (strn2(i)+dfail1m.lt.0.) then
157             efail(i)=0.0
158         endif
159         if (dfail1s-abs(strn4(i)).lt.0.) then
160             efail(i)=0.0
161         endif
```

For the case where maximum strain parameters are not defined, efail(i) is degraded following fiber tensile failure, at which point the history variable ef(i) changes from a value of 1 to 0. In each time-step following fiber tensile failure, 0.01 is subtracted from efail(i), and after 100 time-steps efail(i) is 0 which marks the ply for deletion. To avoid a negative value of efail(i), the efmin constant acts as a limiting maximum:

```
162        else
163         efail(i)=efail(i)-.01*(1.-ef(i))
164         efail(i)=  max(efmin,efail(i))
165        endif
```

Ply deletion can also occur from violating the effective failure strain parameter, erodefl (EFS in the MAT54 user input deck):

```
166         if (effstn(i).gt.erodefl) then
167         efail(i)=0.0
168         endif
```

The variable fail(i) is a secondary parameter which keeps track of deletion, and is determined from the value of efail(i). The initialized value of fail(i) is zero, so given that efail(i) is not given a zero value, fail(i) will take a value of 1.

```
169         fail(i) =  max(fail(i),(.5+sign(.5,efail(i)-.01)))
170      55 continue
```

The compliance matrix is calculated again taking any new failures into account. First, constitutive properties are redefined by using the newly defined history variables in an unnumbered do loop (lines 171-181):

```
171       do i=lft,llt
172       eg(i) =em(i)*ef(i)
173       eh(i) =eg(i)*ed(i)
174       ex(i) =ymx
175       ey(i) =ymy
176       prx(i)=eh(i)*nux
177       pry(i)=eh(i)*nuy
178       gxy(i)=sxy
179       pxy(i)=1.0/(1.-prx(i)*pry(i))
180       c12(i)=eh(i)*pxy(i)*prx(i)*ey(i)
181       enddo
```

The compliance matrix is then calculated within the do loop numbered 60 (lines 182-203) while taking into consideration the sign of the products of local stresses (stg1(i), stg2(i) and stg4(i)) and strain increments (d1(i), d2(i), and d4(i)). The resulting compliance matrix is:

$$\boldsymbol{C} = \begin{bmatrix} \frac{E_1 \cdot ef \cdot ec}{1-eh \cdot v_{12} v_{21}} & \frac{eh \cdot E_2 v_{12}}{1-eh \cdot v_{12} v_{21}} & 0 \\ \frac{eh \cdot E_2 v_{12}}{1-eh \cdot v_{12} v_{21}} & \frac{E_2 \cdot em \cdot ed}{1-eh \cdot v_{12} v_{21}} & 0 \\ 0 & 0 & \frac{G_{12} \cdot em \cdot ed}{1+G_{12} \alpha \sigma_{12}^2} \end{bmatrix} \quad \text{Eq. (57)}$$

```
      do 60 i=lft,llt
      if( stg1(i)*d1(i).gt.0.) then
        c11(i)=(.5-sign(.5,ec2(i)))*
     1         (.5-sign(.5,ef2(i)))*pxy(i)*ex(i)
      else
        c11(i)=pxy(i)*ex(i)
      endif
      if( stg2(i)*d2(i).gt.0.) then
        c22(i)=(.5-sign(.5,em2(i)))*
     1         (.5-sign(.5,ed2(i)))*
     2         (.5+sign(.5,efail(i)))*pxy(i)*ey(i)
      else
        c22(i)=pxy(i)*ey(i)
      endif
      if( stg4(i)*d4(i).gt.0.) then
        c44(i)=(.5-sign(.5,em2(i)))*
     1         (.5-sign(.5,ed2(i)))/
     2         (1.0/gxy(i)+0.0*sig4(i)*sig4(i))
      else
        c44(i)=1.0/(1.0/gxy(i)+0.0*sig4(i)*sig4(i))
      endif
   60 continue
```

If a minimum time-step limit ('tsize', called TFAIL in the keyword input file) is defined by the user, elements whose time-steps violate this limit are marked for deletion in the do loops numbered 70-72 (lines 205-214). First, the time-step of the element, dt(i) is determined based on the material density, mesh size, and speed of sound parameters calculated in the main LS-DYNA code.

```
      if(tsize.ne.0.0) then
        do 70 i=lft,llt
          dt(i)=sarea(i)/(sqrt(diagm(i))*cx)
   70   continue
```

The value of dtfail(i), which will be used to determine time-step violation, is determined based on the user input TFAIL (tsize). The TFAIL input parameter can be used in two different ways depending on its magnitude, as specified in the LS-DYNA User's Manual [91],

$$TFAIL = \begin{cases} \leq 0 & \textit{No element deletion by TFAIL} \\ 0 < TFAIL \leq 0.1 & \textit{Element is deleted when its time} - \textit{step is smaller than the given value} \\ > 0.1 & \textit{Element is deleted when the quotient of the time} - \\ & \textit{step and the original timstep drops below the given value} \end{cases}$$

Given this definition of TFAIL, an if statement divides the definition of dtfail(i) according to if tsize is greater than 0.1:

```
208         if(ncycle.eq.0) then
209          if(tsize.gt.0.1) then
210           do 71 i=lft,llt
211     71      dtfail(i)=dt(i)*tsize
212          else
213           do 72 i=lft,llt
214     72      dtfail(i)=tsize
215          endif
216         endif
```

Elements are marked for deletion if their time-step is less than dtfail(i) by setting efail(i) to 0, along will all of the stresses. Note that the fail(i) parameter is an additional failure parameter which was given a value according to the value of efail(i) following the strain-based ply deletions.

```
217         do 75 i=lft,llt
218           if( dt(i).lt.dtfail(i) .or. fail(i).lt.0.1 )  then
219             sig1(i)=0.0
220             sig2(i)=0.0
221             sig3(i)=0.0
222             sig4(i)=0.0
223             sig5(i)=0.0
224             sig6(i)=0.0
225             efail(i)=0.0
226           endif
```

Elements deletion occurs using a separate subroutine, ‘chklay’. The parameter ‘nplane’ is the number of integration points in the plane of the element (nodes), and the following if statement makes sure that the element is a fully integrated shell element with four nodes. If efail(i) of the element is less than zero, the ‘chklay’ subroutine is run and deletes the element.

```
227             if (nplane.eq.4) then
228               if (efail(i).lt.0.01) then
229               call chklay(faillay(i,id_plane),ipt_thk,isnyf)
230               endif
231           endif
232    75   continue
```

After deletion is established, the new crush front elements are identified. This operation is only done once per element, so first an if statement is put in place to check if the integration point number, ‘ipt’ is equal to the number of integration points, ‘nip’, which occurs only 4 times per element since there are 4 integration points in the plane (nodes). Then, the counter ‘jf’ and the increment ‘jinc’ are used to only apply the do loop numbered 74 (lines 235-249) one time per element as it cycles through all of the integration points . The do loop first checks for element deletion:

```
233         if (ipt.eq.nip) then
234           jinc  =4
235           do 74 i=lft,llt
236             if((dt(i).lt.dtfail(i) .or.  fail(i).lt.0.1)) then
```

Recall that the ‘ncrshf’ parameter identifies a node as being at the crush front by assuming a value of 1. If the deleted element was not at the crush front (i.e. the sum of all of its node ‘ncrshf’ values is not 4), the ‘jf’ counter adds 4 to move to the next element.

```
237               if (ncrshf(ix1(i)+numnp)+ncrshf(ix2(i)+numnp)+
238      .              ncrshf(ix3(i)+numnp)+ncrshf(ix4(i)+numnp).ne.4)then
239                 jf =jf+jinc
240               endif
```

Otherwise, if the deleted element was at the crush front then the new crush front elements are established by moving onto the next element.

```
241               ncrshf(ix1(i)+numnp)=1
242               ncrshf(ix2(i)+numnp)=1
243               ncrshf(ix3(i)+numnp)=1
244               ncrshf(ix4(i)+numnp)=1
245             endif
246  74       continue
247         endif
248       endif
```

The last task in the material model is to update the stresses and transform them back to the element system. The strains are not transformed back since the transformed strain and strain increment values occupied their own vectors and did not overwrite the global coordinate system strain and strain increments. These operations are performed in the do loop numbered 80 (lines 249-269). First, the local stresses are updated by summing the old stresses (sig1(i)-sig6(i)) with the new stress increment, as calculated using the strain increments (d1(i)-d4(i)) and compliance matrix (c11(i)-c44(i)), as follows:

$$\begin{bmatrix}\sigma_1\\ \sigma_2\\ \sigma_3\\ \sigma_4\\ \sigma_5\\ \sigma_6\end{bmatrix}_n = \begin{bmatrix}\sigma_1\\ \sigma_2\\ 0\\ \sigma_4\\ \sigma_5\\ \sigma_6\end{bmatrix}_{n-1} + \begin{bmatrix}c_{11} & c_{12} & 0 & 0 & 0\\ c_{12} & c_{22} & 0 & 0 & 0\\ 0 & 0 & 0 & 0 & 0\\ 0 & 0 & 0 & c_{44} & 0\\ 0 & 0 & 0 & 0 & 0\\ 0 & 0 & 0 & 0 & 0\end{bmatrix}\begin{bmatrix}d_1\\ d_2\\ 0\\ d_4\\ 0\\ 0\end{bmatrix}$$

$$\vec{\sigma}_n = \vec{\sigma}_{n-1} + \boldsymbol{C}\Delta\vec{\varepsilon} \qquad \text{Eq. (58)}$$

```
249       do 80 i=lft,llt
250       sig1(i)=sig1(i)+c11(i)*d1(i)+c12(i)*d2(i)
251       sig2(i)=sig2(i)+c12(i)*d1(i)+c22(i)*d2(i)
252       sig3(i)=0.0
253       sig4(i)=sig4(i)+c44(i)*d4(i)
254       stg5(i)=sig5(i)
255       stg6(i)=sig6(i)
```

The stress transformation back to the global system occurs in two steps in the same fashion as the first transformations occurred. First the intermediary matrix 'a' is redefined:

$$\begin{bmatrix} a_{11} \\ a_{12} \\ a_{21} \\ a_{22} \end{bmatrix} = \begin{bmatrix} cos\theta & 0 & sin\theta \\ -sin\theta & 0 & cos\theta \\ 0 & sin\theta & cos\theta \\ 0 & cos\theta & -sin\theta \end{bmatrix} \begin{bmatrix} \text{sig1} \\ \text{sig2} \\ \text{sig4} \end{bmatrix} \qquad \text{Eq. (59)}$$

```
256       a11(i) = sig1(i)*q1(i)+sig4(i)*q2(i)
257       a12(i) =-sig1(i)*q2(i)+sig4(i)*q1(i)
258       a21(i) = sig4(i)*q1(i)+sig2(i)*q2(i)
259       a22(i) =-sig4(i)*q2(i)+sig2(i)*q1(i)
```

An extra measure is taken to ensure that the stresses of deleted elements are zero by making the q1(i) and q2(i) values zero if deletion has occurred. Otherwise, the qq1(i) and qq2(i) variables take on the cosine and sine of the ply angle, as before:

```
260       qq1(i)=efail(i)*q1(i)
261       qq2(i)=efail(i)*q2(i)
```

Finally, the transformation of stresses back to the global system is completed by multiplying the 'a' matrix by another set of sines and cosines, resulting in the complete transformation matrix:

$$\begin{bmatrix} \text{sig1} \\ \text{sig2} \\ \text{sig4} \\ \text{sig5} \\ \text{sig6} \end{bmatrix} = \begin{bmatrix} cos^2\theta & sin^2\theta & 2cos\theta sin\theta & 0 & 0 \\ sin^2\theta & cos^2\theta & -2cos\theta sin\theta & 0 & 0 \\ -cos\theta sin\theta & cos\theta sin\theta & cos^2\theta - sin^2\theta & 0 & 0 \\ 0 & 0 & 0 & cos\theta & -sin\theta \\ 0 & 0 & 0 & sin\theta & cos\theta \end{bmatrix} \begin{bmatrix} \text{sig1} \\ \text{sig2} \\ \text{sig4} \\ \text{sig5} \\ \text{sig6} \end{bmatrix} \qquad \text{Eq. (60)}$$

```
262       sig1(i)= qq1(i)*a11(i)+qq2(i)*a21(i)
263       sig2(i)=-qq2(i)*a12(i)+qq1(i)*a22(i)
264       sig4(i)= qq1(i)*a12(i)+qq2(i)*a22(i)
265       sig5(i)=-qq2(i)*stg6(i)+qq1(i)*stg5(i)
266       sig6(i)= qq1(i)*stg6(i)+qq2(i)*stg5(i)
```

The new strain energy of the plies are calculated using the components of stress and strain in the global coordinate system, and the material model code is completed and returns to the main LS-DYNA code.

```
267       einc(i)=e1(i)*sig1(i)+e2(i)*sig2(i)+e4(i)*sig4(i)+
268      1         e5(i)*sig5(i)+e6(i)*sig6(i)+einc(i)
269    80 continue
270       return
271       end
```

E3. Modifications made to source code

E3.1 Elastic response

MAT54 does not allow for the definition of the compressive modulus in the axial and transverse directions, nor the compressive strain-to-failure value in the transverse direction. These three material properties are added to the modified model as new user input parameters, and the material model code is changed such that the appropriate property is used based on the stress state of the element.

New user input parameters are added by adding the following lines of code during the variable declarations at the beginning of the code:

```
ymxc =cm(mx+37)
ymyc =cm(mx+38)
dfail2m =cm(mx+39)
```

Note the locations of these three parameters in the ‘cm’ vector correspond to a new line of the keyword input file, as shown in Figure 180. Initial attempts of adding the new user input parameter DFAIL2M utilized the unused ‘cm’ vector locations (mx+3), (mx+5) and (mx+6), as well as a hard-coded value in the subroutine. Each case produced different results in the baseline sinusoid crush simulation, in one case completely destabilizing the model and causing global buckling, as shown by the load-displacement curve behavior in Figure 181. It is speculated that these ‘cm’ vector locations, although inactive in MAT54, may be referenced elsewhere in the LS-DYNA code. Results using the hard-coded DFAIL2M value on the baseline sinusoid crush were the same as when the ‘cm’ vector locations after (mx+37) were used, thereby verifying that these locations are valid to use for new parameters.

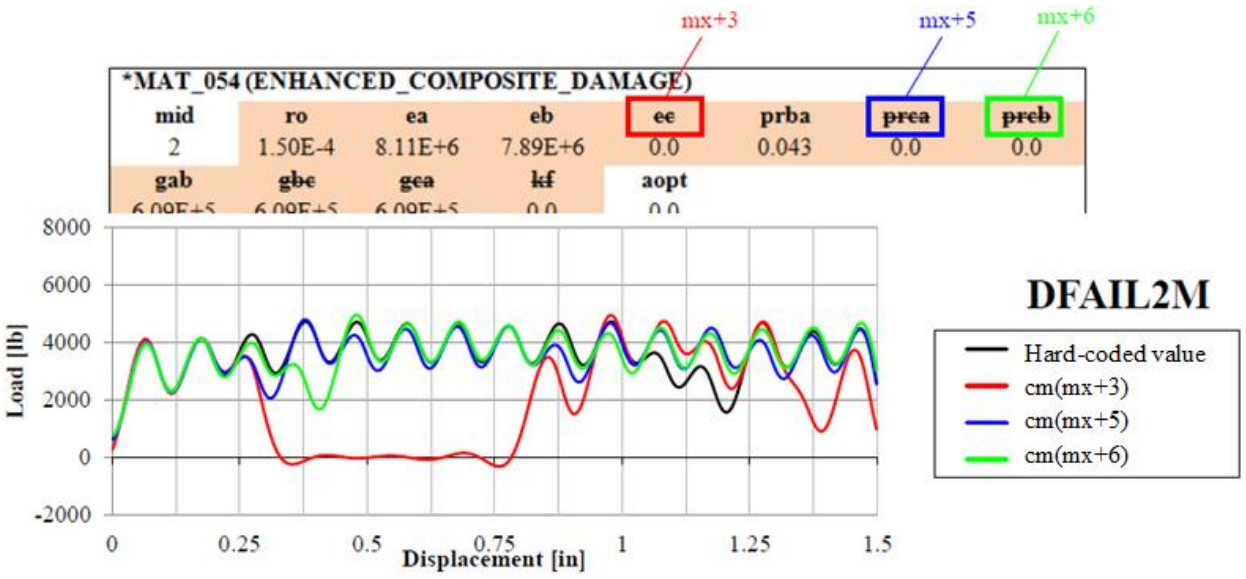

Figure 181. Baseline sinusoid crush simulation results from using different ‘cm’ vector locations for the DFAIL2M parameter in the modified material model.

The code which implements the new compressive moduli replaces code during the two computations of the compliance matrix, both before and after failure is determined. For these computations in the original code, the axial and transverse moduli are defined in lines 097-098

and 174-175. These lines are replaced by an if statement that determines the value of ex(i) and ey(i) for the compliance matrix calculations based on the sign of the stresses as follows,

```
if (sig1(i).gt.0.) then
   ex(i) =ymx
else
   ex(i)=ymxc
endif
if (sig2(i).gt.0.) then
   ey(i) =ymy
else
   ey(i)=ymyc
endif
```

In a similar fashion, the new compressive strain-to-failure parameter in the transverse direction is implemented during the determination of element deletion in the transverse compression case (lines 156-158). The original dfail1m parameter is replaced with the new dfail2m parameter as follows,

```
if (strn2(i)+dfail2m.lt.0.) then
    efail(i)=0.0
endif
```

With these simple changes, the elastic definition of MAT54 is modified.

E3.2 Failure determination

Three new sets of failure criteria are added as options to use in the modified MAT54 model: a set of criteria meant for fabric materials, a maximum crush stress criterion for crush front elements, and a strain-energy based criterion.

E3.2.1 Fabric failure criteria

The MAT54 code is modified to implement the fabric failure criteria by removing the matrix damage terms FBRT and YCFAC, which appear in the fiber failure modes (lines 116-125), and

changing the matrix failure modes to those prescribed by Equation 19. The code for the axial failure criteria of the fabric, which replaces lines 116-125, is as follows:

```
do 50 i=lft,llt
if (stg1(i).gt.0.) then
  ef2(i)=qq2(i)*xt2*  max(0.0,stg1(i))**2+beta*sg44(i)-1.0
  ec2(i)=-1.
else
  ef2(i)=-1.
  xc2(i)= 1/(xc*xc)
  ec2(i)= qq2(i)*xc2(i)*  min(0.0,stg1(i))**2-1.0
endif
```

The new code for the transverse failure criteria of the fabric, which replaces lines 126-133, is as follows:

```
if (stg2(i).gt.0.) then
  em2(i)=qq2(i)*yt2*  max(0.0,stg2(i))**2+beta*sg44(i)-1.0
  ed2(i)=-1.
else
  em2(i)=-1.
  yc2(i)= 1/(yc*yc)
  ed2(i)= qq2(i)*yc2(i)*  min(0.0,stg2(i))**2-1.0
endif
```

E3.2.2 Crush stress criterion

In order to implement the crush stress criterion, a new user input parameter for the crush stress, SIGCR, is introduced in the (mx+47) position of the user input vector as follows,

```
sigcr =cm(mx+47)
```

This cm vector location corresponds to the fifth location on the seventh card of the MAT54 keyword file input deck, see Figure 180.

The code for the crush stress failure criterion is inserted following the Hashin failure criteria. First, an if statement determines if the element is at the crush front by using the qq1 variable. Recall that this variable equals 1.0 unless the element is at the crush front, Equation 40. If the element is at the crush front, then the maximum crush stress criterion is implemented as follows,

```
if (qq1(i).ne.1.0) then
     ecr(i)=stg1(i)/sigcr
else
     ecr(i)=0.0
endif
```

If the element is not at the crush front, then the failure flag ecr is given a zero value. When this failure flag is achieves a value greater than or equal to 1.0, the crush stress failure criterion is violated, and the efail variable takes on a zero value to indicate deletion as follows,

```
if (ecr(i).eq.1.0 .or. ecr(i).gt.1.0 ) then
     efail=0.0
endif
```

E3.2.3 Wolfe strain energy criterion

Wolfe's failure criterion utilizes axial, transverse, and shear strain energy components measured from coupon-level material testing to determine material failure in Equation 11, reproduced below.

$$\left(\frac{\int_{\varepsilon_1}\sigma_1 d\varepsilon_1}{\int_{\varepsilon_1^u}\sigma_1 d\varepsilon_1}\right)^{m_1}+\left(\frac{\int_{\varepsilon_2}\sigma_2 d\varepsilon_2}{\int_{\varepsilon_2^u}\sigma_2 d\varepsilon_2}\right)^{m_2}+\left(\frac{\int_{\varepsilon_6}\sigma_6 d\varepsilon_6}{\int_{\varepsilon_6^u}\sigma_6 d\varepsilon_6}\right)^{m_6}=1 \qquad \text{Eq. (11)}$$

In order to implement this failure criterion into the modified MAT54 material model, several new user input parameters are required to define the ultimate strain energy values of the material,

as listed in Table 23, as well as the three shape functions, m_1, m_2, and m_6. Altogether, eight new user inputs are implemented, as listed in Table 22.

Table 22. New modified MAT54 user input parameters added for Wolfe's strain energy failure criterion.

SEFT	Ultimate axial (fiber) tensile strain energy component
SEFC	Ultimate axial (fiber) compressive strain energy component
SEMT	Ultimate transverse (matrix) tensile strain energy component
SEMC	Ultimate transverse (matrix) compressive strain energy component
SES	Ultimate shear strain energy component
M1	Shape function value for the axial strain energy component
M2	Shape function value for the transverse strain energy component
M6	Shape function value for the shear strain energy component

For the strain energy failure criterion, code is added into MAT54 which computes the updated strain energy components of the element using the updated strain components and trial stresses as follows,

```
einc1(i)=(strn1(i)+d1(i))*stg1(i)
einc2(i)=(strn2(i)+d2(i))*stg2(i)
einc4(i)=(strn4(i)+d4(i))*stg4(i)
```

This operation is performed after the trial stresses stg1(i), stg2(i), and stg4(i) have been computed (lines 109-111). Since both tensile and compressive ultimate strain energies are defined, the Wolfe failure criterion is dependent on the sign of the element stresses. During the computation of the Hashin failure criteria (lines 116-133), if statements segregate operations depending on the sign of the element stresses in order to treat tensile and compressive failure modes individually. This existing code is utilized to assign the appropriate ultimate strain energy values as tensile or compressive, which are later used in the Wolfe criterion. In the following code from the Hashin failure criteria, new lines of code (identified by "ADD") create the variable sef(i) which holds the value of the 1-direction ultimate strain energy, and sem(i) which holds the value of the 2-direction ultimate strain energy as follows,

```
116       if (stg1(i).gt.0.) then
117         ef2(i)=qq2(i)*(xt2fbrt+(xt2-xt2fbrt)*ed(i))*
118      .           max(0.0,stg1(i))**2+beta*sg44(i)-1.0
119         ec2(i)=-1.
ADD         sef(i)=seft
120       else
121         ef2(i)=-1.
122         xc2(i) = ed(i)*xc + (1.0-ed(i))*ycfac*yc
123         xc2(i)  = 1/(xc2(i)*xc2(i))
124         ec2(i)= qq2(i)*xc2(i)*  min(0.0,stg1(i))**2-1.0
ADD         sef(i)=sefc
125       endif
126       if (stg2(i).gt.0.) then
127         em2(i)=qq2(i)*yt2*  max(0.0,stg2(i))**2+sg44(i)-1.0
128         ed2(i)=-1.
ADD         sem(i)=semt
129       else
130         em2(i)=-1.
131         ed2(i)=qq2(i)*sd2*  min(0.0,stg2(i))**2+
132      1         mlt2*stg2(i)/qq1(i)+sg44(i)-1.0
ADD         sem(i)=semc
133       endif
```

This added code allows for the computation of the Wolfe failure criterion after the Hashin failure criteria as follows,

```
          ew(i)=(einc1(i)/sef(i))**m1+(einc2(i)/sem(i))**m2+
         1         (einc4(i)/ses)**m6
```

In this code, the ew(i) term acts as a history variable which stores the value of the calculated Wolfe criterion. If this variable exceeds a value of 1, the element is marked for deletion using efail(i) as follows,

```
          if (ew(i).eq.1. .or. ew(i).gt.1.) then
              efail(i)=0.0
          endif
```

With this additional code, the Wolfe failure criterion is enacted along with the existing Hashin failure criteria. Alternatively, the Wolfe failure criterion is also implemented such that it is only active at the crush front where premature failure predictions may be beneficial to the material model. An if statement is added to the source code calculation of the Wolfe criterion such that the it is only active for the crush front elements as follows,

```
if (qq1(i).ne.1.0) then
    ew(i)=(einc1(i)/sef(i))**m1+(einc2(i)/sem(i))**m2+
1          (einc4(i)/ses)**m6
else
    ew(i)=0.0
endif
```

Recall that the qq1(i) parameter acts as a flag for crush front elements. Simulations of the sinusoid crush element are rerun employing the Wolfe criterion only at the crush front, while setting SOFT to a value of 0.999 to prevent material softening at the crush front.

D3.3 Post-failure degradation

Three new user input parameters are defined in order to implement the post-failure degradation modifications, and are summarized in Table 26. The STROPT parameter is simply for convenience such that the user may choose which post-failure degradation option to implement while the NDGRAD and SIGLIM parameters influence the shape of the stress degradation curve for options 2 and 3.

Table 26. Summary of new user input parameters introduced for the post-failure degradation options in the modified MAT54.

STROPT	Specifies which stress degradation option to use: 0: Regular MAT54 behavior (no modification) 1: Zero stress after failure 2: Linear stress degradation after failure 3: Linear degradation followed by constant stress 4: Logarithmic stress decay after failure
NDGRAD	Number of degradation iterations following failure for STROPT = 2,3; determines the slope of the linear decay
SIGLIM	Percentage of maximum stress allowed during plastic deformation for STROPT = 3

The approach adopted to implement the first stress degradation option is to delete an element if any of its four failure criteria are violated. This achieves the zero stress state result desired for STROPT = 1. Element deletion is governed by the efail(i) variable, and new code is added following the initial assignment of this variable (lines 145-168). The new code is bounded by an if statement such that it is only implemented with STROPT is set by the user to a value of 1. Subsequent if statements within this first statement use the failure criteria history variables ef(i), ec(i), em(i), and ed(i) to set efail(i) to a value of zero in case any of the failure criteria have been violated. This is the only additional code necessary to implement the first stress degradation option as follows,

```
if (stropt.eq.1.) then
  if (ef(i).lt.1.e-8) efail(i)= 0.0
  if (ec(i).lt.1.e-8) efail(i)= 0.0
  if (em(i).lt.1.e-8) efail(i)= 0.0
  if (ed(i).lt.1.e-8) efail(i)= 0.0
endif
```

The remaining stress degradation options require significantly more code to be added in order to implement different types of stress decays following failure. First, several new Fortran variables need to be defined and assigned values before the stress degradation code can be implemented. For stress degradation options STROPT = 2 and 3, the slope of the linear stress decay is governed by the user input parameter NDGRAD which defines the number of iterations during which the decay should occur. The degradation therefore requires that the maximum stress experienced at failure is a value that must be a known value. The maximum stress at failure is only known once failure occurs, and must be saved at this instance before it is overwritten during the next iteration. The following code is added to save the failure stresses immediately following the calculation of the failure criteria (lines 116-133) and before the assignment of failure flags iflagf, iflagc, iflagm, and iflagd (lines 134-137).

```
if (iflagf.ne.1 .and. ef2(i).gt.0) then
  sigff(i)=stg1(i)
endif
if (iflagc.ne.1 .and. ec2(i).gt.0) then
  sigfc(i)=stg1(i)
endif
if (iflagm.ne.1 .and. em2(i).gt.0) then
  sigfm(i)=stg2(i)
endif
if (iflagd.ne.1 .and. ed2(i).gt.0) then
  sigfd(i)=stg2(i)
endif
```

These if statements are only valid during the iteration that failure has occurred, between when failure is determined (ef2(i), ec2(i), em2(i) or ed2(i) is greater than zero) and when the failure flag is marked (iflagf, iflagc, iflagm, or iflagd equals 1). The failure stress variables sigff(i), sigfc(i), sigfm(i), and sigfd(i) can therefore only be written one time to be equal to the 1-direction or 2-direction stress of the element, as dictated by the failure mode.

The amount by which the stress is degraded per iteration is 1/NDGRAD, defined in the code to be the new variable ‘dndg’, multiplied by the maximum stress experienced at failure. A counter variable is used such that stress degradation continues only for the indicated number of iterations, NDGRAD, before allowing the stress to go to zero via element deletion. There are two such counter variables, dmgkf(i) and dmgkm(i), which are unique for the fiber and matrix failure modes such that stress degradation may occur independently in the 1- and 2-directions. For each iteration, the counter is raised by the discrete value dndg such that when the counter reaches the final value of 1, the stress is zero. For STROPT = 2, a degradation iteration limit variable ‘dlim’ is defined to be the value of the counter one iteration prior to reaching a value of one. For example, if the number of iterations were to be 1,000, the dndg would equal 0.001, and dlim would take the value of 0.999. For STROPT = 3, the iteration limit variable ‘dlim2’ is defined in a slightly different manner such that the degradation iterations are limited when the stress has been degraded to the user specified plastic deformation stress. If NDGRAD were to be 1,000 and SIGLIM were 0.2 (20% of maximum stress), then dlim2 would be calculated to be 0.799. The code which adds these new Fortran variables is defined during the initial variable declarations and basic constant operations (lines 31-38) as follows,

```
dndg=1./ndgrad
dlim=1.0-dndg
dlim2=dlim-siglim
```

The bulk of the new code is inserted in place of the stress component updates at the end of the MAT54 subroutine (lines 249-253). For the STROPT = 0 and 1 options, the default MAT54 stress update code is unchanged. For the STROPT = 2, 3, and 4 options, the stress is degraded if there is failure, or updated using the normal MAT54 stress update code if there is no failure. Stress degradation depends on the failure mode experienced, as only the failed stress components

are degraded. In the case of fiber failure, the 1-direction stress sig1(i) is degraded, while in the case of matrix failure, both the 2-direction and shear stresses, sig2(i) and sig4(i), are degraded. A flow chart outlining the Fortran code added to the stress update routine for the stress degradation options is given in Figure 182. Each junction in Figure 182 represents an if statement within the Fortran code. For instance, the first if statement runs the normal MAT54 stress update code (lines 251-253) in the cases where STROPT = 0 or 1 as follows,

```
ADD       if (stropt.eq.0. .or. stropt.eq.1.) then
251          sig1(i)=sig1(i)+c11(i)*d1(i)+c12(i)*d2(i)
252          sig2(i)=sig2(i)+c12(i)*d1(i)+c22(i)*d2(i)
253          sig4(i)=sig4(i)+c44(i)*d4(i)
ADD       endif
```

Subsequent if statements at the initial level of the flow chart separate each of the remaining stress degradation options, STROPT = 2, 3, and 4.

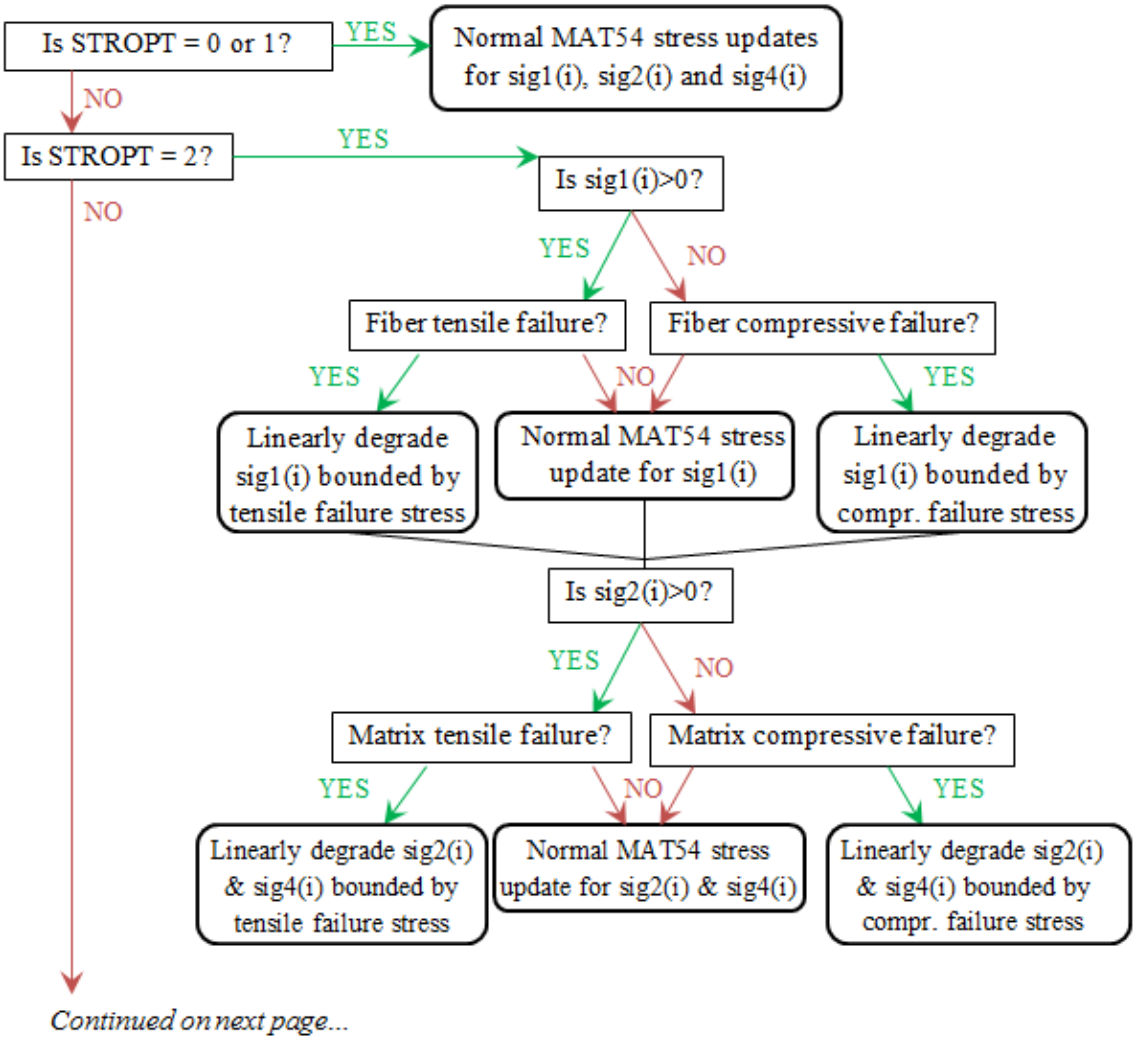

Figure 182. Continued on next page.

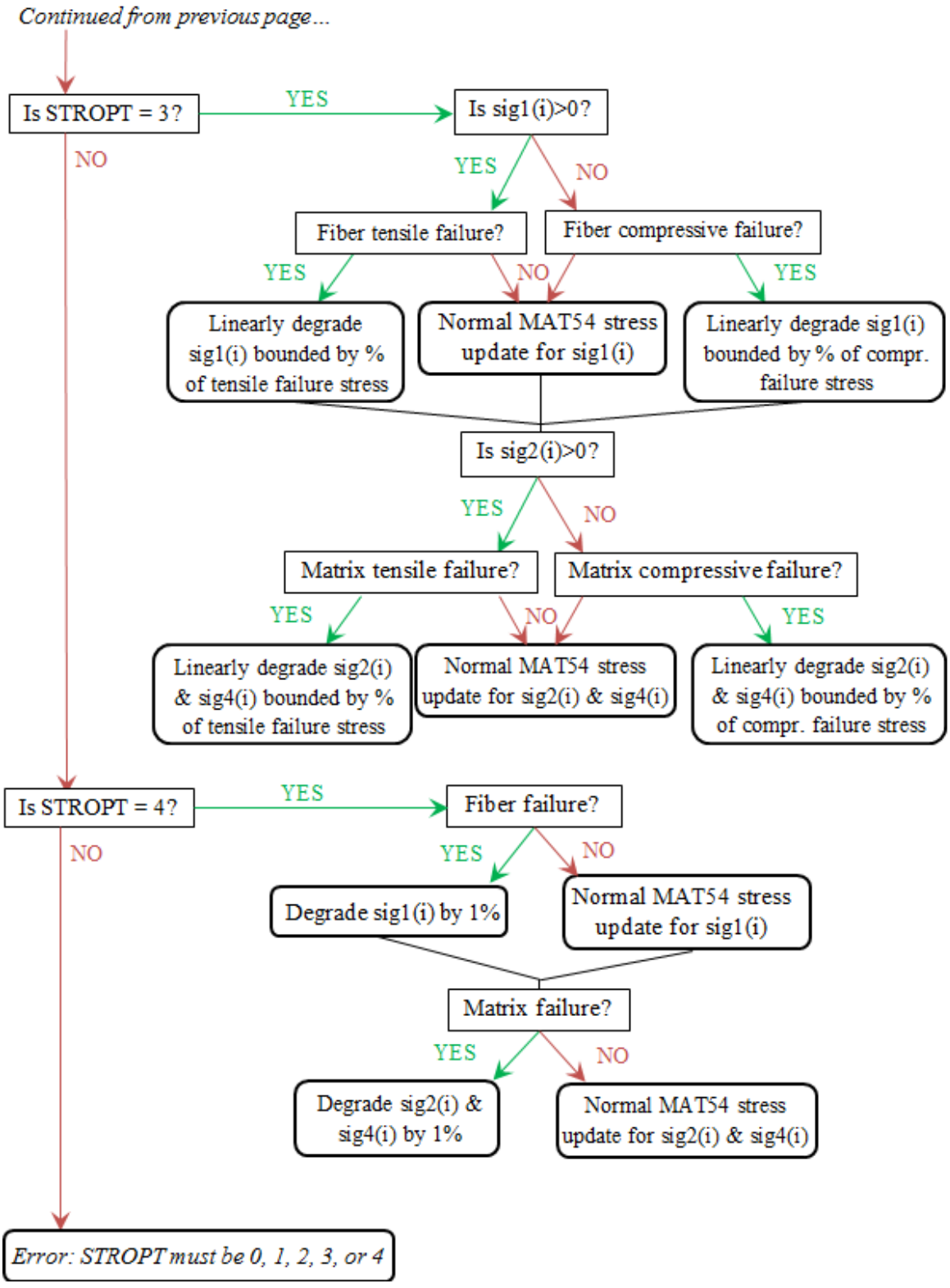

Figure 182. Flow chart outlining Fortran code written for post-failure stress degradation options, added to the MAT54 source code during stress updates at the end of the subroutine.

After line 253, the code for the STROPT = 2 tensile fiber failure mode stress degradation is added in the stress update section of the MAT54 subroutine, as shown below. The first if statement establishes the user input parameter STROPT has a value 2 and the second if statement establishes that the 1-direction component of the element stress is in the tensile mode. There is an else statement at the end of this bundle of code which addresses the compressive mode of the 1-direction stress. The third if statement checks for tensile fiber mode failure, in which case the stress degradation is performed.

```
if (stropt.eq.2.) then
  if (sig1(i).gt.0.) then
    if (ef(i).lt.1.e-8) then
      if (dmgkf(i).lt.dlim) then
        sig1(i)=sig1(i)-(dndg*sigff(i))
        dmgkf(i)=dmgkf(i)+dndg
      else
        sig1(i)= 0.0
        sig2(i)= 0.0
        sig4(i)= 0.0
      endif
    else
      sig1(i)=sig1(i)+c11(i)*d1(i)+c12(i)*d2(i)
      dmgkf(i)= 0.0
    endif
  else
```

In the first run of the code it is assumed that no failure occurs. When no fiber tensile failure has occurred, the else condition of the third if statement is valid and the 1-direction stress is updated by the normal MAT54 code (see line 250), and the counter variable dmgkf(i) is initialized to a zero value. When failure occurs, the third if statement is valid, and the fourth if statement which immediately follows checks that the counter variable dmgkf(i) has not surpassed the iteration limit dlim. The 1-direction stress is degraded by an amount specified by dndg*sigff(i), and the counter is increased by a value of dndg. Once the counter achieves its limiting value dlim, the 1-

2- and 4- components of stress are set to zero. The element cannot be deleted here (efail(i) = 0) since the element deletion subroutine has already been run earlier in the code. Instead, additional code is added to following the initial assignment of efail(i) (lines 145-168) such that the element is deleted on the next iteration. In this way, the stresses are set to zero one iteration prior to the full amount specified by the user input parameter NDGRAD, such that the element is deleted upon the following iteration as specified by the user. The element deletion code added for STROPT = 2 is as follows,

```
if (stropt.eq.2.) then
  if (ef(i).lt.1.e-8) then
    if (sig1(i).lt.dndg*sigff(i)) efail(i)= 0.0
  endif
  if (ec(i).lt.1.e-8) then
    if (sig1(i).gt.dndg*sigfc(i)) efail(i)= 0.0
  endif
  if (em(i).lt.1.e-8) then
    if (sig2(i).lt.dndg*sigfm(i)) efail(i)= 0.0
  endif
  if (ed(i).lt.1.e-8) then
    if (sig2(i).gt.dndg*sigfd(i)) efail(i)= 0.0
  endif
endif
```

The meaning of this code is that if any of the modes of failure are violated, and the relevant component of stress is less than the degraded stress interval (as defined by dndg multiplied by the failure stress), the element is marked for deletion.

The added code for the STROPT = 2 compressive fiber stress degradation mode is in essence the same as the tensile fiber mode, as follows,

```
else
  if (ec(i).lt.1.e-8) then
    if (dmgkf(i).lt.dlim) then
      sig1(i)=sig1(i)-(dndg*sigfc(i))
      dmgkf(i)=dmgkf(i)+dndg
    else
      sig1(i)= 0.0
      sig2(i)= 0.0
      sig4(i)= 0.0
    endif
  else
    sig1(i)=sig1(i)+c11(i)*d1(i)+c12(i)*d2(i)
    dmgkf(i)= 0.0
  endif
endif
```

Similarly, the added code for the STROPT = 2 tensile and compressive matrix degradation modes are the same as the fiber modes, except that the shear stress component of the element is also degraded or updated as follows in the matrix tensile mode portion of the code,

```
if (sig2(i).gt.0.) then
  if (em(i).lt.1.e-8) then
    if (dmgkm(i).lt.dlim) then
      sig2(i)=sig2(i)-(dndg*sigfm(i))
      sig4(i)=sig4(i)-(dndg*sigfs(i))
      dmgkm(i)=dmgkm(i)+dndg
    else
      sig1(i)= 0.0
      sig2(i)= 0.0
      sig4(i)= 0.0
    endif
  else
    sig2(i)=sig2(i)+c12(i)*d1(i)+c22(i)*d2(i)
    sig4(i)=sig4(i)+c44(i)*d4(i)
    dmgkm(i)= 0.0
  endif
else
```

The added code for STROPT = 3 is very similar to that added for STROPT = 2, with a couple exceptions. First, the iteration limit parameter used is dlim2 rather than dlim, and the stresses are

not set to zero once this limit is achieved. Instead, if the limit is achieved, then the stress is forced to remain at the limiting value, as defined by SIGLIM multiplied by the failure stress. For the sake of brevity, only the tensile fiber mode code is given below,

```
if (stropt.eq.3.) then
 if (sig1(i).gt.0.) then
   if (ef(i).lt.1.e-8) then
     if (dmgkf(i).lt.dlim2) then
       sig1(i)=sig1(i)-(dndg*sigff(i))
       dmgkf(i)=dmgkf(i)+dndg
     else
       sig1(i)=siglim*sigff(i)
       dmgkf(i)= 1.0
     endif
   else
     sig1(i)=sig1(i)+c11(i)*d1(i)+c12(i)*d2(i)
     dmgkf(i)= 0.0
   endif
 else
```

For the STROPT = 3 stress degradation option, the element is not deleted due to the degradation, rather it is deleted when the element achieves the maximum strain limits just as the normal deletion mechanism of the default MAT54 material model. No additional code is therefore necessary to address element deletion for this stress degradation option.

Finally, for the STROPT = 4 stress degradation option, the stress update code is modified such that the appropriate stress components are degraded by 1% of their current value each iteration to achieve a logarithmic like degradation after failure. While the linear stress degradation options relied upon the value of the maximum stress saved at the specific failure mode experienced, this degradation option does not require this value and therefore is not dependent on tensile or compressive modes of failure. Only the fiber and matrix modes are considered separately in order to degrade the appropriate stress components for this stress degradation option as follows,

```
 if (stropt.eq.4.) then
  if (ef(i).lt.1.e-8 .or. ec(i).lt.1.e-8) then
    sig1(i)= 0.99 *sig1(i)
  else
    sig1(i)=sig1(i)+c11(i)*d1(i)+c12(i)*d2(i)
  endif
  if (em(i).lt.1.e-8 .or. ed(i).lt.1.e-8) then
    sig2(i)= 0.99 *sig2(i)
    sig4(i)= 0.99 *sig4(i)
  else
    sig2(i)=sig2(i)+c12(i)*d1(i)+c22(i)*d2(i)
    sig4(i)=sig4(i)+c44(i)*d4(i)
  endif
 endif
```

In order to isolate the post-failure stress degradation schemes to be applicable for crush-front only (Figure 149a) or all other elements only (Figure 149b), if statements are added which make use of the crush-front flag Fortran variable qq1 (Equation 40). The code added to implement the STROPT = 1 option is bounded by a new if statement which reads,

```
if (qq1.ne.1.) then
```

in the case of crush-front only degradation (Figure 149a), and

```
if (qq1.eq.1.) then
```

in the case of all other elements only (Figure 149b). These statements apply the STROPT = 1 stress degradation scheme to elements based on their qq1 value, which equals 1 only for all elements except those at the crush-front.

Similar treatment is given to the bundle of code which implements the STROPT = 2, 3, and 4 degradation options. A single if condition is added prior to this bundle of code, which for the case of crush-front only degradation (Figure 149a) is,

```
if (qq1.eq.1.) then
   sig1(i)=sig1(i)+c11(i)*d1(i)+c12(i)*d2(i)
   sig2(i)=sig2(i)+c12(i)*d1(i)+c22(i)*d2(i)
   sig4(i)=sig4(i)+c44(i)*d4(i)
else
```

and for the case of the degradation of all other elements only (Figure 149b) is,

```
if (qq1.ne.1.) then
   sig1(i)=sig1(i)+c11(i)*d1(i)+c12(i)*d2(i)
   sig2(i)=sig2(i)+c12(i)*d1(i)+c22(i)*d2(i)
   sig4(i)=sig4(i)+c44(i)*d4(i)
else
```

These statements impose the regular MAT54 stress updates to elements based on their qq1 value, but regardless of their failure state like the default MAT54. This causes the perfectly plastic behavior for the specified elements. Following this if statement is the else condition of the qq1 value which contains all of the new code for implementing the stress degradations based on the failure state of the element. For the transverse-only degradation version, the 1-direction stress degradation code based on the ef(i) and ec(i) failure states is simply commented out such that the sig1(i) value is plastically deformed as in the case of the default MAT54. This concludes the new code added for the implementation of the four new post-failure stress degradation options in the modified MAT54.

Appendix F: Modified MAT54 User's Manual Entry

The modified version of MAT54 expands upon the capability of the built-in version in the elastic definition, failure criterion selection, and post-failure material degradation scheme. In the elastic region, the governing equations remain the same (see LS-DYNA Theory Manual *MAT_022, Equations 19.22.1 and 19.22.2) and the user has the added capability to define compressive constitutive properties in addition to the regular tensile values. The code uses the appropriate value based on the stress state at each integration point. In addition to the built-in Hashin (*MAT_054) and Tsai-Wu (*MAT_055) criteria, three additional failure criteria are added: Hashin for fabric material systems, maximum crush stress criterion, and the Wolfe strain-energy criterion.

The fabric criteria take the *MAT_054 criteria and utilize the 'fiber' modes in both the axial and transverse directions as follows,

For the tensile axial mode,

$$\sigma_{11} > 0 \quad then \quad {e_f}^2 = \left(\frac{\sigma_{11}}{XT}\right)^2 + \beta\left(\frac{\sigma_{12}}{SC}\right)^2 - 1 \begin{cases} \geq 0 \; failed \\ < 0 \; elastic \end{cases}$$

For the compressive axial mode,

$$\sigma_{11} < 0 \quad then \quad {e_c}^2 = \left(\frac{\sigma_{11}}{XC}\right)^2 - 1 \begin{cases} \geq 0 \; failed \\ < 0 \; elastic \end{cases}$$

For the tensile transverse mode,

$$\sigma_{22} > 0 \quad then \quad {e_m}^2 = \left(\frac{\sigma_{22}}{YT}\right)^2 + \beta\left(\frac{\sigma_{12}}{SC}\right)^2 - 1 \begin{cases} \geq 0 \; failed \\ < 0 \; elastic \end{cases}$$

For the compressive transverse mode,

$$\sigma_{22} < 0 \quad then \quad {e_d}^2 = \left(\frac{\sigma_{22}}{YC}\right)^2 - 1 \begin{cases} \geq 0 \; failed \\ < 0 \; elastic \end{cases}$$

The maximum crush stress criterion describes a maximum value of stress for crush-front elements only in place of the SOFT crush-front damage parameter. The element is eroded when the maximum crush stress criterion is violated. Finally, the Wolfe strain-energy criterion uses maximum strain-energy parameters in the axial, transverse, and shear directions according to Wolfe and Butalia, 1998. The Wolfe criterion is as follows,

$${e_w}^2 = \left(\frac{\int_{\varepsilon_1} \sigma_1 d\varepsilon_1}{SEFT \; or \; SEFC}\right)^{M1} + \left(\frac{\int_{\varepsilon_2} \sigma_2 d\varepsilon_2}{SEMT \; or \; SEMC}\right)^{M2} + \left(\frac{\int_{\varepsilon_6} \sigma_6 d\varepsilon_6}{SES}\right)^{M6} - 1 \begin{cases} \geq 0 \; failed \\ < 0 \; elastic \end{cases}$$

In this equation, the numerator integrals are the strain energy components of the element, the denominator parameters are the user-defined ultimate strain energy components of the material system, and the exponents are user-defined shape function parameters. The user defines both the tensile 'T' and compressive 'C' ultimate strain energy values in the axial/fiber 'F' and transverse/matrix 'M' directions. The code uses the appropriate value to calculate the failure criterion based on the stress state at the integration point.

Finally, several post-failure material degradation options are added such that the user can define the stress state of an element following failure but before element erosion. A post-stress option parameter "STROPT" determines which degradation scheme to use, and its corresponding stress-strain response is shown in the idealized figure below:

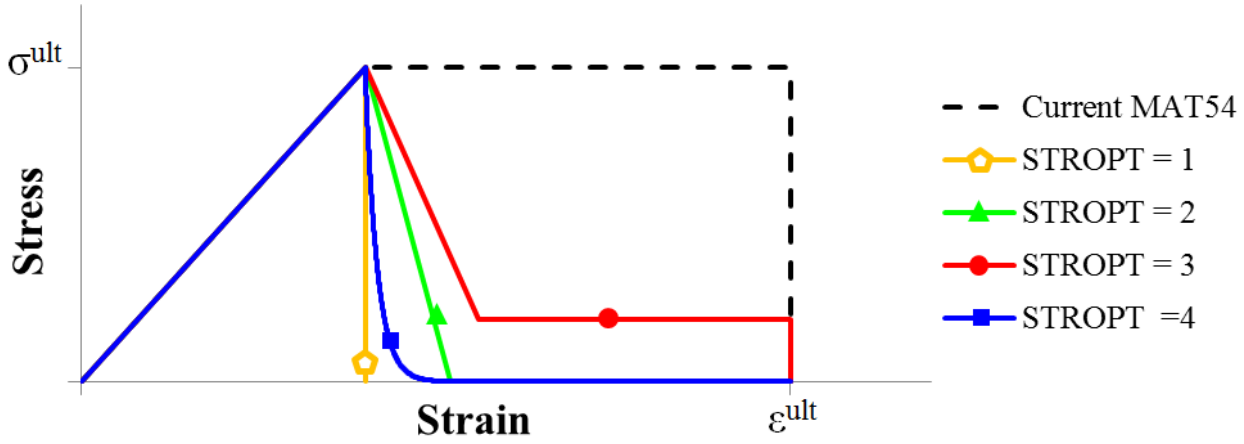

Figure E1. Illustration of stress-strain behavior described by four post-failure degradation schemes specified by the user parameter STROPT.

The first option causes any failure to result in immediate element erosion. The second and third options include a linear degradation until zero stress (STROPT = 2) or until a plastic stress limit (STROPT = 3). An additional user input parameter, 'NDGRAD' is used to define the slope of the linear degradation by specifying the number of degradation iterations (lower NDGRAD = steeper degradation slope). The user input parameter 'SIGLIM' defines the plastic stress limit of the STROPT = 3 scheme as a percentage of the ultimate stress (i.e. SIGLIM = 0.2 means the stress will remain constant at 20% of the ultimate stress value at initial failure).

Card 1

1	2	3	4	5	6	7	8
Variable	MID	RO	EA	EB	(EC)	PRBA	(PRCA)	(PRCB)
Type	AB	F	F	F	F	F	F	F

Card 2

Variable	GAB	GBC	GCA	(KF)	AOPT			
Type	F	F	F	F	F			

Card 3	1	2	3	4	5	6	7	8
Variable	(XP)	(YP)	(ZP)	A1	A2	A3	MANGLE	
Type	F	F	F	F	F	F	F	

Card 4

Variable	V1	V2	V3	(D1)	(D2)	(D3)	DFAILM	DFAILS
Type	F	F	F	F	F	F	F	F

Card 5

Variable	TFAIL	ALPH	SOFT	FBRT	YCFAC	DFAILT	DFAILC	EFS
Type	F	F	F	F	F	F	F	F

Card 6

Variable	XC	XT	YC	YT	SC	CRIT	BETA	DFAILS
Type	F	F	F	F	F	F	F	F

Card 7

Variable	DFAIL2M	EAC	EBC	NDGRAD	STROPT			
Type	F	F	F	F	F			

Card 8

Variable	SIGLIM	SEFT	SEFC	SEMT	SEMC	SES	M2	M6
Type	F	F	F	F	F	F	F	F

VARIABLE	**DESCRIPTION**
MID	Material identification. A unique number or label not exceeding 8 characters.
RO	Mass density
EA	Young's modulus – axial direction, tensile load case
EB	Young's modulus – transverse direction, tensile load case
(EC)	Young's modulus – normal direction (not used)
PRBA	Poisson's ratio v_{ba} (not used)
(PRCA)	Poisson's ratio v_{ca} (not used)
(PRCB)	Poisson's ratio v_{cb} (not used)
GAB	Shear modulus G_{ab}

GBC	Shear modulus G_{bc}
GCA	Shear modulus G_{ca}
(KF)	Bulk modulus of failed material (not used)
AOPT	Material axes option (see Figure E2) EQ.0.0: locally orthotropic material axes determined by element nodes 1, 2, and 4 EQ.2.0: globally orthotropic material axes determined by vector A EQ.3.0: locally orthotropic material axes determined by rotating the cross-product of the vector V and the element normal by an angle (MANGLE) LT.0.0: the absolute value of AOPT is a coordinate system ID number
(XP YP ZP)	Components of vector used to define the local material axes for AOPT = 1.0 (not used)
A1 A2 A3	Components of vector A used to define the local material axes for AOPT = 2.0
MANGLE	Material angle in degrees used to define the local material axes for AOPT = 3.0
V1 V2 V3	Components of vector V used to define the local material axes for AOPT = 3.0
(D1 D2 D3)	Components of vector D used to define the local material axes of a solid element for AOPT = 2.0 (not used)
DFAILM	Transverse tensile failure strain
DFAILS	Shear failure strain
TFAIL	Time step size criteria for element deletion TFAIL $\leq$ 0: no element deletion by time step size. The crashfront algorithm only works if TFAIL is set to a value above zero 0 < TFAIL $\leq$ 0.1: element is deleted when its time step is smaller than TFAIL TFAIL > 1: element is deleted when the quotient of the actual time step and the original time step drops below TFAIL
ALPH	Elastic shear stress non-linear factor (see *MAT_022)
SOFT	Material crush-front strength reduction factor after crushing failure (e.g. 0.6 = 60% of total strength remains)
FBRT	Axial tensile (XT) strength reduction factor after compressive matrix failure

YCFAC	Axial compressive (XC) strength reduction factor after compressive matrix failure
DFAILT	Axial tensile failure strain
DFAILC	Axial compressive failure strain
EFS	Effective failure strain
XC	Axial compressive strength
XT	Axial tensile strength
YC	Transverse compressive strength
YT	Transverse tensile strength
SC	Shear strength
CRIT	Failure criterion selector
BETA	Shear factor in tensile axial failure criterion
DFAILS	Shear failure strain
DFAIL2M	Transverse compressive failure strain
EAC	Young's modulus – axial direction, compressive load case
EBC	Young's modulus – transverse direction, compressive load case
NDGRAD	Number of degradation iterations from maximum stress until zero stress following failure for STROPT = 2, 3
STROPT	Post-failure stress degradation options (see Figure E1) EQ.0.0: Default MAT54: constant stress until failure strain reached (no degradation) EQ.1.0: Immediate ply erosion (no degradation) EQ.2.0: Linear degradation until zero stress EQ.3.0: Linear degradation until a specified plastic stress limit, SIGLIM; element is eroded once failure strain is reached EQ.4.0: Logarithmic decay until failure strain is reached
SIGLIM	Percentage of maximum stress which defines the residual stress, a plastic straining limit for STROPT = 3 (i.e. 0.2 = 20% residual plastic stress)
SEFT	Ultimate strain energy, axial tensile load case
SEFC	Ultimate strain energy, axial compressive load case
SEMT	Ultimate strain energy, transverse tensile load case

SEMC	Ultimate strain energy, transverse compressive load case
SES	Ultimate shear strain energy
M2	Shape function for transverse strain energy term in Wolfe's criterion
M6	Shape function for shear strain energy term in Wolfe's criterion

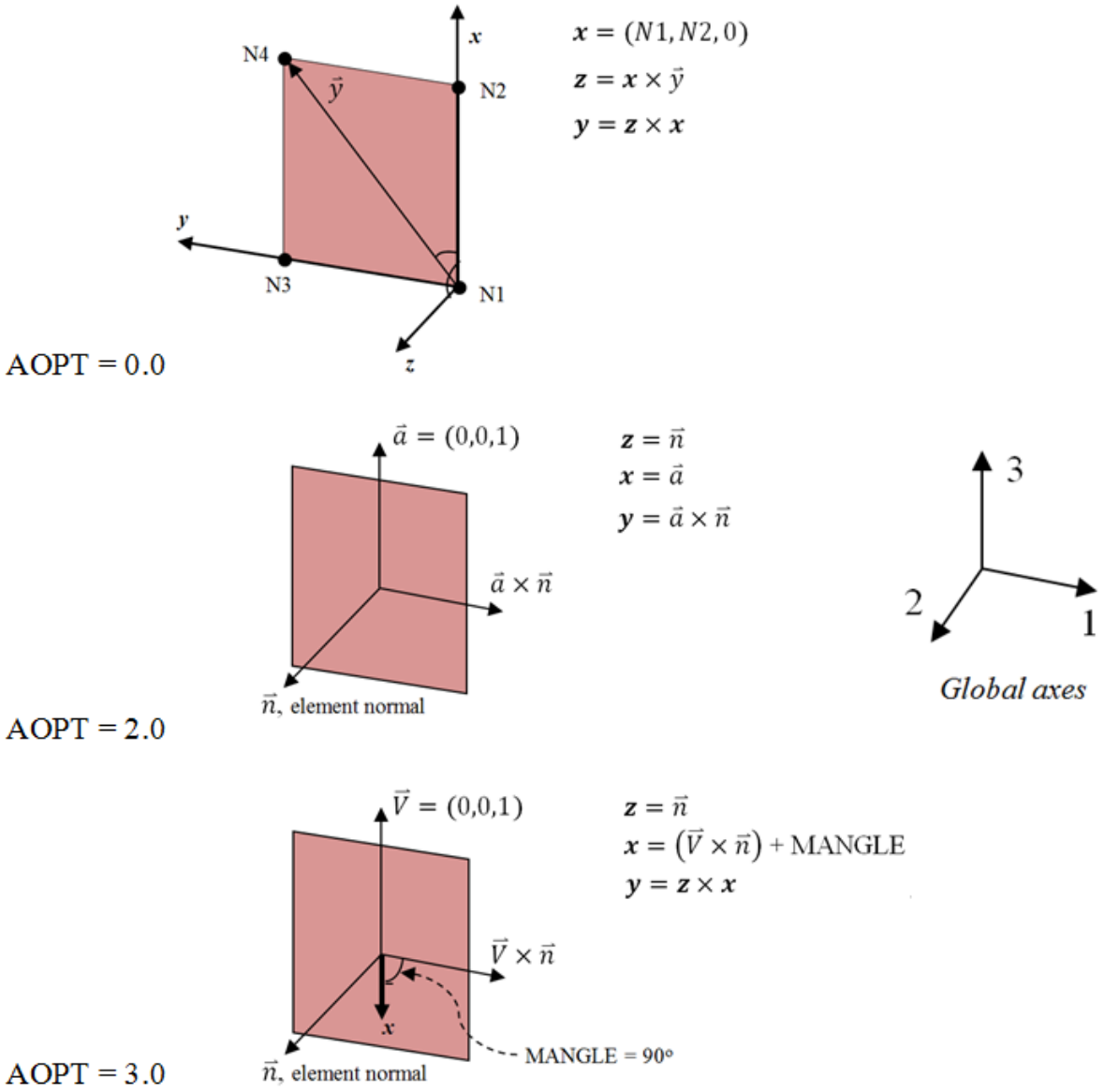

Figure E2. Three ways to define the local material axes using the AOPT parameter and additional user input parameters found in MAT54.

Appendix G: Keyword input file for fabric sinusoid crush

```
*KEYWORD
$---+----1----+----2----+----3----+----4----+----5----+----6----+----7----+----8
*TITLE
Fabric sinusoid crush
$---+----1----+----2----+----3----+----4----+----5----+----6----+----7----+----8
*CONTROL_SHELL
$   wrpang     esort     irnxx    istupd    theory       bwc     miter      proj
       0.0         0        -1         0         2         2         1         0
$  rotascl    intgrd    lamsht    cstyp6    tshell    nfail1    nfail4   psnfail
       0.0         1         0         1
$  psstupd    irquad

*CONTROL_TERMINATION
$   endtim    endcyc     dtmin    endeng    endmas
     0.010
*CONTROL_TIMESTEP
$    dtint    tssfac
       0.0       0.9
$---+----1----+----2----+----3----+----4----+----5----+----6----+----7----+----8
*DATABASE_SPCFORC
$       dt    binary      lcur     ioopt
 .10000E-4         1         0         0
*DATABASE_BINARY_D3PLOT
$  dt/cycl      lcdt      beam     npltc
  .1000E-2         0         0       100
$    ioopt
         0
*DATABASE_EXTENT_BINARY
$    neiph     neips    maxint    strflg    sigflg    epsflg    rltflg    engflg
         0        16         8         1         1         1         1         1
$   cmpflg    ieverp    beamip     dcomp      shge     stssz    n3thdt   ialemat
         1
$  nintsld   pkp_sen      sclp     blank     msscl     therm

$---+----1----+----2----+----3----+----4----+----5----+----6----+----7----+----8
*PART
Loading Plate
$      pid     secid       mid     eosid      hgid      grav    adpopt      tmid
        19         9         9
*PART
Sinusoid
         1         1         1
*PART
Trigger
         2         2         1
$---+----1----+----2----+----3----+----4----+----5----+----6----+----7----+----8
*SECTION_SHELL_TITLE
Loading Plate
$    secid    elform      shrf       nip     propt   qr/irid     icomp     setyp
         9         2     1.000     2.000       0.0       0.0         0         1
$       t1        t2        t3        t4      nloc     marea      idof    edgset
   0.30000   0.30000   0.30000   0.30000        -1
```

```
*SECTION_SHELL_TITLE
Sinusoid
$    secid    elform      shrf       nip     propt   qr/irid     icomp     setyp
         1        16     1.000     8.000       0.0       0.0         1         1
$       t1        t2        t3        t4      nloc     marea      idof    edgset
   0.07286   0.07286   0.07286   0.07286         0
$       b1        b2        b3        b4        b5        b6        b7        b8
         0         0         0         0         0         0         0         0
*SECTION_SHELL_TITLE
Trigger
$    secid    elform      shrf       nip     propt   qr/irid     icomp     setyp
         2        16     1.000     8.000       0.0       0.0         1         1
$       t1        t2        t3        t4      nloc     marea      idof    edgset
   0.05200   0.05200   0.05200   0.05200         0
$       b1        b2        b3        b4        b5        b6        b7        b8
         0         0         0         0         0         0         0         0
$---+----1----+----2----+----3----+----4----+----5----+----6----+----7----+----8
*MAT_RIGID_TITLE
Loading plate
$      mid        ro         e        pr         n    couple         m     alias
         9    21.180  .3000E+8   0.33000       0.0       0.0       0.0       0.0
$      cmo      con1      con2
     1.000         4         7
$      lco
       0.0
*MAT_ENHANCED_COMPOSITE_DAMAGE_TITLE
Composite
$      mid        ro        ea        eb        ec      prba      prca      prcb
         1  .1500E-3  8110000.  7890000.  1000000.   0.04300       0.0       0.0
$      gab       gbc       gca        kf      aopt
  609000.0  609000.0  609000.0       0.0     3.000
$       xp        yp        zp        a1        a2        a3    mangle
       0.0       0.0       0.0       0.0       0.0       0.0    90.000
$       v1        v2        v3        d1        d2        d3    dfailm    dfails
       0.0       0.0     1.000       0.0       0.0       0.0   0.06000   0.03000
$    tfail      alph      soft      fbrt     ycfac    dfailt    dfailc       efs
 .11530E-8   0.10000   0.73000   0.50000     1.200   0.01640  -0.01300       0.0
$       xc        xt        yc        yt        sc      crit      beta
  103000.0  132000.0  102000.0  112000.0  19000.00    54.000   0.50000
$---+----1----+----2----+----3----+----4----+----5----+----6----+----7----+----8
*DAMPING_PART_STIFFNESS
$      pid      beta
         1   0.05000
*DAMPING_PART_STIFFNESS
$      pid      beta
         2   0.05000
$---+----1----+----2----+----3----+----4----+----5----+----6----+----7----+----8
*BOUNDARY_PRESCRIBED_MOTION_SET_ID
$       id
         1
$     nsid       dof       vad      lcid        sf       vid     death     birth
         5         3         2       123       0.0         0       0.0       0.0
*BOUNDARY_SPC_SET_ID
$       id
         1
```

```
$     nsid       cid      dofx      dofy      dofz     dofrx     dofry     dofrz
         2         0         1         1         1         0         0         0
$---+----1----+----2----+----3----+----4----+----5----+----6----+----7----+----8
*CONTACT_RIGID_NODES_TO_RIGID_BODY_ID
$      cid
         1
$     ssid      msid     sstyp     mstyp    sboxid    mboxid       spr       mpr
         1        19         2         3         0         0         0         0
$       fs        fd        dc        vc       vdc    penchk        bt        dt
   0.50000   0.50000       0.0       0.0       0.0         0       0.0 .1000E+21
$      sfs       sfm       sst       mst      sfst      sfmt       fsf       vsf
     1.000     1.000       0.0       0.0     1.000     1.000     1.000     1.000
$     lcid       fcm        us
        82         2       0.0
$     soft    sofscl    lcidab    maxpar     sbopt     depth     bsort    frcfrq
         0       0.0         0       0.0       0.0         0         0         0
$   penmax    thkopt    shlthk     snlog      isym     i2d3d    sldthk    sldstf
       0.0         0         0         0         0         0       0.0       0.0
$     igap    ignore    dprfac    dtstif     blank     blank    flangl
         1         0       0.0       0.0                           0.0
$---+----1----+----2----+----3----+----4----+----5----+----6----+----7----+----8
*DEFINE_CURVE_TITLE
Loading
$     lcid      sidr       sfa       sfo      offa      offo    dattyp
       123         0     1.000     1.000       0.0       0.0         0
$    abscissa (time)    ordinate (value)
        0.000000E+00        0.000000E+00
        0.200000E-01       -0.300000E+01
*DEFINE_CURVE_TITLE
for Contact
$     lcid      sidr       sfa       sfo      offa      offo    dattyp
        82         0     1.000     1.000       0.0       0.0         0
$    abscissa (time)    ordinate (value)
        0.000000E+00        0.000000E+00
        0.100000E+00        0.250000E+02
        0.200000E+00        0.150000E+03
        0.300000E+00        0.750000E+03
$---+----1----+----2----+----3----+----4----+----5----+----6----+----7----+----8
*NODE
$    nid               x               y               z      tc      rc
       1 6.125742275E-17 0.000000000E+00 1.224606354E-16
...
$---+----1----+----2----+----3----+----4----+----5----+----6----+----7----+----8
*ELEMENT_SHELL
$    eid     pid      n1      n2      n3      n4
       1       1     183     185     178     179
...
$---+----1----+----2----+----3----+----4----+----5----+----6----+----7----+----8
*END
```

Appendix H: Disclaimer on work performed

The work presented in this dissertation was funded jointly by Boeing and the FAA as a part of the AMTAS Composites Crashworthiness Research Program during 2008-2013. The work presented in this dissertation reflects the work done by Bonnie Wade, with assistance from the following students. Any work otherwise referenced in this dissertation that was not completed by Bonnie Wade is credited as such in the body of the dissertation.

Bonnie Wade: Conducted all sinusoid (semi-circular, high, and low) crush testing of plain-weave fabric specimens. Conducted all tubular shape (tube, 2x channels, 2x corners) crush testing, assisted by Gally Galgana for test preparation, pictures, and test video.

Conducted a study on the failure strain parameters which lead to the ability to model both UD and fabric material systems using the same basic model definition and two separate contact types, by only making slight changes for different material systems. This study lead to the "revision two" sinusoid and shapes crush models (updated solver, precision, control cards, part definition, material properties) which solved several unknown instability issues.

Interpreted and modified MAT54 source code. Modifications made upon the elastic definition, failure criterion, and post-failure behavior. Single element and crush models rerun using modified code.

Francesco Deleo: Developed initial "revision one" sinusoid and shapes crush models. Conducted initial single element MAT54 study with assistance from Bonnie Wade.

Morgan Osborne: Conducted complete MAT54 single element study using "revision two" model definition (updated solver, precision, control cards, part definition, material properties), with guidance from Bonnie Wade.

Francesca Garattoni: Conducted flat and sinusoid crush tests of UD material specimens prior to beginning of funded AMTAS program. The findings of this work are published in [85]. The measured load-displacement curve from one UD sinusoid crush test was used in this dissertation as an experimental reference curve for the MAT54 analysis performed by Bonnie Wade.